Star Formation in Dwarf Galaxies: Using the Radio Continuum as an extinction-free probe

By

Ged Kitchener

A thesis submitted to The University of Hertfordshire
in partial fulfilment of the requirements of the degree of
Doctor of Philosophy

Centre for Astrophysics Research

October 2015

Typeset in LaTeX 2_ε.

Except where acknowledged in the customary manner, the material presented in this thesis is, to the best of my knowledge, original and has not been submitted in whole or part for a degree in any university.

Ged Kitchener

Abstract

To eliminate uncertainties introduced by extinction by dust in the optical, we examine to what extent the radio continuum (RC) can probe star formation in dwarf galaxies. Star formation (SF) drives galaxy formation and evolution; acquiring accurate measurements of SF thus becomes crucial in order to understand galaxies.

As radio technology improves further, RC surveys will probe the fainter, more quiescent regime of the radio sky. Having a robust manner by which to convert RC luminosities to star formation rate (SFR) has the potential to provide millions of independent SFR measurements out to intermediate redshifts.

In order to calibrate the RC to infer SFR, the 40 dwarf galaxies that make up the LITTLE THINGS sample were chosen as the bedrock of the thesis due to the large range of galactic parameters that they cover. RC observations of these galaxies were taken with the VLA between *L*- and *Ka*-band (1–33 GHz) using the B-, C-, and D-arrays, yielding images with 3–10″ resolution and rms noise levels between 3 and $15\,\mu\mathrm{Jy\,beam^{-1}}$.

On a global scale, 27 out of the 40 dwarf galaxies exhibited RC emission above the detection threshold, 17 of which were new RC detections. The general picture is an interstellar medium (ISM) largely void of RC emission, interspersed by isolated pockets of RC associated with SF regions; this general picture agreed with what was expected given current models of dwarf galaxies—weaker magnetic fields in the ISM leading to a higher escape of CRe (and resulting reduction in $\mathrm{RC_{NTh}}$ emission). This was also backed-up by the relatively low $\mathrm{RC_{NTh}}$ fraction—$61 \pm 7\%$ at *C*-band.

The observed RC–SFR relation was calibrated to allow the observed RC luminosity of a gas rich dwarf galaxy to be used to infer the SFR; the calibration takes the form $\mathrm{SFR}\,[\mathrm{M_\odot\,yr^{-1}}] = 5 \times 10^{-18}(\mathrm{RC}\,[\mathrm{W\,Hz^{-1}}])^{0.85}$.

On a resolved basis, only the $\mathrm{RC_{NTh}}$ was examined—this is because whether scales of 1 pc, or 1 kpc are investigated, the relationship between the Hα (current SF) and $\mathrm{RC_{Th}}$ was not expected to change. Calibrating the resolved $\mathrm{RC_{NTh}}$–SFR

relation was best done when using discrete SF regions which varied from 10s up to 100s of pc in size. On these scales, the calibration allows the SFR to be inferred from an observed $\mathrm{RC_{NTh}}$ luminosity, and takes the form $\mathrm{SFR}\,[\mathrm{M_\odot\,yr^{-1}}] = 1.36 \times 10^{-23}(L_{\mathrm{NTh}}\,[\mathrm{W\,Hz^{-1}}])^{1.15}$. This calibration, however, is only valid for resolved regions forming stars at a rate $\gtrsim 2 \times 10^{-4}\mathrm{M_\odot\,yr^{-1}}$. Despite the low flux densities of $\mathrm{RC_{NTh}}$ measured from these discrete SF regions, the $\mathrm{RC_{NTh}}$ still works well as a SFR tracer whereas Hα, which is largely dependent on stars with mass $\gtrsim 18\,\mathrm{M_\odot}$, and is thus dependent on the high mass tail of the stellar IMF, will suffer from stochasticity.

In a few dwarfs, the equipartition magnetic field strength reaches as high as $30\,\mu$G in multiple 100 pc regions, and in one case, $70\,\mu$G. However, generally, the weaker magnetic fields in the ISM give the CRe longer lifetimes, and thus more time to be advected out of the galaxy with the magnetic fields frozen into the gas in outflows, or diffuse. This explains in part the lack of $\mathrm{RC_{NTh}}$ emission observed in the ISM of dwarf galaxies.

Through implementing a simple galactic CRe model, it was found that the $\mathrm{RC_{NTh}}$ emission associated with the CRe can be used as a SF tracer from approximately 5 up to 70 Myr following a burst of SF, while $\mathrm{RC_{Th}}$ can be used in its absence prior to 5 Myr. The $\mathrm{RC_{NTh}}$ luminosity reaches its peak approximately 55 Myr after the SF episode, but actually remains nearly constant over the 60 Myr following the SF episode, highlighting its potential to be used to infer SFR. The CRe model also tracked the evolution of the $\mathrm{RC_{NTh}}$ spectral index with time. Between values of about -0.4 and -0.7, the $\mathrm{RC_{NTh}}$ spectral index can be calibrated to infer the time elapsed since a burst of SF through $t[\mathrm{Myr}] = -25\alpha_{\mathrm{NTh}}$. $\mathrm{RC_{NTh}}$ spectral indices of -0.8 are consistent with ages between 20 and 55 Myr, suggesting that the oft observed spectral index of -0.8 in galaxies may come from the fact that *C*-band $\mathrm{RC_{NTh}}$ emission is dominated by the steep spectral indices of -0.8 from these older SF regions (20–55 Myr).

For the galaxies that displayed $\mathrm{RC_{NTh}}$ emission that was bright enough and sufficiently well resolved, a spectral decomposition of the RC spectrum was performed to infer Hα-independent $\mathrm{RC_{Th}}$, $\mathrm{RC_{NTh}}$, and $\mathrm{RC_{NTh}}$ spectral index maps. The spectral decomposition showed DDO 50 and NGC 1569 to have a low thermal fraction of 23% and 10%, respectively, at *C*-band, while NGC 2366 and NGC 4214 were shown to have higher thermal fractions of 48% and 66%, respectively.

In summary, dwarf galaxies are not only faint in the RC due to their lower SF activity, but they are also *fainter than expected* due to CRe escape. Nonetheless, the RC *can* be used to probe SF in dwarf galaxies not only on a global scale, but also within discrete SF complexes 10s to 100s of pc in size. Theoretically, the RC can be used

right from the onset of a burst of SF, where $\mathrm{RC_{Th}}$ will dominate, up to $\sim 70\,\mathrm{Myr}$, at which point $\mathrm{RC_{NTh}}$ will dominate. Calibrated by the RC observations in this thesis, both resolved and global SFRs of gas rich, low mass galaxies can be inferred with an uncertainty of ± 0.2 dex; the relations allow SFRs of between approximately 2×10^{-4} and $0.1\mathrm{M}_{\odot}\,\mathrm{yr}^{-1}$ to be inferred.

Acknowledgements

For the majority of people, the acknowledgements section gives more insight to my life's work than the thesis itself. Therefore, I have chosen not to whittle my thoughts down to a few soundbites, but rather to detail life's little happenings which, when amplified with time, have led to the completion of my doctoral thesis. The thesis was in no way earned solo; it is the culmination of a great number of events and personalities, not just during my life, but before.

An interest is borne: My story starts before I was even a twinkle in my Dad's eye: an interest in Space passed down from my maternal Grandfather to his daughter, my Mother. Perhaps my own interest in Space was hereditary, a genetic glitch, but whatever the case, my life seemed destined for the stars. My Mum claims that one of my first words was "*spaceship*", although I have my doubts given the word's complexity! My Mum, recognising my seemingly natural affiliation with Space, decided to complement this by adorning my bookshelf with many a Space encyclopaedia, which I still have to this day.

The interest gains substance: But astronomy became a more formal aspect of my life during the second year of A-level at Writhlington School where, with the enthusiastic help of the best Physics teachers ever: Mr. Hicks and Mr. Scattergood—both great teachers in their own right, Mr. Hicks embellished his classes with his "*picture the scene: hair down to here...*" stories, while Big D lit up the room with his omnipresent smile—I finally had some science to add to my lifelong awe. My intoxication with Space was so great at this point, that the prospect of enveloping myself in a bubble of astrophysical qualifications was a no-brainer. Enter the University of Exeter: I opted to start a BSc in Physics with Astrophysics. There were some inspirational professors there, but I would like to single out Prof. Mark McCaughrean. He made the tutorials interesting and was always willing to chat afterwards.

Immersion into research: After Exeter, I realised that a career in astronomy was the next logical step, but upon realising that the research environment of a Ph.D was a jump too far, I enrolled myself on a self-funded Masters project at the University of Bristol under the supervision of Dr. Ben Maughan. He was a fantastic supervisor, always supportive and patient, and showed me the ropes of programming—a skill that eventually would allow me to hit the ground running in the Ph.D. I remember the day of the Ph.D interview well: at around midday, I was invited to speak briefly with Prof. Elias Brinks. Elias and I started talking and rapidly descended into a reminiscing session—*memorias mexicanas: la comida, el clima, la cultura. Cómo las extrañamos!* Before we knew it, there were 5 minutes left of our slot, and we quickly squeezed some talk of potential science. Soon after, I was offered the Ph.D under his supervision—could I have asked for a more human, approachable supervisor, with the added benefit of 30 years experience? I don't think so. And so, in October 2011, my 3 years and 6 months started of the Ph.D program at the University of Hertfordshire. My experience of working in astronomy is best encapsulated by one of Confucius' greatest observations: "*the man who loves his job never works a day in his life*".

The people: Professionally speaking, my most heartfelt appreciation goes to Elias, the black-belt in radio astronomy. He was always willing to explain the intricacies of interferometry and star formation, and I will be forever indebted to the time he devoted to my development. I want to also single out Volker Heesen who has helped a great deal, especially with his expertise on magnetic fields. In addition to the *dynamic duo*, I would also like to mention Dan Smith who, amongst helping out with his IR-related expertise, was kind enough to give me a mock viva, and Urvashi Rau and Martin Hardcastle who have themselves spent a good amount of time explaining concepts with me. A special thank you is also extended to John Atkinson who tirelessly kept the STRI cyber world ticking over. For my first paper, I would also like to thank Aritra Basu for sharing his equipartition scripts, the anonymous referee who helped improve the manuscript with their suggestions, and my two examiners—Dr. Jim Geach and Dr. Rob Beswick— who gave me a memorable 3 and half hour viva. In addition to these, I think a great disservice would be done if I were to ignore the faceless hoards of people on the internet who post solutions to programming difficulties, especially on `stackoverflow.com/` and `tex.stackexchange.com/`! Along the way, it has been a pleasure sharing my Ph.D stories with those outside of the astronomy community: my beloved wife, Ylvi; my darling siblings, Jack and Char, and my lifelong friends from back home in the Radstock area, Luke, Chris, and Simon.

In terms of institutions, I would also like to acknowledge the combined support of the STFC (UK) and the University of Hertforshire, and also the indirect support from the National Science Foundation (US) and the National Radio Astronomy Observatory (US). The investment from these institutions allowed me to pursue a career that I thoroughly enjoyed, while simultaneously developing my industrial skills. Bar becoming a millionaire, this period of my life will probably be the closest I ever get to a 'jet-set lifestlye'—visiting numerous conferences throughout the world has given me unforgettable memories.

The Ph.D allowed me to open up, especially with outreach, where in a beautiful way, the story almost comes full circle: I was gifted fantastic opportunities and enviable resources by the University to pass on my knowledge to the next generation of budding astronomers. Occasionally, I see over-enthusiasm in the little ones and can't help but see myself when I was that age.

The end of the beginning: As much as I have enjoyed the journey, and the privilege of working alongside world experts (the real celebrities) and state-of-the-art instruments, I feel now is a natural moment to move on, and away from academia. I will miss it dearly, but will never forget.

Contents

List of Figures

List of Tables

1

Introduction

1.1 Preamble

Star formation (SF) is an important, on-going process in the current Universe; it is what drives galaxy formation and evolution. Acquiring accurate measurements of SF thus becomes crucial in order to understand galaxies. Many regions of the electromagnetic spectrum are utilised to ascertain the star formation rate (SFR), although they all have their inherent limitations such as dust attenuation in optical bands. The radio continuum (RC) is not directly affected by dust, and therefore provides a tantalisingly simple method with which to measure SFR. As radio technology improves further, *viz.* the development related to the Square Kilometer Array (SKA), RC surveys will probe the fainter, more quiescent regime of the radio sky. Having a robust manner by which to convert RC luminosities to SFR has the potential to provide millions of independent SFR measurements out to intermediate redshifts.

A well-calibrated and understood RC–SFR relation is indispensable for interpreting future large, all-sky RC surveys. With the increased sensitivity of instruments like the SKA, surveys will possess the ability to observe deeper than ever before,

which means probing the fainter end of the galaxy luminosity function. These fainter objects will likely be normal star forming galaxies, as opposed to the most actively SF galaxies which are just the tip of the iceberg. Their metallicities are expected to be lower than that of the Galaxy. Therefore, a well-calibrated RC–SFR relation across a range of metallicities will allow the conversion of a large population of RC luminosities to SFRs.

To calibrate the RC–SFR relation with the intention of applying it to large population of galaxies, dwarf galaxies are good calibrators in the sense that they span a range of metallicities. Also, dwarf galaxies lack Active Galactic Nuclei and, due to their low mass, their SF is more stochastic than, e.g., in spirals, and so the *raw* SF process is laid bare, free from large-scale effects such as spiral density waves.

Of all the objects in the local Universe, dwarf galaxies are probably the best analogues of the first ever galaxies—they are physically small, have low mass, and have low quantities of dust. Therefore understanding how the RC originates from SF processes in these local analogues can justifiably pave a way to understanding how RC originates from SF processes when the first galaxies started to form stars.

Calibrating the RC–SFR relation contributes another method with which to gather SFR measures of large, all-sky populations. This would provide independent measurements of Cosmic SFR out to intermediate redshifts (e.g., Murphy, 2009; Lacki et al., 2010; Padovani, 2011), complementing other intermediate all sky surveys such as the $22\mu\mathrm{m}$ WISE survey (e.g., Yan et al., 2013). As an off-shoot, the RC analysis can also provide sanity checks on *theoretical* $\mathrm{RC_{Th}}$–Hα conversion factors (e.g., that of Deeg et al., 1997 or Murphy et al., 2011).

1.2 Star Formation in Dwarf Galaxies

Dwarf galaxies fall towards the lower end of the galaxy mass function and closely resemble some of the properties of galaxies at early epochs—they are clumpy in their morphology, and have a low dust content. SF is arguably one of the most important processes in the Universe; understanding it in local dwarf galaxies can go some of the way to help improving the understanding of SF at these early cosmological times (with some important caveats to be mentioned in Section 1.2.3). There are many tracers used to probe SF, but this study opts to use the RC, mainly due to its *unambiguous* link to SF and its *immunity* from extinction (Condon, 1992). The RC has never been successfully calibrated to probe SF in a large population of dwarf galaxies—which is exactly the motivation behind this study. The remainder of Chapter 1 expands on

the points raised in this paragraph.

Star formation has been an integral process of the Universe for most of its existence. Since re-ionisation of the Universe, SF has been responsible for the creation of most of the energetic photons, galactic winds, and metal enrichment, and has contributed to the ideal environment for life to develop.

Spiral galaxies dominate SF in the local Universe (SF at intermediate redshifts was dominated by larger galaxies, which have since evolved into the 'red and dead' ellipticals observed locally; see downsizing in Cowie et al., 1996), and the rate of SF in spirals is high enough that secondary effects (i.e., the emission of SF tracers) are strong enough to be observed. So why study SF in dwarf galaxies, as opposed to spiral galaxies?

1.2.1 Simple Star Formation

To answer why SF should be studied in dwarf galaxies, the fundamental difference between spiral galaxies and dwarf galaxies must first be brought to the fore: their mass. Dwarf galaxies, having a lower mass ($M_{tot} \lesssim 10^9\,\mathrm{M}_\odot$, dominated by dark matter), generally lack the presence of strong spiral density waves. Without such structures, the dwarf galaxy's gas remains at the whim of random processes. Instead of being compressed in spiral arms (a global process), the gas follows local effects and, since they are local, by definition this implies multiple independent regions. SF in dwarf galaxies is thus stochastic in nature, in both a temporal and spatial sense. This stochasticity essentially means that SF can be studied without having to factor in external inductors such as AGN, spiral arm shocks, or gravitational interactions.

1.2.2 Star Formation Tracers

For stars to form, a reservoir of gas is required. The SF process is inefficient in that typically only 2–5% of the mass involved is converted into stellar mass (e.g., Bigiel et al., 2008; Walter et al., 2008; Leroy et al., 2008; Leroy et al., 2012), rising to 10% in the most extreme cases. In the simplest model, SF begins when gas on scales of a few 100 pc crosses a density threshold (Toomre, 1964). The Kennicutt–Schmidt relation empirically quantifies this effect where, when integrated along the line of sight, the SFR surface density, Σ_{SFR} or SFRD, is related to the gas surface density, Σ_{gas}, through the power law relation

$$\Sigma_{\mathrm{SFR}} \propto \Sigma_{\mathrm{gas}}^{n}, \tag{1.1}$$

where $n = 1.40 \pm 0.15$ (e.g., Kennicutt, 1998, Kennicutt & Evans, 2012). Towards smaller scales, the relation described by Equation 1.1 breaks down. This is expected because at sufficiently small scales, the radiation from newly formed stars disperses the gas cloud in which the stars were formed, inflating a bubble surrounded by a shell of ionised Hydrogen—the stars and gas become disconnected.

The Kennicutt–Schmidt relation essentially looks at the gas reservoir available for future SF—it is more a predictor of SF rather than a SFR indicator. Stars form from molecular gas, H_2, rather than from the atomic phase. H_2 is usually traced by CO. Again, this is not a SF tracer, but a proxy for the quantity of gas available to form stars.

Once the stars have formed, the energy output from stars is used to trace the SF activity instead of the gas itself. The following paragraphs briefly describe the mechanism of how certain observables come about following the formation of stars:

Hα: Formally speaking, Hα is the J $= 3 - 2$ Balmer line emission of ionised Hydrogen. It occurs because photons of $\lambda < 912$Å originating from the most massive, short-lived stars ($M > 18 M_\odot$, $t_{\rm life} < 10$ Myr; Hunter & Elmegreen, 2004) ionise surrounding Hydrogen. The free protons may then recapture free electrons, initially in high-energy states, but which can cascade down to more stable levels. A common transition is for the electron to cascade from the $3^{\rm rd}$ to the $2^{\rm nd}$ level, emitting a precise amount of energy in the process—this Hα emission—an example of line emission. However, the plasma in the H II region also emits a continuum, primarily due to the very same free electrons interacting with free ions. This is Bremsstrahlung emission, and lasts as long as there remain massive stars to maintain a Strömgren sphere, which is of order 10 Myr (Leroy et al., 2012). The $\mathrm{RC}_{\rm Th}$ is mostly confined to H II regions, and is dependent on these most massive, short-lived stars which end their existence as supernovae (SNe) approximately 1–10 Myr after the SF episode. Some of the ionising photons may leak out of the H II regions creating a diffuse component (Hunter & Gallagher, 1992; Ferguson et al., 1996). This diffuse component becomes more dominant for galaxies with lower SFRD such as dwarf galaxies (e.g., Helmboldt et al., 2005; Helmboldt, 2005; Oey et al., 2007). Calibrating Hα emission as a SFR tracer has proven to be successful (e.g., Kennicutt & Kent, 1983; Hunter & Elmegreen, 2004; Kennicutt et al., 2008), however it is sensitive to extinction by dust.

FUV: Photons in the FUV bracket (1344–1786 Å) originate directly from the photospheres of hot young stars. FUV emission is better than Hα at representing the SFR of a galaxy as a larger proportion of the stellar population create FUV photons than

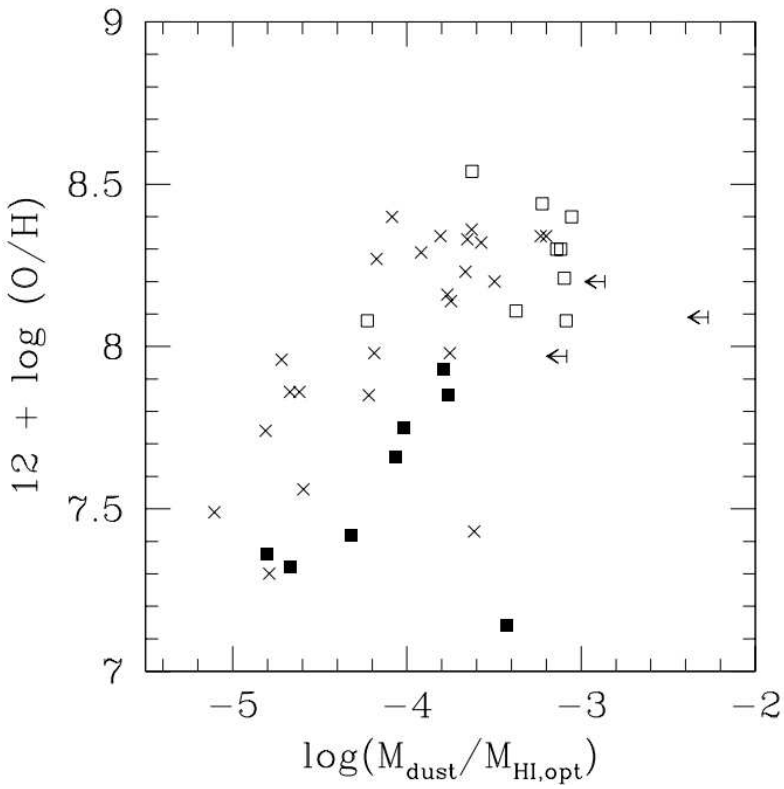

FIGURE 1.1: Dust-to-gas ratio in dwarf galaxies. The lower the metallicity of a dwarf galaxy, the lower the proportion of mass tied up in dust there is (Lisenfeld & Ferrara, 1998).

ionising photons; this also makes FUV-inferred SFRs less sensitive to the population of the high-mass end of the stellar IMFs. For a given SFR, the Hα emission can underestimate the SFR given by FUV by a factor of 2, increasing to a factor of 10 for the least active dwarfs (SFR $\sim 10^{-4}\,\mathrm{M}_{\odot}\,\mathrm{yr}^{-1}$) (Wyder et al., 2007; Lee et al., 2009). This is because only the highest mass stars ($M > 18\mathrm{M}_{\odot}$) produce a significant number of photons to ionise the surrounding H I; having a deficit of these stars would affect the amount of Hα emission, while the FUV emission would not necessarily be affected as much since a larger fraction of the stellar population contributes to the FUV emission (Weidner & Kroupa, 2005). Accordingly, Lee et al. (2009) conclude that, in dwarf galaxies, FUV emission is a better indicator of current SF than Hα.

FUV has successfully been used to calibrate large all-sky surveys (e.g., Lee et al., 2007; Lee et al., 2009), however dust attenuation ordinarily has a larger effect on FUV than on Hα and this provides an argument against using FUV. However, this is not a serious issue in dwarf galaxies since they have lower dust content when compared to spirals (e.g., Lisenfeld & Ferrara, 1998; Bigiel et al., 2008; Ficut-Vicas et al. 2015, in prep.), which provides another incentive to using FUV as a direct measure of current SF (see Figure 1.1).

24 μm MIR: The UV photons from the OB stellar associations heat dust in their immediate vicinity, although the origin of the dust is open to debate: the dust may have been produced recently *in situ* as a result of the supernovae (e.g., Indebetouw et al., 2014) or from post-AGB stars related to the SF event (e.g., Valiante et al., 2009; Zhukovska & Henning, 2013), or may be dust in the general ISM that was formed by the previous generations of stars.

70 μm FIR: The FIR emission originates from the blackbody radiation of diffuse ISM dust heated in part by the UV radiation field, which means that $70\mu\mathrm{m}$ FIR is sometimes used as a SF tracer. The relation between the SFR with the FIR is not quite as obvious as with the MIR because some of the dust-heating responsible for the FIR emission is caused by the interstellar radiation field (ISRF) of the old stellar population; Irwin et al. (2013) suggest that the ISRF is the *main* contributor to dust heating, which contrasts with MIR emitting dust, which comes from stochastic heating by UV photons of OB stars, indicating a recent SF episode.

Infrared wavelengths have been used to infer SFR of large all-sky surveys (e.g., Yun et al., 2001; Kennicutt et al., 2003; Skrutskie et al., 2006). However, an assumption about the blackbody shape of the dust needs to be made, as well as the contribution from older stars. In addition to the physical mechanism that brings about FIR emission, there are also the technical aspects: deep FIR observations rely on space-based observatories (e.g., *Spitzer* and *Herschel*) that have limited lifetimes and apertures. The modest apertures lead to resolutions that cannot compete with those currently available at optical or radio wavelengths.

SFR prescriptions: Using multiple regions of the electromagnetic spectrum together to infer SFR can overcome the limitations of using a single band. These SFR prescriptions use the assumption that the energy input from SF spreads itself over the electromagnetic spectrum in a distinctive way. Observed flux densities at various points on the spectrum can be compared with a calibrated model spectrum (e.g., da Cunha et al., 2008; Galametz et al., 2013). Another method to infer SFR is to assume that the energy that is not radiated in one band is instead reradiated in another (e.g., Calzetti et al., 2007; Leroy et al., 2012).

SFR prescriptions have been successfully used (e.g., Calzetti et al., 2007; Leroy et al., 2012; Galametz et al., 2013), but require matched resolution images across multiple regions of the electromagnetic spectrum. In practice, this makes prescriptions difficult to implement on a large selection of sources such as an all-sky survey.

Radio Continuum: As will be seen in Section 1.3.1, the RC has an unambiguous link to SF. The only objects that can contaminate this RC emission are AGN (which are always located in the centres of spiral galaxies, and never in the arms, let alone in dwarf galaxies) and Anomalous Microwave Emission (AME, which can be significant at frequencies as low as $\sim 20\,\mathrm{GHz}$, e.g., Dickinson, 2013).

Condon et al. (2002) developed a RC–SFR relation, although it was based on data from the Milky Way, and was applied to spiral galaxies on a global scale. More recently, Heesen et al. (2014) used long wavelengths dominated by $\mathrm{RC_{NTh}}$ emission to examine how the RC–SFR behaves on a resolved basis in a sample that mainly comprised spiral galaxies. Murphy et al. (2012) used shorter wavelengths dominated by $\mathrm{RC_{Th}}$ emission to examine the RC–SFR, finding that the $33\,\mathrm{GHz}$ emission provides a "robust star formation rate (SFR) indicator".

Deriving a well-calibrated RC–SFR relation based on dwarf galaxies will be valuable when applied to large, all-sky RC surveys. With the increased sensitivity of instruments like the SKA, surveys will possess the ability to observe deeper than ever before, which means probing the fainter end of the galaxy luminosity function. These fainter objects will likely be normal galaxies in a quiescent mode of SF, as opposed to the most actively star forming galaxies which are just the tip of the iceberg. Therefore, a RC–SFR relation based on observations of dwarf galaxies may provide the best means by which to convert large sets of RC measurements to SFR quantities.

Despite its promise, the stochastic origin of the RC is potentially an issue. $\mathrm{RC_{NTh}}$ emission originates from SNe, which themselves go supernova randomly; this results in a stochastic injection of new CRe. However, this does not mean that the $\mathrm{RC_{NTh}}$ itself is stochastic: the lifetimes of CRe are much longer than the lifetime of SNR: with relevancy to *C*-band, the CRe lifetime is $\sim 10\,\mathrm{Myr}$—this is about 1000 times longer than the lifetime of a single SNR which is $\sim 10^4\,\mathrm{yr}$.

1.2.3 High-redshift analogues

The first ever galaxies formed at a redshift of ~ 10, or $\sim 0.5\,\mathrm{Gyr}$ (Wright, 2006) after the Big Bang. Of all the objects in the local Universe, dwarf galaxies are probably one of the closest analogues to these first ever galaxies in a range of properties—they are physically small, have low-mass, possess low quantities of dust and heavy elements in general, and are clumpy in their morphology (e.g., GN-z11, Oesch et al., 2016).

SF in the early Universe would likely have been dominated by galaxies harbouring these types of characteristics. For example, GN-z11 is one of the most distant galaxies discovered having a redshift of 11.1 or $13.4\,\mathrm{Gyr}$ old (Oesch et al., 2016): it

has a stellar mass of $1 \times 10^9 \mathrm{M}_\odot$, and undoubtedly a low metallicity making it much like local dwarf galaxies. However, this comes with a gas fraction of 99% and SFR of $24 \pm 10 \mathrm{M}_\odot\,\mathrm{yr}^{-1}$ which is very uncharacteristic of dwarfs in the local Universe—this means our "close analogue" claim is only correct in a limited sense.

At intermediate redshifts, SF was dominated by larger galaxies, which after a period of high SFR, depleted their supply of gas. Currently, the low quantities of gas in these galaxies mean that there is little SF (hence the term: 'dead' ellipticals). This leads to a stellar population dominated by older, cooler stars (hence the term: 'red' ellipticals). This long-term trend of SF changing from being predominantly in large galaxies to now being in smaller galaxies goes by the name of 'downsizing' (Cowie et al., 1996).

With low mass, large scale structure such as spiral density waves were probably not prevalent, and SF occurred stochastically giving the first galaxies a clumpy appearance. This is backed up by observations of galaxies at high redshift, where their light distribution is less likely to be fit by a series of ellipses, although this may be related to the higher merger rates (e.g, Lintott et al., 2008; Häußler et al., 2013; Illingworth et al., 2013).

Dwarf galaxies, too, have a clumpy morphology, due to episodic and sporadic SF. The clumpy morphology coupled with the lack of spiral arms translates to magnetic fields being dominated by a turbulent component. Many dwarf galaxies have been shown to be solid body rotators, and with this lack of large-scale shear, the process by which ordered fields are amplified is not very efficient.

Local dwarf galaxies have $12 + \log_{10}(\mathrm{O/H})$ metallicities of less than ~ 8.0 (solar metallicity being 8.69 ± 0.05; Asplund et al., 2009). Some of most metal poor galaxies known are the dwarf galaxies IZw 18 and SBS 0335-052, both about 1.5 dex lower than solar metallicity (Kunth & Östlin, 2000).

Therefore understanding how the RC relates to SF in these local analogues can justifiably pave a way to understanding how RC relates to SF when the first galaxies started to form stars.

1.3 Why the Radio Continuum?

To study SF in dwarf galaxies, a choice of observable needs to be made: in this study, the primary focus is on the radio continuum, the justification of which is outlined in this Section.

Optical bands have been used to directly (e.g., through UV or UBV photons from

the photospheres of stars) or indirectly (e.g., through Hα line emission from surrounding ionised Hydrogen) trace ongoing star formation, albeit with inherent limitations: internal (*in situ*) and external (foreground) extinction due to dust.

The dust internal to the star forming regions can be assumed to be in equilibrium with the ambient interstellar radiation field. The result is that the absorbed energy from stars must be recycled as blackbody radiation at mid- to far-infrared wavelengths. This concept has motivated the development of what are now referred to as "optical + infrared" star formation rate prescriptions (e.g., Calzetti et al., 2010; Leroy et al., 2012)—prescriptions that supplement optical tracers with infrared tracers to account for reradiated energy from optical photons. Even with these multifrequency star formation rate prescriptions, the external extinction still hinders accurate measurements.

One technique to avoid external extinction is to observe star formation at long wavelengths (where long means anything larger than the size of the absorbing dust grains). Any photon with a wavelength greater than a few μm satisfies this and includes infrared, millimetre, and radio wavelengths.

These viable wavelengths all have their own unique advantages and disadvantages. This study, believing that the advantages outweigh the disadvantages, has chosen radio emission to be the main weapon of choice. Radio wavelengths:

- have an unambiguous origin related to SF (Condon, 1992);
- are not contaminated by emission from old population stars, unlike, e.g., far-infrared observations (Irwin et al., 2013);
- eliminate the necessity to account for both internal and external extinction due to dust grains;
- are long enough to allow the implementation of interferometry to increase the resolution of observations (see Sections 1.3.6 and 3.2.1);
- have a higher flux density than millimetre wavelengths[1];
- allow a window through which to study magnetic fields (e.g., Beck & Krause, 2005).

These points will be described in detail in the remainder of this section.

[1] Although, they do have a lower flux density than infrared wavelengths

1.3.1 Radio Continuum Link to Star Formation

The radio continuum comprises two main contributions: a thermal component ($\mathrm{RC_{Th}}$) and a non–thermal component ($\mathrm{RC_{NTh}}$). Both these components have a very clear and unambiguous link with recent and ongoing star formation.

During SF, a proportion of the energy released is transferred to electrons. In both the cases of $\mathrm{RC_{Th}}$ and $\mathrm{RC_{NTh}}$ emission, it is the acceleration of, primarily, these electrons that results in the RC radiation. The reason why an accelerating electron emits radiation at all is explained in detail in Appendix A, but the take-home formula is the *Larmor formula* which states the classical power, P, expected from an accelerating point charge,

$$P = \frac{1}{6\pi\epsilon_0 c^3}\Big(qa\Big)^2, \tag{1.2}$$

where ϵ_0 is the permittivity of free space, c is the speed of light, and q is the charge of the particle that experiences the acceleration, a (Longair, 1981).

In the case of the $\mathrm{RC_{Th}}$ mechanism, the acceleration of the electrons is caused by the electrostatic force between thermal electrons and ions, while in the case of $\mathrm{RC_{NTh}}$ mechanism, the acceleration comes from the Lorentz force on ultra-relativistic electrons from magnetic fields.

The RC emission process in dwarf galaxies is illustrated in Figure 1.2, while Sections 1.3.2 and 1.3.3 detail the emission mechanisms of the $\mathrm{RC_{Th}}$ and $\mathrm{RC_{NTh}}$ components, respectively. These sections are condensed wisdom from a combination of Longair (1981), Wilson et al. (2009), and Condon & Ransom (2010).

1.3.2 Thermal RC—Brehmsstrahlung

The $\mathrm{RC_{Th}}$ comes about as follows: photons of $\lambda \leq 912\text{Å}$ ionise hydrogen surrounding the most massive, short-lived stars ($M > 18\,M_\odot$, $t_{\mathrm{life}} < 10\,\mathrm{Myr}$; Hunter & Elmegreen, 2004). The resulting plasma then radiates due to, primarily, free electrons interacting with free ions leading to Bremsstrahlung emission. The $\mathrm{RC_{Th}}$ is mostly confined to H II regions, and is dependent on these most massive, short-lived stars which end their existence as supernovae (SNe) approximately 1–10 Myr after the SF episode.

Theory: Bremsstrahlung emission results from the deflection of freely moving charges (see Figure 1.3). As the electron approaches the ion, both the parallel and perpendicular components of its velocity increase; upon passing the point of closest approach, the parallel component of the velocity decreases as the ion pulls the electron back,

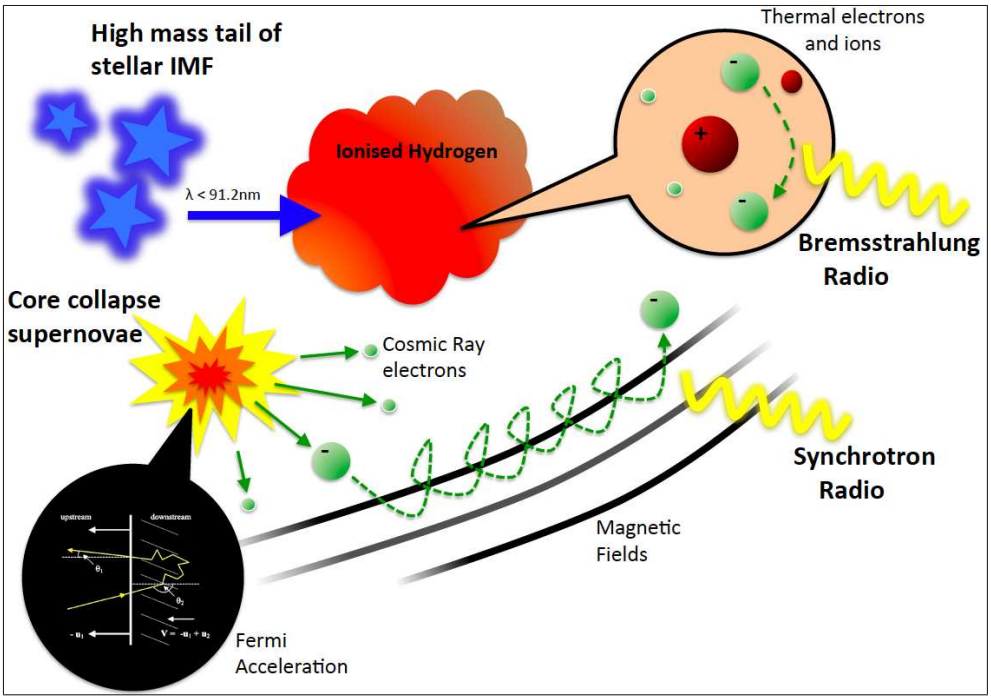

FIGURE 1.2: Annotated illustration of the RC emission mechanism in galaxies.

while the perpendicular component remains positive as the electron continues to be deflected.

This deflection-induced emission has a dependence that goes as the square of the charge-to-mass ratio of a particle, q^2/m^2 (substituting $a = F/m$ in Equation 1.2) and since masses of electrons are ~ 2000 times less than that of protons, free-free emission is dominated by deflected motions of electrons by a factor of $\sim 4 \times 10^6$ compared to ions. Therefore, the theory will concentrate on the dynamics of electrons.

The macroscopic temperature of H II regions is $\sim 10^4$ K. Microscopically, the constituent particles follow a thermal distribution, where since each monotonic particle has 3 degrees of freedom (all translational), the average energy, E_{particle}, of each particle is

$$\frac{3}{2} k_B T = 2.07 \times 10^{-19}\,\text{J} \tag{1.3}$$

where k_B is the Boltzmann constant, while the average energy radiated by a single electron-ion interaction is much less, being

$$E_{\text{interaction}}(b, v) = \frac{\pi}{4} \frac{Z^2 e^6}{c^3 m_e^2} \left(\frac{1}{b^3 v} \right) \tag{1.4}$$

(Condon & Ransom, 2010) for a given impact parameter, b, and electron velocity, v (where Z is the atomic number of the near stationary ion causing the deflection, and e and m_e are the charge and mass of an electron, respectively). Of course, the

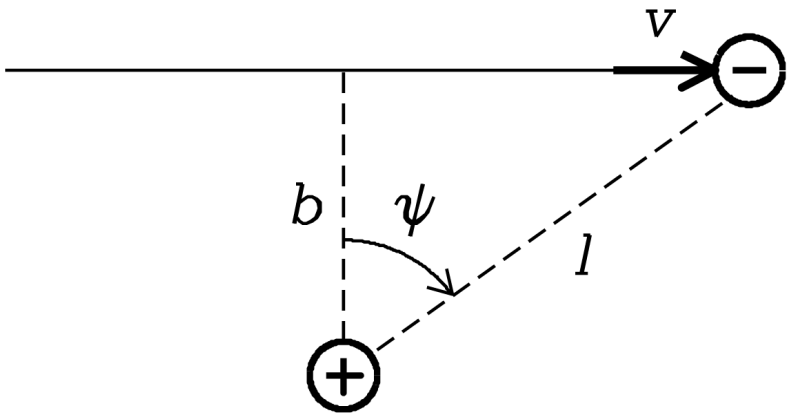

FIGURE 1.3: Schematic of the thermal RC emission mechanism (Condon & Ransom, 2010). As the electron approaches the ion, both the parallel and perpendicular components of its velocity increase; once the electron passes its point of closest approach, the parallel component of the velocity decreases as the ion pulls the electron back, while the perpendicular component remains positive as the electron continues to be deflected.

H II region comprises a population of electrons travelling in random directions, but adhering to a thermal energy distribution. Therefore, to find the total luminosity from a H II region, these electron-ion interactions must be integrated over the range of impact parameters ($b_{\min}$ and $b_{\max}$) and velocities (0 and ∞).

The characteristic spectrum of $\mathrm{RC_{Th}}$ at high frequencies finds its origins in the absorption coefficient, κ_ν, which describes the amount of absorption per unit length; it is approximated by

$$\kappa_\nu \propto \nu^{-2.1}. \tag{1.5}$$

If the absorption occurs along a cylinder whose axis lies along the line of sight, then this describes the total opacity,

$$\tau_\nu = \int_{\mathrm{l.o.s}} -\kappa_\nu \, \mathrm{d}s, \tag{1.6}$$

where s defines the distance along the line of sight. In the Rayleigh-Jeans limit (where frequencies are low, or wavelengths are long), the $\exp(h\nu/k_BT)$-term in the Planck equation can be approximated by a Taylor expansion, the first two terms of which help significantly to simplify the blackbody radiance of an object to

$$I_\nu = 2\frac{k_BT}{c^2}\,\nu^2 \tag{1.7}$$

where I_ν is the intensity of radiation ($\mathrm{J\,s^{-1}\,sr^{-1}\,m^{-2}}$) emitted over some frequency range. This intensity is subject to the opacity which then leads to

$$I_\nu\tau_\nu \propto \nu^{-0.1}. \tag{1.8}$$

Theoretical: The common origin of Hα emission and the $\mathrm{RC_{Th}}$, i.e., the population of thermal electrons in the H II region, forges a direct link between the two observables (e.g., Deeg et al., 1997; Murphy et al., 2011). In the case of Deeg et al. (1997), they relate the radio continuum flux density, $\mathrm{RC_{Th}}$, at a frequency ν, to be directly proportional to the Hα flux, $F_{\mathrm{H}\alpha}$, by

$$\frac{\mathrm{RC_{Th}}}{\mathrm{W\,m^{-2}}} = 1.14 \times 10^{-25} \left(\frac{\nu}{\mathrm{GHz}}\right)^{-0.1} \left(\frac{T_e}{10^4\,\mathrm{K}}\right)^{0.34} \frac{\mathrm{F_{H\alpha}}}{\mathrm{ergs\,s^{-1}\,cm^{-2}}} \tag{1.9}$$

with an additional weak dependence on the electron temperature, T_e.

1.3.3 Non-thermal RC—Synchrotron

The $\mathrm{RC_{NTh}}$ finds its origins in the remnants of core–collapse SNe (SNR) whose progenitors are massive, short-lived stars (Maeder & Meynet, 1989 find the lifetime of $120\mathrm{M}_\odot$ stars to be $3.4\,$Myr, whilst $8\mathrm{M}_\odot$ stars have lifetimes of $55\,$Myr). The shock in the SNR accelerates Cosmic Ray electrons (CRe) to ultra–relativistic velocities (see Reynolds, 2008), which then spiral around magnetic fields producing synchrotron radiation. Between 4 and $8\,$GHz, CRe will typically emit over a timescale of $6\,$Myr in magnetic field strengths of $10\,\mu$G. Over this timescale, an ensemble of CRe may diffuse or be advected out to typically $1\,$kpc from the SF region of origin. This diffusion lengthscale, L_D, is calculated through the diffusion expression $(4Dt_{\mathrm{syn}})^{1/2}$ where D is the diffusion coefficient (taken to be 3–5 $\times\, 10^{24}\mathrm{m^2\,s^{-1}}$; Strong et al., 2007) and the timescale, t_{syn}, is around $6\,$Myr (for a CRe emitting at $6\,$GHz in a magnetic field strength of 10μG; see Section 5.4.1).

Theory: Synchrotron emission is the relativistic extreme of cyclotron emission, which itself results from the deflection (acceleration) of charged particles due to the Lorentz force from magnetic fields (see Figure 1.4). The electron has mass, m_e, charge, e, and it's velocity-vector, $\vec{v}$, is constantly altered by the perpendicular force, $\vec{F}$, acted upon it due to a magnetic field, $\vec{B}$. If the velocity vector is perpendicular to the magnetic field line, then the electron will follow a circular path, where the centripetal force comes entirely from the Lorentz force. From this, the radius of the circle, otherwise known as the radius of gyration can be found, which is

$$r_g = \frac{\gamma m_e c}{eB} \tag{1.10}$$

where, since the electron is ultra-relativistic, the velocity of the electron has been approximated by the speed of light and the rest-frame momentum has been scaled up by the Lorentz factor, γ. Invariably though, the electron will have some component

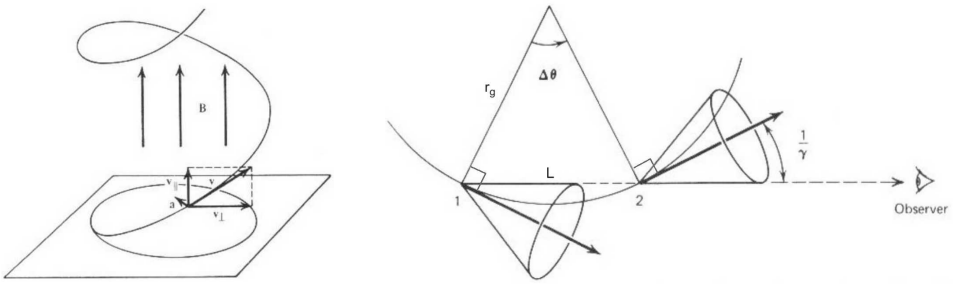

FIGURE 1.4: Schematics of the synchrotron emission mechanism (Lecture 8 of PHYS 4011—HEA by A. De Angelis). *Left:* Velocity parallel to magnetic field is untouched by magnetic force, whilst velocity perpendicular to magnetic field is. The result is helical motion. *Right:* Due to the cone-like solid angle through which emission is mainly directed, synchrotron emission is predominantly viewed when the electron is between two distinct positions (marked 1 and 2) which are separated by an angle, θ.

of its velocity parallel to the magnetic field lines; in this case, it will follow a helical motion.

For a typical magnetic field strength of $10\,\mu$G (see Section 4.4.6 or, e.g., Heesen et al., 2014) and Lorentz factor of 10000 (so that the peak frequency of synchrotron emission is relevant for this study), the radius of gyration is approximately 17 million km (~ 0.1 AU). Even travelling at very close to the speed of light, it would take a long time to complete one orbit, making its gyrofrequency very small (0.003 Hz). This frequency is a world away from the GHz-values of the radio regime of the electromagnetic spectrum.

So how does the electron emit radiation at frequencies much higher than that predicted by this naive classical interpretation? In a sentence: *the observed emission is dominated by the short pulse of light emitted when the electron travels towards the observer; the short pulse can be constructed by multiple photons mainly in the GHz regime*. This is explained in more detail in the rest of this section.

In the rest frame of the CRe, the radiation emitted due to the acceleration is isotropic. However, since the observer sees the electron as relativistic, isotropic emission is not observed; instead the emission is seen to be concentrated in the CRe's direction of travel in a process called *beaming* (see Figure 1.5). Over any given solid angle, the power P' will not necessarily be equal to P, but the total power over $4\pi r^2$ is the same since the power 4-vector is a *Lorentz invariant*.

The beaming ultimately means that the amplitude of the observed electric field varies strongly with time: when the CRe is travelling towards the observer, there is a sharp jump in the amplitude of the electric field, but at all other times, the electric field is much less. Each time the CRe gyrates about the magnetic field line, a strong pulse is observed followed by longer periods of near 'silence' (see Figure 1.5).

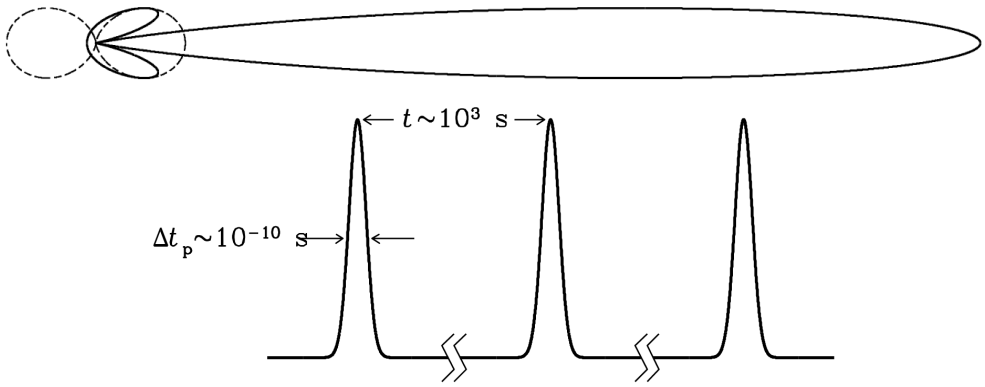

FIGURE 1.5: Schematic of synchrotron radiation from a single ultra-relativistic electron (Condon & Ransom, 2010). *Top:* Dipole radiation observed from a charge moving ultra-relativistically from left to right. Isotropic emission is not observed; instead the emission is seen to be concentrated in the CRe's direction of travel in a process called *beaming*. *Bottom:* Observed amplitude of the electric field originating from a gyrating ultra-relativistic CRe. The values correspond to a CRe with a Lorentz factor of 10^4 gyrating in a magnetic field of strength $5\,\mu$G.

But how do these pulses relate to the spectrum of Synchrotron emission? Of course, there is no photon that has this characteristic Shah function—photons, by their very definition, have a single frequency—and so multiple photons, each with their own amplitude and frequency, have to be created to make the characteristic shape of the stop-start Shah function (the pulse of electric field). Note that the Fourier transform of an observed electric field has a clear link to the spectrum making said electric field[2].

By using the relativistic case of Equation 1.2, and by integrating over all pitch angles (the CRe are assumed to be isotropic especially in a turbulent magnetic field), then the power radiated by the CRe is

$$P_{\mathrm{CRe}} = \frac{2}{3}\frac{\sigma_T c}{\mu_0}\Big(B\gamma\Big)^2 \tag{1.11}$$

where μ_0 is the permeability of free space. The population of CRe follow a power-law distribution which, initially upon injection, is heavily dependent on the CRe's Lorentz factor:

$$dN_{\mathrm{CRe}} = k\gamma^{-2.7}d\gamma. \tag{1.12}$$

The reason that the CRe follow a power law is due to the way in which they gain their energy. When a SN progenitor explodes as a SN, a shock is propagated through

[2]Take an oscillating electric field, where the amplitude does not vary with time (the electric field vector is changing with time, but the amplitude (the envelope between which it is oscillating) is constant with time): this would be a straight horizontal line on a amplitude vs. time axis. The Fourier transform of this is a δ-function: the amplitude is given by a photon with a well-defined frequency. This makes sense, as there is only one frequency and amplitude that could give the electric field.

the ISM which interacts with any fields or particles already present. The shock will therefore encounter a population of CRe. If the velocity vectors of the individual CRe are initially distributed isotropically, then around half of them will eventually cross the shock front, and in doing so, gain some energy. Once on the other side of the shock front, the turbulent magnetic field makes the population of CRe isotropic once more meaning that, again, a proportion of CRe observe the shock to be moving towards them once more. These CRe cross the shock front and gain more energy. The process of CRe crossing the shock front, becoming isotropic, and then escaping or recrossing is repeated. Clearly, since some CRe are scattered away from the shock front each time, there are fewer CRe that can attain higher energies.

Empirical: Unlike the $\mathrm{RC_{Th}}$ (which has accompanying Hα emission borne out of the same physical conditions), the $\mathrm{RC_{NTh}}$ has no such 'counterpart'. Estimating the $\mathrm{RC_{NTh}}$ emission through a proxy is not possible; it must be observed directly.

An empirical relation for the $\mathrm{RC_{NTh}}$ luminosity, L_{NTh}, can be acquired by first noting that the $\mathrm{RC_{NTh}}$ luminosity of a galaxy is directly proportional to its supernova rate, f_{SN}, through

$$\frac{L_{\mathrm{NTh}}}{\mathrm{W\,Hz^{-1}}} = 1.3 \times 10^{23} \left(\frac{\nu}{\mathrm{GHz}}\right)^{\alpha_{\mathrm{NTh}}} \left(\frac{f_{\mathrm{SN}}}{\mathrm{yr^{-1}}}\right) \tag{1.13}$$

(Condon, 1992) where α_{NTh} is the spectral index of $\mathrm{RC_{NTh}}$ emission, defined through

$$\frac{L_1}{L_2} = \left(\frac{\nu_1}{\nu_2}\right)^{\alpha_{\mathrm{NTh}}} \tag{1.14}$$

where L_1 is the luminosity or flux observed at a frequency of ν_1, L_2 is the luminosity or flux observed at a frequency of ν_2. Despite being calculated from Milky Way data, it has been shown that magnetic field strengths in these dwarf galaxies are similar to spirals (see comparison of the results of Heesen et al., 2014 with that of Section 4.4.6), so for now, we assume that Equation 1.13 holds in dwarf galaxies, too. But how does the supernova rate relate to SFR? For this, the form of the stellar IMF needs to be known, which we take from Kroupa (2001). The supernova rate is dependent only on the shape of the stellar IMF for masses above $8\,M_\odot$.

In the Kroupa (2001) stellar IMF, the number of stars, N, within a stellar mass bin ranging from m to $m + \mathrm{d}m$ is described by $dN/dm \propto m^{-2.3}$ for stars with $M > 1M_\odot$. Therefore, the average stellar mass of a $M > 8M_\odot$ star (i.e., a supernova progenitor)

can be calculated by integrating over the relevant range of the stellar IMF:

$$\begin{aligned} M_{\rm SN,avg} &= \frac{\text{Total mass of SN progenitors}}{\text{Total number of SN progenitors}} \\ &= \frac{\int_8^{120} m \frac{dN}{dm}\,{\rm d}m}{\int_8^{120} \frac{dN}{dm}\,{\rm d}m} \\ &= \frac{-\frac{1}{0.3}\left[m^{-0.3}\right]_8^{120}}{-\frac{1}{1.3}\left[m^{-1.3}\right]_8^{120}} \end{aligned} \tag{1.15}$$

which yields the average mass of a SN progenitor to be $M_{\rm SN,avg} = 19.9 M_\odot$. Kroupa (2001) also state that these supernova progenitors comprise 17% of the total stellar mass produced in a star formation event. Therefore, a total of $M_{\rm SN,avg}/0.17$ in stellar mass needs to be produced to create a single SN progenitor. Given the production rate of stellar mass, SFR, the time taken to create a SN progenitor on average would be:

$$\begin{aligned} \frac{t_{\rm SN,avg}}{\rm yr} &= \frac{\text{Mass required to make SN progenitor}}{\text{Formation rate of stellar mass}} \\ &= \frac{117 M_\odot}{\rm SFR[M_\odot\,yr^{-1}]}. \end{aligned} \tag{1.16}$$

Equation 1.16 can be turned on its head to instead describe the *rate* at which supernovae progenitors are created:

$$\frac{f_{\rm SN,avg}}{\rm yr^{-1}} = \frac{\rm SFR[M_\odot\,yr^{-1}]}{117 M_\odot}. \tag{1.17}$$

Therefore, the $\rm RC_{NTh}$ luminosity and the SFR can be related by combining Equations 1.17 and 1.13 which gives:

$$\begin{aligned} \frac{L_{\rm NTh}}{\rm W\,Hz^{-1}} &= 1.3\times10^{23}\left(\frac{\nu}{\rm GHz}\right)^{-\alpha_{\rm NTh}}\left(\frac{f_{\rm SN}}{\rm yr^{-1}}\right) \\ &= 1.3\times10^{23}\left(\frac{\nu}{\rm GHz}\right)^{-\alpha_{\rm NTh}}\frac{\rm SFR[M_\odot\,yr^{-1}]}{117 M_\odot} \\ &= 1.11\times10^{21}\left(\frac{\nu}{\rm GHz}\right)^{-\alpha_{\rm NTh}}{\rm SFR[M_\odot\,yr^{-1}]}. \end{aligned} \tag{1.18}$$

1.3.4 Separating $\rm RC_{Th}$ and $\rm RC_{NTh}$

The $\rm RC_{Th}$ and $\rm RC_{NTh}$ operate on different time and spatial scales, but are separable. Using the $\rm RC_{Th}$–Hα conversion factor in Equation 6.2, the $\rm RC_{NTh}$ component can then be calculated by subtracting $\rm RC_{Th}$ from the total RC on a spatially resolved basis (see Figure 1.6). This method relies on having Hα fluxes, which must be corrected for absorption from foreground and *in situ* dust. Even then, the conversion factor in Equation 6.2 has some uncertainty. This method has been used by, e.g., Niklas &

Beck (1997), Murphy et al. (2011), and Tabatabaei et al. (2013). The scale of $\mathrm{RC_{NTh}}$ emission is visibly greater than that of $\mathrm{RC_{Th}}$ emission.

There exists an Hα-independent way to infer the $\mathrm{RC_{Th}}$ and $\mathrm{RC_{NTh}}$ components: by a spectral decomposition. This works based on the premise that the two components each have a distinctive spectral form such that the total RC emission observed at a frequency, ν, is

$$A\left(\frac{\nu}{\nu_0}\right)^{-0.1} + B\left(\frac{\nu}{\nu_0}\right)^{\alpha_{\mathrm{NTh}}} \tag{1.19}$$

where A and B are normalisations, which translate into intensities at a reference frequency, ν_0 (which is generally taken as $1\,\mathrm{GHz}$ in most low-frequency studies). With multiple independent spectral points, the unknown parameters A, B, and α_{NTh} can be inferred (see Figure 1.7).

On galactic scales, the infrared to radio regime ($\sim 100\mu\mathrm{m}$–$1\,\mathrm{m}$) of the electromagnetic spectrum is dominated by three contributions: $\mathrm{RC_{Th}}$, $\mathrm{RC_{NTh}}$, and modified blackbody radiation from heated dust. As can be seen from Figure 1.7, the flux density reaches a minimum at around $100\,\mathrm{GHz}$ or $0.3\,\mathrm{mm}$. From this point towards longer wavelengths, the flux density increases following a power law with an exponent of typically ~ -0.7.

1.3.5 Immunity from Extinction of the Radio Continuum

The proportion of emission absorbed along the line of sight due to dust decreases when longer wavelengths are used (e.g., Schlegel et al., 1998; Schlafly & Finkbeiner, 2011). Scattering of electromagnetic radiation is greatest when the scattering particles are larger than or similar in size to the incident light. Most dust in the ISM is on the order of a few $\mu\mathrm{m}$ in size—while this greatly affects optical wavelengths, it is far too small to have any appreciable affect on RC wavelengths. In fact, particles would have to be millimetres in size or larger for appreciable scattering to occur. In the ISM, such large grains are not expected in large quantities, and thus RC photons propagate largely unhindered.

While objects such as dust grains are not expected to directly absorb RC, they can indirectly affect the RC. Take for example a shell of Hydrogen containing some *in situ* dust surrounding newly formed stars. An ionising photon may enter the Hydrogen-dust shell, but may be absorbed or scattered by dust before it has the chance to ionise a Hydrogen atom—this is then one fewer free electron to go towards Brehmsstrahlung radiation.

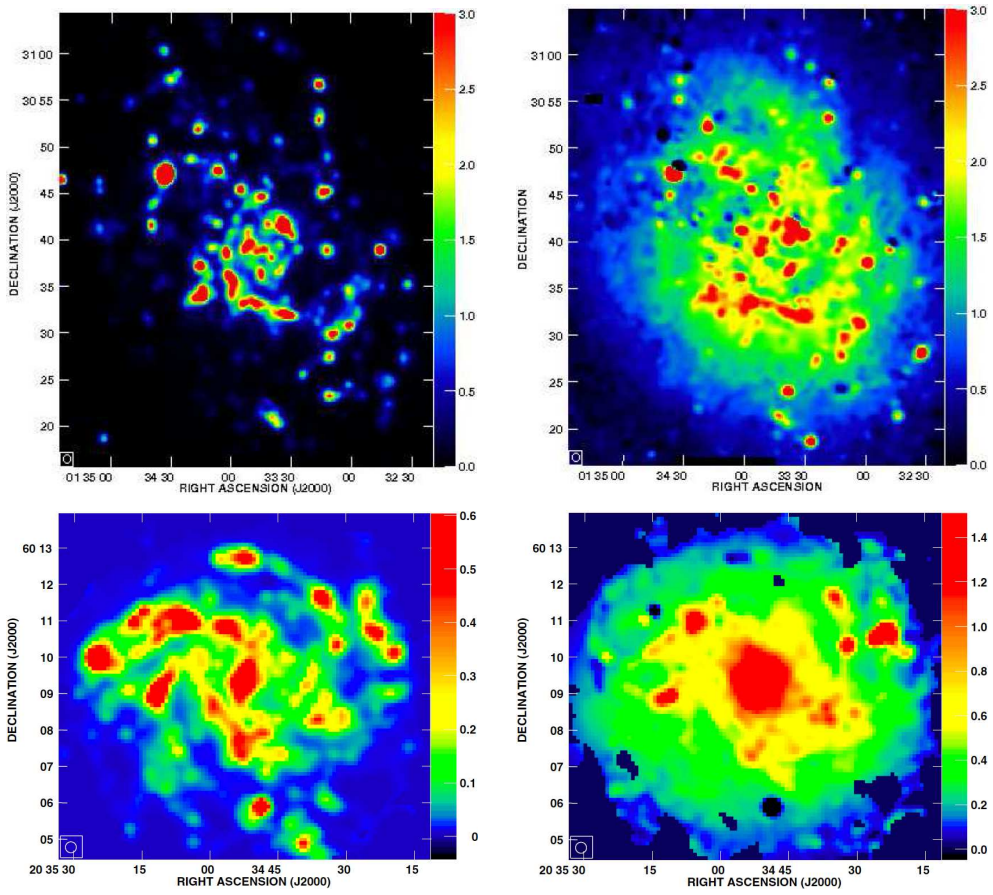

FIGURE 1.6: By using scaled line emission (e.g., Hα, Pa-α) or fitting a RC spectrum to the form $A\nu^{-0.1} + B\nu^{\alpha_{\rm NTh}}$, where A and B are normalisations (see Equation 1.19), the RC can be split into its thermal and non-thermal components. *Left:* The thermal component. *Right:* The non-thermal component. The top panels show M 33 at 20 cm (Tabatabaei et al., 2013), while the bottom panels show NGC 6946 at 3.5 cm (Tabatabaei et al., 2013). The scale of $\rm RC_{NTh}$ emission is visibly greater than that of $\rm RC_{Th}$ emission. For a *spectral* decomposition of the RC, see Figure 1.7.

Also, briefly, the RC is vulnerable to both synchrotron self-absorption and free-free self-absorption towards very long wavelengths (greater than $\sim$ 1 m). In this study, the longest wavelength used is 20 cm, so this is not an issue.

1.3.6 Workable Resolution of Radio Continuum Observations

The longer the wavelength of the RC used, the stronger the non-thermal emission (Equation 1.19) is expected to be. This bodes well for RC studies, albeit at the expense of resolution. The resolution of a diffraction limited telescope is

$$\theta_{\rm res} = \frac{\lambda}{D} \tag{1.20}$$

scaling linearly with the wavelength being observed, λ, and the width of the aperture in the optical system, D. While resolving local objects (e.g., 100 pc regions at a

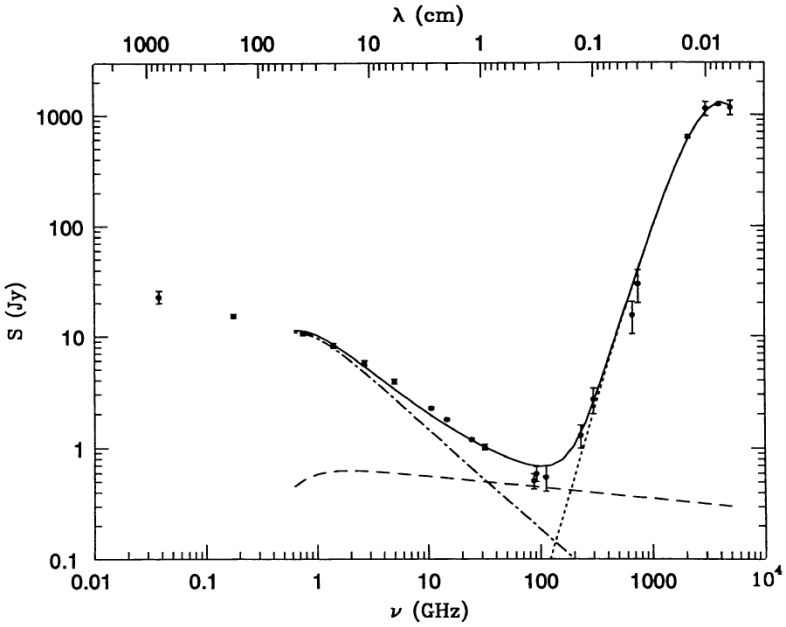

FIGURE 1.7: On galactic scales, the infrared to radio regime ($\sim 100\mu$m–1 m) of the electromagnetic spectrum is dominated by three contributions: $\mathrm{RC_{Th}}$, $\mathrm{RC_{NTh}}$, and thermal dust emission (dotted). The strength of the RC increases towards longer wavelengths which justifies using lower frequency observations. Towards low frequency where contribution from dust is minimal, a large enough spectral coverage allows the RC spectrum to be decomposed into its two components: the $\mathrm{RC_{Th}}$ (dashed) and the $\mathrm{RC_{NTh}}$ (dot-dashed). The example spectrum is of M 82 and has been taken from Condon (1992). For a *resolved* decomposition of the RC, see Figure 1.6.

distance of 3 Mpc) is possible with infrared telescopes (e.g., *Spitzer* at 24 μm) of modest apertures (approximately 0.8 m), at longer wavelengths, the resolution becomes an issue for resolved studies (e.g., a diffraction-limited resolution of $\sim 12''$ at 850 μm with the JCMT).

To get a similar resolution at radio wavelengths (e.g., $\lambda = 5$ cm or $\nu = 6$ GHz), the dishes would need to be impossibly wide—1.5 km in diameter. Fortunately, such long wavelengths facilitate the implementation of interferometry[3], and this technique allows the resolution to increase to useful dimensions. The theory behind interferometry is explained in some detail in Section 3.2.1

1.4 History: Radio Continuum in Dwarf Galaxies

The RC, in an astronomical sense, was first reported more than 80 years ago by Jansky (1933) who, having initially attributed his radio detection as originating from

[3]Interferometry is also possible for shorter wavelengths. Precision technology has allowed interferometry to be used in astronomy at millimetre (ALMA), submillimetre (SMA), and even optical wavelengths (VLTI).

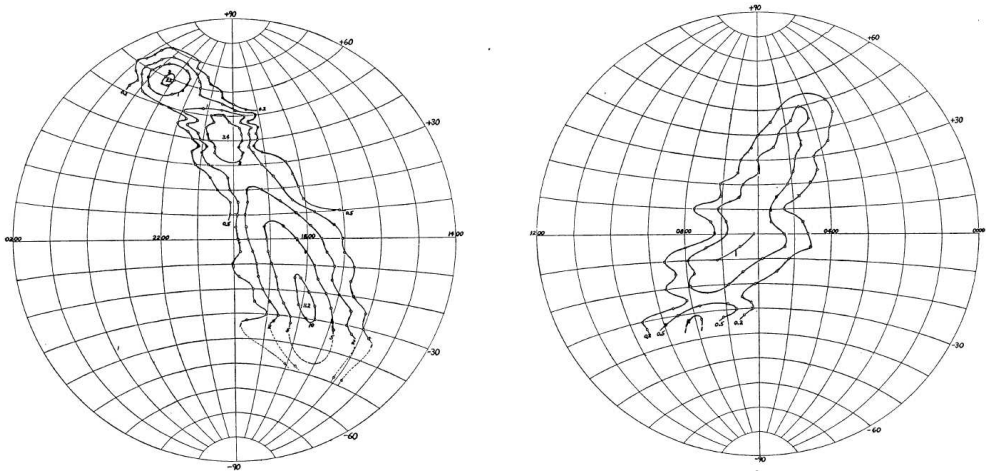

FIGURE 1.8: The first all-sky RC map (Reber, 1944). The resolution is about 10° and successfully locates RC emission coincident near Sagittarius, Cygnus, and Cassiopeia.

the Sun, had in fact inadvertently observed the Galactic centre. Soon after, technological and intellectual advances in radio engineering, mainly accelerated by the demands of World War II, gave radio astronomy the jump start it needed. The first all-sky radio map can be attributed to Reber (1944) and was done at $0.16\,\mathrm{GHz}$. It successfully located significant RC emission near Sagittarius, Cygnus, and Cassiopeia, although the resolution was about 10° (see Figure 1.8). The application of interferometry to radio astronomy opened the possibility of improving resolution. One of the first interferometers to be used was the Long Michelson Interferometer in Cambridge which, at $0.08\,\mathrm{GHz}$, collected 50 sources into the 1C catalogue. This was the pioneering Cambridge catalogue, but was overtaken by its successors, particularly the 3C catalogue at $0.16\,\mathrm{GHz}$ (Edge et al., 1959), which many astronomers still refer to today.

At this point, Galactic surveys were shedding light on the nature of the RC in the Milky Way—an unbroken band of synchrotron emission coincident with the galactic plane was observed interspersed with unresolved peaks in emission. There were also loops, holes, and filaments that started to become apparent when maps reached 1° resolution (Mathewson et al., 1962), and this, coupled with the theory of synchrotron emission, led to the early work on galactic magnetic fields (e.g., Parker, 1966).

The improvements in resolution also opened radio astronomy to sources of RC beyond the Milky Way. One of the first direct, unambiguous detections of an extragalactic source was of M 31 at $0.16\,\mathrm{GHz}$ (Brown & Hazard, 1951), which was later observed with a resolution of $4'$ at $0.41\,\mathrm{GHz}$ Pooley (1969) (see Figure 1.9).

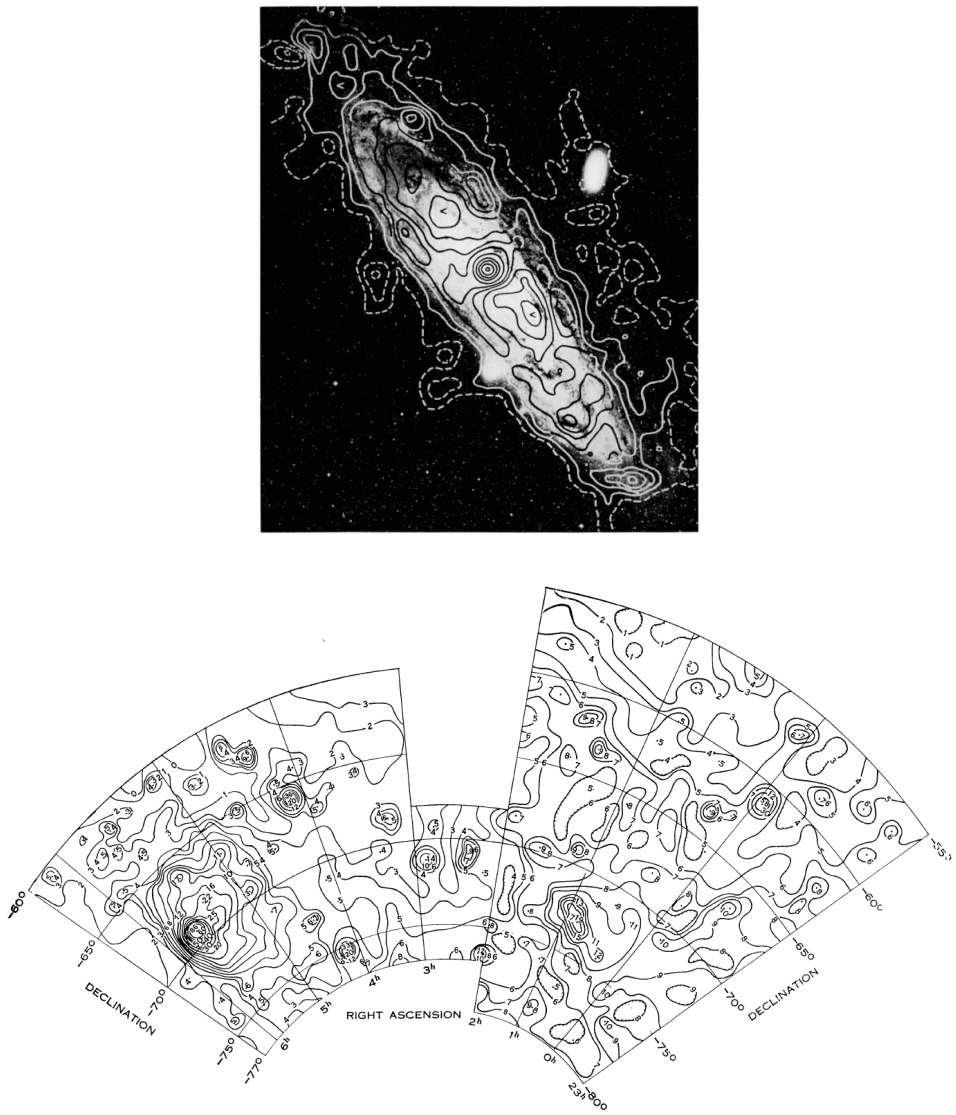

FIGURE 1.9: Early resolved RC maps of galaxies. *Top:* A spiral galaxy, M 31 (Pooley, 1969). *Bottom:* The dwarf galaxies, LMC and SMC (Mathewson & Healey, 1964).

But dwarf galaxies, being fainter than spiral galaxies, took longer to make their debut in RC surveys. Brown & Hazard (1961) collated RC fluxes for a range of galaxy types, and was perhaps one of the first ever studies to find that dwarf galaxies displayed a RC deficiency stating that "it appears likely that they [irregular galaxies] are relatively weak radio emitters in comparison with Sb and Sc spirals". One of the first detailed resolved studies of a dwarf galaxy was of the LMC and SMC (Mathewson & Healey, 1964) (see Figure 1.9)—just like in optical bands, the RC was seen to exhibit a clumpy morphology.

1.4.1 Global Radio Continuum

One consequence of limitations in instrument sensitivity[4] is that studies can be forced into an approach based on the integrated properties of the population being investigated. This approach gained traction, especially so in the 1980s. Even so, there was not too much joy with regards to detections of dwarf galaxies: studies were often characterised by upper limits on globally integrated quantities (e.g., van der Kruit & Allen, 1976; Altschuler et al., 1984; Klein, 1986; Price & Duric, 1992; Klein et al., 1992; Hoeppe et al., 1994).

Studies into the RC emission of dwarf galaxies as a population have been few and far between. All-sky surveys never reached the sensitivities to probe significant numbers of dwarf galaxies—the NRAO VLA Sky Survey (NVSS; Condon et al., 1998) and Faint Images of the Radio Sky at Twenty-cm (FIRST; White et al., 1997) were only able to detect the brightest few. Despite NVSS non-detections of individual galaxies, Roychowdhury & Chengalur (2012) used 57 stacked NVSS images to infer magnetic field properties in faint dwarf galaxies.

The best detection rate of the RC in dwarf galaxies from the literature was that of Klein (1986), and even then, the detection rate was 40%. In fact, on closer inspection, those 40% are actually dominated by 1–3 σ detections and were likely influenced by the unwitting inclusion of background galaxies in the large Effelsberg beam.

This last point is particularly pertinent: studies of dwarf galaxies have mainly been limited to integrated quantities, and in doing so would have introduced significant contamination from background sources along the same line of sight as the galaxy disk. Figure 1.10 shows how significant this effect can be: with good resolution (bottom panel), a *C*-band observation of NGC 2366 exhibits a clear double-lobed RC source. However, when smoothed to a resolution of one arcminute (top panel), to mimic the primary beam resolution of a single dish, the background source becomes confused with NGC 2366's emission, and in all likelihood the presence of the strong, contaminating background source would not be recognised and NGC 2366 would erroneously be attributed a RC excess.

Performing integrated analysis with a higher resolution can provide a means by which to judge the impact that contamination had on those early studies. The integrated analysis of our work (which forms the basis of Chapter 4) improves on the work done by other studies—especially single-dish studies—since contamination from background sources in our images was relatively easy to eliminate with

[4]For example, prior to 2012, the VLA offered a total bandwidth of 0.1 GHz for observations between 2 and 4 GHz. After the upgrades, the bandwidth was increased 20-fold to 2 GHz.

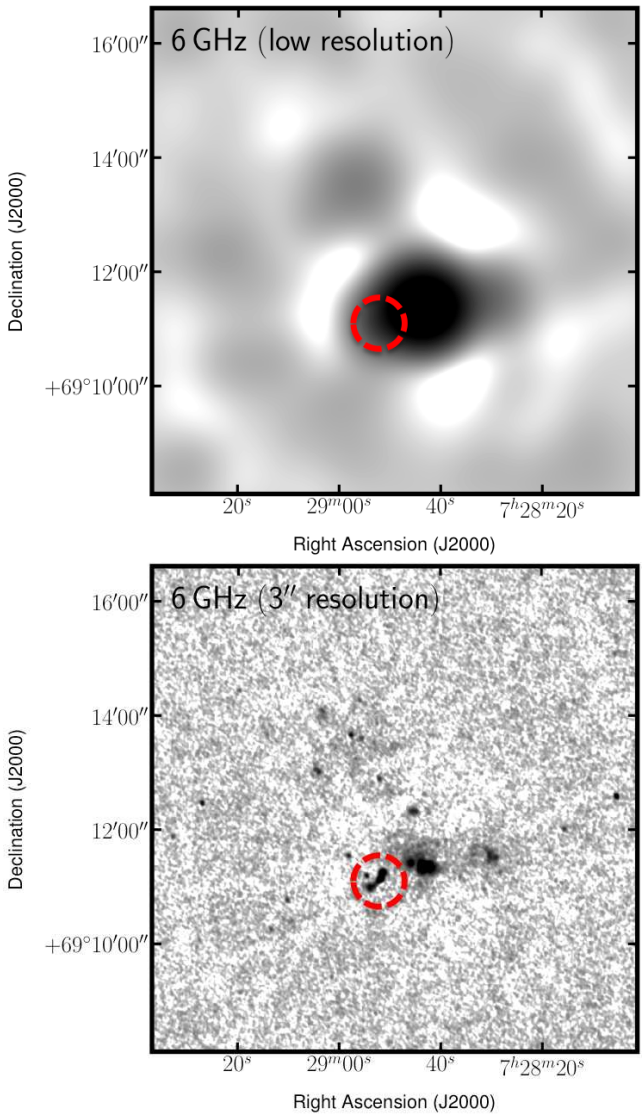

FIGURE 1.10: An example of how easy it is for contamination to slip into integrated quantities unnoticed at a resolution of 1′. In this example, we show NGC 2366 at *C*-band with a resolution of 1′ (top) and at the native resolution of 3″ (bottom; see Chapter 4). The red dashed circle highlights the location of a double lobed radio source which is *not* related to NGC 2366.

the high resolution.

1.4.2 Localised Radio Continuum

To date, resolved observations of dwarf galaxies have been reserved for the elite few: the near and bright IC 10 (Heesen et al., 2011), IC 1613 (Chyży et al., 2011), NGC 4214 (see Figure 1.11; Kepley et al., 2011), NGC 1569 (Lisenfeld et al., 2004; Kepley et al., 2010), and the Magellanic Clouds (e.g., Filipovic et al., 1995; Filipovic et al., 1998; Leverenz & Filipović, 2013).

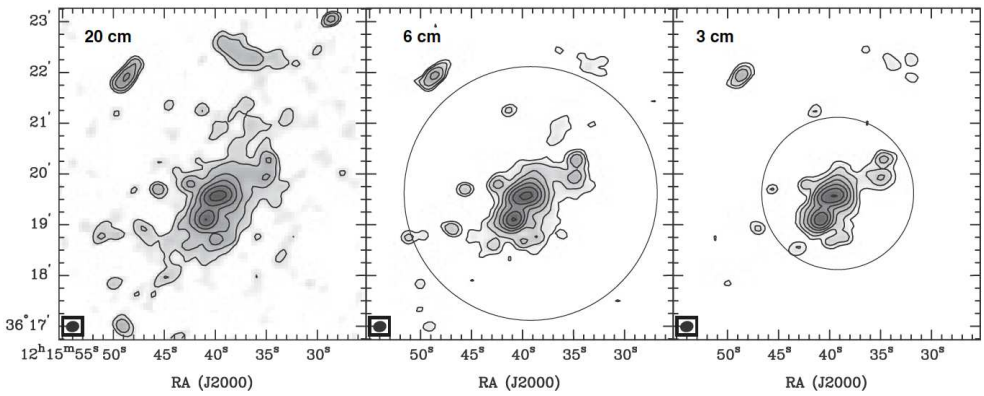

FIGURE 1.11: An example of the quality of RC observations prior to the upgrades of the VLA in 2011. This is NGC 4214 at *L*-, *C*-, and *X*-band (20, 6, and 3 cm, respectively) where the first contours correspond to 150, 75, and 72 μJy beam^{-1} where the beam is about $14'' \times 11''$ (Kepley et al., 2011).

The RC has only just recently been explored to investigate to what extent it can provide reliable SFRs on a resolved basis in nearby spiral galaxies (Heesen et al., 2014). However, it is yet to be done in a large sample of dwarf galaxies.

The data for all of these studies were acquired mainly from the VLA, prior to 2011, before its major upgrade increasing receiver sensitivity as well as introducing a 20-fold increase of bandwidth coverage across many bands. For this reason, revisiting the resolved RC in these galaxies gained renewed interest. We do just this in Chapter 5, significantly expanding on the few existing studies of resolved RC observations of dwarf galaxies.

1.4.3 Resolved Spectral Index of the Radio Continuum

Investigating the spectral index of the radio continuum on a resolved basis not only requires large amounts of instrument time to reach a meaningful depth, but requires matched resolution observations at comparable depth across multiple bands.

Studies into the spectral index requires dedication and, in the case of the VLA, will often take years to acquire the data across multiple configurations. Therefore, studies into the RC spectral index in dwarf galaxies can be counted on one's hand: e.g., IC 10 (Heesen et al., 2011), NGC 4214 (Kepley et al., 2011), and NGC 1569 (Lisenfeld et al., 2004; Kepley et al., 2010). The spectral index distribution of the total RC is shown for NGC 1569 and IC 10 in Figure 1.12.

The spectral index of RC emission is related to the time elapsed since the injection of the CRe. Studying the spectral index can potentially provide insight into the structure of galactic magnetic fields, and as it will turn out in Chapter 6, is actually

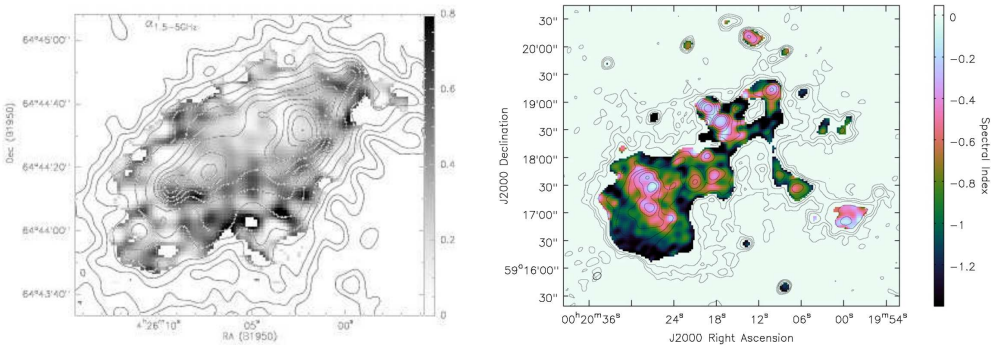

FIGURE 1.12: The resolved spectral index of RC emission in dwarf galaxies. *Left:* Between 1.5 and 5.0 GHz in NGC 1569 (Lisenfeld et al., 2004). *Right:* Between 4.5 and 7.8 GHz in IC 10 (Heesen et al., 2011).

an important measurable property whose understanding can reduce the scatter in RC–SFR relations.

1.4.4 The RC–FIR Relation

The Radio Continuum (RC) – Far Infrared (FIR) relation of galaxies holds over 4 orders of magnitude in luminosity, irrespective of galaxy type (Helou et al., 1985; de Jong et al., 1985; Yun et al., 2001). It displays a mere 0.26 dex scatter (Yun et al., 2001) and has been observed to hold to a redshift of 3 (Appleton et al., 2004) (see Figure 1.13).

The radio continuum comprises two main contributions: a thermal component ($\mathrm{RC_{Th}}$) and a nonthermal component ($\mathrm{RC_{NTh}}$) each of which have a very clear and unambiguous link with recent and ongoing star formation (see Section 1.3.1). The FIR originates from the modified black-body radiation of interstellar dust that is heated by the ISRF (e.g., Li et al., 2010; Irwin et al., 2013), which is a mix of radiation from newly formed stars and from the older population.

Ever since the 1980s, the community has grown rather attached to the RC–FIR relation. The reason behind this may be as simple as the fact that the RC–FIR relation exhibits such a tight relation. However, in some respects, the RC–FIR relation is just a red herring: both emission mechanisms are the indirect consequence of SF, so why calibrate the RC–FIR relation at all?

On a simple level, the tight relation can be attributed to a link between magnetic field properties and dust content. A model for this scenario was put forward by Völk (1989). The classical scenario leading to the RC–FIR relation is that of a galaxy acting as a *calorimeter* (Völk, 1989)—one that retains both its dust-heating photons and CRe. The model assumes that dust-heating photons (e.g., optical and UV) are absorbed

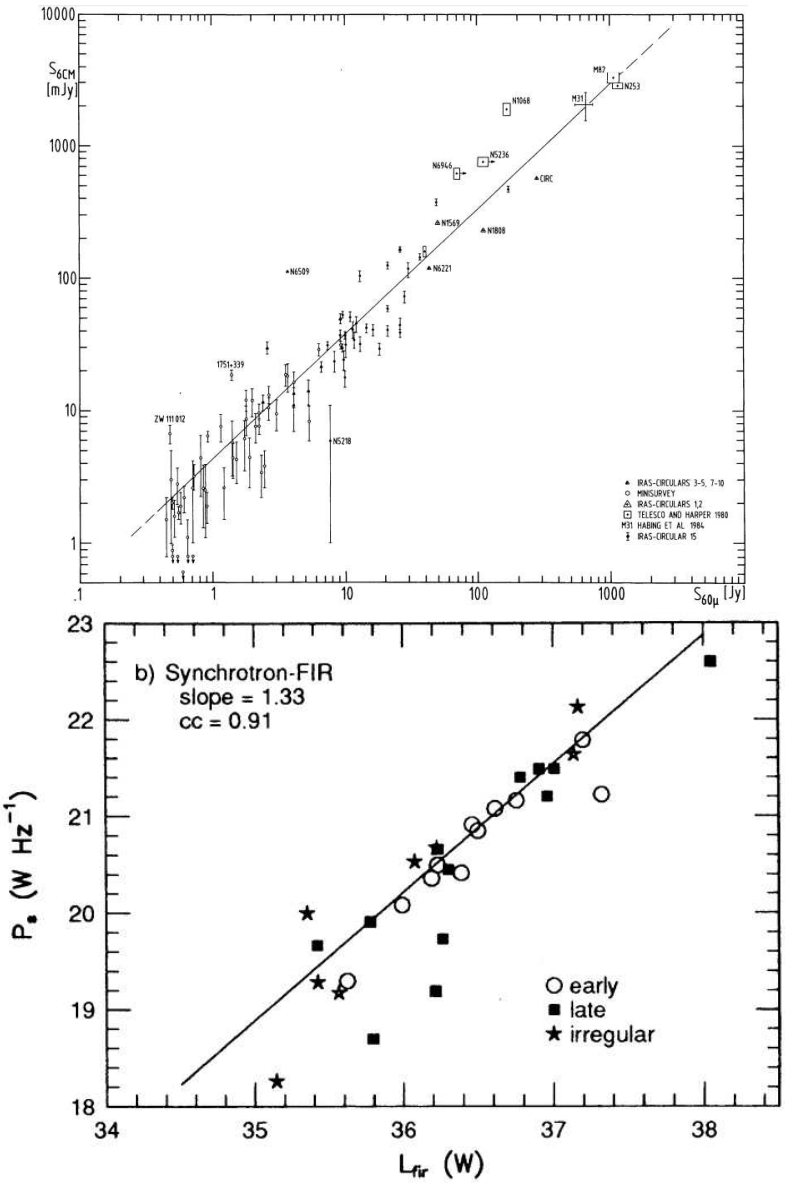

FIGURE 1.13: *Top:* The *total* RC–FIR relation for a range of galaxy types, taken from the seminal study of de Jong et al. (1985). *Bottom:* The *non-thermal* RC–FIR relation from Price & Duric (1992) who included a high proportion of irregular galaxies in their study.

by dust which eventually reradiates the energy gained as FIR. It also requires that magnetic fields retain all CRe which eventually produce synchrotron radiation. Since all the energy contained within the CRe is radiated, the strength of the magnetic field is irrelevant, i.e., whether the energy contained in the CRe is radiated over 1 Myr in a relatively strong magnetic field, or over 1 Gyr in a weaker magnetic field, the total energy emitted is the same. The calorimeter assumption implies that the mean-free-path of dust-heating photons is less than the galaxy disk scale height (taken to be $\sim$ 400 pc in dwarf galaxies; Banerjee et al., 2011), and that the typical energy loss

timescale of CRe is less than the diffusion timescale to traverse the scale height.

Clearly, the calorimeter model is not perfect as dust-heating photons *are* observed coming from galaxies, and $\mathrm{RC_{NTh}}$ emission *is* observed in the haloes of larger spirals (Heesen et al., 2009). Therefore, for galaxies to follow the RC–FIR relation, the escape of CRe from galactic magnetic fields must be in proportion to the escape of dust-heating photons from the disk. Some of the earliest evidence of this comes from Klein et al. (1991) who state that the deficiency of $\mathrm{RC_{NTh}}$ 'happens to be balanced' by a lack of dust in Blue Compact Dwarfs (BCDs). This is known as the 'conspiracy' between the emission at RC and FIR wavelengths (e.g., Bell, 2003; Dale et al., 2009; Lacki et al., 2010).

1.4.5 A Deficiency of Radio Continuum in Dwarf Galaxies

Dwarf galaxies, having a lower SFR than spirals, are of course faint at RC wavelengths. But dwarf galaxies are not only faint in the RC, but they are *fainter than expected*—the consensus is that, given the amount of RC expected from the observed SF, dwarf galaxies do exhibit a deficiency of RC emission. Studies have tended to focus on low frequency RC ($\lesssim 10\,\mathrm{GHz}$) where emission tends to be dominated by the $\mathrm{RC_{NTh}}$ component. This has led the community to explain the deficiency of RC as a result of a deficiency in the $\mathrm{RC_{NTh}}$ component alone:

- "it appears likely that they [irregular galaxies] are relatively weak radio emitters in comparison with Sb and Sc spirals" (Brown & Hazard, 1961);
- "deficiency of synchrotron emission in low-mass galaxies is interpreted in terms of [a lack of] CRe confinement" (Klein et al., 1991);
- "the radio luminosity of less luminous (and generally less massive) galaxies may be low if CRe loss by diffusion is important" (Yun et al., 2001);
- "our models indicate that CRe escape from low surface density galaxies ... [is] decreasing [the] radio emission" (Lacki et al., 2010).

In addition to the loss of CRe, there may be other factors at work conspiring to reduce the production of $\mathrm{RC_{NTh}}$ emission. Dwarf galaxies can lack differential rotation (Gallagher & Hunter, 1984), and are not able to stretch small scale magnetic field perturbations (this α–Ω process happens in larger, grand-design spirals leading to ordered fields of $\sim 5\,\mu\mathrm{G}$ between the optical arms; Beck, 2009). This leads to the ISM in dwarf galaxies having a lower magnetic field strength than in spirals (e.g., Roychowdhury & Chengalur, 2012, measure $2\,\mu\mathrm{G}$ on average across the disks of 57

stacked dwarf galaxies), and thus a lower luminosity which gives the CRe more time to escape before they radiate away all of their energy.

The low mass of dwarf galaxies leads to episodic SF (e.g., Stinson et al., 2007, liken the SF history of isolated dwarf galaxies to 'breathing') and makes them vulnerable to the energy input following major SF episodes. The buoyancy of hot plasma manifests itself as Parker instabilities (Parker, 1966) and advective winds taking resident CRe out of the galaxy and into the intragalactic medium (Heesen et al., 2009; Dubois & Teyssier, 2010; Heesen et al., 2011). The resulting reduction in the number of CRe resident in the galaxy's magnetic fields would lower the $\mathrm{RC_{NTh}}$ luminosity.

However, it is not solely fewer CRe and lower magnetic field strengths that are responsible for RC emission—there is also a $\mathrm{RC_{Th}}$ component—the deficiency of RC emission could just as plausibly be explained by an underproduction of the $\mathrm{RC_{Th}}$ component.

One way in which the $\mathrm{RC_{Th}}$ may become deficient for a given SFR is through a truncated stellar IMF. A truncated stellar IMF in dwarf galaxies may lead to fewer high mass stars being formed for a given SFR (Wyder et al., 2007; Lee et al., 2009; Ploeckinger et al., 2015); with fewer high mass stars producing the ionising photons needed to create H II regions, less Hα (and $\mathrm{RC_{Th}}$) is emitted. For the least active dwarf galaxies ($\mathrm{SFR} \sim 10^{-4}\,\mathrm{M_\odot\,yr^1}$), the H$\alpha$ emission underestimates the SFR given by FUV by a factor of 10. Only the highest mass stars ($M > 18\,\mathrm{M_\odot}$) produce a significant number of photons to ionise the surrounding H I; having a deficit of these stars significantly reduces the amount of Hα emission, while the FUV emission is not affected as much since a larger fraction of the stellar population contributes to the FUV emission. However, Koda et al. (2012) do find O stars in stellar clusters as small as $100\,\mathrm{M_\odot}$ coming to the conclusion that the stellar IMF is universal, and not truncated, although in clusters of such low mass, stochasticity would dominate.

1.5 Thesis Objective

In summary, the RC has good prospects for being used as SFR indicator, however, in order to calibrate such a RC–SFR relation, the RC must first be understood at a fundamental level. In particular, it is important to ascertain to what extent the assumption of galaxies acting as a calorimeter holds. This seems to break down in dwarfs with CRe being lost from these small systems.

But in order to understand the RC-SFR better one needs to push it to extremes. One extreme would be starbursts, the other is low mass, low metallicity dwarfs. It is

these low mass dwarfs on which this thesis concentrates, paying particular attention to low frequency observations ($\lesssim 10\,\mathrm{GHz}$; $\gtrsim 3\,\mathrm{cm}$).

In Chapters 2 and 3, we will outline the galaxies chosen to calibrate the RC–SFR relation, and the steps taken to ensure the resulting images were suitable for such a calibration. Then, in Chapter 4, we will investigate the integrated RC and SF properties of the sample to gauge how the RC acts on galactic scales. After this global examination of the dwarf galaxies, we will then make full use of the resolved data in Chapter 5 to dig into local properties of the $\mathrm{RC_{NTh}}$ component. Finally, to include effects of time in the RC–SFR calibration, Chapter 6 will introduce the spectral index as means by which to do so. We will summarise our findings in Chapter 7.

2

Sample

2.1 The Dwarf Galaxies

LITTLE THINGS[1] (Local Irregulars That Trace Luminosity Extremes, The H I Nearby Galaxy Survey) is a large VLA project designed primarily to probe the SF process in dwarf galaxies. It was a natural spin-off from the successful THINGS project that focussed mainly on spiral galaxies.

The final sample, and that used in this thesis was the result of whittling down a larger 112-strong sample of dwarf galaxies, BCDs, and Sm galaxies (Hunter & Elmegreen, 2004, 2006). The final sample comprised 40 gas-rich dwarf galaxies all within 11 Mpc. Table 2.1 collates the properties of the dwarf galaxies that make up LITTLE THINGS, while a more detailed account can be found in Hunter et al. (2012).

[1]Based on data from the LITTLE THINGS Survey (Hunter et al., 2012), funded in part by the National Science Foundation through grants AST-0707563, AST-0707426, AST-0707468, and AST-0707835 to US-based LITTLE THINGS team members and with generous support from the National Radio Astronomy Observatory.

Gas Content

Each galaxy in the sample was chosen to be gas-rich; since the project's goal was to probe SF processes, this obviously is a prerequisite. This introduces a bias in that any process examined is restricted to gas-rich systems.

Galaxy Inclination and distance

To probe the internal SF process, each galaxy was required to be adequately spatially resolved. With this in mind, the dwarf galaxies were chosen to be no more distant than 11 Mpc, and to have inclinations less than $70°$. For example, for a face-on galaxy at a distance of 3 Mpc, a 40×40 pc resolution ($\sim 3''$ circular synthesised beam) can be achieved when observing at *C*-band (4–8 GHz) in C-configuration.

Immediate Environment

The dwarf galaxies were chosen to reside in relative isolation. External factors such as tidal interactions, mergers, and ram pressure can induce SF activity, and any galaxies that exhibited this type of behaviour were excluded to ensure that any SF observed was the result of internal processes only. In reality, dwarf galaxies are found in a whole range of environments, so while choosing only those in relative isolation may be seen as introducing a bias, we remind the reader that the sample was chosen to probe internal SF processes, so this is the preferred approach.

Mass

The H I masses of the dwarf galaxies range from as low as $1.6 \times 10^5\,\mathrm{M}_\odot$ (LGS 3) up to $7.1 \times 10^9\,\mathrm{M}_\odot$ (DDO 50). Such a large range in mass was chosen as, to first order, it is the quantity of mass that is responsible for the luminosity (e.g., the Tully–Fisher relation of Tully & Fisher, 1977), the SFR (e.g., the Kennicutt–Schmidt relation of Kennicutt, 1998), and the metallicity (e.g., the mass–metallicity relation of Skillman et al., 1989). The mass-dependent properties of each galaxy also exhibit a good range: 4 dex in SFR and a factor of 50 in metallicity. This coverage of galaxy properties is key as a large sample probes an equally large parameter space.

2.2 Ancillary Data

As previously mentioned, the LITTLE THINGS sample was chosen to study the star formation process. Accordingly, if the RC is to be tested on its ability to act as a

TABLE 2.1: **THE LITTLE THINGS GALAXY SAMPLE**

(1) Galaxy name; (2) Selected alternate identifications obtained from NED; (3) Distance; (4) Reference for the distance to the galaxy. If no reference is given, the distance was determined from the galaxy's radial velocity, given by de Vaucouleurs et al. (1991), corrected for infall to the Virgo Cluster (Mould et al. 2000) and a Hubble constant of 73 km s^{-1} Mpc^{-1}; (5) V-band absolute magnitude; (6) R_H is the Holmberg radius, the radius of the galaxy at a B-band isophote, corrected for reddening, of 26.7 mag arcsec^{-2}; (7) R_D is the disk scale length measured from V-band images (Hunter & Elmegreen, 2006); (8) Foreground reddening from Burstein & Heiles (1984); (9) SFR$_D^{H\alpha}$ is the SF rate, measured from Hα, normalised to the area πR_D^2 (Hunter & Elmegreen, 2004); (10) SFR$_D^{FUV}$ is the SF rate determined from *GALEX* FUV fluxes (Hunter et al., 2010); (11) Oxygen abundance (values in parentheses were determined from the empirical relationship between oxygen abundance and M_B given by Richer & McCall (1995) and are particularly uncertain); (12) Reference for the oxygen abundance: (1) Dalcanton et al. 2009; (2) Karachentsev et al. 2004; (3) Karachentsev et al. 2003a; (4) Karachentsev et al. 2006; (5) Dolphin et al. 2002; (6) Sakai et al. 2004; (7) Dolphin et al. 2003; (8) Karachentsev et al. 2003b; (9) Tolstoy et al. 1995a; (10) Karachentsev et al. 2002; (11) Meschin et al. 2009; (12) Sakai et al. 1999; (13) Pietrzynski et al. 2006; (14) Miller et al. 2001; (15) Freedman et al. 2001; (16) Grocholski et al. 2008; (17) Tolstoy et al. 1995b; (18) Gieren et al. 2006; (19) Momany et al. 2002; (20) Gieren et al. 2008; (21) Schulte-Ladbeck et al. 2001; (22) Lynds et al. 1998; (23) Méndez et al. 2002; (24) van Zee & Haynes 2006; (25) Hunter & Hoffman 1999; (26) Skillman, Kennicutt, & Hodge 1989; (27) Moustakas et al. 2010; (28) Richer & McCall 1995; (29) van Zee et al. 2006; (30) Kniazev et al. 2005; (31) Croxall et al. 2009; (32) Lee et al. 2003b; (33) Skillman et al. 1997; (34) Lequex et al. 1979; (35) Lee et al. 2003a; (36) Kobulnicky & Skillman 1997; (37) González-Delgado et al. 1994; (38) Moustakas & Kennicutt (2006); (39) Masegosa et al. 1991; (40) Lee et al. 2005; (41) Viallefond & Thuan 1983; (42) Gonźalez-Riestra et al. 1988.

Galaxy	Other names	D (Mpc)	Ref	M_V (mag)	R_H (arcmin)	R_D (kpc)	E($B-V$)	$\log_{10}\Sigma_{SFR,D}^{H\alpha}$ ($M_\odot$yr^{-1} kpc^{-2})	$\log_{10}\Sigma_{SFR,D}^{FUV}$ ($M_\odot$yr^{-1} kpc^{-2})	$12+\log_{10}$O/H	Ref.
(1)	(2)	(3)	(4)	(5)	(6)	(7)	(8)	(9)	(10)	(11)	(12)
CVnIdwA	UGCA 292	3.6	1	-12.4	0.87	0.57 ± 0.12	0.01	-2.58 ± 0.01	-2.48 ± 0.01	7.3 ± 0.06	24
DDO 43	PGC 21073, UGC 3860	7.8	2	-15.1	0.89	0.41 ± 0.03	0.05	-1.78 ± 0.01	-1.55 ± 0.01	8.3 ± 0.09	25
DDO 46	PGC 21585, UGC 3966	6.1	···	-14.7	···	1.14 ± 0.06	0.05	-2.89 ± 0.01	-2.46 ± 0.01	8.1 ± 0.1	25
DDO 47	PGC 21600, UGC 3974	5.2	3	-15.5	2.24	1.37 ± 0.06	0.02	-2.70 ± 0.01	-2.40 ± 0.01	7.8 ± 0.2	26
DDO 50	PGC 23324, UGC 4305, Holmberg II, VIIZw 223	3.4	1	-16.6	3.97	1.10 ± 0.05	0.02	-1.67 ± 0.01	-1.55 ± 0.01	7.7 ± 0.14	27

Table 2.1 continued on next page

Table 2.1 – continued from previous page

Galaxy	Other names	D		M_V	R_H	R_D		$\log_{10}\Sigma^{H\alpha}_{SFR,D}$	$\log_{10}\Sigma^{FUV}_{SFR,D}$		
		(Mpc)	Ref	(mag)	(arcmin)	(kpc)	$E(B-V)$	($M_\odot \mathrm{yr}^{-1}\,\mathrm{kpc}^{-2}$)	($M_\odot \mathrm{yr}^{-1}\,\mathrm{kpc}^{-2}$)	$12+\log_{10}\mathrm{O/H}$	Ref.
(1)	(2)	(3)	(4)	(5)	(6)	(7)	(8)	(9)	(10)	(11)	(12)
DDO 52	PGC 23769, UGC 4426	10.3	4	-15.4	1.08	1.30 ± 0.13	0.03	-3.20 ± 0.01	-2.43 ± 0.01	(7.7)	28
DDO 53	PGC 24050, UGC 4459, VIIZw 238	3.6	1	-13.8	1.37	0.72 ± 0.06	0.03	-2.42 ± 0.01	-2.41 ± 0.01	7.6 ± 0.11	27
DDO 63	PGC 27605, Holmberg I, UGC 5139, Mailyan 044	3.9	1	-14.8	2.17	0.68 ± 0.01	0.01	-2.32 ± 0.01	-1.95 ± 0.00	7.6 ± 0.11	27
DDO 69	PGC 28868, UGC 5364, Leo A	0.8	5	-11.7	2.40	0.19 ± 0.01	0.00	-2.83 ± 0.01	-2.22 ± 0.01	7.4 ± 0.10	29
DDO 70	PGC 28913, UGC 5373, Sextans B	1.3	6	-14.1	3.71	0.48 ± 0.01	0.01	-2.85 ± 0.01	-2.16 ± 0.00	7.5 ± 0.06	30
DDO 75	PGC 29653, UGCA 205, Sextans A	1.3	7	-13.9	3.09	0.22 ± 0.01	0.02	-1.28 ± 0.01	-1.07 ± 0.01	7.5 ± 0.06	30
DDO 87	PGC 32405, UGC 5918, VIIZw 347	7.7	···	-15.0	1.15	1.31 ± 0.12	0.00	-1.36 ± 0.01	-1.00 ± 0.01	7.8 ± 0.04	31
DDO 101	PGC 37449, UGC 6900	6.4	···	-15.0	1.05	0.94 ± 0.03	0.01	-2.85 ± 0.01	-2.81 ± 0.01	8.7 ± 0.03	25
DDO 126	PGC 40791, UGC 7559	4.9	8	-14.9	1.76	0.87 ± 0.03	0.00	-2.37 ± 0.01	-2.10 ± 0.01	(7.8)	28
DDO 133	PGC 41636, UGC 7698	3.5	···	-14.8	2.33	1.24 ± 0.09	0.00	-2.88 ± 0.01	-2.62 ± 0.01	8.2 ± 0.09	25
DDO 154	PGC 43869, UGC 8024, NGC 4789A	3.7	···	-14.2	1.55	0.59 ± 0.03	0.01	-2.50 ± 0.01	-1.93 ± 0.01	7.5 ± 0.09	27
DDO 155	PGC 44491, UGC 8091, GR 8, LSBC D646-07	2.2	9	-12.5	0.95	0.15 ± 0.01	0.01	-1.44 ± 0.01	···	7.7 ± 0.06	29
DDO 165	PGC 45372, UGC 8201, IIZw 499, Mailyan 82	4.6	10	-15.6	2.14	2.26 ± 0.08	0.01	-3.67 ± 0.01	···	7.6 ± 0.08	27
DDO 167	PGC 45939, UGC 8308	4.2	8	-13.0	0.75	0.33 ± 0.05	0.00	-2.36 ± 0.01	-1.83 ± 0.01	7.7 ± 0.2	26
DDO 168	PGC 46039, UGC 8320	4.3	8	-15.7	2.32	0.82 ± 0.01	0.00	-2.27 ± 0.01	-2.04 ± 0.01	8.3 ± 0.07	25
DDO 187	PGC 50961, UGC 9128	2.2	1	-12.7	1.06	0.18 ± 0.01	0.00	-2.52 ± 0.01	-1.98 ± 0.01	7.7 ± 0.09	32
DDO 210	PGC 65367, Aquarius Dwarf	0.9	10	-10.9	1.31	0.17 ± 0.01	0.03	···	-2.71 ± 0.06	(7.2)	28
DDO 216	PGC 71538, UGC 12613, Peg DIG, Pegasus Dwarf	1.1	11	-13.7	4.00	0.54 ± 0.01	0.02	-4.10 ± 0.07	-3.21 ± 0.01	7.9 ± 0.15	33
F564-V3	LSBC D564-08	8.7	4	-14.0	···	0.53 ± 0.03	0.02	···	-2.79 ± 0.02	(7.6)	28
Haro 29	PGC 40665, UGCA 281, Mrk 209, I Zw 36	5.8	21	-14.6	0.84	0.29 ± 0.01	0.00	-0.77 ± 0.01	-1.07 ± 0.01	7.9 ± 0.07	41
Haro 36	PGC 43124, UGC 7950	9.3	···	-15.9	···	0.69 ± 0.01	0.00	-1.86 ± 0.01	-1.55 ± 0.01	8.4 ± 0.08	25
IC 10	PGC 1305, UGC 192	0.7	12	-16.3	···	0.40 ± 0.01	0.75	-1.11 ± 0.01	···	8.2 ± 0.12	34
IC 1613	PGC 3844, UGC 668, DDO 8	0.7	13	-14.6	9.10	0.58 ± 0.02	0.00	-2.56 ± 0.01	-1.99 ± 0.01	7.6 ± 0.05	35
LGS 3	PGC 3792, Pisces dwarf	0.7	14	-9.7	0.96	0.23 ± 0.02	0.04	···	-3.88 ± 0.06	(7.0)	28
M81 DwA	PGC 23521	3.5	15	-11.7	···	0.26 ± 0.00	0.02	···	-2.26 ± 0.01	(7.3)	28
Mrk 178	PGC 35684, UGC 6541	3.9	8	-14.1	1.01	0.33 ± 0.01	0.00	-1.60 ± 0.01	-1.66 ± 0.01	7.7 ± 0.02	42

Table 2.1 continued on next page

Table 2.1 – continued from previous page

Galaxy	Other names	D		M_V	R_H	R_D		$\log_{10}\Sigma^{H\alpha}_{SFR,D}$	$\log_{10}\Sigma^{FUV}_{SFR,D}$		
		(Mpc)	Ref	(mag)	(arcmin)	(kpc)	$E(B-V)$	($M_\odot$yr^{-1} kpc^{-2})	($M_\odot$yr^{-1} kpc^{-2})	$12+\log_{10}$ O/H	Ref.
(1)	(2)	(3)	(4)	(5)	(6)	(7)	(8)	(9)	(10)	(11)	(12)
NGC 1569	PGC 15345, UGC 3056, Arp 210, VIIZw 16	3.4	16	-18.2	···	0.38 ± 0.02	0.51	0.19 ± 0.01	-0.01 ± 0.01	8.2 ± 0.05	36
NGC 2366	PGC 21102, UGC 3851, DDO 42	3.4	17	-16.8	4.72	1.36 ± 0.04	0.04	-1.67 ± 0.01	-1.66 ± 0.01	7.9 ± 0.01	37
NGC 3738	PGC 35856, UGC 6565, Arp 234	4.9	3	-17.1	2.40	0.78 ± 0.01	0.00	-1.66 ± 0.01	-1.53 ± 0.01	8.4 ± 0.01	25
NGC 4163	PGC 38881, NGC 4167, UGC 7199	2.9	1	-14.4	1.47	0.27 ± 0.03	0.00	-2.28 ± 0.13	-1.74 ± 0.01	7.9 ± 0.2	38
NGC 4214	PGC 39225, UGC 7278	3.0	1	-17.6	4.67	0.75 ± 0.01	0.00	-1.03 ± 0.01	-1.08 ± 0.01	8.2 ± 0.06	39
Sag DIG	PGC 63287, Lowal's Object	1.1	19	-12.5	···	0.23 ± 0.03	0.14	-2.97 ± 0.04	-2.11 ± 0.01	7.3 ± 0.1	35
UGC 8508	PGC 47495, IZw 60	2.6	1	-13.6	1.28	0.27 ± 0.01	0.00	-2.03 ± 0.01	···	7.9 ± 0.2	38
VII Zw 403	PGC 35286, UGC 6456	4.4	22,23	-14.3	1.11	0.52 ± 0.02	0.02	-1.71 ± 0.01	-1.67 ± 0.01	7.7 ± 0.01	25
WLM	PGC 143, UGCA 444, DDO 221, Wolf-Lundmark-Melott	1.0	20	-14.4	5.81	0.57 ± 0.03	0.02	-2.77 ± 0.01	-2.05 ± 0.01	7.8 ± 0.06	40

star formation tracer, a number of other tracers are also required in order to make qualitative comparisons.

The LITTLE THINGS project has been highly successful in acquiring a plethora of spatially resolved data on each of the 40 dwarf galaxies. The RC images (which will be covered in Chapter 3) are complemented by broadband continuum images including, among others, *GALEX* FUV, *Spitzer* MIR and FIR, and Hα line emission (see Hunter et al., 2012; Zhang et al., 2012, for details of the ancillary data). An explanation on the relevancy of each emission band to SF can be found in Section 1.2.2.

The maps used were of:

- Hα line emission: the FWHM of the filter used for the Hα observations was 30 Å centred on 6562.8 Å (Hunter & Elmegreen, 2004), while the FWHM of the resolution was $\sim 2''$. The maps have been continuum subtracted and the fluxes corrected for [NII] contribution. Hunter et al. (2012) used Burstein & Heiles (1982) values to correct Hα and FUV maps for foreground reddening. Internal extinction can generally be neglected due to the fact that these dwarfs are low–metallicity and consequently their dust-to-gas ratio is reduced with respect to spirals (Ficut-Vicas et al. in prep.), although it can be important in some of the more actively star forming dwarfs;

- Far-Ultraviolet broadband emission: the FUV data were taken with *GALEX* in the 1350–1750 Å band (effective wavelength of 1516 Å) with a resolution of $4''$ at the FWHM. The data were calibrated with the GR4/5 pipeline except DDO 165 and NGC 4214 which have been processed through the GR6 pipeline (Zhang et al., 2012). The resulting images have been sky subtracted and were geometrically transformed to match the optical *V*-band orientation. UGC 8508 was not observed due to bright foreground stars, and IC 10 was not observed due to its low Galactic latitude placing it in a region of high extinction. For surface brightness measurements, and hence for extended emission, the estimated uncertainty for the *GALEX* FUV maps is 0.15 mag (Gil de Paz et al., 2007);

- Infrared broadband emission: the IR data were observed using the *Spitzer* space telescope using the Multiband Imaging Photometer for Spitzer (MIPS). The two observation bands used were MIR (effective wavelength of 24μm with a resolution of $6''$ at the FWHM) and FIR (effective wavelength of 70μm with a resolution of $17''.5$ at the FWHM). The *Spitzer* 24 and 70μm maps were taken from either the Local Volume Legacy (LVL) survey (see Dale et al., 2009, for details) or the *Spitzer* Infrared Nearby Galaxies Survey (SINGS). A pixel-dependent

background subtraction was performed and images were convolved with a custom kernel to make a near Gaussian PSF. For the Spitzer $24\mu\mathrm{m}$ maps, the photometric uncertainty is 2% for both unresolved sources and extended emission (Engelbracht et al., 2007).

3

Data Reduction

This chapter concerns itself with the reasons behind using the VLA and the reduction of the raw data. During the Ph.D, the success of the VLA radio continuum proposals to observe LITTLE THINGS galaxies provided a raft of raw data from B- to D-configuration, using *L*- to *Ku*-band. In this chapter, we will describe how we approached the data acquisition and reduction, expanding on those aspects that are particular to the current project.

3.1 Data Acquisition

3.1.1 Choice of instrument: The Very Large Array

For the purposes of the study, the VLA was chosen as the most suitable instrument with which to tackle the question: *can the RC be used as an extinction-free indicator of SF in dwarf galaxies?* for its combination of high resolution and sensitivity.

The NRAO Very Large Array (VLA) is an expandable Y-shaped array of 27 interconnected radio telescopes. Its expandable nature allows it to be in one of 4 main configurations—A, B, C, or D—the properties of which are summarised in Table 3.1.

FIGURE 3.1: *Left:* The NRAO Very Large Array (VLA) is an expandable Y-shaped array of 27 interconnected radio telescopes. *Centre:* Each of the radio telescopes has an identical dish 25 m in size. *Right:* Each radio dish focusses the radiation towards a complex of feed horns. There is a separate receiver for each of the radio bands from *4*-band though to *Q*-band (4 m to 7 mm) with full polarisation. Images taken from images.nrao.edu, www.toddmckinney.com, and www.kcvs.ca.

Each of the radio telescopes has an identical dish $25\,\mathrm{m}$ in size. Each radio dish focusses the radiation towards a complex of feed horns. There is a separate receiver for each of the radio bands from *L*-band though to *Q*-band ($20.0\,\mathrm{cm}$ to $0.7\,\mathrm{cm}$) with significant bandwidth and at full polarisation (see Table 3.2 for details on each band).

Dwarf galaxies are intrinsically faint, and this was the main factor pushing towards use of the VLA. Its 27 dishes provide a total collecting area of $13000\,\mathrm{m}^2$ which is equivalent to a single dish of $130\,\mathrm{m}$ in diameter.

It is not just the raw collecting power that is important. The ability to evenly sample the (u, v) plane is a factor as well. A well-sampled (u, v) plane will give the image good fidelity. In this respect the VLA's configuration is ideal. The VLA has a carefully designed Y-shape, where each of the three arms are made of logarithmically spaced dishes. There are three ways of 'filling in' the (u, v) plane: 1) increasing the bandwidth, 2) observing for up to $8\,\mathrm{hours}$, and 3) using a range of baseline lengths and orientations (more antennas). Increasing the bandwidth essentially radially smears the (u, v) points while observing for longer allows the rotation of the Earth to rotate the orientation of the baselines with respect to the source creating elliptical tracks in the (u, v) plane (Figure 3.2 shows four consecutive scans, each scan separated by approximately an hour). Over the period of an observation, these methods translate into good coverage of the (u, v) plane making it sensitive to emission on a large range of angular scales.

The ability to sample as much of the (u, v) plane as possible is important as it leads to better image fidelity, and makes sensitivity to emission on a large range of scales possible. This is particularly relevant to this study of dwarf galaxies as SF processes happen on spatial scales ranging from kpc ($1'$ at $3.5\,\mathrm{Mpc}$) down to pc scales ($1/20$ arcsec at $3.5\,\mathrm{Mpc}$). In this study, processes on scales of 10s to 100s of pc

TABLE 3.1: **PROPERTIES OF THE 4 MAIN VLA CONFIGURATIONS**
(1) Name of configuration; (2) Max baseline length; (3) Minimum baseline length; (4) Largest angular scale of structure that is observable at *C*-band.

Configuration	$b_{\rm max}$ (km)	$b_{\rm min}$ (km)	LAS (*C*-band) (arcmin)
(1)	(2)	(3)	(4)
A	36.4	0.68	8.9
B	11.1	0.21	29
C	3.4	0.035	240
D	1.03	0.035	240

TABLE 3.2: **PROPERTIES OF THE VLA BANDS USED IN THIS STUDY**
(1) Name of band; (2) Low-frequency edge of band; (3) High-frequency edge of band; (3) Total bandwidth available using the 8-bit samplers.

Band	Low (GHz)	High (GHz)	Bandwidth (GHz)
(1)	(2)	(3)	(4)
L	1	2	1
S	2	4	2
C	4	8	2
X	8	12	2
Ku	12	18	2

are investigated.

3.1.2 Successful VLA Proposals

In the course of the Ph.D, we gathered a large volume of data with which to study the RC in dwarf galaxies. Currently, our projects have accumulated over 75 hours of VLA observations, mostly in C-configuration[1], which is summarised in Table 3.3. Based on the original 40 hours of observations at *C*-band (project ID: 12A-234), proposals were submitted for observations of a subset of the original sample at *L*, *S*, *X*, and *Ku*-bands (project IDs 13B-041 and 14B-359). The instrumental configurations of the VLA for these observations are summarised in Table 3.4.

[1]The VLA can be moved into 4 main configurations: A, B, C, and D. The longest baseline in A-configuration is 36 km, while only 1 km in D-configuration.

TABLE 3.3: **VLA RADIO CONTINUUM OBSERVATIONS OF LITTLE THINGS**
(1) Configuration of VLA observations; (2) Bands for which time was awarded; (3 & 4) The amount of time awarded and the total time observed; (5) Notes.

Configuration	Bands	Time Awarded (hr)	Time Observed (hr)	Notes
(1)	(2)	(3)	(4)	(5)
Project ID: 12A-234				
C	C	37	37 (100%)	Priority=A
CnB	C	3	3 (100%)	Priority=A
Project ID: 13B-041				
B	L	3.75	3.75 (100%)	Priority=A
B	L	8.75	0 (0%)	Priority=C
C	L, S, X	37.5	3.75 (10%)	Priority=C
D	Ku	15	12 (80%)	Priority=C
Project ID: 14B-259				
B	L, S	23	18 (78%)	Priority=B; on-going
C	L, S, X	21	21 (100%)	Priority=A
D	-	23	—	Priority=B; awaiting D-configuration

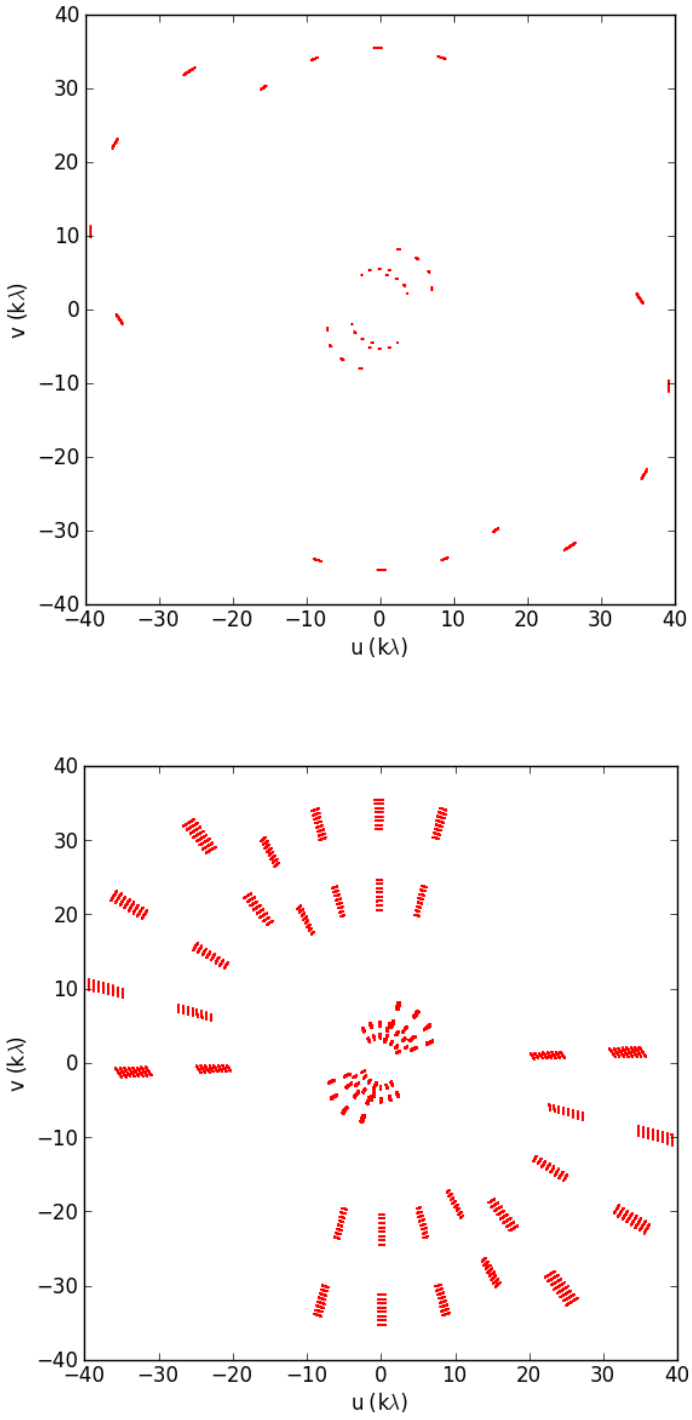

FIGURE 3.2: The (u, v) plane coverage of the VLA. The examples show (u, v) points for baselines containing antenna $ea22$. One way to 'fill in' the (u, v) plane is to increase the bandwidth—many more (u, v) points are generated when 16 spectral windows are used (lower panel) than when only a single spectral window is used (upper panel). Another way is to observe for longer periods—both panels show four consecutive scans, each scan separated by approximately an hour.

Table 3.5 shows the observations obtained for each dwarf galaxy. Most notably, I now have in my possession 1 hour of VLA observations in 5 different VLA bands each (*L*, *S*, *C*, *X*, and *Ku*) for 7 dwarf galaxies: DDO 50, Haro 29, NGC 2366, NGC 3738, NGC 4214, VII Zw 403, and WLM. There are 2 further dwarfs that have been observed in 4 bands (Mrk 178 and NGC 1569). Altogether, this is a substantial set of spectral information for 9 dwarf galaxies[2].

The success of the proposals has translated into a significant proportion of time devoted to writing scheduling blocks (the scripts designed to control the VLA dishes during an observation run). The NRAO graphic user interface for scheduling observations (Observation Preparation Tool—OPT), while easy-on-the-eye and navigation-friendly, is tediously slow. Consequently, it was decided to automate the creation of scheduling blocks with the intention of directly importing them into the OPT (thus avoiding the OPT GUI as much as possible).

The code took parameters from a file to record important transitions in a given object's daily motion through the observer's sky (e.g., time of day when reaching altitude of 30° whilst rising, time of day when falling to altitude of 30° whilst setting, etc.). It collates information on the observability of all objects in the scheduling block at a given time.

Avoiding low elevations (antenna shadowing becomes intrusive with elevations lower than 30 degrees) and high elevations (antenna slewing times become excessive with elevations higher than 80 degrees), the code decides whether to split a scheduling block into a 'rising' block and a 'setting' block. Finally, it creates an `xml` file, an example of which can be found in Appendix B.2.

The first excursion into the OPT took 2–3 weeks—time spent scheduling 40 hours of awarded time into 9 scheduling blocks (January 2012). With the first use of the code (November 2014), the creation of $\sim$ 50 scheduling blocks (for $\sim$ 60 hours of awarded time) took just an afternoon.

Once the scheduling blocks were validated, submitted, and executed, the resulting measurement sets could be downloaded from the NRAO archive[3]. Some of the scheduling blocks were assigned a priority of C (A is highest), and so were not guaranteed to be executed[4].

[2] This subset consists of the brighter dwarf galaxies and was selected on the basis of the observed *C*-band RC.

[3] `archive.nrao.edu/archive/advquery.jsp`

[4] On a lighter note, the VLA was officially renamed as the Karl G. Jansky Very Large Array in March 2012—the first scheduling block to be executed with its newfound identity was ours!

TABLE 3.4: **TECHINCAL SETUP OF VLA RADIO CONTINUUM OBSERVATIONS OF LITTLE THINGS**

(1) Configuration; (2) Band (note that all observations used the 8-bit sampler); (3) Average integration time for observation (galaxy and calibrators together); (3) Scan time for setup; (5, 6 & 7) For IF1, the central frequency and bandwidth, the number of spectral windows (SpWs), and the number of channels per spectral window; (8, 9 & 10) For IF2, the central frequency and bandwidth, the number of spectral windows, and the number of channels per spectral window.

Config.	Band	Int. Time	Scan Time	IF1 (A0/C0)			IF2 (B0/D0)		
		(minutes)	(seconds)	(GHz)	(SpWs)	(chan.)	(GHz)	(SpWs)	(chan.)
(1)	(2)	(3)	(4)	(5)	(6)	(7)	(8)	(9)	(10)
Project ID: 12A-234									
C	C	60	5	5.000 ± 0.512	8	64	7.400 ± 0.512	8	64
CnB	C	60	3	5.000 ± 0.512	8	64	7.400 ± 0.512	8	64
Project ID: 13B-041									
B	L	60	3	1.250 ± 0.256	8	64	1.750 ± 0.256	8	64
C	L	75	5	1.264 ± 0.256	8	64	1.776 ± 0.256	8	64
C	S	75	5	2.500 ± 0.512	8	64	3.500 ± 0.512	8	64
C	X	75	3	8.500 ± 0.512	8	64	9.500 ± 0.512	8	64
D	Ku	60	3	13.000 ± 0.512	8	64	17.000 ± 0.512	8	64
Project ID: 14B-359									
B	L	60	3	1.264 ± 0.256	8	64	1.776 ± 0.256	8	64
B	S	60	3	2.500 ± 0.512	8	64	3.500 ± 0.512	8	64
C	L	60	5	1.264 ± 0.256	8	64	1.776 ± 0.256	8	64
C	S	60	5	2.500 ± 0.512	8	64	3.500 ± 0.512	8	64
C	X	60	3	8.500 ± 0.512	8	64	9.500 ± 0.512	8	64

TABLE 3.5: **VLA RADIO CONTINUUM OBSERVATIONS OF THE LITTLE THINGS GALAXIES**

(1) Galaxy; (2 & 3) B- and C-configuration at *L*-band; (4 & 5) B- and C-configuration at *S*-band; (6 & 7) C- and D-configuration at *C*-band; (8 & 9) C- and D-configuration at *X*-band; (10) D-configuration at either *Ku* or *K*-band; (11) The total number of VLA bands covered by our projects per galaxy.

Galaxy	*L*-band		*S*-band		*C*-band		*X*-band		*K*-bands	Bands covered
	B	C	B	C	C	D	C	D	D	
(1)	(2)	(3)	(4)	(5)	(6)	(7)	(8)	(9)	(10)	(11)
CVI n DwA					✔					1
DDO 43					✔					1
DDO 46					✔					1
DDO 47					✔					1
DDO 50	✔	✔	✔	✔	✔		✔		✔	5
DDO 52					✔					1
DDO 53					✔					1
DDO 63					✔					1
DDO 69					✔					1
DDO 70					✔					1
DDO 75					✔					1
DDO 87					✔					1
DDO 101					✔					1
DDO 126					✔					1
DDO 133					✔					1
DDO 154					✔					1
DDO 155					✔		✔		✔	3
DDO 165					✔					1
DDO 167					✔					1
DDO 168					✔					1
DDO 187					✔					1
DDO 210					✔					1
DDO 216					✔					1
F564 V3					✔					1
Haro 29	✔	✔	✔	✔	✔		✔		✔	5
Haro 36					✔					1
IC 10					✔					1
IC 1613					✔					1
M81 DwA					✔					1
Mrk 178	✔	✔	✔	✔	✔		✔			4
NGC 1569	✔		✔		✔		✔			4
NGC 2366	✔	✔	✔	✔	✔		✔		✔	5
NGC 3738	✔	✔	✔	✔	✔		✔		✔	5
NGC 4163					✔					1
NGC 4214	✔		✔	✔	✔		✔		✔	5
Sag DIG					✔					1
UGC 8508					✔					1
VII Zw 403	✔	✔	✔	✔	✔		✔		✔	5
WLM	✔	✔		✔	✔		✔		✔	5

3.2 Data reduction overview

3.2.1 Interferometry Theory

Before detailing the calibration pipeline, an overview of the theory behind interferometry will be given. In a sentence: *the observed data is the Fourier transform of the sky brightness, along with additional effects introduced by the instrument and atmosphere.* Much of the following information in this chapter is based on Condon & Ransom (2010) and Taylor et al. (1999).

Figure 3.3 is a schematic showing two dishes (receivers) separated by a distance, $\vec{b}$, observing a distant source in the direction $\vec{s}$. The signal V_1 is delayed by a geometric delay, τ_g, while the signal V_2 is delayed by an artificial delay, τ_0. The objective is to make τ_0 equal to τ_g such that the signals remain in phase. In practice, an incident planar wave will illuminate dish-2 before dish-1 and so a delay, τ_0, is introduced to the output of dish-2 such that the oscillating voltages V_1 and V_2 induced by the incident electric field arrive at the correlator in phase. This delay is a function of $\vec{s_0}$ (the angle at which the dish is pointed) and the length of the baseline.

When the two voltages are multiplied, the output is time-averaged giving the response,

$$R = \langle V_1 V_2 \rangle = \left(\frac{V^2}{2} \right) \cos \omega \tau_g, \tag{3.1}$$

where ω is the angular frequency of the oscillating electric field. The square of the wave's electric field amplitude is proportional to the wave's intensity, and therefore, the product of these two identical voltages, and thus R, is also proportional to the intensity of the incident electromagnetic wave.

The $\cos()$-term essentially describes the phase of the correlated signal. By definition, if a single unresolved source is positioned exactly at $\vec{s_0}$, the phase of the correlated signal is 0 i.e., the signals arrive at the correlator in phase making the response, R, a maximum. However, if a single unresolved source were to be placed a small angular distance from the observation's *phase centre* ($\vec{s_0}$), then the response, R, would reduce since the time delay, τ_g, is calibrated only for a wave originating from the direction of $\vec{s_0}$.

In fact, as a function of angular distance from $\vec{s_0}$, the response oscillates between maximum and minimum value with a phase of ϕ—the argument of the $\cos()$-term in Equation 3.1—which can be expressed as $2\pi f \tau_g$, or alternatively

$$\phi = 2\pi \frac{b \cos \theta}{\lambda} \tag{3.2}$$

where θ is the angle that the $\vec{s_0}$ makes with the plane of the baseline. The response of

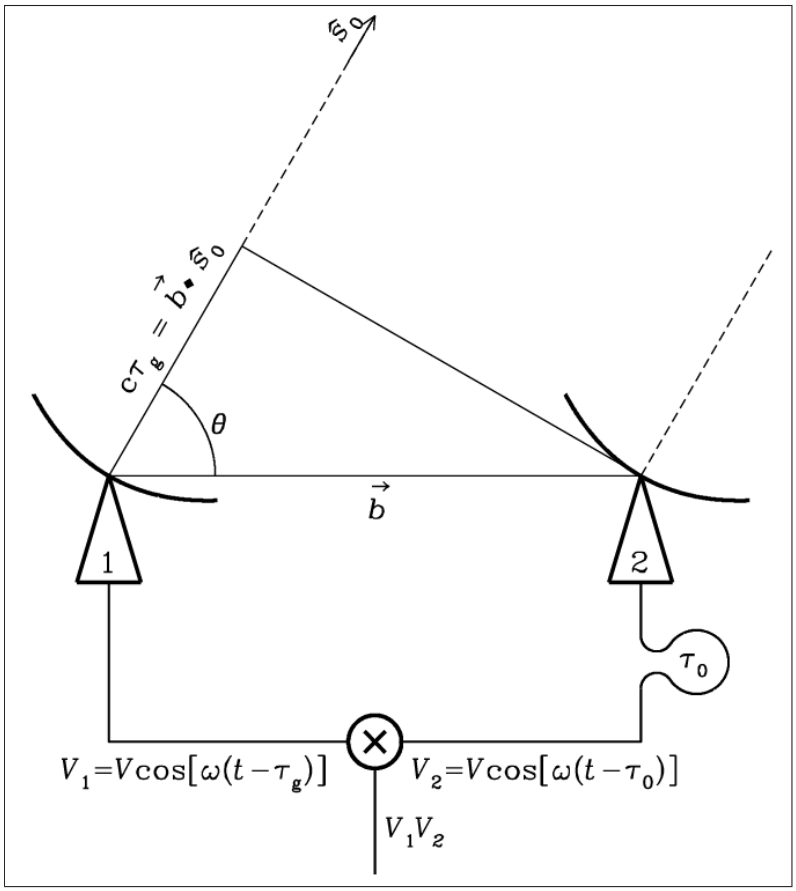

FIGURE 3.3: Schematic of a simple 2-element interferometer taken from Condon & Ransom (2010). The two dishes (receivers) separated by a distance $\vec{b}$ observe a distant source in the direction $\vec{s}$. Effectively, the signal V_1 is delayed by a geometric delay, τ_g, while the signal V_2 is delayed by an artificial delay, τ_0. The objective is to make τ_0 equal to τ_g such that the signals remain in phase. In practice, an incident planar wave will illuminate dish-2 before dish-1 and so a delay is introduced to the output of dish-2 such that the voltages V_1 and V_2 arrive at the correlator in phase.

the interferometer a small angular distance away from $\vec{s_0}$ would be lower than at $\vec{s_0}$. Points of sky further from $\vec{s_0}$ would yield lower responses, and further still would return to a maximum. To quantify this angular distance, we need to examine how ϕ changes with respect to θ, i.e., $d\phi/d\theta$ which is

$$\frac{d\phi}{d\theta} = \frac{\Delta\phi}{\Delta\theta} = -2\pi\frac{b\sin\theta}{\lambda}. \tag{3.3}$$

This angular distance, $\Delta\theta$ corresponds to the maximum-to-maximum change in phase, $\Delta\phi = 2\pi$ rad, and so Equation 3.3 can be rearranged resulting in

$$\Delta\theta = \frac{\lambda}{b\sin\theta} \tag{3.4}$$

which is similar in form to the resolution of a diffraction limited aperture (see Equation 1.20). The angular separation, $\Delta\theta$, of these response maxima is known as the

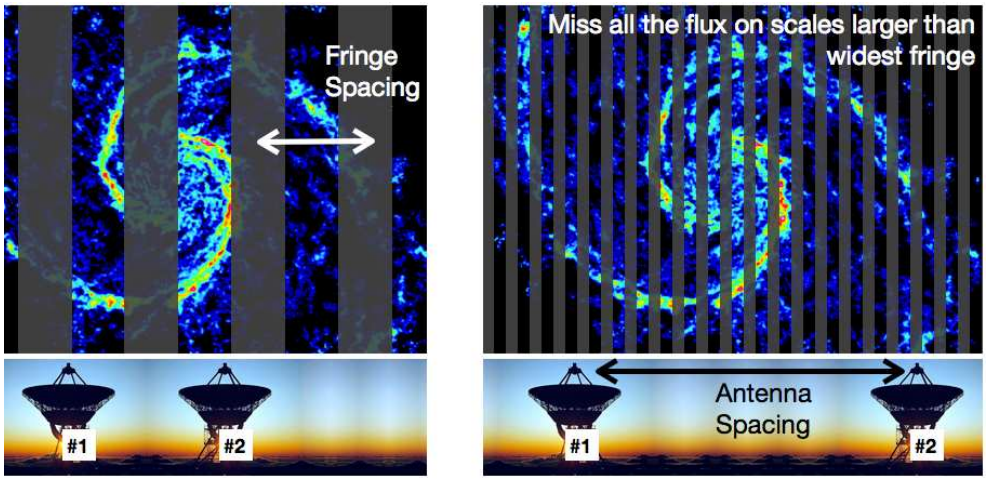

FIGURE 3.4: Graphical illustration of fringe spacing. A receiver works just like an emitter in reverse. Therefore, instead of interpreting an interferometer as receiving a response that is dependent on the part of the sky being observed, it can just as easily be represented by the two dishes emitting their own signal onto the sky plane. In this example, the real sky brightness distribution (image) are overlaid by the response pattern (fringes) of a short (left) and long baseline (right). Note: The images show a square wave response for illustrative purposes, whereas the response is actually a continuous oscillation between minima and maxima.

fringe spacing. It is essentially the resolution of a single baseline, and is proportional to the wavelength of light, while inversely proportional to the projected baseline length, $b \sin \theta$.

A receiver works just like an emitter in reverse. Therefore, instead of interpreting an interferometer as receiving a response that is dependent on the part of the sky being observed, it can just as easily be represented by the two dishes emitting their own signal onto the sky plane. In Figure 3.4, the real sky brightness distribution (a spiral galaxy in this example) is overlaid by a simplified response pattern (fringes) of a short baseline (left) and longer baseline (right).

These fringes make the interferometer totally insensitive to uniform emission on scales larger than the fringe spacing. The fact that the interferometer is insensitive to large scale sources means that the data is less likely to be contaminated by a low surface brightness plateau. For instance, foreground emission such as Galactic synchrotron emission (which tends to be large scale as it is relatively close) or the Cosmic Microwave Background, both remain invisible to the interferometer.

As mentioned, the fringes come about due to the fact that the response (i.e., the correlation of signal from two dishes) is dependent on sky position (angular distance from $\vec{s_0}$). But these fringes do not extend over the whole sky; they are also subject to the response pattern of the individual antennas of the interferometer. The result is that the fringes are modified by the primary beam attenuation. Figure 3.5 shows this

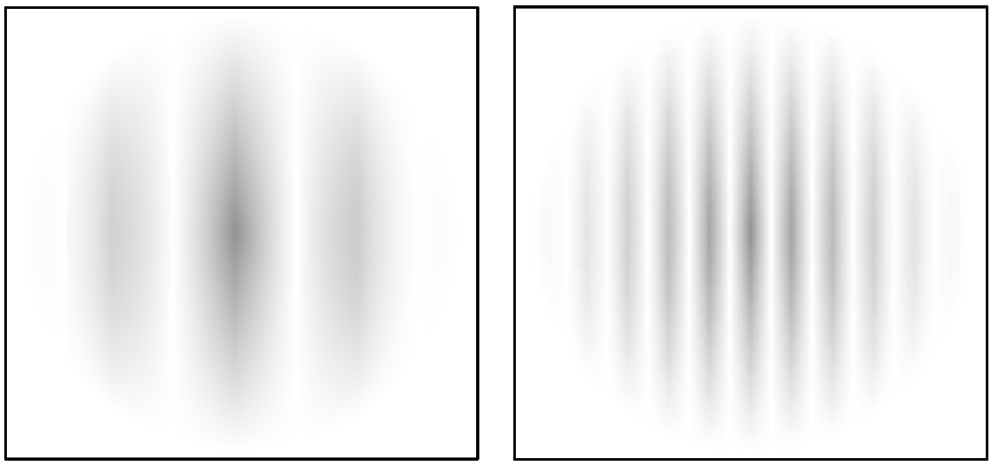

FIGURE 3.5: The fringe spacings are also subject to the response of a single dish, i.e., the primary beam attenuation. For comparison, the panels show a short (left) and a long (right) baseline orientated the same way, and subject to the same primary beam.

graphically: both a short and a long baseline orientated the same way, and subject to the same primary beam.

A cross section over this modified fringe pattern would reveal the form of a sinc^2-function. The sinc^2-function is the Fourier transform of the triangle function, which itself is the convolution of two square functions (the two slits in Young's double slit experiment, or the two dishes in the baseline). The correlation (multiplication) of signal from the two dishes is analogous to convolution in the Fourier domain, and hence the correlation of signal leads to the sinc^2-function.

3.2.2 The (u,v) plane

The $b \sin\theta$ term is effectively the projected length of the baseline as observed from the source at $\vec{s_0}$. There are a total of $N(N-1)/2$ baselines and all are calibrated such that the delay time makes signal from $\vec{s_0}$ arrive in phase. Each baseline makes an individual point on the (u, v) plane—the position of which can either be defined by an intensity measured at a u- and a v-coordinate, or by a vector of a magnitude and direction.

The positioning of antennas is important so as to sample as much of the (u, v) plane as possible, and ideally, as uniformly as possible. For example, in 1D, a 3-element interferometer with antennas placed at regular intervals along a line is an inefficient configuration: there are 3 baselines, but 1 baseline becomes redundant in that it samples exactly the same (u, v) space as one of the other baselines. Similarly, a 4-element interferometer with antennas placed at the vertices of a square is also an

inefficient configuration: there are $N(N-1)/2 = 6$ baselines, but 2 of the baselines are redundant in that they sample exactly the same (u, v) space as others.

Each (u, v) point essentially projects a unique response pattern onto the sky plane. This response of a given baseline (a (u, v) point) is called its *visibility*. The visibility of a single baseline to a source distributed over a patch of sky is

$$V = \int A(\vec{s})\, I(\vec{s})\, e^{-i2\pi \frac{\vec{b}\cdot\vec{s}}{\lambda}}\, \mathrm{d}\Omega. \tag{3.5}$$

(Wilson et al., 2009) where Ω is the solid angle on the sky plane, and the terms that are dependent on s are:

- $A(\vec{s})$: the primary beam on the plane of the sky. The value is zero at sufficient distance from s_0;
- $I(\vec{s})$: the source brightness distribution in the plane of the sky—the integral of $I(\vec{s})$ is essentially the sum of brightness from all the infinitesimally small patches of sky;
- $\exp(-i2\pi\vec{b}\cdot\vec{s}/\lambda)$: the fringe pattern of the baseline projected onto the plane of the sky.

If these three terms are integrated over the whole of the sky, then this yields the total response for that visibility.

Instead of using $\vec{b}$ and $\vec{s}$, we can define:

$$\mathrm{d}\Omega = \frac{\mathrm{d}l\,\mathrm{d}m}{(1-l^2-m^2)^{1/2}} \tag{3.6}$$

and

$$\frac{\vec{b}\cdot\vec{s}}{\lambda} = ul + vm + wn \tag{3.7}$$

where l and m are the direction cosines. These can be substituted back into Equation 3.5 to yield

$$V = \int A(l,m)\, I(l,m)\, \frac{1}{(1-l^2-m^2)^{1/2}}\, e^{-i2\pi[ul+vm+wn]}\, \mathrm{d}l\mathrm{d}m. \tag{3.8}$$

Given the visibility observed, Equation 3.8 needs to be inverted to find the intensity at (l,m) which corresponds to a position on the sky.

3.2.3 The Data

With the upgrades to the VLA being completed in 2010, the *C*-band (4–8 GHz) bandwidth has increased 20-fold to 2 GHz in total. While this bandwidth is of great scientific value, it does constitute its own problems: for full polarisation observations

using the 8-bit sampler, the data rate spewed out by the correlator is $\sim 2.2\,\mathrm{Mb\,s^{-1}}$ or $\sim 8\,\mathrm{Gb\,hr^{-1}}$. This data rate quickly produces a vast volume of data collated into a single file (a measurement set). In our case, 9 such measurement sets were obtained containing 40 hours of awarded VLA time, coming to $\sim 308.35\,\mathrm{Gb}$ altogether; calibrating the data increased the size of the measurement sets, and with self-calibration and the creation of images, the disk space used increased significantly.

In addition to the problems introduced by such large quantities of data, the software designed to deal with it is still under development: Common Astronomy Software Applications (CASA; McMullin et al., 2007). It is user-friendly (e.g., GUIs), and is based on an open-source programming language, Python. However, CASA, with VLA data, is detrimentally slow and buggy.

The calibration and imaging of interferometric radio data is adorned with a plethora of customisable features. Much effort and time can be spent tailoring calibration and imaging techniques to match the quality of the data and the intended use of the image. This is fine for a single observation (as was done in the pilot study of IC 10; Heesen et al., 2011); however, it is impossible to achieve such a high level of intimacy with 40 different targets. For such a large sample of galaxies, having a pipeline to flag, calibrate, and image was imperative, not just for questions of time, but also for consistency. Consequently, a VLA pipeline was created from scratch designed to perform pre-calibration flagging, calibration, post-calibration flagging, and imaging of each galaxy using CASA. The general structure is shown in Figure 3.6 and is explained in more detail in Sections 3.3–3.6. The pipeline was designed for use in CASA. The limiting factor in the calibration and imaging was the time taken to do it. The script takes a number of parameters from a parameter file and from there runs through unaided performing flagging, calibration, and imaging. The aim was to calibrate and image each galaxy in a consistent manner.

3.3 Pre-calibration flagging

Before calibrating the data, it is advisable to flag bad data (e.g., RFI). If left unchecked, RFI will ultimately affect the quality of the calibration as it effectively pushes up the amplitude of visibilities. In turn, this will affect the appearance of the final image, where the image can appear blotchy due to poorly calibrated phase, or with periodic streaks due to strongly affected baselines. Therefore, a flagging procedure is applied to the measurement set before any calibration is done.

In Figure 3.7, the primary calibrator's visibilities are shown of a single baseline on

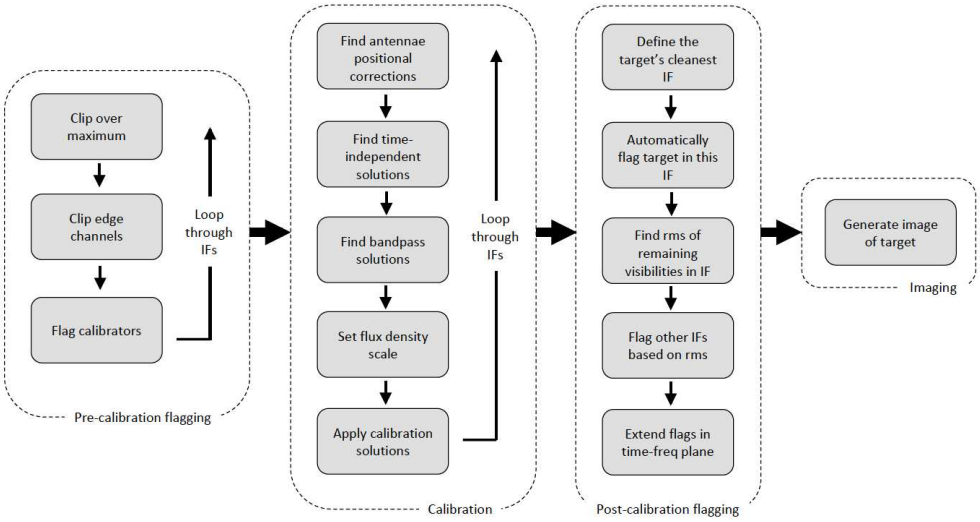

FIGURE 3.6: Flow diagram of the flag-calibrate-image procedure. The main steps were to do a pre-calibration flag, then to calibrate, and then a post-calibration flag. Once this was all complete, the imaging process could start.

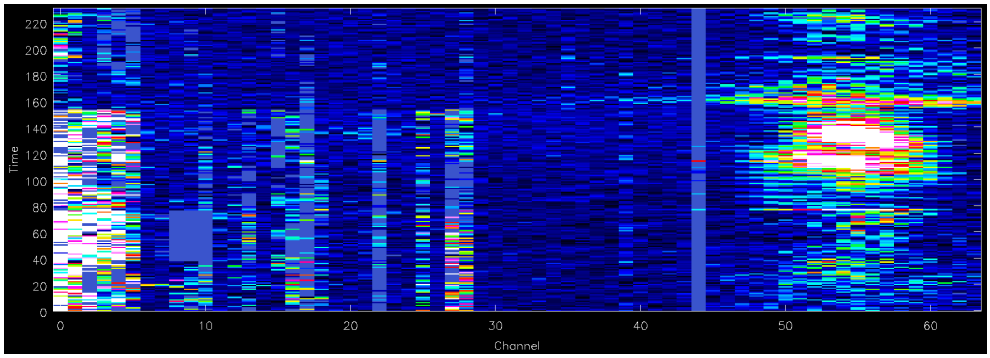

FIGURE 3.7: The amplitudes of visibilities in the time-frequency plane of a single baseline. RFI manifests itself as the abnormally high amplitudes (hot colours) atop the plateau of unaffected visibilities (cool colours). This example is heavily affected by RFI showing the manner in which RFI can appear: wideband and narrowband (which refer to how widespread the RFI is along the frequency axis), and persistent and intermittent (which refers to how widespread the RFI is along the temporal axis).

the time-frequency plane. There is some obvious RFI, most of which is well above the typical observed values of 0.001–0.010[5]. Thus any values greater than an arbitrary level of 10 are immediately clipped.

The frequency range of the observations were split into 16 spectral windows, each comprising 64 channels. It was decided to flag the first and last channels in all spectral windows as sensitivity at the edges of each spectral window is lower than in the centre.

[5]These values are uncalibrated amplitudes; they do not have units in the traditional sense (e.g., Jy, Candels, etc.), but have 'instrumental' units

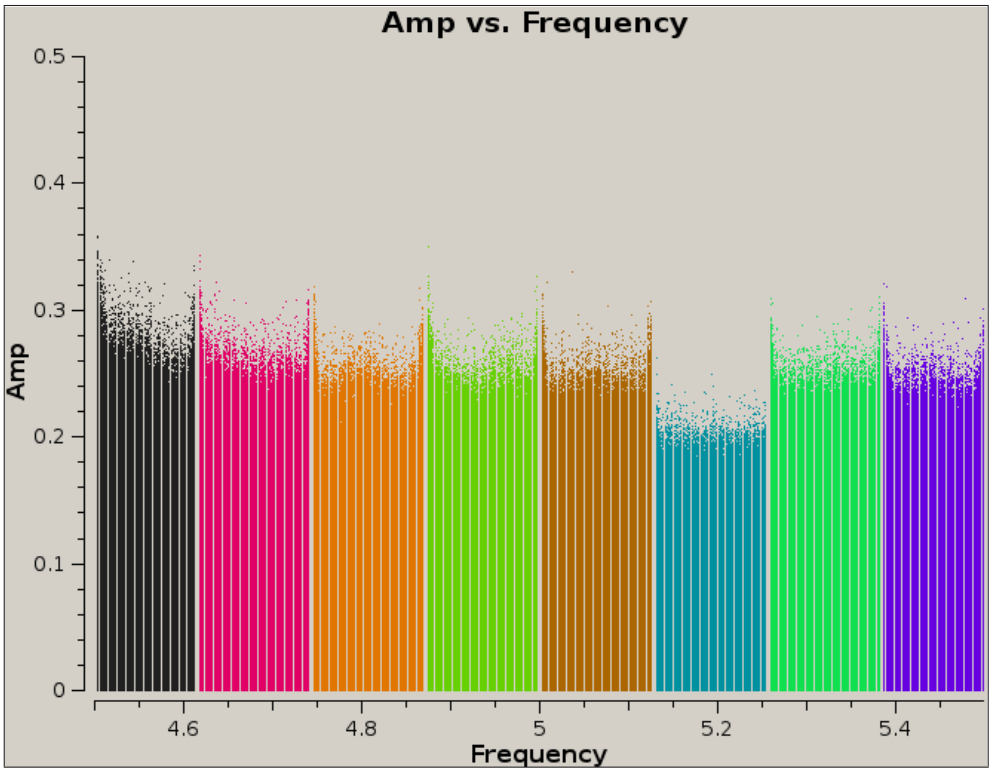

FIGURE 3.8: The amplitude of visibilities in 8 spectral windows is shown using CASA's `plotms` function. Each spectral window is given a unique colour to show the spectral window boundaries. The edges of each spectral window exhibit elevated levels of noise, which justified their exclusion from the imaging process.

The 16 spectral windows are separated into two sets of 8; each set referred to as an IF or sub-band of the VLA. The first 8 spectral windows are grouped into a sub-band called AC, while the last 8 are grouped into a sub-band called BD). Each of these 2 sub-bands have diminished sensitivity near their edges, and therefore the first 8 channels are flagged in each sub-band (which correspond to the first 8 channels in the 1^{st} and 9^{th} spectral window), and the final 8 channels are flagged in each sub-band (which correspond to the final 8 channels in the 8^{th} and 16^{th} spectral window).

To justify clipping the spectral window edges, Figure 3.8 shows the amplitude of visibilities in 8 spectral windows using CASA's `plotms` function. Each spectral window is given a unique colour to show the spectral window boundaries. The edges of each spectral window exhibit elevated levels of noise. Generally, these edge channels (the 1^{st} and 64^{th}) were judged to have approximately half the S/N as the central 62 channels. With these values, it was calculated that the 64 channels together would give a 3% worse S/N than if only the central 62 channels were used. This was the justification behind flagging the first and last channels in each spectral window, thus excluding them from the imaging process.

The first 5 seconds of each scan are flagged too by using the `tflagdata: mode='quack'`. Individual scans were often a minute in duration, but the first few seconds of each scan are dominated by the dishes 'settling in to their new positions'. In other words, it is not guaranteed that all dishes are motionless and looking at the same area of sky in these first few seconds of the scan; this results in a loss of signal.

With the measurement set clipped, the spectral window edges flagged, and the first few seconds of each scan flagged, `tflagdata(mode='rflag')` is used. This CASA function iterates through the measurement set on a per baseline, per spectral window basis. It calculates statistics across time to find an appropriate threshold value, and then runs back through the measurement set flagging data above the calculated threshold.

3.4 Calibration

Once the primary and secondary calibrators had the majority of their bad data flagged, calibration solutions were calculated and then applied to the target object.

To understand why calibration is done, it helps to see the observed visibility as a modified version of the true visibility. The true visibility is modified by the way in which the source is observed. Most relevantly, for our wide-bandwidth observations, the true visibility (of a baseline comprising antennas i and j) is altered by antenna-specific complex gains, G_i and G_j, which change as function of time, where the complex gain can be separated into an amplitude and a phase component such that

$$G_i = g_i \, e^{i\theta_i t}. \tag{3.9}$$

The visibility is also modified by antenna-specific bandpasses, B_i and B_j^* which describe the frequency dependent sensitivity across the observing band. Each of these terms alter the visibility, $V_{i,j}^{\rm true}(u,v,f)$, such that

$$\hat{V}_{i,j}^{\rm obs}(u,v,f) = B_i(f)\; B_j^*(f)\; g_i(t) g_j(t)\; V_{i,j}^{\rm true}(u,v,f) e^{i[\theta_i(t) - \theta_j(t)]} \tag{3.10}$$

(Wilson et al., 2009). Any baseline, whatever the length or orientation, would ideally observe an unresolved calibrator at the phase centre as having the same amplitude and zero phase. In practice, calibrators can be resolved (the AGN is a point source, but the associated radio lobes are extended) and so the observed response from the interferometer can change dependent on the baseline length and orientation (i.e., the (u,v) point). For this reason, a resolved model image of the calibrator source can be defined to take the calibrator's structure into account.

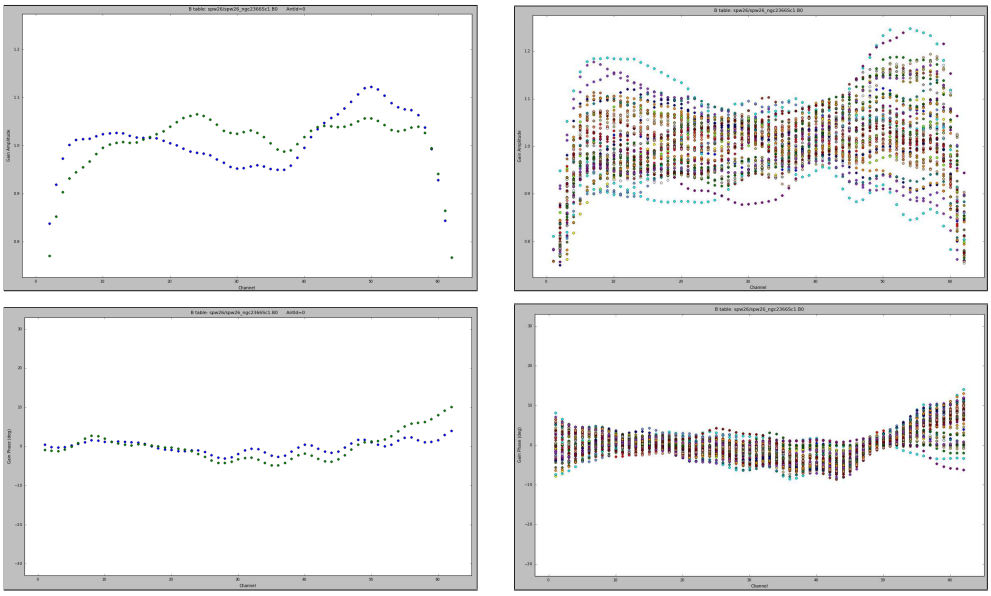

FIGURE 3.9: The bandpass is a spectral response, of which there is a unique form for each antenna and spectral window. The bandpass calibration normalises the whole bandpass to the average value. The panels show the amplitude solutions (top) and phase solutions (bottom) for the bandpass calibration for a single antenna (left) and all antennas (right).

The bandpass calibration derives corrections for the antennas' non-perfect response as a function of frequency. Electronic filters allow varying quantities of flux to pass for a given frequency (see Figure 1.4). In reality, some energy is lost through transmission of the electronic filter, and usually this effect is greater near the edges of the band. The form of the bandpass is essentially its own spectral response. The bandpass calibration applies a correction such that all channels are brought to the same flat response. This is done by normalising the bandpass to the average transmission value over the central channels (see Figure 3.9 for an example of the bandpass solutions).

The complex gain calibration derives corrections for g_i and g_j, and θ_i and θ_j in Equation 3.10 as a function of time. Calibrator sources are not expected to change in intensity over the course of an observation and, therefore, the amplitude of a given visibility is expected to remain constant[6]:

$$\frac{V_{true}}{V_{obs}} = g_i \, g_j. \tag{3.11}$$

[6]The amplitude would not change in an ideal case. Of course with time, the projected length of a baseline may shorten making the baseline sensitive to larger scales of emission; if this is the case, and the calibrator is extended, then the amplitude would increase. For this reason, calibrators that remain unresolved across all baselines were selected when preparing the scheduling blocks.

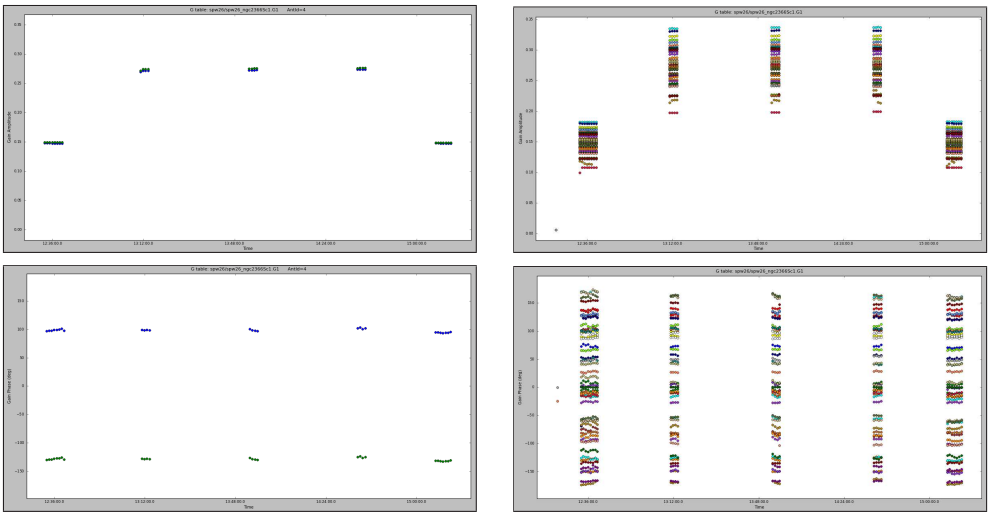

FIGURE 3.10: The complex gain calibration derives corrections for the amplitude, g_i (top) and the phase, θ_i (bottom) for a single antenna (left) and all antennas (right).

At this point, the relative amplitudes need to be converted to absolute amplitudes. The absolute flux calibration of the VLA relies on 4 flux calibrators, the morphology and flux density of which are very well known and regularly monitored. Therefore, by comparing the visibility amplitudes of the secondary calibrator with those of the primary calibrator, the true amplitude of the secondary calibrator, $S_{\rm sec}$, can be calculated through

$$1\,{\rm Jy} \times S_{\rm pri}\,\frac{g_{i,{\rm sec}}\,g_{j,{\rm sec}}}{g_{i,{\rm pri}}\,g_{j,{\rm pri}}} \tag{3.12}$$

where the $\rm pri$ and $\rm sec$ subscripts refer to the primary and secondary calibrators, respectively.

With the calibration solutions calculated, they are then applied to the actual data. If the secondary calibrator and the source of interest were observed simultaneously, then phase solutions could be applied on a per-scan basis. With the VLA, this is not possible, and the next best option is to extrapolate on/interpolate between the secondary calibrator solutions. Ideally, the scheduling block would be structured such that scans of the source of interest are bracketed by scans of the secondary calibrator, where the time between each observation of the secondary calibrator would ensure that changing ionospheric conditions are followed[7].

3.4.1 Post-calibration Verification

As previously stated, the primary and secondary calibrators are unresolved (or at the very least, only slightly resolved), and therefore most baselines should observe

[7] science.nrao.edu/facilities/vla/docs/manuals/oss/performance/gaincal/referencemanual-all-pages

the same unresolved flux density; this manifests itself as a constant flux density as a function of (u, v) distance (baseline length). The calibrators have sufficiently large physical sizes (e.g., AGN) that they should remain constant throughout the observation, although a dependency on frequency is expected. Finally, the phase should be equal to 0, independent of baseline, frequency, or time observed. All of these aspects were checked prior to flagging and imaging (e.g., see Figure 3.11).

The calibrated data of the source of interest is a different matter. It is often resolved, and has many background sources that are displaced from the phase centre. Thus, the phases appear random, and the amplitudes whilst varying wildly for large baselines (short fringe spacings), have larger values for the shorter ones if extended emission is present in the primary beam.

3.5 Post-calibration flagging

Post-calibration flagging was performed to remove low-level RFI or any other features not captured by the pre-calibration flagging. This flagging procedure was distinct from the pre-calibration flagging in that spectral windows were not flagged individually, but rather flagged based on the rms of amplitudes from the observation's cleanest spectral window. To see just how well RFI is flagged, the time-frequency plane of an *L*-band observation of DDO 50 is examined in Figure 3.12. It is clearly heavily affected by RFI (both wideband and narrowband, and both persistent and intermittent in time). The top panel illustrates the extent to which CASA's in-built `tflagdata(mode='tfcrop')` function largely misses RFI. The middle panel shows that the `tflagdata(mode='rflag')` function (based on AIPS; Greisen 2011) fares better but does miss regions of low-level RFI. The bottom panel shows the flagging success based on our rms-based procedure—low-level RFI is better caught because the rms was based on the amplitudes from a *cleaner* spectral window, not on this current spectral window which would naturally harbour a higher rms (as it is significantly affected by high amplitude visibilities, i.e., the RFI). The result is a cleaner spectral window, but with the risk of flagging some good data. The conclusion was reached that removing all RFI, even if it were at the expense of a small amount of good data, was better than including any RFI at all.

RFI would usually yield images characterised by linear streaks (from heavily affected baselines) and a decrease in S/N (from poorly calibrated phases). For example, by removing this RFI, and conservatively flagging 20% of clean data (to ensure that even low-level RFI was flagged), the S/N would increase by 11%.

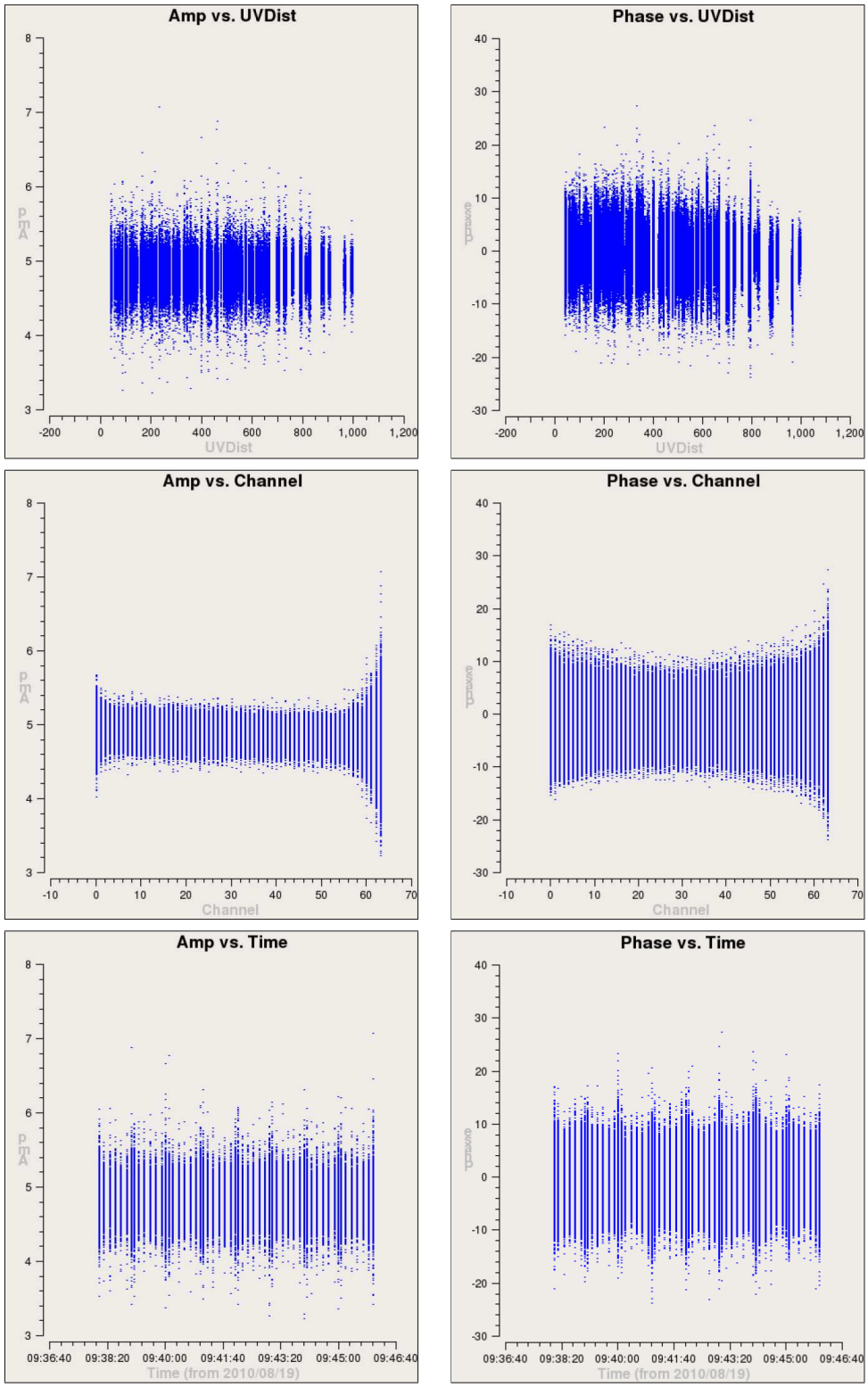

FIGURE 3.11: The calibrated data of the primary calibrator. The calibrated flux density (left panels) and phase (right panels) are shown as a function of baseline length (top), frequency (middle) and time (bottom). A similar picture is expected for the secondary calibrator.

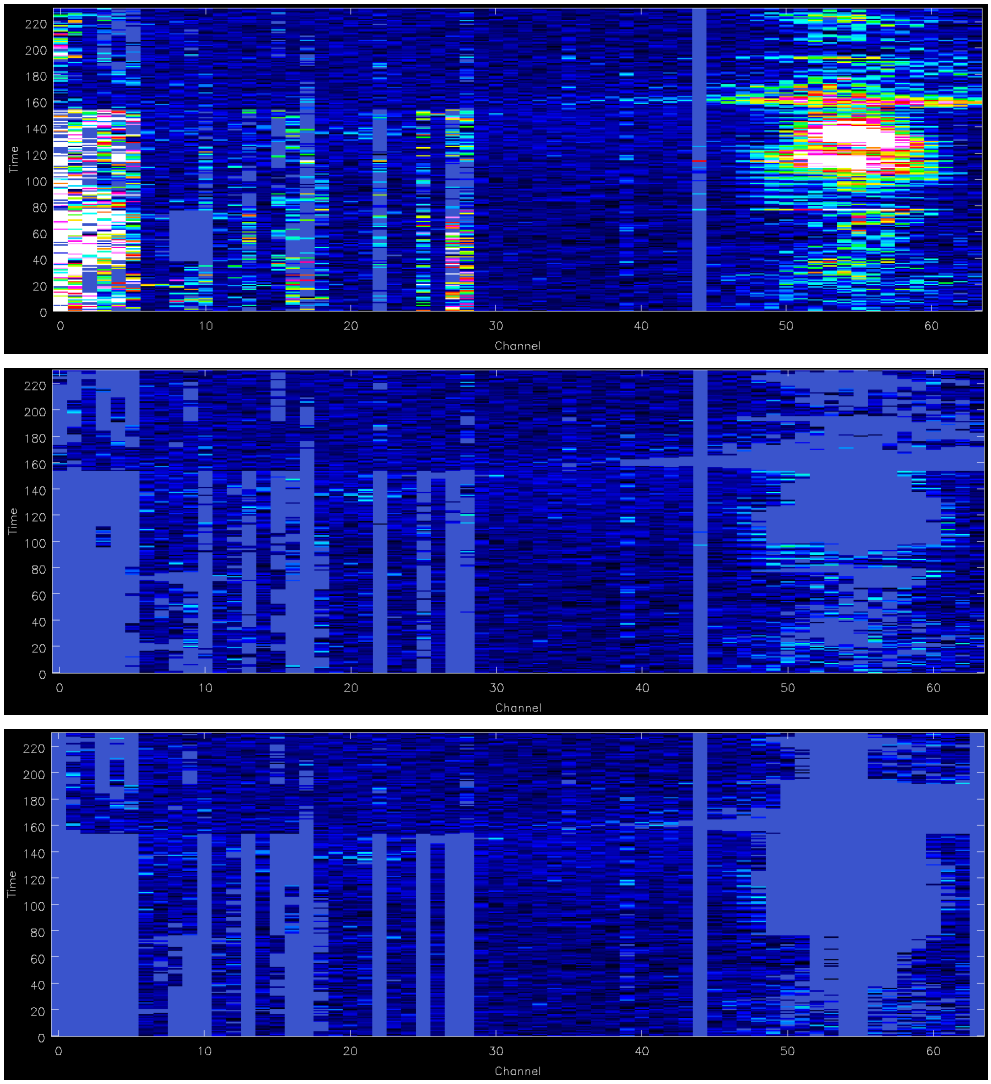

FIGURE 3.12: Relative success of identifying and flagging unwanted signal. To illustrate, CASA's in-built `msview` function is used to show the time-frequency plane of a baseline heavily affected by RFI (both wideband and narrowband, and both persistent and intermittent in time). Flagging is applied using: *top:* CASA's in-built `tflagdata(mode='tfcrop')` function; *middle:* CASA's in-built `tflagdata(mode='rflag')` function (based on AIPS; Greisen 2011); *bottom:* the rms in amplitude of a clean spectral window (which itself had already been flagged using the `tflagdata(mode='rflag')` function).

When the rms-based flagging procedure is applied to the whole measurement set, the true success of this method is realised. Figure 3.13 shows how the amplitudes of millions of visibilities from the measurement set with our rms-based flagging procedure produce a clean measurement set ready for imaging.

Given the low surface brightness of dwarf galaxies, integrated and resolved flux

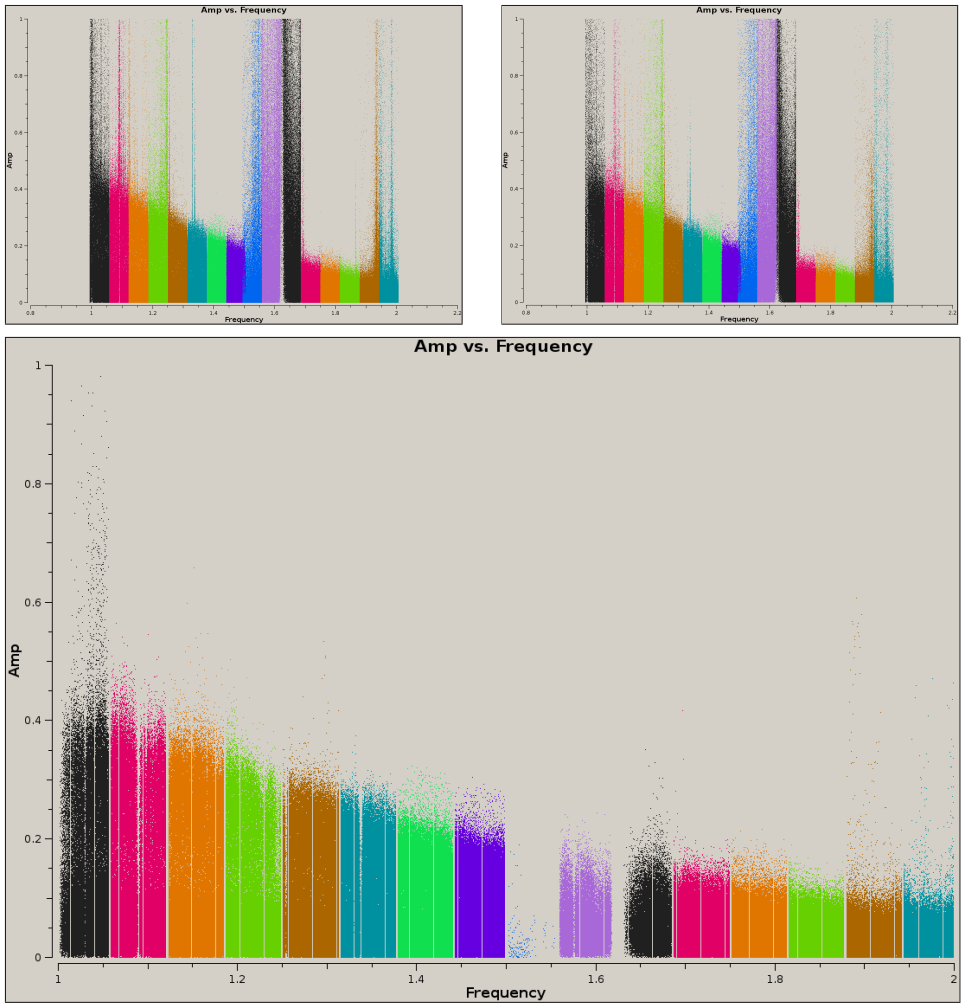

FIGURE 3.13: Relative success of identifying and flagging unwanted signal over all 16 spectral windows. To illustrate, the calibrated amplitudes of visibilities as a function of frequency are shown using CASA's `plotms` function. *Top-left:* No flagging applied. *Top-right:* CASA's in-built `tflagdata(mode='rflag')` function which was mostly successful in flagging narrow-band features. *Bottom:* The 7^{th} spectral window was identified as the cleanest spectral window and flagged using the `tflagdata(mode='rflag')` function. Then, based on the rms of amplitudes in this cleanest spectral window, the other 15 spectral windows were flagged.

densities were often only a few sigma above the rms background level (see Chapters 4 and 5). Thus, the contaminating effects of image artefacts (e.g., from high-amplitude baselines) or noise (e.g., from data contaminated with RFI) posed a limit to accurate flux measurements (when compared to brighter objects such as spiral galaxies). Therefore, it was imperative to flag bad data completely, which our pipeline does well.

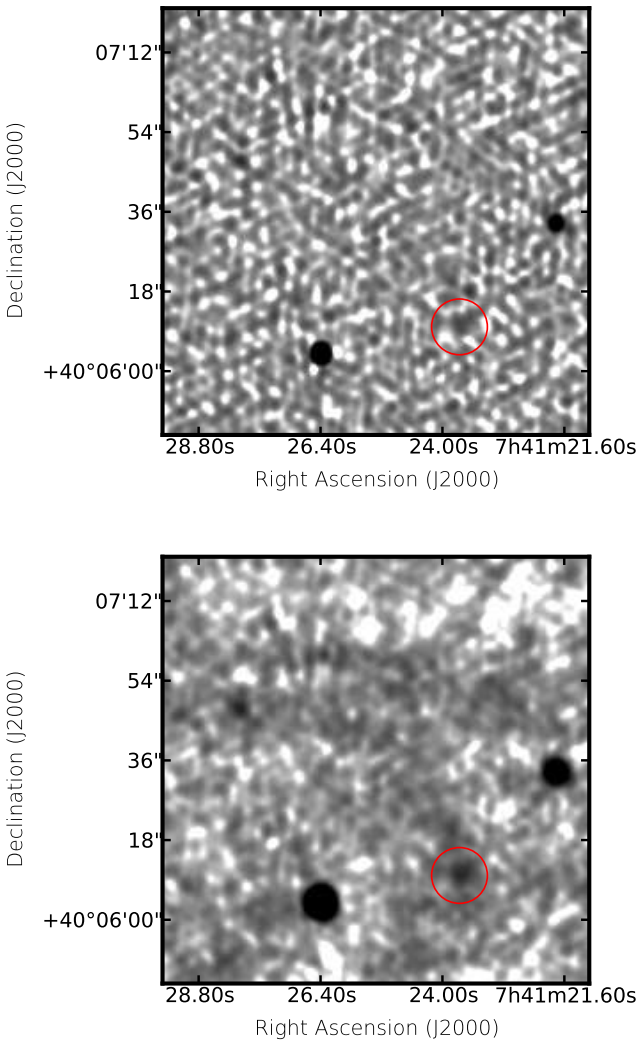

FIGURE 3.14: Images of DDO 46 generated by `robust=0.0` (uniform; upper panel), and `robust=+2.0` (natural; lower panel). For this study of dwarf galaxies, optimising sensitivity was given preference over obtaining the highest possible resolution.

3.6 Imaging

To generate images, CASA's in-built `clean` algorithm was used. The `clean` algorithm works by resampling the (u, v) plane onto a grid. The algorithm then gives each cell a weight, where within each cell, there may reside any number of visibilities (the individual (u, v) points). The manner in which these cells are weighted has direct consequences on the properties of the final image: weighting can be chosen anywhere from between 'super uniform' and 'natural', examples of which are shown in Figure 3.14 illustrating the image generated of DDO 46 when opting for `robust=-2.0` (uniform), `robust=0.0` (Brigg's method), and `robust=+2.0` (natural).

In the case of 'super uniform' weighting, each cell in the grid is given an equal

weight. This effectively means that individual visibilities in a densely packed cell are down-weighted compared to individual visibilities in a sparsely populated cell. This results in the highest possible resolution, but a decrease in S/N as some visibilities are down weighted.

To maximise the S/N, all points on the (u, v) plane must be given equal weighting. But since the (u, v) plane is more densely packed in the inner region (more short baselines than long baselines), the shape of the synthesised beam deviates from a Gaussian form, and the resolution is reduced, although in the case of this study, not detrimentally so.

As will be seen in Chapter 4, dwarf galaxies are faint in the radio continuum. For this very reason, it was decided that the S/N should be maximised as much as possible. Accordingly, 'natural' weighting was chosen over 'uniform' or 'super uniform' weighting when generating the images through `clean`.

A 'quick' image was made to ascertain information on the approximate image size, location of prominent sources, and scale of emission. Using this information, an image of higher quality was made using the `clean` function in CASA (see Appendix B.1 for the typical parameters used when using the `clean` function).

The `clean` process was always done interactively to ensure that all genuine emission had been modelled down to approximately 3–4 times the rms noise level. This was the most computationally expensive portion of the whole process—a typical measurement set of 16 spectral windows would take at least 1–2 hours to clean; it would take far longer still if there were significant amounts of emission to model, or if the image size had to be very large to allow a bright source outside of the primary beam to be modelled.

As an example, Figure 3.15 shows how the `clean` process generates an image from sub-band 6 of *S*-band for NGC 4214. Firstly, the calibrated (u, v) data from the measurement set is Fourier transformed into the image domain; this is the 'dirty' image. Then, through the Högbom algorithm, the image is gradually whittled down by subtracting the 'dirty beam' from the peaks in the 'dirty image'. The Högbom algorithm is not just done on one scale, but is done on multiple scales through the Multi-Scale (MS) algorithm (Rau & Cornwell, 2011). This effectively separates the dirty image into various user-defined scales, and then subtracts appropriately sized 'dirty beams' from each image scale. The location and scale of each subtraction is recorded and placed into a model image. Over many iterations, this model image gets built up as the 'dirty image' gets whittled down.

Once the noise level has been reached, cleaning is terminated to avoid recording

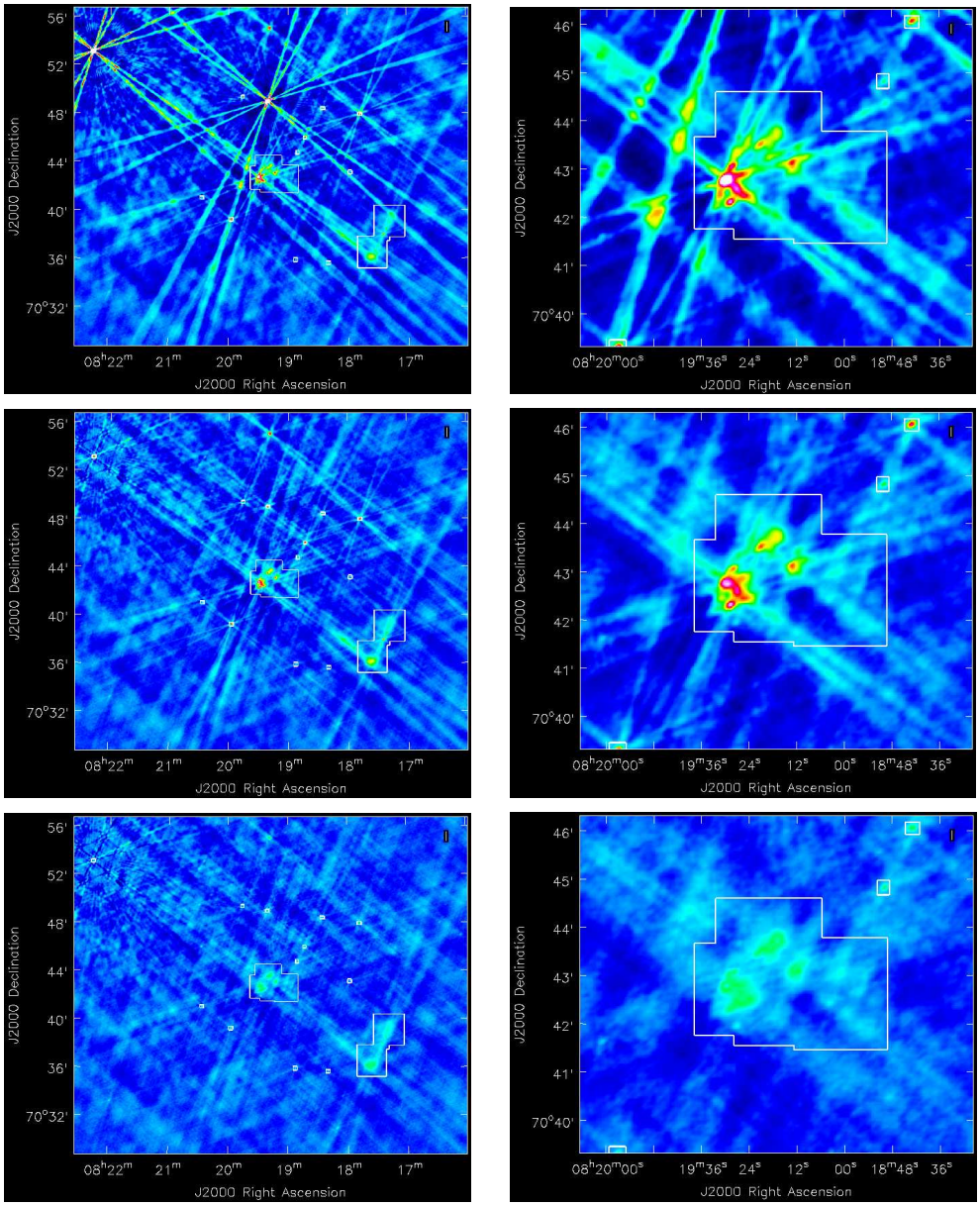

FIGURE 3.15: Example of CASA's `clean` process (DDO 50 at *S*-band). From top to bottom, the residuals are shown after 0, 60, and 300 iterations. The left-most panels show the whole image (which is about twice the FWHM of the primary beam at the central frequency) while the right-most panels show the central portion of image around DDO 50. The white boxes enclose areas of known (or expected) emission.

peaks of noise as genuine emission. The model image is convolved with a synthesised aperture ('clean beam') and then added back on to the residual image to yield the image. This image can then be corrected for the primary beam attenuation to yield an image of flux density (see Figure 3.16).

The choice of which scales to decompose the image into is important: if there is large scale, low surface brightness emission, and only small scales are used in the

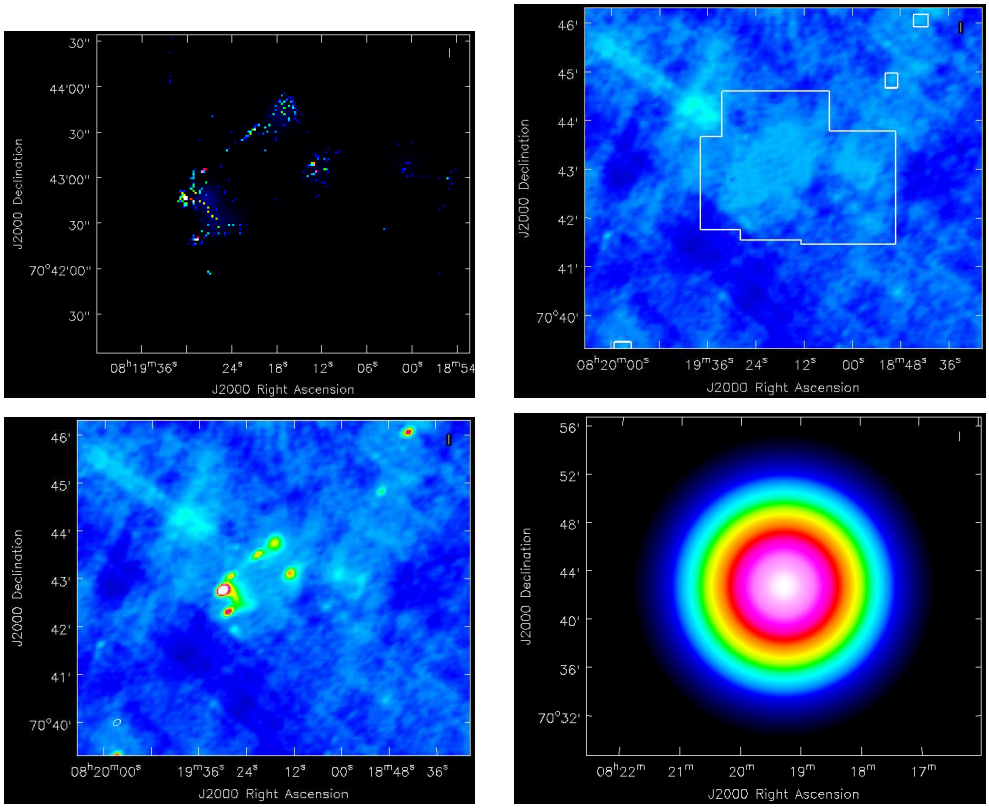

FIGURE 3.16: Example of the output from an invocation of CASA's `clean` algorithm (DDO 50 at *S*-band). The model image (top-left) is convolved with the synthesised aperture ('clean beam') and then added back on to the residual image (top-right) to yield the image (bottom-left). This image can then be corrected for the primary beam attenuation (bottom-right; monochromatic beam plot is shown) to yield an image of flux density.

`clean` function, then those large scale, low surface brightness regions will tend to be poorly represented. Conversely, if there is only unresolved emission, and unnecessarily large scales are used in `clean`, then large scale structures may be found that are not genuine.

3.7 Future Pipeline

The pipeline, now largely customisable, is capable of reducing and imaging these observations efficiently (unlike the first half of the Ph.D where the script was being made piece-by-piece). The rms-based flagging procedure is actually most relevant to *L*-band which is more prone to RFI than the other bands, but yields good results in higher frequency bands, too.

4

Integrated Radio Continuum in Dwarf Galaxies

The data reduced and imaged in Chapter 3 was then used to probe the extent to which the RC could be used as an extinction-free SF indicator. The RC was studied on a global basis and that is to what this Chapter is dedicated. The literature offers a number of single-dish studies of the radio continuum in low surface brightness galaxies such as dwarf galaxies; it makes sense to compare with these.

4.1 Introduction

The Radio Continuum (RC)–Far Infrared (FIR) relation of galaxies holds over 4 orders of magnitude in luminosity, irrespective of galaxy type (Helou et al., 1985; de Jong et al., 1985; Yun et al., 2001). It displays a mere 0.26 dex scatter (Yun et al., 2001) and has been observed to hold to a redshift of 3 (Appleton et al., 2004). The RC (see Condon, 1992, for a review) and the FIR have long been attributed to the input of energy following a star formation (SF) event. In *C*–band (4–8 GHz or 7.50–3.75 cm),

the RC comprises two main contributions: a thermal component, $\mathrm{RC_{Th}}$, and a non-thermal component, $\mathrm{RC_{NTh}}$ (see Section 1.3.1). The $\mathrm{RC_{Th}}$ and $\mathrm{RC_{NTh}}$ both have an unambiguous link to recent star formation, while the FIR originates from the modified blackbody radiation of interstellar dust that is heated by the interstellar radiation field (Li et al., 2010).

The classical scenario leading to the RC–FIR relation is that of a galaxy acting as a calorimeter (Völk, 1989)—one that retains both its dust-heating photons and CRe (see Section 1.4.4). However, this model is not perfect since dust-heating photons are observed coming from galaxies, and $\mathrm{RC_{NTh}}$ emission is observed in the haloes of larger spirals (Heesen et al., 2009). As it turns out, in dwarf galaxies, the escape of CRe from galactic magnetic fields has been found to be in proportion to the escape of dust-heating photons from the disk (e.g., Klein et al., 1991; Bell, 2003; Dale et al., 2009; Lacki et al., 2010).

In the case of dwarf galaxies, observations show that they contain less dust than spirals (Lisenfeld & Ferrara, 1998; Bigiel et al., 2008), yet still follow the RC–FIR relation (Price & Duric, 1992; Yun et al., 2001). To complicate the picture yet further, heating of the diffuse cold dust by photons may not be sufficient to make the RC–FIR relation as tight as is observed; Xu (1990) found that a significant fraction of the heating of diffuse cool dust could not be accounted for by UV radiation in their sample of 40 spiral galaxies. An alternative source to compensate for the insufficient UV–heating could be heating by CRe (e.g., in Ultra–Luminous Infrared Galaxies (ULIRGS); Papadopoulos, 2010); however, it is not known how effective this source of heating is in systems of such low dust densities as dwarf galaxies.

The deficiency of RC emission could be explained by an underproduction of both the $\mathrm{RC_{Th}}$ and $\mathrm{RC_{NTh}}$ components. A truncated stellar IMF in dwarf galaxies may lead to fewer high mass stars being born for a given SFR (Wyder et al., 2007; Lee et al., 2009; Ploeckinger et al., 2015); with fewer high mass stars producing the ionising photons needed to create H II regions, less Hα (and $\mathrm{RC_{Th}}$) is emitted. For the least active dwarf galaxies (SFR $\lesssim 10^{-4}\,M_\odot\,\mathrm{yr}^{-1}$), the H$\alpha$ emission may underestimate the SFR given by FUV by a factor of 10 (Lee et al., 2009). Only the highest mass stars ($M \gtrsim 18\,M_\odot$) produce a significant number of photons to ionise the surrounding H I; having a deficit of these stars significantly reduces the amount of Hα emission, while the FUV emission is not affected as much since a larger fraction of the stellar population contributes to the FUV. However, Koda et al. (2012) find O stars in stellar clusters as small as $100\,\mathrm{M}_\odot$ coming to the conclusion that the stellar IMF is universal, and not truncated.

Likewise, $\mathrm{RC}_{\mathrm{NTh}}$ is reduced in dwarf galaxies. They generally lack differential rotation (Gallagher & Hunter, 1984), and are not able to stretch small scale magnetic field perturbations (this α–ω process happens in larger, grand-design spirals leading to ordered fields of $\sim 5\mu\mathrm{G}$ between the optical arms; Beck, 2009). The energy input from SF can disrupt any ordered fields leading to weak polarised emission. The low mass of dwarf galaxies leads to episodic SF (e.g., Stinson et al., 2007, liken the SF history of isolated dwarf galaxies to 'breathing') and makes them vulnerable to the energy input following major SF episodes. The buoyancy of hot plasma manifests itself as advective winds taking resident CRe out of the galaxy and into the intra-galactic medium (Heesen et al., 2009; Dubois & Teyssier, 2010; Heesen et al., 2011).

The fact that dwarf galaxies follow the RC–FIR relation of spiral galaxies is intriguing, especially when we consider that dwarf galaxies are different from spiral galaxies in terms of their magnetic field (e.g., Chyży et al., 2011; Roychowdhury & Chengalur, 2012), rotation (e.g., Gallagher & Hunter, 1984), dust content (e.g., Lisenfeld & Ferrara, 1998; Bigiel et al., 2008; Ficut-Vicas et al. in prep.), and perhaps stellar IMF (e.g., Weidner & Kroupa, 2005; Lee et al., 2009; Ploeckinger et al., 2015). For all these differences, the RC–SFR and RC–FIR relations are expected to break down in dwarf galaxies.

To more fully understand the role that episodic SF plays in the RC–SFR and RC–FIR relations, examining SF on galactic scales in dwarf galaxies might be simpler than examining their larger, more complex spiral cousins. Dwarf galaxies, generally having had no major mergers to date and being devoid of contamination from Active Galactic Nuclei (AGN), pave a more accessible route to understanding the RC–SFR and RC–FIR relations.

Historically, spatially resolved studies of the RC in dwarf galaxies have been limited by their intrinsically low surface brightness (refer back to Section 1.4 for details). To date, resolved observations of dwarf galaxies have been reserved for the elite few: the near and bright IC 10 (Heesen et al., 2011), IC 1613 (Chyży et al., 2011), NGC 4214 (see Figure 1.11; Kepley et al., 2011), NGC 1569 (Lisenfeld et al., 2004; Kepley et al., 2010), and the Magellanic Clouds (e.g., Filipovic et al., 1995; Filipovic et al., 1998; Leverenz & Filipović, 2013).

The VLA, after recently benefiting from a major upgrade, provided the tantalising prospect of obtaining quality, good signal-to-noise observations of nearby dwarf galaxies. This opportunity was used to recalibrate the RC–SFR and RC–FIR relations in the dwarf galaxy regime.

In particular, this chapter will present VLA *C*-band images of the 40 dwarf galaxies corresponding to the LITTLE THINGS sample (Hunter et al., 2012), mainly focussing on presenting analysis in conjunction with star formation rate (SFR) indicators.

The ultimate aim is to increase our understanding of the RC–SFR relation of low mass, low metallicity systems. With the development of the SKA, calibrating the RC–SFR relation in quiescent/low SFR galaxies will become more important than ever. Our calibration of the RC-SFR relation may provide a better understanding of how this indicator may work at higher redshift, in the domain that will be opened up by the SKA.

This chapter is organised as follows: in Section 4.2 we describe the observations, calibration, and imaging of our sample. We present our results (images and integrated emission) in Section 4.3. We then discuss our results, paying particular attention to the RC–SFR and RC–FIR relations in Sections 4.4.2 and 4.4.3, respectively. We summarise our results in Section 4.5.

4.2 Observations and Data Reduction

In this section, the observations and data reduction are briefly summarised; this is covered in detail in Chapter 3.

4.2.1 Observations

The LITTLE THINGS sample consists of 40 gas-rich dwarf galaxies all within 11 Mpc (refer to Hunter et al., 2012, for sample details) and are summarised in Table 2.1. In general, the sample spans 4 dex in both SFR and gas mass, and a factor of 50 in metallicity.

Observations (Project ID: 12A-234) were taken in 9 observing runs between March and May of 2012 with the VLA. Given the intrinsically faint nature of dwarf galaxies and the desire to obtain a resolved picture of the RC, we opted for the VLA to be arranged in C-configuration, as this was the setup which would give the best compromise between resolution and surface brightness sensitivity[1]. In C-configuration, it was decided to use *C*-band for a number of reasons: a high resolution was possible; only emission on scales of greater than $\sim 4'$ might be absent in (u, v) data (most galaxies had an angular size smaller than this); and there was expected to be a

[1] IC 1613, being 0.7 Mpc away, has a large angular size. Archival observations taken in D-configuration were used (project ID: AH1006) to minimise the effect of missing large scale emission.

roughly equal mix of $\mathrm{RC_{Th}}$ and $\mathrm{RC_{NTh}}$ emission.

For a typical observation of duration $1\,\mathrm{hour}$, the 27 antennas of the VLA at C-band generate a theoretical synthesised beam of width $3\,\mathrm{arcsec}$ at half maximum and an rms noise of 5–$6\,\mu\mathrm{Jy\,beam^{-1}}$ when `robust=0.0` weighting is used[2].

4.2.2 Calibration and Imaging

The VLA data were calibrated using the CASA package, not straying too far from the tutorial of 3C 391 which can be found on the CASA homepage[3].

Flagging and Calibration

Flagging was applied both prior to and after calibration. Two automatic flagging algorithms were utilised, namely `tflagdata(mode='tfcrop')` (Rau & Pramesh 2003) and `tflagdata(mode='rflag')` (based on AIPS; Greisen 2011), to automatically flag bad visibilities. Rogue baselines, scans and channels, as well as wideband radio frequency interference (RFI) were generally caught by the algorithm although the measurement sets were manually checked as well to catch any discrepant visibilities missed by the program.

Calibration was performed in the typical fashion by using one of four NRAO calibrators to calibrate the flux scale, and a nearby ($< 10^\circ$) calibrator to correct the complex gain on timescales of around $10\,\mathrm{minutes}$ (see Table 4.1 for a summary of calibration and imaging properties of LITTLE THINGS).

Radio Continuum Imaging

We generated images of our targets by means of CASA's `clean` function, using the Multi-Scale, Multi-Frequency Synthesis (MS-MFS) algorithm as developed by Rau & Cornwell (2011).

Due to the faint nature of the dwarfs, observations were generally Fourier-transformed using natural weighting (`robust=+2.0`). This ensured that all of the data were used to its full potential (i.e., data from short baselines were not down-weighted).

However, some observations were mapped using Brigg's method (`robust=0.0`) because either 1) the galaxy was sufficiently bright that a good enough S/N was reached using `robust=0.0` weighting, or 2) the natural weighting `clean` left significant image artefacts throughout the image due to the rather sparse sampling of the (u, v) plane. Brigg's `robust=0.0` method ensures that the image is not dominated by

[2] According to the VLA Exposure Calculator (`obs.vla.nrao.edu/ect/`)

[3] `http://casaguides.nrao.edu/index.php?title=\EVLA_Continuum_Tutorial_3C391`

TABLE 4.1: **CALIBRATION AND IMAGING SUMMARY OF PROJECT 12A-234**

(1) Name of dwarf galaxy observed; (2) Date of observation; (3) Name of primary calibrator; (4) Name of secondary calibrator; (5 & 6) J2000 equatorial coordinate of observation (dwarf galaxy) phase centre; (7) Physical scale at distance of galaxy; (8) Resolution of image. Note that some images were made using `robust=0.0` and others using `robust=+2.0` where CASA robust values range between -2.0 (uniform weighting) and $+2.0$ (natural weighting); (9) The rms noise; (10) Comments regarding deviations from the typical imaging process: R signifies that the `clean` algorithm was performed using `robust=0.0` weighting, while N signifies an approach closer to natural weighting; S means that the generated image benefited from self-calibration; P refers to those images that were strongly affected by a bright, nearby background source of ~ 0.1 Jy. Self-calibration failed due to the time varying primary beam, and so to minimise the effect of the offending source, only about a quarter of the bandwidth was used in such a way as to place the offending source as near as possible to the first null of the primary beam.

Galaxy	Date	Pri. Cal.	Sec. Cal.	R.A	Dec.	Scale	Res.	Noise	Notes
						pc arcsec^{-1}	arcsec	μJy beam^{-1}	
(1)	(2)	(3)	(4)	(5)	(6)	(7)	(8)	(9)	(10)
CVn I dwA	2012 Mar 17	3C286	J1310+3220	12 38 40.2	+32 45 40	6.3	3.0×3.0	4.3	N
DDO 43	2012 Mar 22	3C286	J0818+4222	07 28 17.8	+40 46 13	8.5	2.5×2.3	6.9	R,S
DDO 46	2012 Mar 22	3C286	J0818+4222	07 41 26.6	+40 06 39	8.5	3.0×2.8	5.1	N
DDO 47	2012 Mar 20	3C286	J0738+1742	07 41 55.3	+16 48 08	8.0	3.2×3.0	5.0	N
DDO 50	2012 Mar 17	3C147	J0841+7053	08 19 08.7	+70 43 25	5.2	4.4×3.5	5.5	N,S
DDO 52	2012 Mar 22	3C286	J0818+4222	08 28 28.5	+41 51 21	9.3	2.2×2.0	8.3	R,S
DDO 53	2012 Mar 16	3C147	J0841+7053	08 34 08.0	+66 10 37	5.6	4.9×4.0	5.4	N
DDO 63	2012 Mar 25	3C286	J0841+7053	09 40 30.4	+71 11 02	5.9	6.1×3.4	4.6	N
DDO 69	2012 Mar 20	3C286	J0956+2515	09 59 25.0	+30 44 42	1.2	4.1×3.6	4.0	N
DDO 70	2012 Mar 20	3C286	J0925+0019	10 00 00.9	+05 19 50	2.0	4.5×3.4	5.8	N
DDO 75	2012 Mar 20	3C286	J1024−0052	10 10 59.2	−04 41 56	2.0	3.3×2.4	9.7	N,S
DDO 87	2012 Mar 25	3C286	J1048+7143	10 49 34.7	+65 31 46	10.3	3.8×2.2	6.2	R

Table 4.1 continued on next page

Table 4.1 – continued from previous page

Galaxy	Date	Pri. Cal.	Sec. Cal.	R.A	Dec.	Scale	Res.	Noise	Notes
						pc arcsec^{-1}	arcsec	μJy beam^{-1}	
(1)	(2)	(3)	(4)	(5)	(6)	(7)	(8)	(9)	(10)
DDO 101	2012 Mar 17	3C286	J1221+2813	11 55 39.4	+31 31 08	13.9	3.1 × 3.0	15.1	R,S,P
DDO 126	2012 Apr 05	3C286	J1215+3448	12 27 06.5	+37 08 23	7.6	4.6 × 4.0	5.4	N,S
DDO 133	2012 Mar 17	3C286	J1310+3220	12 32 55.4	+31 32 14	9.4	3.8 × 3.7	4.4	N,S
DDO 154	2012 Mar 17	3C286	J1310+3220	12 54 06.2	+27 09 02	6.6	2.2 × 2.2	7.3	R,
DDO 155	2012 Mar 17	3C286	J1309+1154	12 58 39.8	+14 13 10	3.4	3.8 × 3.5	4.7	N
DDO 165	2012 Mar 25	3C286	J1313+6735	13 06 25.3	+67 42 25	7.4	3.7 × 2.8	4.5	R
DDO 167	2012 Apr 20	3C286	J1327+4326	13 13 22.9	+46 19 11	6.5	3.3 × 3.0	5.1	N
DDO 168	2012 Apr 20	3C286	J1327+4326	13 14 27.2	+45 55 46	5.4	3.9 × 3.5	4.4	N
DDO 187	2012 Mar 17	3C286	J1407+2827	14 15 56.7	+23 03 19	3.9	2.7 × 2.5	6.9	R,S
DDO 210	2012 May 19	3C48	J2047−1639	20 46 52.0	−12 50 51	1.4	3.1 × 1.7	4.6	R
DDO 216	2012 Mar 31	3C48	J2253+1608	23 28 35.0	+14 44 30	1.4	3.1 × 2.9	5.1	R
F564-V03	2012 Mar 20	3C286	J0854+2006	09 02 53.9	+20 04 29	9.6	3.3 × 3.0	5.4	N
Haro 29	2012 Apr 20	3C286	1219+484	12 26 16.7	+48 29 38	8.3	3.9 × 3.6	5.1	N
Haro 36	2012 Apr 20	3C286	1219+484	12 46 56.3	+51 36 48	13.9	3.9 × 3.6	5.2	N
IC 1613	2010 Aug 19	3C48	J0108+0135	01 04 49.2	+02 07 48	1.1	9.3 × 7.8	5.1	R
IC 10	2012 Apr 28	3C84	J0102+5824	00 20 17.3	+59 18 14	1.5	2.6 × 2.3	7.8	R
LGS 3	2012 Mar 31	3C48	J0112+2244	01 03 55.2	+21 52 39	0.9	3.0 × 2.8	5.5	R
M81 dwA	2012 Mar 17	3C147	J0841+7053	08 23 57.2	+71 01 51	5.6	2.7 × 1.9	10.8	R,S,P
Mrk 178	2012 Apr 20	3C286	1219+484	11 33 29.0	+49 14 24	6.0	4.4 × 4.0	9.3	N
NGC 1569	2012 Mar 16	3C147	J0449+6332	04 30 49.8	+64 50 51	3.9	2.7 × 2.3	6.8	R
NGC 2366	2012 Mar 16	3C147	J0841+7053	07 28 48.8	+69 12 22	4.9	4.2 × 3.4	5.1	N
NGC 3738	2012 Apr 20	3C286	J1146+5356	11 35 49.0	+54 31 23	7.6	2.5 × 2.5	7.6	N,S
NGC 4163	2012 Apr 05	3C286	J1215+3448	12 12 09.2	+36 10 13	4.3	3.3 × 2.9	4.5	N
NGC 4214	2012 Apr 05	3C286	J1215+3448	12 15 39.2	+36 19 38	4.5	4.5 × 4.0	6.3	N,S
Sag DIG	2012 May 19	3C48	J1911−2006	19 30 00.6	−17 40 56	1.7	3.5 × 1.4	8.2	R
UGC 8508	2012 Apr 20	3C286	J1349+5341	13 30 44.9	+54 54 29	4.0	2.6 × 2.5	6.0	N

Table 4.1 continued on next page

Table 4.1 – continued from previous page

Galaxy	Date	Pri. Cal.	Sec. Cal.	R.A	Dec.	Scale	Res.	Noise	Notes
						pc arcsec^{-1}	arcsec	μJy beam^{-1}	
(1)	(2)	(3)	(4)	(5)	(6)	(7)	(8)	(9)	(10)
VIIZw 403	2012 Mar 25	3C286	J1153+8058	11 27 58.2	+78 59 39	6.8	5.8×3.7	5.8	N
WLM	2012 May 19	3C48	J2348−1631	00 01 59.2	−15 27 41	1.5	5.0×1.5	5.3	R

visibilities representing the more numerous short baselines. This method increases the resolution, results in a synthesised beam that more closely resembles a Gaussian shape, and improves the image quality, at the expense however of a slight ($\sim 20\%$) increase of the rms noise (see Figure 3.14 for examples of various `robust` values). Typical rms noise values in these cleaned images fell between 4 and $8\,\mu\mathrm{Jy\,beam}^{-1}$ in close agreement with theoretical values. Table 4.1 states whether the image of the galaxy was generated using `robust=0.0` weighting (R) or an approach closer to natural weighting (N).

Self-calibration (phase only) was performed on 11 of our 40 observations to improve the dynamic range across the image; these are marked in Table 4.1 (S symbol in column 10). In only one case (NGC 4214) the emission originating from the galaxy itself produced strong enough artefacts to warrant self-calibration; in all other cases, the offending source was an unresolved background object.

Two observations (DDO 101 and M81 DwA; again marked in Table 4.1) harboured the strongest background sources in our survey (flux density of $> 0.1\,\mathrm{Jy}$ located approximately $9'$ and $6'$ from the observation's phase centre, respectively). Self-calibration was not successful in sufficiently improving the dynamic range. This was attributed to the fact that both offending sources resided near the edge of the primary beam (the primary beam has a full-width half-maximum (FWHM) of $10'$ at $4.5\,$GHz and $5.7'$ at 7.9 GHz) and, due to the antennas operating on an alt-az mount, these sources show a time-varying signal due to the source passing through the sidelobes of the primary beam. The result is that the MS–MFS `clean` algorithm cannot successfully remove the sidelobes of the confusing source. Since these sources are not of interest to the current chapter, and the fact that they lie beyond the FWHM of the primary beam anyway, we decided to select solely the spectral windows least affected by the offending background source, i.e., by choosing 2 or 3 spectral windows for which the offending source was located close to the first null of the primary beam. In doing this, the rms noise was approximately doubled to $15\,\mu\mathrm{Jy\,beam}^{-1}$ while the side lobes of the confusing source were considerably suppressed. We note that in an earlier study, Stil & Israel (2002) do not list a flux density for DDO 101 for the same reason.

We maintained as much consistency as possible by using the same calibration and imaging pipeline for all observations. We ended up with good quality images prior to primary beam correction: a flat noise background lacking in significant structure; no artefacts from nearby strong ($> 0.5\,\mathrm{mJy}$) sources[4]; and all genuine emission

[4]Images that still harboured significant artefacts had them masked out by hand

present in the (u,v) data[5] successfully modelled by the MS-MFS algorithm (i.e., residual maps comprise a Gaussian intensity distribution consistent with pure noise, having an average of 0 and variance of σ)[6]. The observation and imaging properties of LITTLE THINGS is summarised in Table 4.1.

4.2.3 Ancillary Data

The LITTLE THINGS project has been highly successful in acquiring a plethora of spatially resolved data on 40 dwarf galaxies. The RC images are complemented by broadband continuum images including, among others, *GALEX* FUV, *Spitzer* MIR and FIR, and Hα line emission (see Section 2.2 and Hunter et al., 2012; Zhang et al., 2012, for details of the ancillary data).

4.3 Results

4.3.1 Radio Continuum Images

All radio continuum flux density maps of the LITTLE THINGS sample presented here are available in Appendix C; as an example, maps of DDO 50 are provided in Figure 4.1 which show RC flux density contours superposed on ancillary LITTLE THINGS images (Hunter et al., 2012). As the dwarf galaxies are faint, extended RC emission does not show well when plotting contours at the native resolution. Therefore, for the lowest surface brightness contour, we smooth the RC image with a Gaussian kernel up to 2.5 times the native resolution, and use a contour level of $2.5\,\sigma_{\rm smooth}$ where $\sigma_{\rm smooth}$ is the rms noise in the smoothed map. The remaining contours are drawn at $(2+2^n)\sigma_{\rm native}$, where $\sigma_{\rm native}$ is the rms noise in the original maps (i.e., before smoothing) and $n \geq 0$. The figures in the Appendix include Hα, FUV, and *Spitzer* 24 and 70μm images where available.

4.3.2 Integrated Emission from the Disk

Masking out Emission Not Related to the Target Object

Contamination by background sources in the RC is an issue since their emission is often brighter than or similar to the emission originating from the dwarf galaxy.

[5]Here, a distinction is made between emission in the sky plane (all emission which is physically present in the galaxy) and emission to which the interferometer is sensitive (the emission on small enough scales that can end up in the (u,v) data).

[6]Complete retrieval of flux to which the interferometer is sensitive was checked by looking for a negative bowl—two observations exhibited a slight bowl and were of NGC 1569 and NGC 4214.

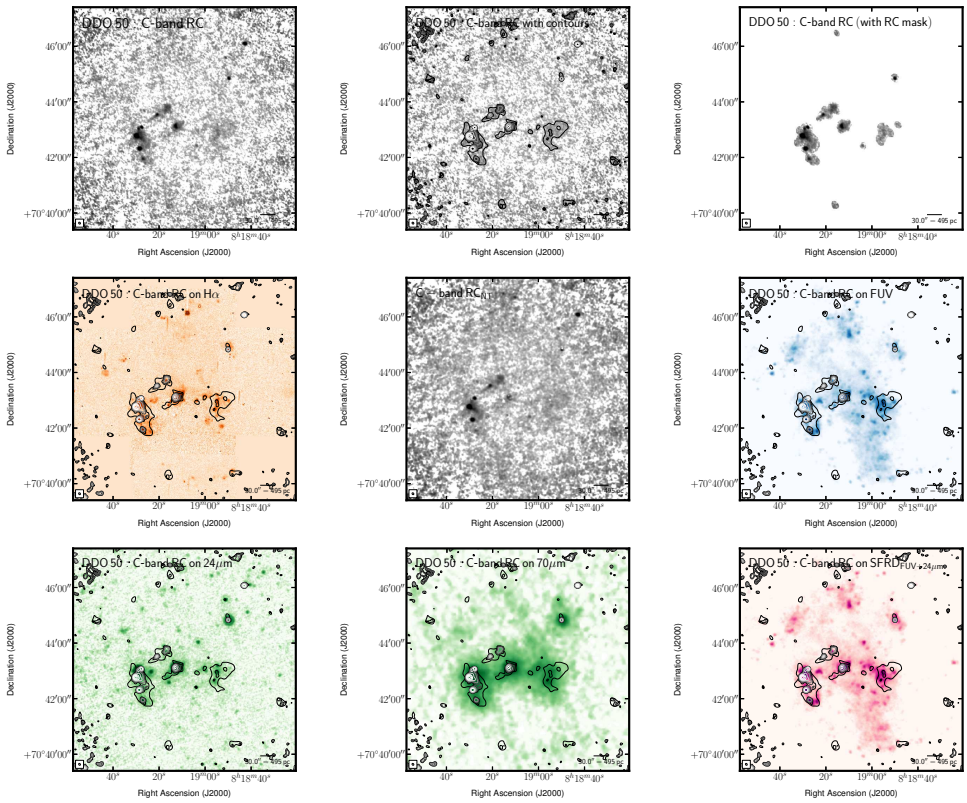

FIGURE 4.1: Multi-wavelength coverage of DDO 50 displaying a $8.0' \times 8.0'$ area. We show total RC flux density at the native resolution (top-left) and again with contours (top-centre). The lowest contour highlights low–surface brightness emission at a level of $34.4\,\mu\mathrm{Jy\,beam^{-1}}$—this is 2.5 times the rms after smoothing the native image by a factor of 2.5. The other contours are placed following $(2 + 2^n)\sigma_{\mathrm{native}}$, where $n \geq 0$ and both the rms ($\sigma_{\mathrm{native}} = 5.50\,\mu\mathrm{Jy\,beam^{-1}}$) and the resolution ($\mathrm{FWHM_{native}} = 4.4 \times 3.5$ arcsec) are taken from the native resolution image. These same contours are also superposed on ancillary LITTLE THINGS images where possible: Hα (middle left); $\mathrm{RC_{NTh}}$ obtained by subtracting the expected $\mathrm{RC_{Th}}$ based on the Hα-$\mathrm{RC_{Th}}$ scaling factor of Deeg et al. (1997) from the total RC (middle-centre); *GALEX* FUV (middle-right); *Spitzer* 24 μm (bottom-left); *Spitzer* 70 μm (bottom centre); FUV+24μm–inferred SFRD from Leroy et al., 2012 (bottom-right). We also show the RC that was isolated by the RC–based masking technique (see Section 4.3.3; top-right). The greyscale intensity scales used are arbitrary to best highlight structure.

Our resolved maps, which typically have resolution elements of $\sim 3''$, made it possible to remove the effects of contamination by singling out emission that was not related to galactic emission. Low resolution observations reported in the literature are predominantly single dish and will have suffered from contamination to varying degrees (refer back to Figure 1.10 for an example of how easily contamination interferes with observations of dwarf galaxies).

We identified significant RC emission by inspecting each field by eye, and classifying features in a manner similar to Chomiuk & Wilcots (2009). Flux was attributed as originating from either:

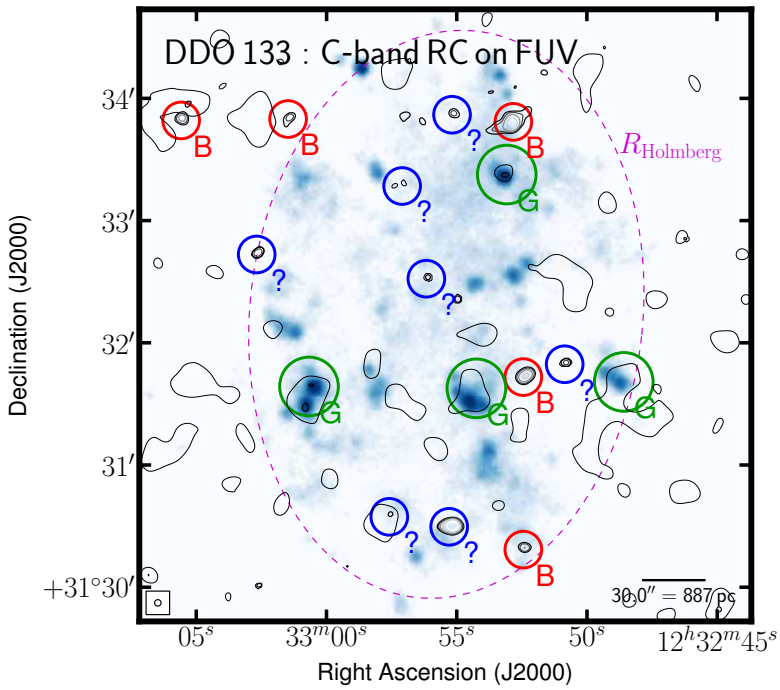

FIGURE 4.2: *GALEX* FUV emission of DDO 133 overlaid by our RC contours. Our procedures allowed us to attribute RC emission as being from: the galaxy itself (G; green); a background galaxy (B; red); an unknown or ambiguous source (?; blue). We also overlay the optical disk size (defined by the Holmberg radius; purple dashed ellipse).

- 1) the dwarf galaxy (exactly coincident with a SF tracer);
- 2) a background galaxy (e.g., see Padovani, 2011, for a discussion on the importance of normal star–forming galaxies on the micro-Jansky RC population);
- 3) ambiguous emission of unknown origin (i.e., unable to discern between a) background origin, or b) non-thermal emission from unresolved SNRs or diffuse non–thermal emission). As an example, we show DDO 133 in Figure 4.2 along with the classification attributed to each source of RC emission.

RC emission originating from the same line-of-sight as H II regions was assumed to originate from the dwarf galaxy. The FWHM of the filter used for the Hα observations was 30 Å centred on 6562.8 Å (Hunter & Elmegreen, 2004), meaning that the observed emission in galaxies receding or approaching at greater than $\sim 700\,\mathrm{km\,s^{-1}}$ would be missed. All galaxies in our sample have heliocentric velocities and rotational speeds well below this value (Hunter et al., 2012), and so all observed Hα emission must be from the dwarf galaxy.

To discern background galaxies and ambiguous emission (points 2 and 3), we used our RC images ($\mathrm{RC_{NTh}}$ where possible), and then applied the following procedures to determine which sources likely did not belong to our dwarf galaxy:

Isolating obvious background galaxies Background galaxies and SNRs look similar when unresolved, however SNRs are not expected to be very far from SF regions. This is because the stellar velocity dispersion in dwarf galaxies is low. The *B*-band absolute magnitudes of the LITTLE THINGS targets are typically between -13 and -16. These magnitudes correspond to predicted stellar velocity dispersions between 5 and $13\,\mathrm{km\,s^{-1}}$ according to the *B*-band absolute magnitude–stellar velocity dispersion relation (Johnson & Swaters in prep.). Mateo (1998) measure $\gtrsim 7\,\mathrm{km\,s^{-1}}$, while Martin et al. (2007) find dispersions as low as $4\,\mathrm{km\,s^{-1}}$. But the stellar velocity dispersion would be even lower for the sub-population of high mass stars (i.e., the core-collapse supernova progenitors) since these would generally sink to the bottom of gravitational potentials. Thus, we take an all-encompassing $5\,\mathrm{km\,s^{-1}}$ as the stellar velocity dispersion for the stars that eventually lead to the injection of CRe (and the associated $\mathrm{RC_{NTh}}$ emission). Given that a SN progenitor may live up to $55\,\mathrm{Myr}$, we defined a maximum projected distance from obvious SFR regions ($5\,\sigma$ FUV or Hα emission; preferably FUV since it was the more sensitive to SF) within which $\mathrm{RC_{NTh}}$ emission (e.g., SNRs) could be expected; this was 250 pc or $10''$ for a face-on galaxy at a distance of 5 Mpc.

Any significant RC source, unresolved or extended, that was outside this region was marked as a background source and was removed by placing a mask over the source. For a Gaussian-like synthesised beam, 99% of the power of an unresolved source is contained within $3 \times \mathrm{FWHM_{native}}$, and so this was the size of the mask placed over the background source. Even for a strong background source (e.g., $1\,\mathrm{mJy}$), this removal technique leaves at most $10\,\mu\mathrm{Jy}$ unmasked in the image, whilst not masking out too much of the dwarf galaxy.

Cross-matching with line-of-sight optical counterparts We manually cross matched unresolved sources of RC emission with the NASA/IPAC Extragalactic Database[7] (NED). If an archived galaxy was found within $2''$ (approximately half the FWHM of the synthesised beam at the native resolution) of the unresolved RC source, we characterised that source as being a background galaxy.

Ambiguous sources After cross matching with NED, there remained sources that we could not attribute as coming from a background galaxy, but at the same time were not close enough to a SF site to be confidently classified as originating from the target galaxy; we refer to these sources of RC emission as 'ambiguous'. To illustrate our definition of 'ambiguous' RC emission, we present four of our observations that

[7] http://ned.ipac.caltech.edu/forms/nearposn.html

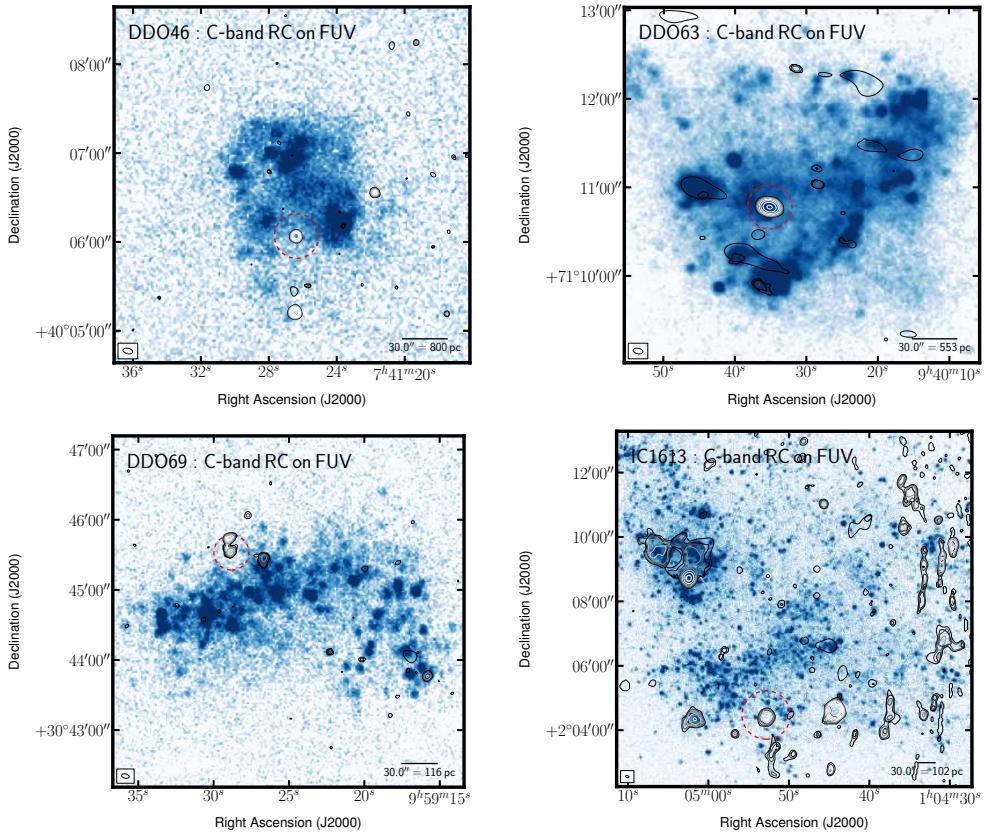

FIGURE 4.3: Examples of our definition of 'ambiguous' emission (red dashed circles). We show DDO 46 and DDO 63 that each contain an unresolved source of 1 mJy (top-left panel) and 1.4 mJy (top-right panel), respectively. We also show DDO 69 and IC 1613 that both contain an extended source (bottom panels). The RC emission could not be attributed as definitely coming from a background galaxy, but at the same time was not close enough to a SF site to be confidently classified as originating from the target galaxy; accordingly, these sources were assigned 'ambiguous'.

contained such a source in Figure 4.3; we show DDO 46 and DDO 63 that each contained a strong unresolved source, and also DDO 69 and IC 1613 that each contained significant extended emission.

Most observations contained an 'ambiguous' source; none of these had a non-thermal luminosity that exceeded a reference threshold—that of a known bright SNR (1×10^{19} W Hz^{-1} or 3.3 mJy at 5 Mpc at 6 GHz)—and so may indeed be classified as SNRs. This reference luminosity was based on SNR N4449-12 in the dwarf galaxy NGC 4449 having $S_{6\mathrm{cm}} = 4.84$ mJy and $\alpha = -0.7$ between 20 cm and 6 cm at a distance of 4.2 Mpc in 2002 (Chomiuk & Wilcots, 2009). For comparison, this is 10 times the luminosity of Cassiopeia A. Since the luminosity terminally declines for the majority of the SNR's lifetime, we treat the observed luminosity of SNR N4449-12 in

2002 as an approximate empirical upper limit to the luminosity of a supernova remnant. We justify our use of SNR N4449-12 as it was the most luminous from a sample of 43 SNRs from 4 irregular galaxies (35 of which are in galaxies that overlap with our sample, namely: NGC 1569, NGC 2366, and NGC 4214).

Radio Continuum Source Counts

In similar conditions to our observations, Huynh et al. (2012) made a 900 arcminute^2 image at 5.5 GHz with a restoring beam of $4.9'' \times 2.0''$ using the Australia Telescope Compact Array (ATCA) reaching an rms noise of $12\,\mu\mathrm{Jy\,beam^{-1}}$. After correcting for incompleteness, they present their source counts (sources sr^1 Jy^{-1}) in 10 flux density bins ranging between 50 and $5000\,\mu$Jy (see their Table 2).

Our images were generated using a restoring beam of approximately $3''$ and attained an rms noise of $6\,\mu\mathrm{Jy\,beam^{-1}}$. Therefore, the sensitivity per beam in our data is comparable to that from Huynh et al. (2012). To compare the RC source counts from this study to that of Huynh et al. (2012), we opt to count sources only from within a $4'$ circular aperture centred on the image pointing. To define our completeness, we ran a Monte Carlo simulation where we found that for sources of $5\,\sigma_{\mathrm{rms}}$, we had a detection rate of 90%, where σ_{rms} is the rms noise in the image.

We correct the Huynh et al. (2012) bins to 6.2 GHz (the effective frequency for most of our images) assuming a spectral index of -0.7 and, for each bin, we cycled through our images counting all sources that had flux densities in the range ΔS. Sources were not counted if, in the given bin, the low end of the bin was less than 5 times the rms noise from the image (this only affected the two lowest bins because of a few high rms images). No attempt was made to count resolved sources as originating from the same source (e.g., radio lobes, multiple SF regions from a dwarf, etc.). The *C*-band source counts are presented in Table 4.2.

Table 4.2 presents (1) the flux density bin (corrected from Huynh et al. (2012), (2) the midpoint of the flux density bin, (3) the number of sources found in the images from this study, (4) the number of sources found per steradian normalised to the midpoint of the flux density bin, and (5) the ratio of the observed RC source count rate from this study (column 4) to that of Huynh et al. (2012). The ratios observed in Column 5 of Table 4.2 shows that our source counts largely agree within the errors. As we point our observations to a regions of known SF activity (i.e., the dwarf galaxies), we would expect a bias towards larger number counts–we indeed see a few bins where we observe a significantly high number of RC sources.

TABLE 4.2: **COMPARISON OF *C*-BAND SOURCE COUNTS AT 6.2 GHZ COMPARED WITH HUYNH ET AL. (2012)**

(1) flux density bins taken from Huynh et al. (2012) converted to 6.2 GHz assuming a spectral index of -0.7; (2) the midpoint of the flux density bin; (3) number of $> 5\,\sigma_{\rm rms}$ RC source counts taken from a $4'$ circular aperture centred on the image pointing; no attempt was made to count resolved sources as a single source (e.g., radio lobes, multiple SF regions from a dwarf, etc.); (4) the RC source count rate—the number of sources found per steradian normalised to the midpoint of the flux density bin; (5) the ratio of the observed RC source count rate from this study (column 4) to that of Huynh et al. (2012).

ΔS (μJy)	$\langle S \rangle$ (μJy)	N	$\mathrm{d}N/\mathrm{d}S$ (sources sr^{-1} Jy^{-1})	Ratio
(1)	(2)	(3)	(4)	(5)
46–73	53	33	1570×10^7	0.94 ± 0.16
73–116	94	17	437×10^7	0.63 ± 0.15
116–183	151	19	296×10^7	1.26 ± 0.29
183–290	246	14	134×10^7	2.14 ± 0.57
290–460	394	9	54×10^7	1.40 ± 0.47
460–728	605	11	43×10^7	1.25 ± 0.38
728–1155	983	3	7×10^7	0.73 ± 0.42
1155–1831	1537	4	6×10^7	1.52 ± 0.76
1831–2901	2019	5	6×10^7	3.10 ± 1.39
2901–4598	3453	2	1×10^7	0.87 ± 0.62

Disk Integrated Quantities

With background sources removed (see § 4.3.2), emission was integrated from within the dwarf galaxy's optical disk (see Table 4.3 for the disk parameters). The semi-major axis of the disk was based on optical isophotes: using either the Holmberg radius (defined as the isophote where the *B*-band surface brightness drops to a magnitude of 26.66; Hunter & Elmegreen, 2006) or 3 times the *V*-band disk scale length (Hunter & Elmegreen, 2006) if the *B*-band radius was not defined. The major-to-minor axis ratio and position angle were taken from Hunter & Elmegreen (2006). All emission outside this radius was masked. This technique isolates all emission that originates from the galaxy's disk, including any low surface brightness emission below our sensitivity limit.

Are Large-scale RC Structures Expected to be Missed?

Owing to the way that interferometers function, large angular structures in the sky may be completely missed as their corresponding visibilities are not recorded by the

TABLE 4.3: **INTEGRATED EMISSION OVER THE DISK OF THE LITTLE THINGS GALAXIES**

(1) Name of dwarf galaxy. The superscript V means that disk properties (columns 2–5) are taken from *V*–band data; otherwise, properties are taken from *B*–band; (2 & 3) Equatorial coordinates (J2000) of centre of optical disk; (4 & 5) Size (major and minor axes) and position angle (P.A) of optical disk (Hunter & Elmegreen, 2006); (6) Proportion of the disk isolated by the RC-based masking technique; (7) *C*-band (~ 6 GHz) radio continuum flux density. The RC quantity in parentheses is the amount that was regarded as 'ambiguous'; (8) Hα flux (units of 10^{-13} ergs s^{-1} cm^{-2}); (9) *GALEX* FUV flux density; (10) *Spitzer* 24μm MIR flux density; (11) *Spitzer* 70μm FIR flux density; (12) *C*-band (~ 6 GHz) radio continuum non-thermal (synchrotron) flux density. All $\mathrm{RC_{NTh}}$ emission is assumed to be synchrotron and is inferred by subtracting the $\mathrm{RC_{Th}}$ component from the total RC (Deeg et al., 1997). The quantity in parentheses is the amount that was regarded as 'ambiguous'; (13) Equipartition magnetic field strength in the plane of the sky (see Equation 3 of Beck & Krause, 2005).

Galaxy	R.A	Dec.	Size	P.A	$f_{\rm disk}$	*C*-band RC	Hα	FUV	24μm MIR	70μm FIR	*C*-band $\mathrm{RC_{NTh}}$	$B_{\rm eq}$
	hh mm ss.s	$^\circ\,'\,''$	($'$)	($^\circ$)	(%)	(mJy)		(mJy)	(10^{-2} Jy)	(10^{-2} Jy)	(mJy)	(μG)
(1)	(2)	(3)	(4)	(5)	(6)	(7)	(8)	(9)	(10)	(11)	(12)	
CVn I dwA	12 38 40.2	+32 45 40	1.7×1.4	80	26	0.09 ± 0.04 (-0.03)	1.95 ± 0.03	1.04 ± 0.02	0.16 ± 0.01	2.48 ± 0.04	-0.06 ± 0.04 (-0.03)	< 6
DDO 43	07 28 17.8	+40 46 13	1.8×1.2	6	1	0.09 ± 0.02 (0.00)	1.28 ± 0.03	1.07 ± 0.01	...	...	0.07 ± 0.02 (0.00)	12
DDO 46$^{\rm V}$	07 41 26.6	+40 06 39	3.8×3.4	84	3	1.49 ± 0.05 (1.30)	1.09 ± 0.02	1.76 ± 0.01	...	...	1.44 ± 0.05 (1.31)	14
DDO 47	07 41 55.3	+16 48 08	4.5×2.3	-79	7	0.51 ± 0.05 (0.10)	3.01 ± 0.03	3.02 ± 0.02	...	...	0.45 ± 0.05 (0.10)	7
DDO 50	08 19 08.7	+70 43 25	7.9×5.7	18	6	8.79 ± 0.13 (0.67)	60.49 ± 0.49	42.16 ± 0.19	17.95 ± 0.03	319.50 ± 0.29	5.69 ± 0.14 (0.61)	11
DDO 52	08 28 28.5	+41 51 21	2.2×1.4	4	1	-0.01 ± 0.03 (0.00)	0.29 ± 0.01	0.61 ± 0.00	-0.04 ± 0.00	1.81 ± 0.05	-0.01 ± 0.03 (0.00)	< 13
DDO 53	08 34 08.0	+66 10 37	2.7×1.4	81	20	0.79 ± 0.05 (0.22)	4.51 ± 0.04	2.71 ± 0.03	2.53 ± 0.00	25.16 ± 0.03	0.48 ± 0.05 (0.20)	7
DDO 63	09 40 30.4	+71 11 02	4.3×4.3	0	11	2.20 ± 0.07 (1.56)	4.46 ± 0.04	5.17 ± 0.04	1.85 ± 0.02	3.72 ± 0.13	1.96 ± 0.07 (1.55)	9
DDO 69	09 59 25.0	+30 44 42	4.8×2.7	-64	6	0.98 ± 0.05 (0.81)	1.71 ± 0.01	4.87 ± 0.03	-0.65 ± 0.01	11.60 ± 0.07	0.96 ± 0.05 (0.80)	11
DDO 70	10 00 00.9	+05 19 50	7.4×4.4	88	4	2.33 ± 0.09 (1.61)	6.38 ± 0.04	11.72 ± 0.06	0.61 ± 0.01	62.10 ± 0.13	2.07 ± 0.09 (1.60)	10
DDO 75	10 10 59.2	$-$04 41 56	6.2×5.2	42	23	1.31 ± 0.32 (0.00)	40.29 ± 0.10	29.88 ± 0.09	0.29 ± 0.02	77.16 ± 0.19	-0.60 ± 0.32 (0.00)	< 6
DDO 87	10 49 34.7	+65 31 46	2.3×1.3	76	4	0.11 ± 0.04 (0.10)	0.68 ± 0.01	0.65 ± 0.01	0.09 ± 0.00	5.97 ± 0.03	0.11 ± 0.04 (0.10)	< 8
DDO 101	11 55 39.4	+31 31 08	2.1×1.5	-69	4	0.00 ± 0.08 (0.00)	0.82 ± 0.01	0.39 ± 0.00	0.24 ± 0.00	-0.66 ± 0.03	0.00 ± 0.08 (0.00)	< 11
DDO 126	12 27 06.5	+37 08 23	3.5×1.7	-41	17	1.00 ± 0.06 (0.00)	3.66 ± 0.08	2.91 ± 0.03	0.33 ± 0.01	15.05 ± 0.10	0.74 ± 0.06 (0.00)	7

Table 4.3 continued on next page

Table 4.3 – continued from previous page

Galaxy	R.A	Dec.	Size	P.A	$f_{\rm disk}$	*C*-band RC	Hα	FUV	24μm MIR	70μm FIR	*C*-band RC$_{\rm NTh}$	$B_{\rm eq}$
	hh mm ss.s	$^\circ$ $'$ $''$	($'$)	($^\circ$)	(%)	(mJy)		(mJy)	(10^{-2} Jy)	(10^{-2} Jy)	(mJy)	(μG)
(1)	(2)	(3)	(4)	(5)	(6)	(7)	(8)	(9)	(10)	(11)	(12)	
DDO 133	12 32 55.4	+31 32 14	4.7×3.2	-6	5	0.77 ± 0.05 (0.47)	4.54 ± 0.03	4.06 ± 0.02	0.66 ± 0.01	31.30 ± 0.12	0.63 ± 0.05 (0.47)	8
DDO 154	12 54 06.2	+27 09 02	3.1×1.6	46	0	-0.01 ± 0.01 (0.00)	2.21 ± 0.02	3.76 ± 0.02	0.26 ± 0.01	3.12 ± 0.04	-0.01 ± 0.01 (0.00)	< 15
DDO 155	12 58 39.8	+14 13 10	1.9×1.3	51	39	0.63 ± 0.06 (0.00)	4.85 ± 0.05	...	0.22 ± 0.00	16.15 ± 0.05	0.26 ± 0.06 (0.00)	7
DDO 165	13 06 25.3	+67 42 25	4.3×2.3	89	2	0.10 ± 0.04 (0.01)	1.53 ± 0.01	...	0.05 ± 0.01	7.19 ± 0.06	0.09 ± 0.04 (0.01)	< 7
DDO 167	13 13 22.9	+46 19 11	1.5×1.0	-24	0	0.00 ± 0.00 (0.00)	0.80 ± 0.01	1.05 ± 0.01	...	...	...	...
DDO 168	13 14 27.2	+45 55 46	4.6×2.9	-25	5	0.73 ± 0.05 (0.12)	5.95 ± 0.03	5.57 ± 0.03	0.70 ± 0.01	39.74 ± 0.10	0.55 ± 0.05 (0.11)	8
DDO 187	14 15 56.7	+23 03 19	2.1×1.7	37	1	0.00 ± 0.02 (0.00)	0.57 ± 0.01	1.15 ± 0.02	-0.02 ± 0.01	-2.29 ± 0.08	0.00 ± 0.02 (0.00)	< 13
DDO 210	20 46 52.0	$-$12 50 50	2.6×1.3	-85	3	0.44 ± 0.03 (0.32)	...	0.80 ± 0.01	-0.17 ± 0.00	5.37 ± 0.04	...	...
DDO 216	23 28 35.0	+14 44 30	8.0×3.6	-58	0	0.04 ± 0.02 (0.05)	0.11 ± 0.01	2.03 ± 0.01	-0.00 ± 0.01	9.52 ± 0.08	0.04 ± 0.02 (0.05)	< 8
F564-V03[V]	09 02 53.9	+20 04 29	1.3×1.0	7	7	0.06 ± 0.03 (0.00)	...	0.10 ± 0.00	...	...	...	...
Haro 29	12 26 16.7	+48 29 38	1.7×1.4	85	20	2.05 ± 0.05 (0.00)	2.20 ± 0.09	2.86 ± 0.08	5.93 ± 0.01	31.61 ± 0.05	2.04 ± 0.05 (0.00)	14
Haro 36[V]	12 46 56.3	+51 36 48	1.5×1.2	90	42	0.95 ± 0.06 (0.00)	2.44 ± 0.03	2.87 ± 0.07	0.94 ± 0.00	23.59 ± 0.06	0.77 ± 0.06 (0.00)	9
IC 1613	01 04 49.2	+02 07 48	18.2×14.7	71	20	7.81 ± 0.28 (0.68)	56.21 ± 0.87	93.95 ± 0.99	7.11 ± 0.16	416.90 ± 1.77	4.97 ± 0.28 (0.65)	6
IC 10[V]	00 20 17.5	+59 18 14	11.6×9.1	-38	21	98.82 ± 0.36 (0.00)	1191.00 ± 5.73	...	...	...	16.15 ± 0.65 (0.00)	13
LGS 3	01 03 55.2	+21 52 39	1.9×1.0	-3	1	0.02 ± 0.02 (0.00)	...	0.08 ± 0.00	...	...	...	...
M81 dwA[V]	08 23 57.2	+71 01 51	1.5×1.1	86	1	0.02 ± 0.03 (0.00)	...	0.38 ± 0.00	...	...	...	...
Mrk 178	11 33 29.0	+49 14 24	2.0×0.9	-51	28	1.08 ± 0.08 (0.00)	0.51 ± 0.01	...	0.45 ± 0.00	0.45 ± 0.00	1.05 ± 0.08 (0.00)	10
NGC 1569[V]	04 30 49.8	+64 50 51	2.3×1.3	-59	99	151.60 ± 0.24 (1.70)	489.60 ± 3.03	750.60 ± 12.15	709.10 ± 2.69	3596.00 ± 2.69	105.10 ± 0.37 (1.50)	24
NGC 2366	07 28 48.8	+69 12 22	9.4×4.0	33	15	14.24 ± 0.17 (0.10)	95.87 ± 1.11	37.01 ± 0.23	65.23 ± 0.01	489.90 ± 0.30	6.16 ± 0.20 (0.08)	8
NGC 3738	11 35 49.0	+54 31 23	4.8×4.8	0	17	2.78 ± 0.14 (0.00)	16.26 ± 0.17	11.22 ± 0.17	11.64 ± 0.01	247.20 ± 0.41	1.63 ± 0.14 (0.00)	11
NGC 4163	12 12 09.2	+36 10 13	2.9×1.9	18	2	0.04 ± 0.02 (0.02)	1.48 ± 0.02	2.68 ± 0.06	0.44 ± 0.01	9.67 ± 0.10	0.03 ± 0.02 (0.02)	< 8
NGC 4214	12 15 39.2	+36 19 38	9.3×8.5	16	17	30.83 ± 0.25 (0.58)	181.60 ± 0.92	82.05 ± 0.42	200.10 ± 0.06	2398.00 ± 1.11	15.86 ± 0.26 (0.45)	10
Sag DIG[V]	19 30 00.6	$-$17 40 56	4.3×2.3	88	2	0.44 ± 0.07 (0.43)	1.28 ± 0.01	4.55 ± 0.02	...	...	0.44 ± 0.07 (0.43)	13
UGC 8508	13 30 44.9	+54 54 29	2.5×1.4	-60	23	1.17 ± 0.05 (0.66)	2.85 ± 0.04	...	0.40 ± 0.01	13.04 ± 0.04	0.97 ± 0.05 (0.63)	9
VIIZw 403	11 27 58.2	+78 59 39	2.2×1.1	-11	30	1.48 ± 0.05 (0.00)	7.51 ± 0.15	3.69 ± 0.08	1.87 ± 2.38	56.98 ± 1.37	0.82 ± 0.05 (0.00)	8
WLM	00 01 59.2	$-$15 27 41	11.6×5.1	-2	1	0.80 ± 0.06 (0.16)	16.81 ± 0.06	29.54 ± 0.10	4.40 ± 0.01	113.20 ± 0.18	0.57 ± 0.06 (0.16)	9

interferometer and would therefore be absent in the (u,v) data. In C-configuration, the largest possible angular scale, $\theta_{\rm LAS}$, observed at C-band is 4 arcminutes[8]; beyond this threshold, it is assumed that structures are totally missed.

There are only 7 galaxies with an angular size greater than $4'$ (see column 4 of Table 4.3). Under the assumption that RC emission coincides with optical emission, it is only these galaxies that are vulnerable to having large angular structures absent in the (u,v) data. Even so, star formation in dwarf galaxies is intermittent on scales of Gyr, whereas CRe age over much shorter timescales of 10s of Myr; therefore, significant quantities of extended emission (e.g., from a CRe halo) are not expected.

4.3.3 Optimising the RC Signal-to-noise ratio

The majority of galaxies only exhibit significant RC in isolated pockets which is attributed to the episodic nature of SF in dwarf galaxies (e.g., Stinson et al., 2007) combined with the surface brightness sensitivity set by our observations. When integrated over the disk, the signal from most galaxies ends up being dominated by the contribution of noise from the individual beams within the integration area: the uncertainty, δN, is given by $\sigma_{\rm rms}\sqrt{N}$, where $\sigma_{\rm rms}$ is the rms noise level and N is the number of individual beams. This motivates the use of masks to isolate genuine emission from background noise (i.e., reduce the integration area which is proportional to N) in order to improve the RC signal–to–noise.

Radio Continuum–based Mask

Our resolved maps allow us to single out emission from background noise, and hence reduce the effects of signal dilution that can plague single dish studies.

Firstly, we note that given a Gaussian distribution of N independent thermal noise peaks, the peak value falling furthest from the mean is given by

$$\sigma_{\rm max}(\sigma_{\rm rms}, N) = \sigma_{\rm rms} \times \sqrt{2}\,{\rm erf}^{-1}\left(1-\frac{1}{N}\right) \tag{4.1}$$

where $\sigma_{\rm rms}$ is the rms of N beams and ${\rm erf}^{-1}$ is the inverse error function. Beams with flux density values higher than this are interpreted as significant. The total number of independent beams ranged between 200 and $20,000$ per image, meaning that $\sigma_{\rm max}$ ranged between $2.8\,\sigma$ and $4.1\,\sigma$ per image, respectively. Since analysis was performed on images of varying sizes and resolutions, defining $\sigma_{\rm max}$ on an image-by-image basis was more robust than using a fixed value for all images, thus reducing subjectivity.

[8] science.nrao.edu/facilities/vla/docs/manuals/oss/performance/resolution

To isolate all unresolved (and strong extended) emission, we defined $\sigma_{\rm max}$ in the native resolution image, and defined all pixels with a value greater than $\sigma_{\rm max}$ to be significant unresolved (or strong extended) emission; that is to say, the mask was defined as

$$S_{i,j} = \begin{cases} S_{i,j}, & \text{if } S_{i,j} > \sigma_{\rm max}(\sigma_{\rm rms}, N), \\ \text{masked}, & \text{if } S_{i,j} \leq \sigma_{\rm max}(\sigma_{\rm rms}, N) \end{cases} \tag{4.2}$$

where $S_{i,j}$ refers to the surface brightness (Jy beam^{-1}) in the RC image at the pixel coordinate (i, j).

To catch faint extended emission, we first removed the pixels that exceeded $\sigma_{\rm max}$ from the map, and then smoothed the image up to 2.5 times the native resolution. These pixels were removed since a significant point source when smoothed may still appear as significant, even though the area of sky into which we smooth is void of emission. This would detrimentally affect our S/N as the unresolved source would be interpreted as originating from a larger area of sky. We define $\sigma_{\rm max}$ in the smoothed image (which is lower than that of the native resolution image since there are fewer independent beams), and define all pixels with a value greater than $\sigma_{\rm max}$ to be significant extended emission.

In assuming that the RC background was void of emission (confusion limit not reached), the statistical fluctuations of the background follow a Gaussian distribution centred on zero. Accordingly, so as not to overestimate integrated flux (i.e., by including only positive peaks above our threshold), we also included peaks more negative than the negative threshold in the masked RC image.

The RC–based mask (which until now, isolated (i, j) pixel positions) was then extended appropriately to mimic the RC resolution. This was done by extending the isolated pixels by $\sim 3 \times {\rm FWHM}_{\rm native}$ to ensure that $\sim 99\%$ of the flux from individual beams was isolated.

Background sources were then masked out. This was achieved by placing a mask of size $3 \times {\rm FWHM}_{\rm native}$ centred on the background source. This ensured that 99% of the flux from the offending source would be cut out of the image.

As an example, we show the disk-integrated RC emission for a typical dwarf galaxy (DDO 168), and show the improvement we get when we use our masking technique (see Figure 4.4). When the RC is integrated over the entire disk, it is consistent with noise ($-0.22 \pm 0.25\,{\rm mJy}$); when the RC–based mask is applied, we record a $12\,\sigma$ signal ($0.62 \pm 0.05\,{\rm mJy}$). We note that the isolated RC tends to fall within significant regions of $70\mu{\rm m}$ emission or coincides with regions of star formation.

The method employed to isolate RC emission is similar to, but more objective

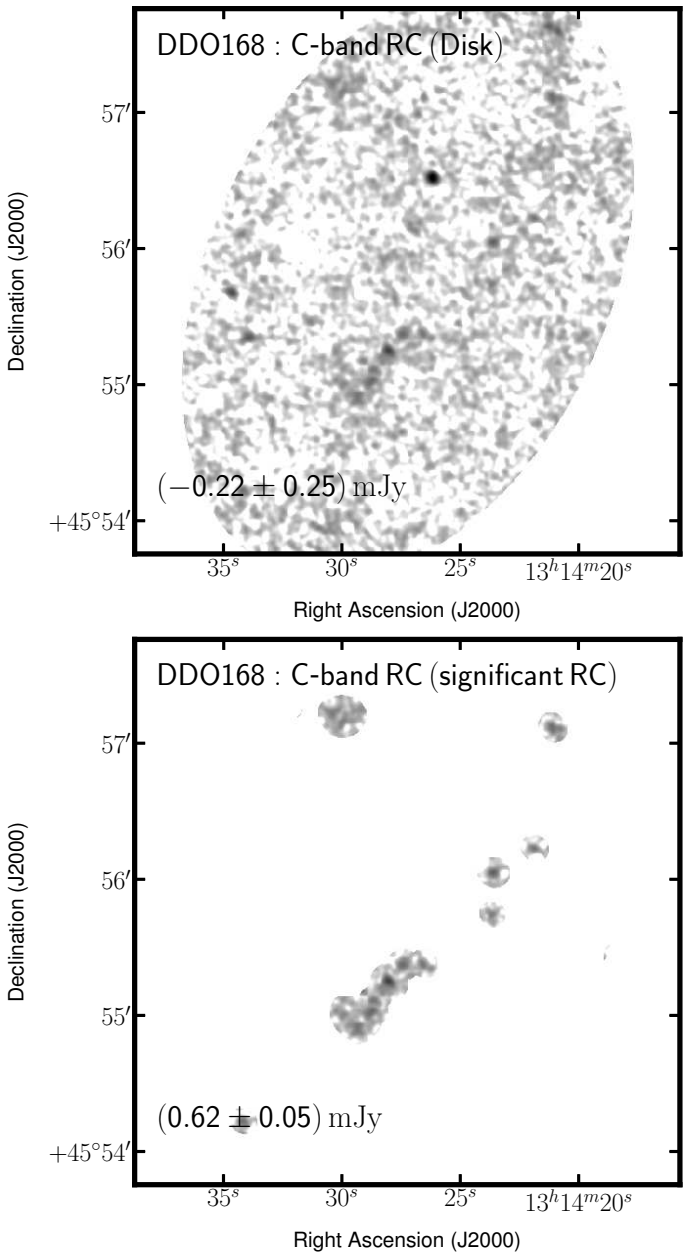

FIGURE 4.4: Image of RC emission from the disk (top panel) and that isolated using the RC–based masking technique (bottom panel) for DDO 168. An improvement in S/N is gained when using this masking technique. Significant amounts of low surface brightness emission are retained while areas dominated by noise are suppressed.

than, that employed by Chyży et al. (2011) who integrate emission in their dwarf galaxies by using "polygonal areas encompassing all visible radio emission." For the same reason that significant quantities of RC emission is not expected to be present in the ISM, this masking process should not lead to significant quantities of RC emission being masked.

Global Quantities

We used the RC-based mask to extract RC fluxes from the galaxy disk[9]. For all other emission (Hα, FUV, 24 μm, 70 μm) and the SFR, quantities were integrated over the entire galaxy disk without masking. Table 4.3 lists these integrated quantities.

A total of 26 out of the 40 LITTLE THINGS galaxies exhibit significant RC emission that originates from the dwarf; 17 are new RC detections.

The RC-FIR relation traditionally samples the parameter space above FIR luminosities of $\sim 10^{22}\,\mathrm{WHz^{-1}}$; we extend this to lower luminosities by 3 dex. Similarly, studies into the RC–SFR relation do not extend to the values typical of dwarf galaxies (e.g., Heesen et al., 2014). We extend on their parameter space by 2 dex down to SFRs of $10^{-4}\,\mathrm{M_\odot\,yr^{-1}}$.

4.4 Discussion

4.4.1 The Radio Continuum

Comparison with Literature Flux Densities

There are very few significant RC detections of dwarf galaxies in the literature. Of the galaxies that overlap with our sample, the literature is dominated by non-detections (e.g., Altschuler et al., 1984; Wynn-Williams & Becklin, 1986; Klein et al., 1992; Hoeppe et al., 1994). On closer inspection, the seemingly high Klein (1986) detection rate of 40% is actually dominated by 1–3 σ detections and was likely influenced by the unwitting inclusion of background galaxies in the large Effelsberg beam. Therefore, we are very limited by the number of dwarf galaxies with flux densities in the literature which we can confidently compare with. The solid RC detections in the literature mostly come from deeper case studies of individual dwarf galaxies, e.g:

NGC 1569: Lisenfeld et al. (2004) find a VLA 8.415 GHz flux density of 125 ± 12 mJy and spectral index of -0.47, which makes its equivalent 6.2 GHz flux density 144 ± 14 mJy which agrees with our measurement of 151.6 ± 0.3 mJy;

[9] Integrating RC quantities over the whole disk, for the majority of observations, yielded insignificant values drowned out by noise. Given that the RC emission expected from the ISM is small compared to the bright SF regions, the small amount of emission that may be included would be outweighed by the increase in noise.

NGC 4214: Kepley et al. (2011) find a VLA 4.86 GHz flux density of 34.0 ± 6.8 mJy (D-array) and spectral index of -0.43, which makes its equivalent 6.2 GHz flux density 30 ± 6 mJy which agrees with our measurement of 30.8 ± 0.3 mJy. We note that there is the possibility that we have missed large scale emission;

DDO 50: Tongue & Westpfahl (1995) find a VLA 6 cm flux density of 11.7 ± 0.1 mJy (D-array) which is $\sim 20\%$ higher than the 8.9 ± 0.1 mJy at 6.2 GHz that we measured. We note that there is the possibility that we have missed large scale emission;

NGC 3738: Stil & Israel (2002) find a 1.4 GHz flux density of 13 ± 2 mJy and we find a 6.2 GHz flux density of 2.9 ± 0.2 mJy. This implies a spectral index of -1.02 ± 0.04 which is quite steep. Our image was strongly affected by artefacts from a nearby bright source, as would have been their image;

Haro 29: Condon et al. (1998) find a 1.4 GHz flux density of 4.5 ± 0.5 mJy and we find a 6.2 GHz flux density of 2.1 ± 0.1 mJy. This implies a spectral index of -0.51 ± 0.08 which is reasonable;

NGC 2366: In the absence of a literature flux density at *C*–band, we resort to a comparison with an *L*–band value. Condon et al. (2002) find a 1.4 GHz flux density of 19.9 mJy and we a 6.2 GHz flux density of 14.2 ± 0.2 mJy. This implies a spectral index of -0.23 ± 0.10 which is reasonable. In light of this, it is unlikely that we have missed large scale emission which would flatten the spectral index and would imply emission even more dominated by $\mathrm{RC_{Th}}$ emission than derived here;

Others: Klein (1986) find a number of $\sim 4\,\sigma$ detections at 6.3 GHz: 3.5 ± 1.0 mJy for DDO 126; 4 ± 1 mJy for DDO 133; 9 ± 2 mJy for DDO 52. However, we observe less than a mJy for each of these. In all cases, we find nearby background galaxies that will have entered their $2'30''$ single dish beam and contributed to their flux density to some degree.

Composition of the Radio Continuum: Thermal and Non–thermal

We assume that, at *C*-band, the total RC emission is comprised of two contributions: the $\mathrm{RC_{Th}}$ and the $\mathrm{RC_{NTh}}$. Since Hα and the $\mathrm{RC_{Th}}$ both have their origins in warm ($\sim 10^4$ K) plasma, a tight spatial correlation between the two emissions is expected (e.g., Deeg et al., 1997; Murphy et al., 2011). The Hα–$\mathrm{RC_{Th}}$ relation taken from Deeg

et al. (1997) assumes the form

$$\frac{\mathrm{RC_{Th}}}{\mathrm{W\,m^{-2}}} = 1.14 \times 10^{-25} \left(\frac{\nu}{\mathrm{GHz}}\right)^{-0.1} \times \left(\frac{T_e}{10^4\,\mathrm{K}}\right)^{0.34} \frac{\mathrm{F_{H\alpha}}}{\mathrm{ergs\,s^{-1}\,cm^{-2}}}. \quad (4.3)$$

On a spatially resolved basis, the $\mathrm{RC_{Th}}$ flux density (see Equation 6.2) can be subtracted from the total RC, yielding the $\mathrm{RC_{NTh}}$ flux density distribution (an electron temperature of 10^4 K was assumed).

After the removal of known background galaxies and 'ambiguous' sources, the RC–based mask was used to isolate both RC emission and $\mathrm{RC_{Th}}$ (scaled Hα) emission. We find that the average thermal fraction for our sample is $39 \pm 7\%$ (upper limit), whilst the non–thermal fraction is $61 \pm 7\%$ (lower limit). For comparison, thermal fractions in dwarf galaxies have been quoted as 30% at 1.4 GHz for a sample of stacked faint dwarfs (Roychowdhury & Chengalur, 2012), 50% in IC 10 at *C*–band (Heesen et al., 2011), 23% in NGC 1569 at 1.49 GHz (Lisenfeld et al., 2004), and 23% in NGC 4449 at 1.49 GHz (Niklas et al., 1997).

The $\mathrm{RC_{NTh}}$ fraction is quoted as a lower limit for two reasons: 1) our masking technique masks out regions that are consistent with noise (it is in these regions where low surface brightness $\mathrm{RC_{NTh}}$ may exist), and 2) our interferometric observations may miss extended ($\gtrsim 4'$) emission due to lack of short spacing data ($\mathrm{RC_{NTh}}$ naturally diffuses through the ISM and so it is the $\mathrm{RC_{NTh}}$ component that is more prone to being missed). Individual H II regions in our dwarf galaxies do not exceed scales of $4'$ and so the $\mathrm{RC_{Th}}$ emission from these regions is unlikely to be missed by our observations.

In dwarf galaxies, the RC emission tied up in SNRs forms a low contribution. Chomiuk & Wilcots (2009) find that, at 20 cm, discrete SNRs make up 6% of the non–thermal RC in NGC 1569 and NGC 4449, and 7% of the total RC in NGC 2366.

We do not remove significant quantities of low surface brightness RC emission through our masking procedure. For the dwarf galaxies that exhibit significant pockets of RC emission, this amount is consistent with the RC emission when integrated over the entire disk (see Figure 4.5). We note however, that uncertainties on disk-integrated quantities can become very large. In Figure 4.5, the galaxies (data points) above/to the left of the dashed line (1:1 ratio) are possible evidence of a negative bowl, while points under/to the right of the line indicate that the RC–based masking technique failed to retrieve low-surface brightness emission.

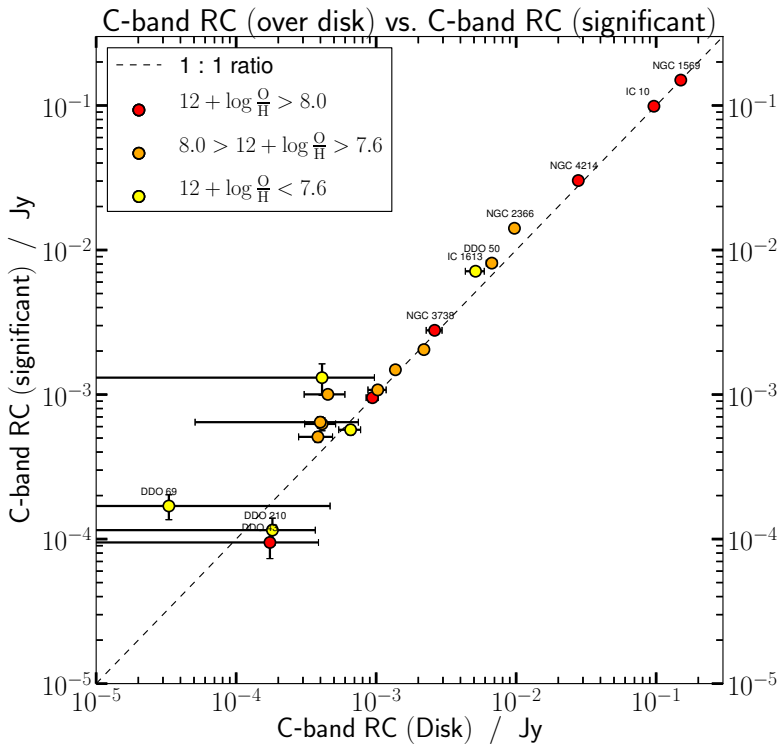

FIGURE 4.5: Comparison of RC-masked flux densities against disk-integrated values. For each galaxy, the two values are consistent with one another; this means that significant quantities of low surface brightness emission are not lost when using the RC-based mask. Note, however, that uncertainties on disk-integrated quantities can become very large. Points have been coloured by metallicity, taken from Table 2.1.

4.4.2 The RC–SFR Relation

Using the ancillary data mentioned in Section 4.2.3, SFRs were measured and compared with our RC measurements. We employ FUV-inferred SFRs following the Leroy et al. (2012) prescription which corrects the FUV-inferred SFR for any internal extinction (which is relevant mostly for our more actively star forming dwarfs). The FUV has been proven to be a reliable SF indicator at low SFR in comparison to Hα–inferred SFRs (e.g., Lee et al., 2009; Ficut-Vicas et al. in prep.), and the timescale of $\mathrm{RC_{NTh}}$ emission is more similar to FUV–inferred SF timescales than to, e.g., Hα–inferred SF timescales. Galactic foreground extinction is taken into account separately (see Hunter et al., 2012, for details). To correct for internal extinction, Bigiel et al. (2008) and Leroy et al. (2012) use *Spitzer* 24μm dust emission to empirically correct *GALEX* FUV fluxes for the fraction of dust-obscured SF on the assumption that a proportion of energy absorbed by internal dust is reradiated at 24μm (this is based on the original idea by Calzetti et al., 2007, who use Hα instead of FUV). We use

$$\frac{\Sigma_{\mathrm{SFR}}}{\mathrm{M_\odot\,yr^{-1}\,kpc^{-2}}} = 0.081\frac{I_{\mathrm{FUV}}}{\mathrm{MJy\,sr^{-1}}} + 0.0032\frac{I_{24\mu\mathrm{m}}}{\mathrm{MJy\,sr^{-1}}}. \tag{4.4}$$

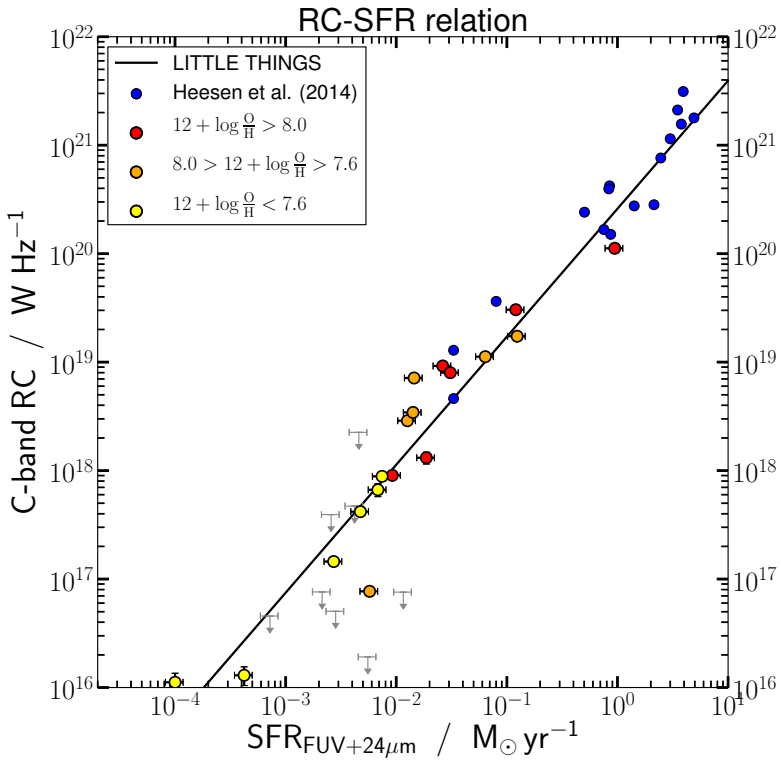

FIGURE 4.6: We compare our RC and SFR coverage with that of Heesen et al. (2014) who studied mainly spiral galaxies. Obvious background and 'ambiguous' sources have been removed from all images. Their WSRT 22 cm data have been corrected to 6 GHz assuming a spectral index of -0.7. The LITTLE THINGS galaxies have been coloured according to their metallicity, while insignificant flux densities are marked as $3\,\sigma$ upper limits (grey). The solid black line is the best-fit power law gradient to the LITTLE THINGS sample.

Figure 4.6 shows how our data extend on the RC and SFR coverage of a study of mainly spiral galaxies (Heesen et al., 2014), whereas Figure 4.7 concentrates on the RC–SFR relation of just our sample. We used FUV–inferred SFRs and, where *Spitzer* 24 μm was available, corrected for internal dust extinction using the prescription in Equation 4.4. For those galaxies where *Spitzer* 24 μm was not available, we used the FUV–inferred SFR without any correction. The RC–based masking technique was used to isolate the RC signal (see Section 4.3.3) thus providing the best measurement of the integrated RC emission; the FUV–inferred SFR was integrated over the entire galaxy disk. The top panel of Figure 4.7 shows the relation when we include the 'ambiguous' RC sources, whereas the bottom panel shows the relation with 'ambiguous' sources removed.

We compare our RC–SFR relation with that derived by Condon et al. (2002) (see their Equation 27). They relate the integrated total RC of an unresolved galaxy to the

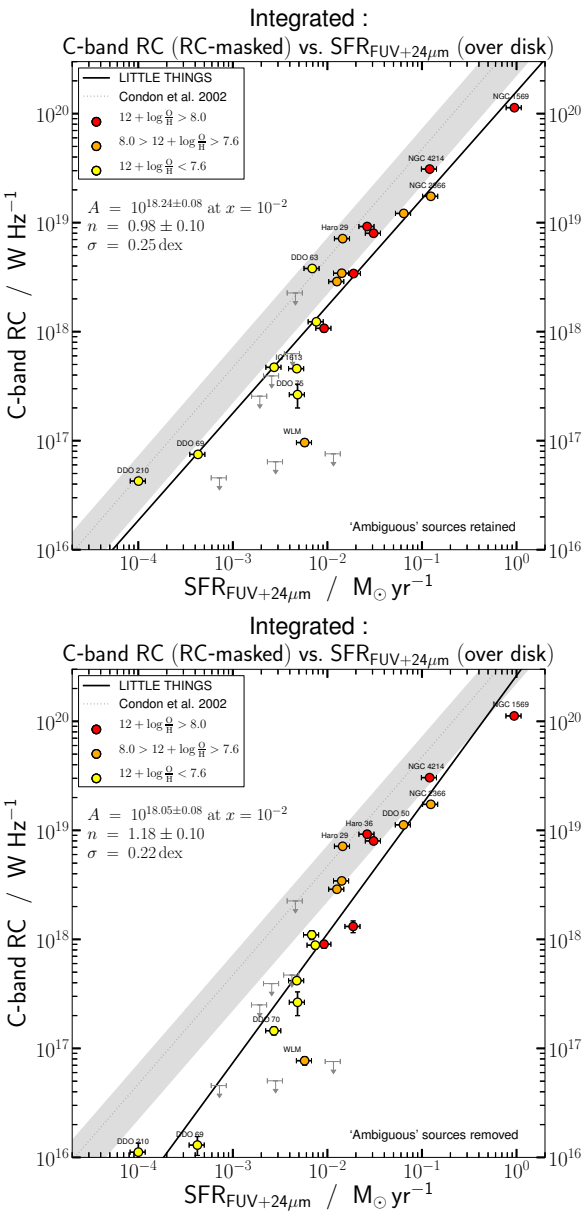

FIGURE 4.7: Galaxy-wide total *C*-band luminosity as a function of the FUV-inferred SFR (Leroy et al., 2012); SFRs have been corrected for internal extinction from dust if 24μm data were available using the Leroy et al. (2012) prescription. Note that the abscissa and ordinal values were yielded by integrating emission over distinct regions. Definite background sources have been removed, whilst the 'ambiguous' sources have been retained (top panel) and removed (bottom panel). The solid line is the best-fit power law to our sample. We show the Condon et al. (2002) RC–SFR relation as described in Equation 4.5. The errors introduced by our conversion are reflected by the grey shaded band, and the $3\,\sigma$ upper limits of RC emission are shown by the grey arrows.

SFR and find

$$\frac{L_{6\,\mathrm{GHz}}}{\mathrm{W\,Hz^{-1}}} = (4.8 \pm 2.5) \times 10^{20} \frac{\mathrm{SFR}}{\mathrm{M_\odot\,yr^{-1}}} \tag{4.5}$$

or, alternatively, in surface brightness units,

$$\frac{S_{6\,\mathrm{GHz}}}{\mathrm{MJy\,sr^{-1}}} = (4.0 \pm 2.1)\frac{\mathrm{SFRD}}{\mathrm{M_\odot\,yr^{-1}\,kpc^{-2}}}. \quad (4.6)$$

Their relation is derived for high-mass star formation above $5M_\odot$, but is extrapolated down to $0.1M_\odot$ using a Salpeter stellar IMF. The SFR expressed by the Leroy et al. (2012) prescription is based on a Miller-Scalo stellar IMF however and their derived SFRs are lower than the Salpeter IMF by a factor of 1.59 in the same mass range, so we correct for this. We converted the Condon et al. (2002) 1.4 GHz luminosity to *C*–band luminosity, $L_{6\mathrm{GHz}}$, using a spectral index of -0.7. The error (in Equation 4.5 and the grey band in Figure 4.7) takes into account the uncertainties of our conversion i.e., an uncertainty in the spectral index of 0.1 and a canonical factor of 2 uncertainty in the SFR (Leroy et al., 2012).

We performed a bivariate linear regression to quantify the relation between the RC luminosity and SFR. We first linearised the data by taking the log of both the abscissa (RC) and ordinal values assuming the data followed a power law function of the form $y = Ax^n$ or $\log(y) = n\log(x) + c$, where $c = \log(A)$. We used the `odr`[10] module from `scipy`, which takes four arrays of the data points (the data points: $\log x$ and $\log y$; the $1\,\sigma$ errors in log–space: $\frac{\delta x}{x}$ and $\frac{\delta y}{y}$) and the model function, and works to minimise the squares of the orthogonal distance between data points and the model, ultimately returning best-fit values and their standard deviations. Data points with low significance (less than $3\,\sigma$) were excluded from the fit as these were the images dominated by noise (including low level image artefacts, RFI, etc.) and thus susceptible to recording image artefacts as genuine emission.

We find that the RC–SFR relation in Figure 4.7 (top panel) runs parallel to but falls below the Condon et al. (2002) relation. LITTLE THINGS dwarfs are radio 'quiet/dim'. For a given SFR, the total RC observed in these dwarf galaxies is on average a factor of 2 below the Condon et al. (2002) relation. The brightest galaxies are largely consistent with the Condon et al. (2002) RC–SFR relation; the majority of the deviation comes from the dwarf galaxies that have a SFR $\lesssim 1 \times 10^{-2}\,\mathrm{M_\odot\,yr^{-1}}$. We find a linear power-law gradient of $\sim 1.0 \pm 0.1$ with a scatter of 0.25 dex.

A number of dwarfs in Figure 4.7 (top panel) are significantly radio 'bright/loud' with respect to the rest of our sample. These data points (e.g., DDO 63 and DDO 210) are faint dwarf galaxies dominated by 'ambiguous' RC emission. If these 'ambiguous' sources are background galaxies that themselves lie on the Condon et al. (2002) RC–SFR relation, then we would infer that the dwarf galaxy too lies on the Condon relation. This would have been an important issue in earlier studies (e.g., de Jong et

[10] www.scipy.org/doc/api_docs/SciPy.odr.odrpack.html

al., 1985): significant contamination from background galaxies (the kind of galaxies on which the RC–SFR is based) may have made the dwarf galaxies appear to stay true to the RC–SFR relation.

Given that our dwarf galaxies may be affected by contamination from the emission of unrelated background sources, we perform the same analysis but, this time, assuming that the 'ambiguous' sources of RC emission are of background origin and removing them before taking integrated quantities. In doing this, while we may remove, at worst, 10% of genuine RC emission (RC emission from SNRs contribute $< 10\%$ of the total RC in dwarf galaxies; Chomiuk & Wilcots, 2009), contamination from background sources will be entirely removed. We present the RC–SFR relation (free from 'ambiguous' emission) in Figure 4.7 (bottom panel). This ensures that all of the isolated emission is from the dwarf itself, however, it is possible that we remove a fraction of dwarf emission (e.g., a SNR that we erroneously assume is a background galaxy).

We find that removing the 'ambiguous' sources significantly alters our results. Our RC–SFR then diverges from the Condon et al. (2002) relation. The divergence starts to become significant for systems that have a SFR of about 0.1–$0.01\,\mathrm{M_\odot\,yr^{-1}}$ and is characterised by a power-law index of 1.2 ± 0.1 with a scatter of 0.2 dex. Our brightest galaxies remain largely consistent with the Condon et al. (2002) RC–SFR relation, but as lower SFRs are probed, the RC luminosity drops at a faster rate—not only are the dwarf galaxies radio 'quiet/dim' with respect to the Condon et al. (2002) RC–SFR relation, but this effect is stronger for lower SFRs—the RC luminosity observed in dwarfs with a SFR of $\sim 1 \times 10^{-4}\mathrm{M_\odot\,yr^{-1}}$ is about a factor of 10 lower than that predicted by the Condon et al. (2002) relation. Interestingly, this is the same factor of 10 that Hα–inferred SFRs undercut FUV-inferred SFRs in dwarf galaxies (Lee et al., 2009).

When breaking the RC into its $\mathrm{RC_{Th}}$ and $\mathrm{RC_{NTh}}$ components, we find the $\mathrm{RC_{Th}}$–SFR relation also has a slope of 1.2 which does not agree with Koda et al. (2012). It is important to note that this is essentially a Hα-FUV plot: the $\mathrm{RC_{Th}}$ values are based on the Hα emission and are thus not independently determined; in turn, the SFR relies heavily on the FUV. In other words, this might hint to a variable stellar IMF as proposed by Lee et al. (2009) for systems with a SFR in the range of 10^{-4} to $10^{-1}\,\mathrm{M_\odot\,yr^{-1}}$. However, around half of the dwarfs are consistent with the Condon et al. (2002) linear trend at the $1\,\sigma$ level, while all the dwarfs are consistent with Condon et al. (2002) at the $2\,\sigma$ level which is consistent with a random distribution of ~ 40

data points[11] (suggesting that the observed scatter is purely observational).

Therefore, given that the LITTLE THINGS dwarf galaxies are 1) consistent with a linear $\mathrm{RC_{Th}}$–SFR relation (see top panel of Figure 4.8), and 2) dominated by $\mathrm{RC_{NTh}}$ emission ($\mathrm{RC_{Th}}$ to $\mathrm{RC_{NTh}}$ ratio of 39:61), the super-linear RC–SFR relation observed in Figure 4.7 (bottom panel) must be due to a super-linear $\mathrm{RC_{NTh}}$–SFR relation.

This is confirmed in Figure 4.8 (bottom panel) which shows the $\mathrm{RC_{NTh}}$–SFR relation. We find a slope of 1.22 ± 0.13 which agrees with the 1.33 predicted for turbulent magnetic field amplification. The $\mathrm{RC_{NTh}}$ component is discussed in more detail in Section 4.4.6.

The RC surface brightness–SFRD relation is presented in Figure 4.9. Unlike the luminosity plots in Figure 4.7, this is independent of distance and so errors introduced by distance uncertainties are avoided, and the possibility of forcing a linear relation due to flux-to-luminosity scaling is avoided. Additionally, flux-flux relations are easier to compare with other studies for the simple fact that they require one fewer variable (i.e., the distance). Figure 4.9 could thus be used as a baseline for future studies of normal star forming galaxies—especially those studies that do not have reliable distance measurements (e.g., only photometric redshift of optical counterparts).

We find a tight, linear RC–SFRD relation in Figure 4.9. However, given the SFRD observed across the disk, the RC flux density is about half of what is expected from the Condon et al. (2002) relation.

4.4.3 The RC–FIR Relation

The FIR is known to be well correlated with the RC (e.g., de Jong et al., 1985; Price & Duric, 1992; Yun et al., 2001). In particular, Yun et al. (2001) related the integrated $1.4\,\mathrm{GHz}$ RC of an unresolved galaxy to the *IRAS* $60\mu\mathrm{m}$ luminosity and found:

$$\frac{\mathrm{L_{6GHz}}}{\mathrm{W\,Hz^{-1}}} = (2.24 \pm 0.67) \times 10^{-3} \left(\frac{\mathrm{L_{70\mu m}}}{\mathrm{W\,Hz^{-1}}} \right)^{0.99} \tag{4.7}$$

where the *IRAS* $60\mu\mathrm{m}$ luminosity was converted to a 'luminosity density' (i.e., from W to $\mathrm{W\,Hz^{-1}}$) by noting that the response from the *IRAS* $60\mu\mathrm{m}$ filter is equivalent to a perfectly tranmitting filter with a bandwidth of 2.6×10^{12} Hz. The *IRAS* $60\mu\mathrm{m}$ 'luminosity density' was converted to the equivalent *Spitzer* $70\mu\mathrm{m}$ luminosity by scaling up by a factor of 1.27 ($\beta = 1.82$ and $T_{\mathrm{dust}} = 35\,\mathrm{K}$; this assumes the Yun et al., 2001 galaxies are in a quiescent mode of SF, and that there is no significant emission from

[11] $\sim 25/40$ expected within 1σ and $39.5/40$ expected within 2σ

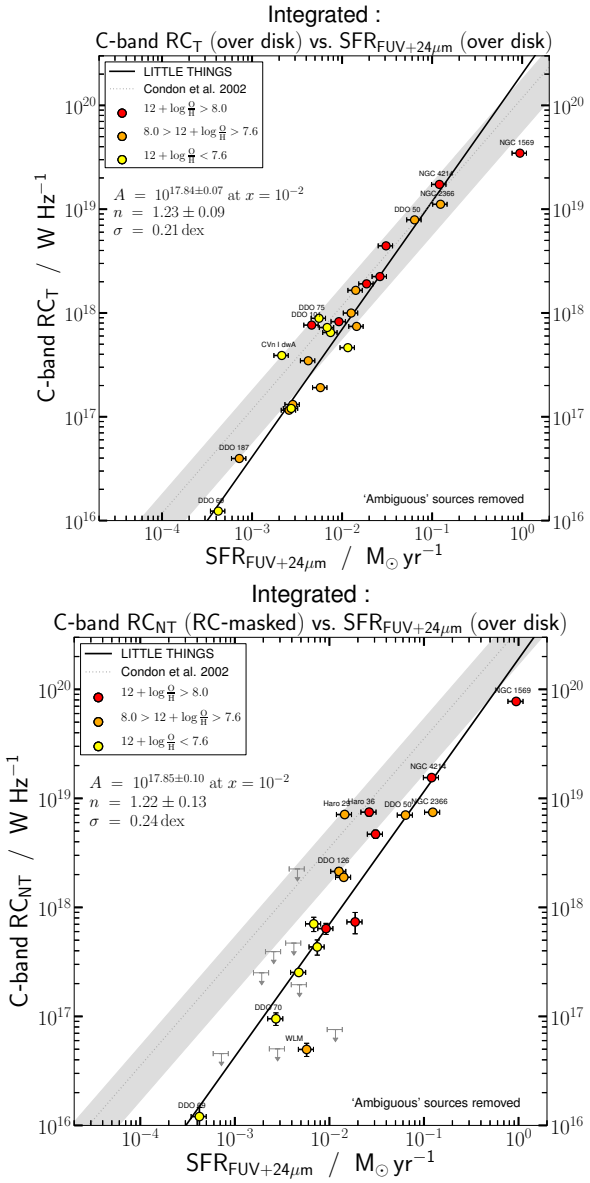

FIGURE 4.8: Galaxy-wide total *C*-band $\mathrm{RC_{Th}}$ (top) and $\mathrm{RC_{NTh}}$ (bottom) luminosity as a function of the FUV-inferred SFR (Leroy et al., 2012); SFRs have been corrected for internal extinction from dust if 24μm data were available using the Leroy et al. (2012) prescription. Note that the abscissa and ordinal values were yielded by integrating emission over distinct regions. Both definite background sources and 'ambiguous' sources have been removed. The solid line is the best-fit power law to our sample. We show the Condon et al. (2002) RC–SFR relation as described in Equation 4.5 corrected by 0.25 (to represent just the $\mathrm{RC_{Th}}$ component) and by 0.75 (to represent just the $\mathrm{RC_{NTh}}$ component). The errors introduced by our conversion are reflected by the grey shaded band, and the $3\,\sigma$ upper limits of RC emission are shown by the grey arrows.

warm dust). The Yun et al. (2001) VLA 1.4 GHz RC data were also converted, by a factor of 2.83, to derive predicted equivalent VLA 6 GHz flux densities assuming a constant spectral index of -0.7 between *L*- and *C*-band of the galaxies in their sample. The uncertainty given takes into account an uncertainty in the spectral index

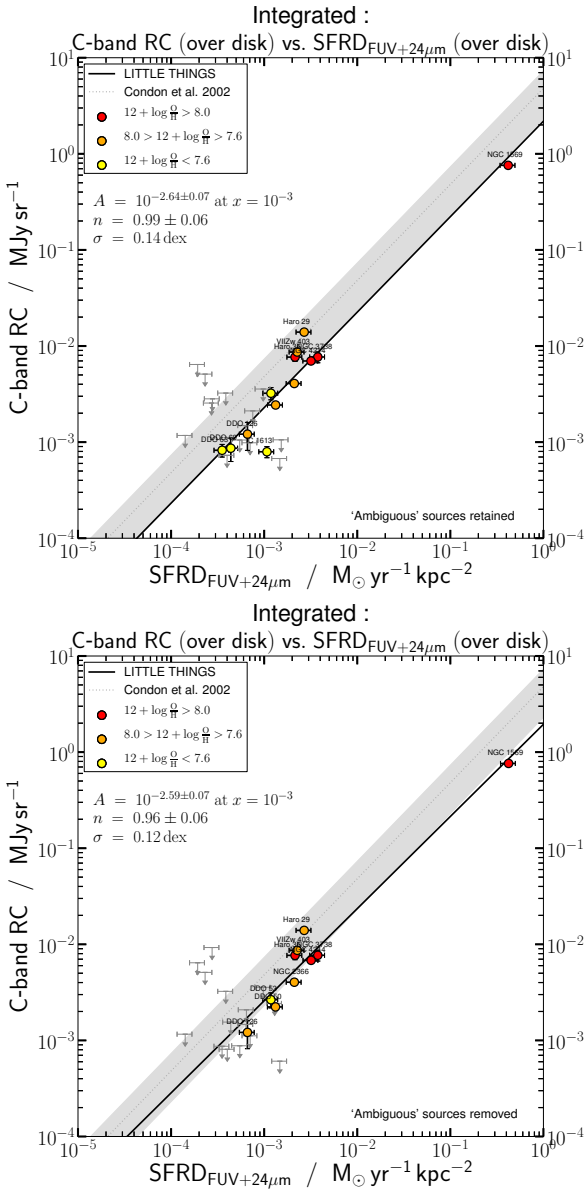

FIGURE 4.9: Galaxy-wide total *C*-band surface brightness as a function of the FUV-inferred SFRD (Leroy et al., 2012); SFRD has been corrected for internal extinction from dust if 24μm data were available using the Leroy et al. (2012) prescription. Definite background sources have been removed, whilst the 'ambiguous' sources have been retained (top panel) and removed (bottom panel). Surface brightness measurements have been taken over the whole disk. The solid line is the best-fit power law to our sample. We show the Condon et al. (2002) RC–SFRD relation as described in Equation 4.6. The errors introduced by our conversion are reflected by the grey shaded band, and the $3\,\sigma$ upper limits of RC emission are shown by the grey arrows.

of 0.1 and a 15 K uncertainty in the dust temperature. Figure 4.10 shows how our dwarf galaxies compare to those compiled by Yun et al. (2001). Our detections fill in the low mass, low metallicity range, extending the traditionally sampled range by 4 orders of magnitude.

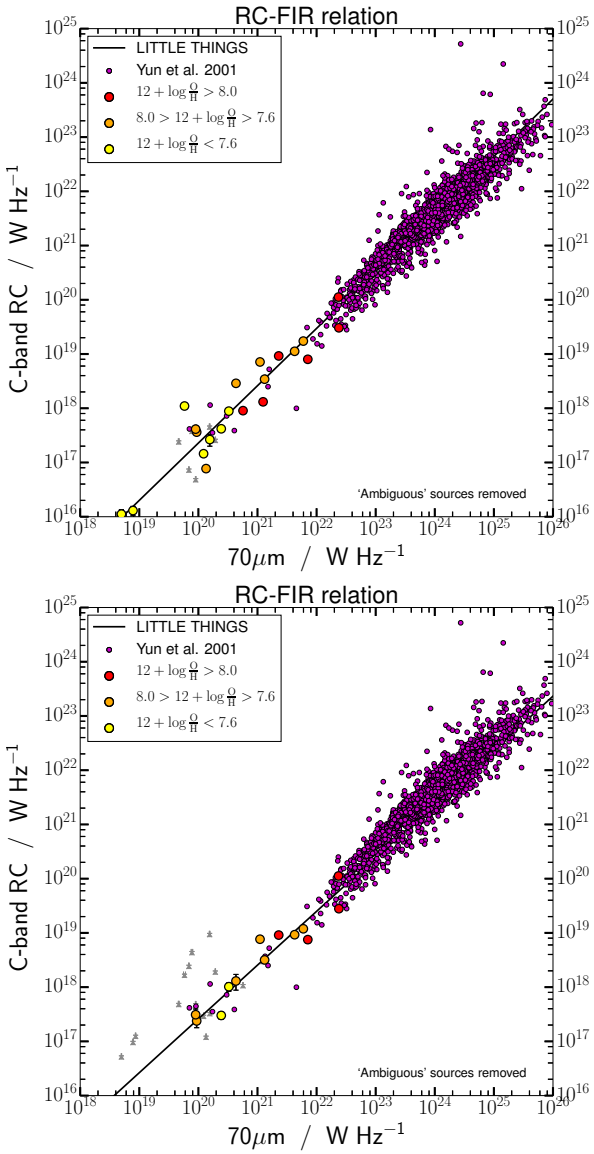

FIGURE 4.10: Comparison of RC and FIR luminosities from this study to those from Yun et al. (2001) (their VLA 1.4 GHz data have been corrected to 6 GHz and the *IRAS* 60μm data to *Spitzer* 70μm). Both definite background and 'ambiguous' RC sources have been removed from the LITTLE THINGS galaxies. Integrated quantities have been taken from regions of significant RC emission (i.e., the RC-based mask; top panel) and from over the whole disk (bottom panel). The LITTLE THINGS galaxies that exhibited less than 3σ RC emission are represented by grey stars.

As Figure 4.10 shows, whether emission is integrated over the whole disk or from just the significant regions of RC emission (i.e., the RC-based mask), the LITTLE THINGS galaxies remain consistent as a whole with the Yun et al. (2001) population (purple points).

To get a closer look at the LITTLE THINGS galaxies, Figure 4.11 concentrates on

the RC–FIR parameter space relevant to our sample. The top panel shows the relation when we include the 'ambiguous' sources, whereas the bottom panel shows the relation with 'ambiguous' sources removed. We find that the RC–FIR relation in Figure 4.11 (top panel) is slightly sub-linear; it has a power-law gradient of $\sim 0.9 \pm 0.1$ with a scatter of 0.3 dex. We attribute its near linear slope, in part, to the contaminating background sources (which themselves are probably the type of galaxy prevalent in the Yun et al. (2001) sample).

A number of dwarfs in Figure 4.11 (top panel) are significantly radio 'bright/loud' with respect to the Yun et al. (2001) sample. These data points (e.g., DDO 63, DDO 210, and UGC 8508) harbour 'ambiguous' RC emission. Given that our dwarf galaxies may be affected by a RC excess introduced by including RC emission from unrelated background sources, we assume that the 'ambiguous' sources of RC emission are of background origin and remove them from our analysis. We present the RC–FIR relation free from 'ambiguous' emission in Figure 4.11 (bottom panel). This ensures that all of the isolated emission is from the dwarf itself, however, it is possible that we remove a fraction of dwarf emission (e.g., a SNR that we erroneously assume is a background galaxy).

Removing the 'ambiguous' sources does not significantly alter the results, although the RC–FIR relation does become consistent with a linear slope at the $1\,\sigma$ level (power-law index of 1.06 ± 0.08 with a scatter of 0.24 dex).

4.4.4 q-parameter

Yun et al. (2001) found that the integrated FIR and RC flux densities of galaxies forged a linear relation. The log of the ratio of the *IRAS* FIR (a weighted combination of 60 and 100μm flux) to VLA 1.4 GHz flux densities of his sample,

$$q_{\rm FIR:1.4} = \log\left(\frac{\rm FIR\ [Jy]}{\rm RC\ [Jy]}\right), \tag{4.8}$$

was 2.34 ± 0.01. Since our RC and FIR measurements were made in different bands to those used in Yun et al. (2001), we convert their $q_{\rm FIR:1.4}$ to $q_{70:6} = 2.68 \pm 0.12$, where the subscript 70 and 6 refer to the 70μm FIR and 6 GHz RC, respectively. The uncertainty is calculated by assuming a 0.1 uncertainty on the spectral index between *L*- and *C*-band, and 15 K uncertainty on the dust temperature.

The RC–FIR (flux density) relation of our sample is shown in Figure 4.12. The LITTLE THINGS dwarfs continue the RC–FIR 'conspiracy', following a trend consistent with linearity. There appears to be a sharp threshold at 70μm FIR ~ 1 Jy (6 GHz RC ~ 2 mJy): above this threshold, the scatter of the galaxies around the

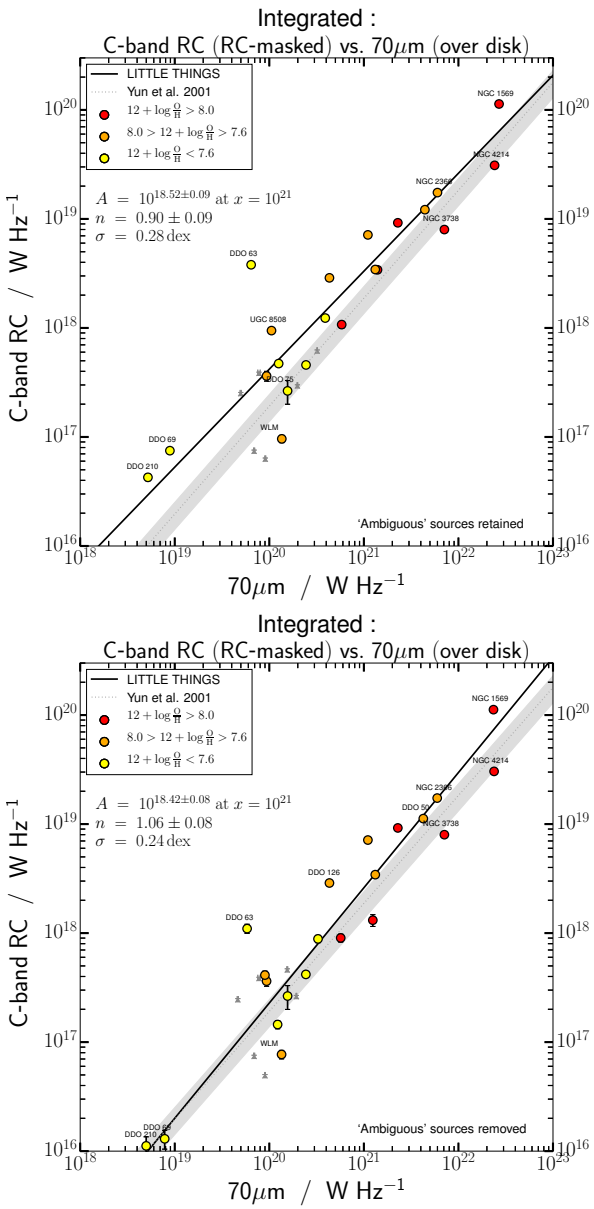

FIGURE 4.11: Galaxy-wide total *C*-band luminosity as a function of *Spitzer* 70μm FIR. Definite background sources have been removed, whilst the 'ambiguous' sources were retained in the top panel and removed in the bottom panels. The solid line is the best-fit power law to our sample. We show the Yun et al. (2001) RC–FIR relation as described in Equation 4.7. The uncertainties introduced by our conversion are reflected by the grey shaded band. The LITTLE THINGS galaxies that exhibited less than $3\,\sigma$ RC emission are represented by grey stars.

relation is smaller than those galaxies below the threshold.

In the least active dwarfs (which dominate the low end of the RC–FIR relation in Figure 4.12), where SF is sporadic and episodic, the RC-to-FIR ratio observed is dependent on time since the RC and FIR emission mechanisms have unique timescales. Thus, in these galaxies, scatter in observed quantities will be large. In the more active

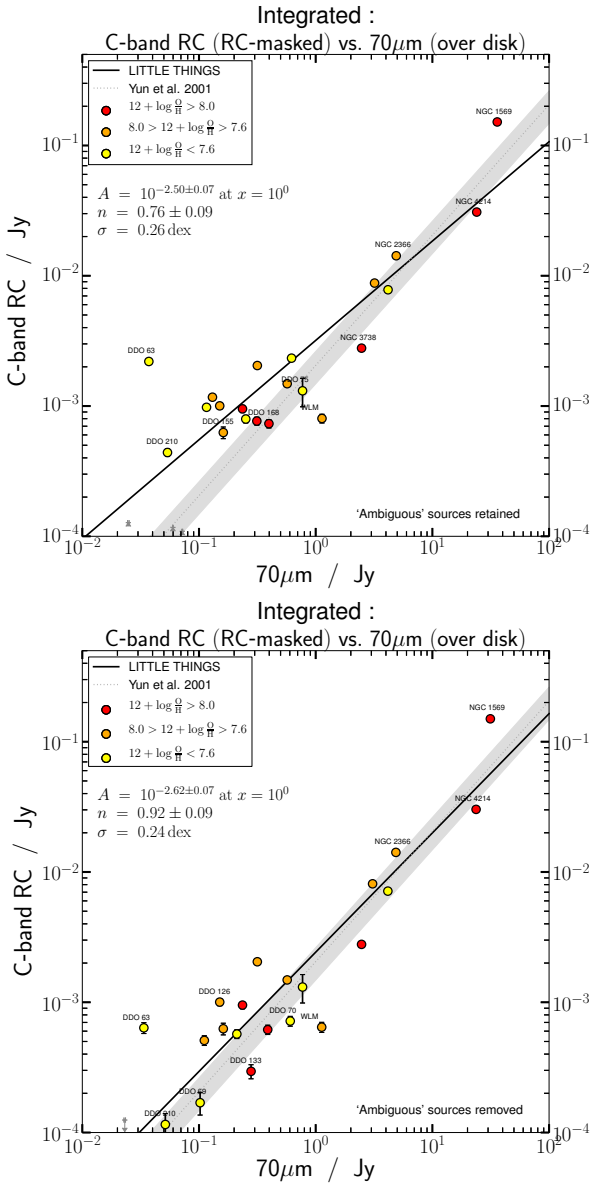

FIGURE 4.12: Galaxy-wide total *C*-band flux density as a function of *Spitzer* 70μm FIR. Definite background sources have been removed, whilst the 'ambiguous' sources were retained in the top panel but removed in the bottom panel. The solid line is the best-fit power law to our sample. We show the Yun et al. (2001) RC–FIR relation as described in Equation 4.8. The uncertainties introduced by our conversion are reflected by the grey shaded band. The LITTLE THINGS galaxies that exhibited less than $3\,\sigma$ RC emission are represented by grey stars.

galaxies (that dominate the high-end of Figure 4.12), SF regions are more numerous and so the time-averaged SFR is more stable (like spiral galaxies)—in this respect, these more active dwarf galaxies are similar to spirals. This threshold may be a watershed between 'dwarf/irregular galaxies' and 'dwarf spirals', which may also be seen in the luminosity plot of Figure 4.11.

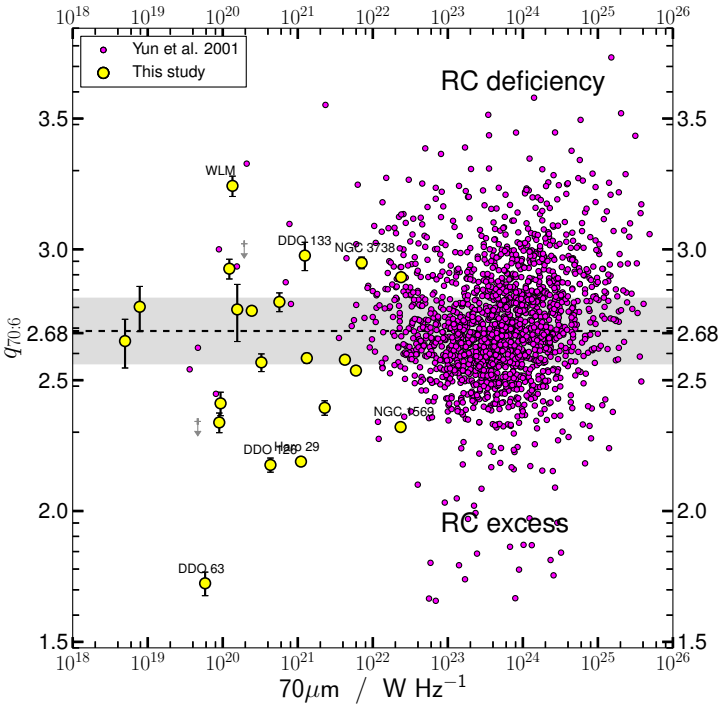

FIGURE 4.13: $q_{70:6}$ parameter as a function of 70μm luminosity. Both obvious and 'ambiguous' background sources have been removed. We also show the Yun et al. (2001) data points (purple) and their q-parameter appropriately corrected to our observation bands (dashed). The errors introduced by our conversion are reflected by the grey shaded band.

Alternatively, the RC and FIR flux densities can be examined through the q-parameter (see Figure 4.13). This time, we plot values as a function of 70μm FIR luminosity. Again, the LITTLE THINGS dwarfs are consistent, as a population, with the Yun et al. (2001) sample.

In dwarfs, there is a difference between the mechanisms for generating RC and FIR emission. While $\mathrm{RC}_{\mathrm{NTh}}$ emission is highly dependent on the massive stars in dwarfs, FIR emission is not as dependent since a lower proportion of dust-heating comes from massive stars and, in fact, it is the ISRF that is the main contributor to dust-heating (Irwin et al., 2013). Therefore, an extra factor is introduced to the RC–FIR 'conspiracy': it is not just the escape of CRe that goes in line with the escape of FUV photons, but the ISRF also plays a role, too.

4.4.5 The Interplay Between SF, RC and FIR

Current empirical relations derived from large populations of medium to large-sized galaxies (e.g., in this chapter we concentrate particularly on the L-band RC: Yun et al., 2001; Condon et al., 2002) show that galaxy-wide RC emission is directly proportional to both the SFR and FIR emission of a galaxy. In these types of galaxies,

emission is bright meaning that contamination is a minor issue.

Since contamination is an issue in our dwarf galaxies (especially at the faint end), we decide to err on the side of caution by basing results on the removal of all possible background sources (both obvious and 'ambiguous'). When doing this, the RC emission in dwarf galaxies is found to be directly proportional to FIR, but not to SFR.

The interplay between the SF, total *C*-band RC, and FIR can be summarised in two equations. First, from Figure 4.7, the RC–SFR relation we find to be

$$\frac{\mathrm{RC}}{\mathrm{W\,Hz^{-1}}} = 10^{18.05\pm0.08}\left(\frac{\mathrm{SFR}}{10^{-2}\mathrm{M_\odot\,yr^{-1}}}\right)^{1.18\pm0.10}. \tag{4.9}$$

Then, there is the RC–FIR relation (Figure 4.11) which we find to be

$$\frac{\mathrm{RC}}{\mathrm{W\,Hz^{-1}}} = 10^{18.42\pm0.08}\left(\frac{70\mu\mathrm{m\ FIR}}{10^{21}\mathrm{W\,Hz^{-1}}}\right)^{1.06\pm0.08}. \tag{4.10}$$

What do Equations 4.9 and 4.10 mean in a physical sense? There appears to be a change in the RC–SFR relation for systems forming stars at about 0.1–$1.0\,\mathrm{M_\odot\,yr^{-1}}$. Above this star formation activity, galaxies follow a linear relation (e.g., Condon et al., 2002), whereas below this, the relation steepens to a power–law index of 1.2 ± 0.1. This may indicate a transition between 'dwarf/irregular galaxies' and 'dwarf spirals'. In fact, some of the larger dwarf galaxies in this study exhibit tentative spiral arms. The terms 'spiral' and 'dwarf' stem from a somewhat black-or-white mindset. In reality, the 'spiralness' of a galaxy is not so clearcut, and galaxies occupy a continuous spectrum in terms of their morphology.

This steepening of the RC–SFR relation below 0.1–$1.0\,\mathrm{M_\odot\,yr^{-1}}$ may be explained by the escape of CRe from the dwarf galaxy; this is explained in more detail in Section 4.4.6.

4.4.6 Cosmic Ray Electrons and Magnetic Fields

In spiral galaxies, the $\mathrm{RC_{Th}}$ fraction seldom exceeds 25% at *C*–band; however, the $\mathrm{RC_{Th}}$ fraction of our dwarf galaxies is 39% on average. This is despite the fact that $\mathrm{RC_{Th}}$ emission, in an absolute sense, may be reduced (e.g., the truncated stellar IMF scenario of Lee et al., 2009). For the dwarf galaxies to have a larger thermal fraction than larger galaxies (despite being deficient in $\mathrm{RC_{Th}}$), there must be a proportionally larger reduction in their $\mathrm{RC_{NTh}}$ emission. To explain a reduction in the $\mathrm{RC_{NTh}}$ emission, we investigate the synchrotron emissivity in an optically thin region,

$$\epsilon_{\mathrm{NTh}} \propto n_{\mathrm{CRe}} B_\perp^{\frac{\gamma+1}{2}}, \tag{4.11}$$

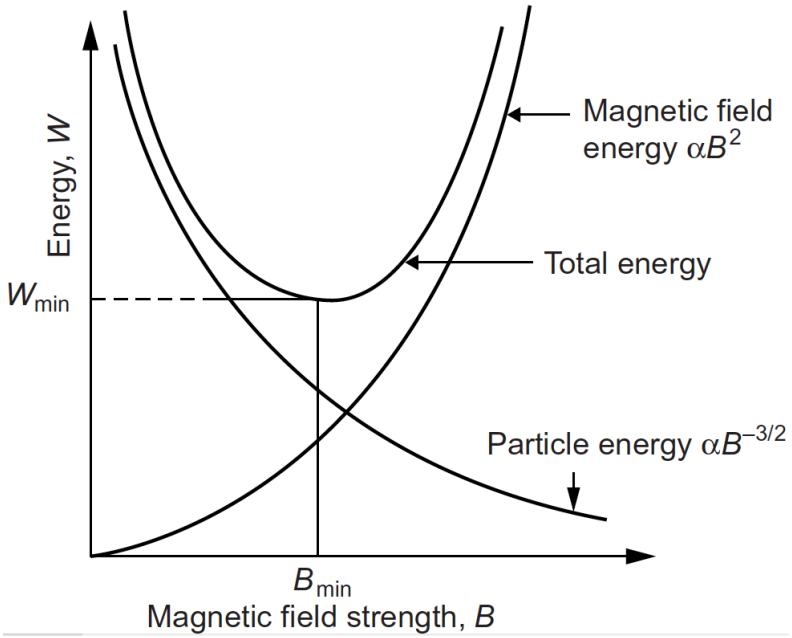

FIGURE 4.14: Energy contained within the magnetic field and the CRe as a function of magnetic field strength (taken from Longair, 1981). The magnetic field strength, $B_{\rm min}$, associated with the minimum energy, $W_{\rm min}$, approximates the magnetic field strength for which the energy densities of the field and the CRe are equal (intersection of the curves).

where $n_{\rm CR}$ is the number density of CRe present in the dwarf's galactic magnetic field, $B_{\perp}$ is the strength of the transverse magnetic field, and γ is the power–law slope of the CRe injection spectrum.

The $\mathrm{RC_{NTh}}$ emission depends both on the energy density contained within the magnetic field and that contained within the population of CRe. Generally, it cannot be known whether the energy in the synchrotron radiation comes predominantly from the magnetic field (relatively few CRe in a strong magnetic field) or predominantly from the CRe (many CRe in a weaker magnetic field).

However, the combined energy densities associated with the magnetic field and the CRe is usually assumed to be at a minimum (see Section 16.5 of Longair, 1981). In galaxies, this is a reasonable assumption. If the energy densities are not equal, they will tend to balance: for example, if the energy density is dominated by the CRe, then they will rise out of the galactic disk in Parker lobes due to their buoyancy, expand, and escape thus reducing their energy density. As Figure 4.14 shows, the magnetic field strength associated with the minimum energy, $B_{\rm min}$, approximates the magnetic field strength for which the energy densities of the field and the CRe are equal, $B_{\rm eq}$.

It is, however, conceivable that dwarf galaxies in particular deviate from equipartition which would lead to a reduction in synchrotron emission (see Figure 4.8) in

two different ways:

1) a low number density of CRe ($n_{\rm CRe}$) present in the dwarf's galactic magnetic field. Dwarf galaxies in particular are prone to galactic outflows since they have low masses, and winds can advect plasma and resident CRe away from the galaxy.

2) the magnetic field strength (B) being lower than the equipartition value at which the energy density of the magnetic field is equal to that of the cosmic rays (electrons and protons combined). In the standard paradigm of a mean field α–ω dynamo, the key ingredients are turbulence and shear. Dwarf galaxies may be sites of weak, large-scale, ordered magnetic fields, so magnetic field amplification may be less efficient. However, the turbulent field in and around the SF regions may not necessarily be weaker than that found in spirals (e.g., Tabatabaei et al., 2013) as 30μG is observed across some 100 pc regions.

In the following, the magnetic field strength in our sample of dwarf galaxies is estimated under the assumption of equipartition; this is the only practical way of estimating the field strengths. The script used was based on `bfield`[12] (Aritra Basu, priv. comm.) which uses the equipartition formula for the total magnetic field (see Equation 3 from Beck & Krause, 2005). We made the assumption that the proton–to–electron number density ratio is 100 (Beck & Krause, 2005) and that the dwarf galaxy has a scale height of 400 pc independent of distance from the centre (Banerjee et al., 2011).

The average transverse magnetic field strength of our sample is estimated to be $9.4\pm3.8\,\mu$G (see column 13 of Table 4.3 for galaxy specific values) which is in excess of the $\sim 2\mu$G found in ~ 50 faint dwarf galaxies from the NVSS catalogue (Roychowdhury & Chengalur, 2012). It is stressed that these high values come from the manner in which $\rm RC_{NTh}$ flux densities were extracted: the RC–based mask was used to isolate significant regions of $\rm RC_{NTh}$ emission which means we were generally looking at just regions of active SF, whereas Roychowdhury & Chengalur (2012) used unresolved dwarfs and were thus integrating emission over the whole dwarf, effectively integrating over areas with and without RC and thus 'diluting' their measurement of the magnetic field strength.

The transverse field strength we measured is identical to the $9.7\,\mu$G found in the WSRT SINGS sample (Heesen et al., 2014). Given that we observe the $\rm RC_{NTh}$ emission to be deficient (see Figure 4.8), this suggests that the magnetic field may actually not be low in comparison with equipartition; rather, the CRe are escaping leading to less synchrotron emission.

[12] www3.mpifr-bonn.mpg.de/staff/mkrause/

Our resolved data allowed the magnetic field strength to be measured on a resolved basis. In a few dwarf galaxies (e.g., NGC 1569, NGC 2366, NGC 4214), there were numerous regions where the magnetic field strength was measured to be as high as 30–40 μG in localised 100 pc regions (approximate area of the synthesised beam). In fact, the brightest $\mathrm{RC_{NTh}}$ flux density in our sample came from a ~ 100 pc region in NGC 1569—the flux density from this unresolved region implied a magnetic field strength of 70 μG. These are strong magnetic fields akin to those found in the SF regions of larger spirals (e.g., the turbulent magnetic fields in NGC 6946's SF regions Tabatabaei et al., 2013). With such magnetic field strengths, CRe could lose all their energy before diffusing into the ISM (rendering the region a local *calorimeter*. For less intense SF regions, CRe may have sufficient time to escape into the ISM. Once here,

- 1) the CRe, now radiating at a much slower rate, diffuse or are advected into the intragalactic medium (IGM) before they have the time to radiate all their energy—this is the 'non-calorimetric' model that leads to the RC–FIR 'conspiracy' (e.g., Bell, 2003; Dale et al., 2009; Lacki et al., 2010), or
- 2) the CRe continue to diffuse to 1 kpc but, because they continue to radiate and lose energy, the frequency of synchrotron emission shifts gradually to lower frequencies to the extent that emission falls outside of *C*-band.

Hence, while the ISM (disk) could be populated by CRe, it can be void of large-scale $\mathrm{RC_{NTh}}$ emission at 6 GHz (*C*–band) for these aforementioned reasons. However, in the majority of the LITTLE THINGS sample, it is most likely the case that the deficiency of large-scale $\mathrm{RC_{NTh}}$ emission is caused by the intermittent nature of SF.

4.5 Summary

We used the VLA in C-array to make *C*–band ($\nu = 6$ GHz or $\lambda = 5$ cm) observations of 40 dwarf galaxies taken from LITTLE THINGS (Hunter et al., 2012). Our images have a resolution of 3–8″ and an rms noise of 3–15$\mu\mathrm{Jy\,beam^{-1}}$ (in the centre of the map prior to correction for primary beam attenuation).

We summarise our findings as follows:

- Contamination from background sources was a prominent issue in earlier, low resolution studies. Earlier studies reporting linear relations (e.g, RC–SFR; the RC–FIR 'conspiracy') in dwarf galaxies could, in part, be attributed to contamination from background galaxies that themselves fall on such relations;

- Our resolution allowed us to single out background sources. A total of 27 out of the 40 LITTLE THINGS galaxies exhibit significant RC emission originating from the galaxy itself; 17 are new RC detections. The flux densities of our brighter dwarfs agree with the literature;

- We find that the average thermal fraction is $39 \pm 7\%$ at 6 GHz, whilst the non–thermal fraction is $61 \pm 7\%$. The $\mathrm{RC_{NTh}}$ fraction is lower than that found in larger spirals; this is despite the fact that the $\mathrm{RC_{Th}}$ emission may be reduced, in an absolute sense (Lee et al., 2009), in dwarf galaxies;

- Arguably, the most important aspect of this chapter is the inversion of the RC–SFR relation described in Equation 4.9. This inversion allows the SFR to be inferred from a RC luminosity, and is given by

$$\frac{\mathrm{SFR}}{\mathrm{M_\odot\,yr^{-1}}} = 5 \times 10^{-18} \left(\frac{\mathrm{RC}}{\mathrm{W\,Hz^{-1}}} \right)^{0.85} ; \tag{4.12}$$

- The LITTLE THINGS galaxies diverge from the Condon et al. (2002) RC–SFR relation at a SFR of $0.1\mathrm{M_\odot\,yr^{-1}}$. The sample has a power–law slope of $\sim 1.2 \pm 0.1$ with a scatter of 0.2 dex. For SFRs of about $10^{-4}\mathrm{M_\odot\,yr^{-1}}$, the observed RC is a factor of 10 deficient from that predicted from the Condon et al. (2002) relation. We interpret this as an underproduction of the $\mathrm{RC_{NTh}}$ component due to CRe escape;

- Within the uncertainties, the dwarf galaxies are consistent with the linear Yun et al. (2001) RC–FIR (flux density) trend (see Figure 4.12). The scatter of the relation increases significantly below 70μm FIR ~ 1 Jy (6 GHz RC ~ 2 mJy);

- Within the uncertainties, our data are consistent with the linear Yun et al. (2001) RC–FIR (luminosity) trend (see Figure 4.11) suggesting that the 'conspiracy' of the RC–FIR relation continues to hold even for dwarf galaxies;

- In a few dwarf galaxies, the equipartition magnetic field strength reaches as high as $30\,\mu$G in multiple 100 pc regions, and in one case, $70\,\mu$G;

- Most SF regions do not possess such strong magnetic field strengths. The average strength of the transverse magnetic field is $\sim 9.4\mu$G (from only the regions that exhibited significant RC emission). This value is consistent with that of larger galaxies (e.g., 9.7μG in WSRT SINGS; Heesen et al., 2014). This suggests that it is the escape of CRe that is responsible for the deficient $\mathrm{RC_{NTh}}$ emission (see Figure 4.8). Once in the ISM, the CRe may: 1) radiate at a slower rate than

in SF regions, and move into the IGM before they have the time to radiate all their energy, or 2) continue to diffuse but, because they continue to radiate and lose energy, the frequency of synchrotron emission shifts gradually to lower frequencies to the extent that emission falls outside of *C*-band. As a result, interstellar regions can be largely void of $\mathrm{RC_{NTh}}$ emission.

5

Resolved Radio Continuum in Dwarf Galaxies

The integrated RC was examined in Chapter 4; however, the resolution and sensitivity of the data allow for a resolved study, and this is the subject of this chapter. To date, there has not been a resolved RC study of such a large sample of dwarf galaxies.

5.1 Introduction

The RC finds its origin in recent SF and thus can be calibrated as a SFR indicator. The $\mathrm{RC_{Th}}$ comes from the free-free interactions of electrons and ions within the H II regions surrounding the most massive, short-lived stars. The $\mathrm{RC_{NTh}}$ finds its origins in the SNR; supernova shocks accelerate CRe to ultra–relativistic velocities, which then spiral around magnetic fields producing the $\mathrm{RC_{NTh}}$ radiation. CRe typically last 10s of Myr after their initial acceleration, and an ensemble of CRe may diffuse or be advected out to around a kpc from the SF region of origin. Further details can be found in Section 1.3.3.

The $\mathrm{RC_{Th}}$ and $\mathrm{RC_{NTh}}$ operate on different time and spatial scales. Hence to calibrate the RC as a SFR indicator, special attention needs to be paid to the spatial and temporal behaviour of the RC's two components.

In principle, the $\mathrm{RC_{Th}}$ can be calibrated as a SFR indicator: on sub-galactic scales, Hα (an oft used proxy for SF) and $\mathrm{RC_{Th}}$ display a strong spatial correlation since the physical conditions that drive the emission mechanisms are the same (i.e., ionised Hydrogen, mainly in H II regions). The CRe however have the ability to diffuse or be advected away from SF regions, ultimately resulting in a spatial disconnect between SF and $\mathrm{RC_{NTh}}$ emission (e.g., Heesen et al., 2014). Despite this complication, the $\mathrm{RC_{NTh}}$ does have good prospects as a SF indicator as it is not affected by dust attenuation, and is much less affected by changes in the high mass tail of the stellar IMF than Hα[1], and therefore offers an alternative to inferring the SFR.

But spatial scales do not provide the whole picture: time-dependent processes are important too. In spiral galaxies, the number of SF complexes is large enough that, when averaged over time, the SFR remains roughly constant. The result is a steady production of SNR, and with it, $\mathrm{RC_{NTh}}$ emission. Dwarf galaxies do not exhibit as much SF and, as such, SF is more stochastic in nature due to the lack of large scale SF inducing processes such as spiral arm shocks.

As smaller scales are sampled, SFR relations are expected to show increased scatter. When sufficiently small scales are sampled where a *single* SF complex is examined, the intrinsic scatter of often used tracers becomes significant (e.g., Leroy et al., 2012 calculate the scatter of FUV-inferred SFRs to be 0.44 dex).

This time and spatial dependency of the $\mathrm{RC_{NTh}}$ thus introduces a stumbling block to calibrating it as a SFR indicator. The $\mathrm{RC_{NTh}}$ needs to be well understood in order to calibrate it as a SFR indicator. This chapter aims to answer: *to what extent can the RC_{NTh} be used to probe SF in dwarf galaxies on a resolved basis*?

This chapter is organised as follows: the results (images and resolved emission) are presented in Section 5.3 and a detailed discussion is given in Section 5.4.1, paying particular attention to the RC–SFR relation; the analysis is summarised and tied together in Section 5.5.

5.2 Observations and Data Reduction

The dwarf galaxies observed in this study are a sub-sample of LITTLE THINGS—details of the entire sample can be found in Chapter 2. As this study concerns itself

[1] Hα emission is dependent on the part of the stellar IMF populated by stars with mass $\gtrsim 18\ M_{\odot}$, while the $\mathrm{RC_{NTh}}$ emission is dependent on stars with mass $\gtrsim 8\ M\odot$

TABLE 5.1: **CALIBRATION AND IMAGING SUMMARY OF PROJECT 12A-234 FOR THE 27 GALAXIES THAT EXHIBITED SIGNIFICANT RC EMISSION**

(1) Name of dwarf galaxy observed; (2) Date of observation; (3) Name of primary calibrator; (4) Name of secondary calibrator; (5 & 6) J2000 equatorial coordinate of observation (dwarf galaxy) phase centre; (7) Physical scale at distance of galaxy; (8) Resolution of image. Note that some images were made using `robust=0.0` and others using `robust=+2.0` where CASA robust values range between -2.0 (uniform weighting) and $+2.0$ (natural weighting); (9) The rms noise; (10) Comments regarding deviations from the typical imaging process: R signifies that the `clean` algorithm was performed using uniform weighting, while N signifies an approach closer to natural weighting; S means that the generated image benefited from self-calibration; P refers to those images that were strongly affected by a bright, nearby background source of ~ 0.1 Jy. Self-calibration failed due to the time varying primary beam, and so to minimise the effect of the offending source, only about a quarter of the bandwidth was used in such a way as to place the first null of the primary beam as close as possible to the offending source.

Galaxy	Date	Pri. Cal.	Sec. Cal.	R.A	Dec.	Scale	Res.	Noise	Notes
						pc arcsec^{-1}	arcsec	μJy beam^{-1}	
(1)	(2)	(3)	(4)	(5)	(6)	(7)	(8)	(9)	(10)
DDO 43	2012 Mar 22	3C286	J0818+4222	07 28 17.8	+40 46 13	8.5	2.5×2.3	6.9	R,S
DDO 46	2012 Mar 22	3C286	J0818+4222	07 41 26.6	+40 06 39	8.5	3.0×2.8	5.1	N
DDO 47	2012 Mar 20	3C286	J0738+1742	07 41 55.3	+16 48 08	8.0	3.2×3.0	5.0	N
DDO 50	2012 Mar 17	3C147	J0841+7053	08 19 08.7	+70 43 25	5.2	4.4×3.5	5.5	N,S
DDO 53	2012 Mar 16	3C147	J0841+7053	08 34 08.0	+66 10 37	5.6	4.9×4.0	5.4	N
DDO 63	2012 Mar 25	3C286	J0841+7053	09 40 30.4	+71 11 02	5.9	6.1×3.4	4.6	N
DDO 69	2012 Mar 20	3C286	J0956+2515	09 59 25.0	+30 44 42	1.2	4.1×3.6	4.0	N
DDO 70	2012 Mar 20	3C286	J0925+0019	10 00 00.9	+05 19 50	2.0	4.5×3.4	5.8	N
DDO 75	2012 Mar 20	3C286	J1024−0052	10 10 59.2	−04 41 56	2.0	3.3×2.4	9.7	N,S
DDO 126	2012 Apr 05	3C286	J1215+3448	12 27 06.5	+37 08 23	7.6	4.6×4.0	5.4	N,S

Table 5.1 continued on next page

Table 5.1 – continued from previous page

Galaxy	Date	Pri. Cal.	Sec. Cal.	R.A	Dec.	Scale	Res.	Noise	Notes
						pc arcsec^{-1}	arcsec	μJy beam^{-1}	
(1)	(2)	(3)	(4)	(5)	(6)	(7)	(8)	(9)	(10)
DDO 133	2012 Mar 17	3C286	J1310+3220	12 32 55.4	+31 32 14	9.4	3.8×3.7	4.4	N,S
DDO 155	2012 Mar 17	3C286	J1309+1154	12 58 39.8	+14 13 10	3.4	3.8×3.5	4.7	N
DDO 168	2012 Apr 20	3C286	J1327+4326	13 14 27.2	+45 55 46	5.4	3.9×3.5	4.4	N
DDO 210	2012 May 19	3C48	J2047−1639	20 46 52.0	−12 50 51	1.4	3.1×1.7	4.6	R
Haro 29	2012 Apr 20	3C286	1219+484	12 26 16.7	+48 29 38	8.3	3.9×3.6	5.1	N
Haro 36	2012 Apr 20	3C286	1219+484	12 46 56.3	+51 36 48	13.9	3.9×3.6	5.2	N
IC 1613	2010 Aug 19	3C48	J0108+0135	01 04 49.2	+02 07 48	1.1	9.3×7.8	5.1	R
IC 10	2012 Apr 28	3C84	J0102+5824	00 20 17.3	+59 18 14	1.5	2.6×2.3	7.8	R
Mrk 178	2012 Apr 20	3C286	1219+484	11 33 29.0	+49 14 24	6.0	4.4×4.0	9.3	N
NGC 1569	2012 Mar 16	3C147	J0449+6332	04 30 49.8	+64 50 51	3.9	2.7×2.3	6.8	R
NGC 2366	2012 Mar 16	3C147	J0841+7053	07 28 48.8	+69 12 22	4.9	4.2×3.4	5.1	N
NGC 3738	2012 Apr 20	3C286	J1146+5356	11 35 49.0	+54 31 23	7.6	2.5×2.5	7.6	N,S
NGC 4214	2012 Apr 05	3C286	J1215+3448	12 15 39.2	+36 19 38	4.5	4.5×4.0	6.3	N,S
Sag DIG	2012 May 19	3C48	J1911−2006	19 30 00.6	−17 40 56	1.7	3.5×1.4	8.2	R
UGC 8508	2012 Apr 20	3C286	J1349+5341	13 30 44.9	+54 54 29	4.0	2.6×2.5	6.0	N
VIIZw 403	2012 Mar 25	3C286	J1153+8058	11 27 58.2	+78 59 39	6.8	5.8×3.7	5.8	N
WLM	2012 May 19	3C48	J2348−1631	00 01 59.2	−15 27 41	1.5	5.0×1.5	5.3	R

with the resolved nature of the $\mathrm{RC_{NTh}}$–SFR relation, only those galaxies that exhibited significant emission at *C*-band (4–8 GHz) coincident with SF were chosen; this resulted in 27 out of the original sample of 40. Table 5.1 summarises the properties of this sub-sample.

The *C*-band observations used in this study came from project ID 12A-234. The data reduction and calibration was performed in the same way as in Chapter 3: in brief, observations were taken with the VLA in its C-configuration; the data were calibrated using CASA; the usual calibration steps were implemented through using one of four NRAO calibrators to calibrate the flux scale, and a nearby ($< 10^{\circ}$) calibrator to correct the complex gain on timescales of around 10 minutes. Both prior to and after calibration, visibilities were automatically flagged by `tflagdata(mode='tfcrop')` (Rau & Pramesh 2003) and `tflagdata(mode='rflag')` (based on AIPS; Greisen 2011) and then inspected by eye.

As mentioned in Section 4.2.2, images were generally made using natural weighting (`robust=+2.0`) due to the observed low-surface brightness. However, some observations were instead cleaned using Brigg's method (`robust=0.0`) because either the galaxy was sufficiently bright, or the natural weighting `clean` left too many significant image artefacts throughout the image (refer back to Figure 3.14 for examples of images generated using various `robust` values). Typical rms noise values in these cleaned images fell between 4 and 8 $\mu\mathrm{Jy\,beam^{-1}}$. Contamination from both background sources and 'ambiguous' sources was then removed (see Section 4.3.2 and Figure 4.3 for a detailed definition of 'ambiguous').

5.2.1 Ancillary Data

The RC images are complemented by broadband continuum images including, among others: *GALEX* FUV (1350–1750 Å; effective wavelength 1516 Å; 4″ FWHM), *Spitzer* MIR (effective wavelength 24μm; 6″ FWHM) and FIR (effective wavelength 70μm; 17″.5 FWHM), and Hα line emission (see Section 2.2).

5.3 Results

5.3.1 Radio Continuum Images

The majority of galaxies only exhibit significant RC in isolated pockets which is attributed to the episodic nature of SF in dwarf galaxies (e.g., Stinson et al., 2007) combined with the surface brightness sensitivity set by our observations.

5.4 Discussion

To study the dwarf galaxies on a resolved basis, each dwarf galaxy[2] was split into a number of regions with the ultimate aim of taking integrated quantities from each region. Two methods were employed:

Grid method: Galaxies were split using a grid of X pc square cells in the plane of the galaxy, where X is 200, 300, 500, or 700 (see top panel of Figure 5.1 for an example). From each of these cells, an integrated quantity was taken. This has the advantage of being objective, and avoids biasing integrated quantities to only user-defined regions (e.g., Chyży et al., 2011) that exhibit 'obvious' star formation activity. Since the scale of star formation ranges from scales of a few pc up to a kpc, a caveat is introduced in that a single cell may be dominated by noise if it covers a star formation complex $< X$ pc in size, or may inadvertently split a star formation complex between neighbouring cells if the star formation complex happens to be at the edge of a given cell.

Individual Star Formation Complexes method: The galaxies were also split into discrete star forming complexes (see bottom panel of Figure 5.1 for an example). This was done by first smoothing the Hα images to a resolution of 200 pc and then classifying all of the significant discrete complexes. The advantage of this method is that each region should be independent of other regions (i.e., no two regions overlap the same SF complex). However, this approach does rely on defining a smoothing scale (in this case, we use 200 pc)[3], and a threshold (5 times the Hα noise) to define a single SF complex, which makes it more subjective than using a grid of square cells. This also biases the regions to those that have been forming stars over the last 10 Myr, and that most probably have a high $\mathrm{RC}_{\mathrm{Th}}$ fraction. This bias is not an issue however since the purpose of this chapter is to calibrate the RC to infer rates of SF; that is to say, regions actively forming stars are exactly what is required.

In Table 5.2, the integrated quantities from the 200 pc square cells are given; only a sub-set of the data is given as an example. A similar dataset was created for the 300, 500, and 700 pc square cells, as well as for the discrete SF regions. It is from this data upon which the discussion in this chapter is based.

[2]The disk radius and orientation were defined based on the Holmberg disk (where the semi-major and semi-minor axes are defined as the radius where the *B*–band surface brightness falls to 26.66 mag), or, if the *B*–band data were not available, 3 times the *V*–band scale length (Hunter & Elmegreen, 2006)

[3]For comparison, the Tarantula nebula (30 Dor) in the LMC is 200 pc in size, and is one of largest SF complexes in the Local Group.

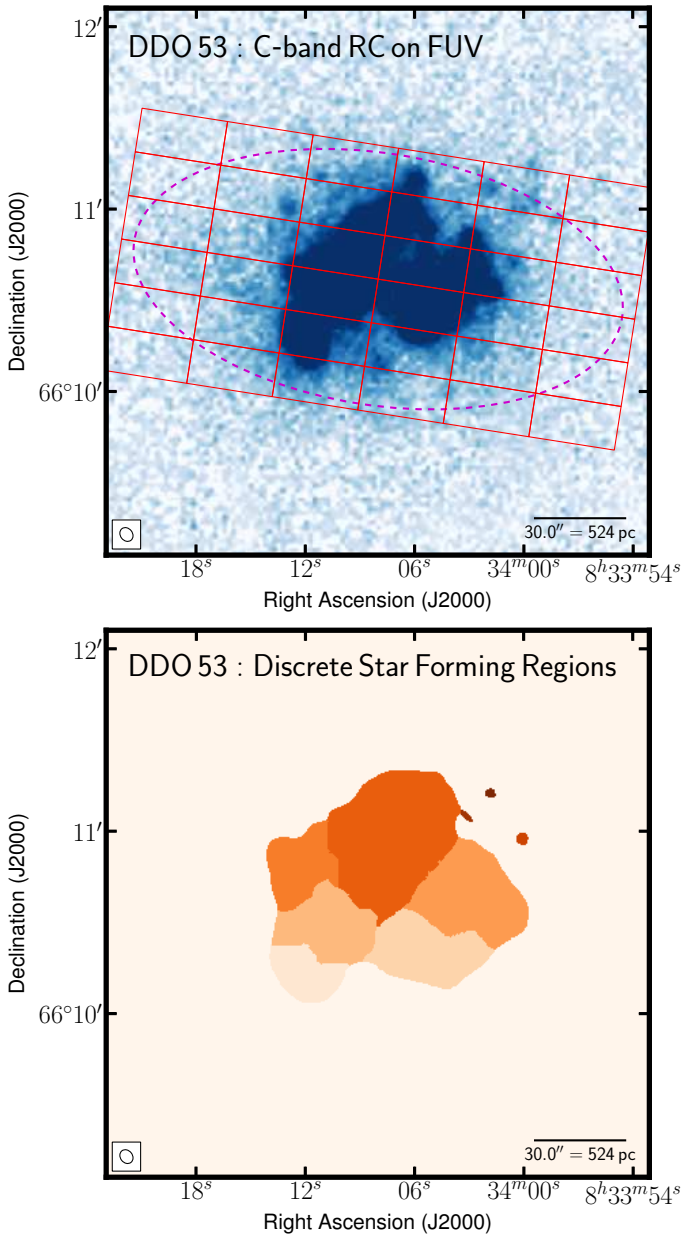

FIGURE 5.1: The two methods employed to break galaxies up into resolved regions, using DDO 53 as an example. *Top:* The grid method: *GALEX* FUV emission of DDO 53 overlaid by our RC contours and a grid (solid rectangles) which comprises 500 pc square cells in the plane of the disk (dashed line). *Bottom:* The isolated SF complexes method: the Hα image was used to define regions attributed to a single SF complex. In both cases, only emission from within the Holmberg radius contributed to the integrated quantities.

The subsequent analysis looks mainly into the $\mathrm{RC_{NTh}}$ component; this is because whether scales of 1 pc, or 1 kpc are investigated, the relationship between the Hα (current SF) and $\mathrm{RC_{Th}}$ is not expected to change since the physical conditions responsible—regions of ionised gas—are the same. Therefore, the $\mathrm{RC_{Th}}$–SFR relation is scale-independent, i.e., it is *not* expected to change based on the spatial scale that is sampled (e.g., see the 33 GHz $\mathrm{RC_{Th}}$–SFR study of Murphy et al., 2012). It is the CRe (and the associated $\mathrm{RC_{NTh}}$ emission) that extends beyond the SF regions from which they originated. We aim to calibrate the $\mathrm{RC_{NTh}}$–SFR relation on a resolved basis, whilst suggesting scales at which it becomes inappropriate to use.

5.4.1 Resolved $\mathrm{RC_{NTh}}$–SFR Relation

To investigate the $\mathrm{RC_{NTh}}$–SFR relation, following the Leroy et al. (2012) SFR prescription was chosen, which uses MIR emission to empirically correct FUV fluxes for the fraction of dust-obscured SF (see Section 4.4.2 for more details). The SFR will ultimately be compared with the $\mathrm{RC_{NTh}}$ luminosity which itself is related to the SFR through

$$\frac{L_{\mathrm{NTh}}}{\mathrm{W\,Hz^{-1}}} = 1.11 \times 10^{21} \left(\frac{\nu}{\mathrm{GHz}}\right)^{\alpha_{\mathrm{NTh}}} \frac{\mathrm{SFR}}{\mathrm{M_\odot\,yr^{-1}}}. \tag{5.1}$$

assuming a constant SFR over a entire galaxy. The derivation of Equation 5.1 was based on the $\mathrm{RC_{NTh}}$ luminosity–SN rate relation from Equation 18 of Condon (1992) and the Kroupa (2001) stellar IMF (see Section 1.3.3); it is based on *L*-band data (1.5 GHz), and implies a $\mathrm{RC_{Th}}$ fraction of about 20%.

Figure 5.2 shows the $\mathrm{RC_{NTh}}$–SFR relation for the whole sample. The quantities are compared with the $\mathrm{RC_{NTh}}$–SFR relation derived in Equation 5.1 but applied to an observing frequency of 6 GHz using an assumed spectral index of -0.5 (as observed in dwarf galaxies NGC 1569 and NGC 4214: Lisenfeld et al., 2004; Kepley et al., 2011).

The data points are binned according to the estimated amount of time elapsed since the most recent onset of SF. This elapsed time was calculated by calibrating the Hα-to-FUV luminosity ratio to give an age. Starburst99 data were used (Leitherer et al., 1999) to model the time evolution of Hα and FUV luminosity (the FUV data is explicitly given, but the Hα luminosity had to be inferred from data that was available: the flux of photons below a wavelength of 912Å). The resultant calibration was

$$\frac{t}{\mathrm{yr}} = 8 \times 10^6 \left(\frac{L_{\mathrm{H}\alpha}}{L_{\mathrm{FUV}}}\right)^{-0.303}. \tag{5.2}$$

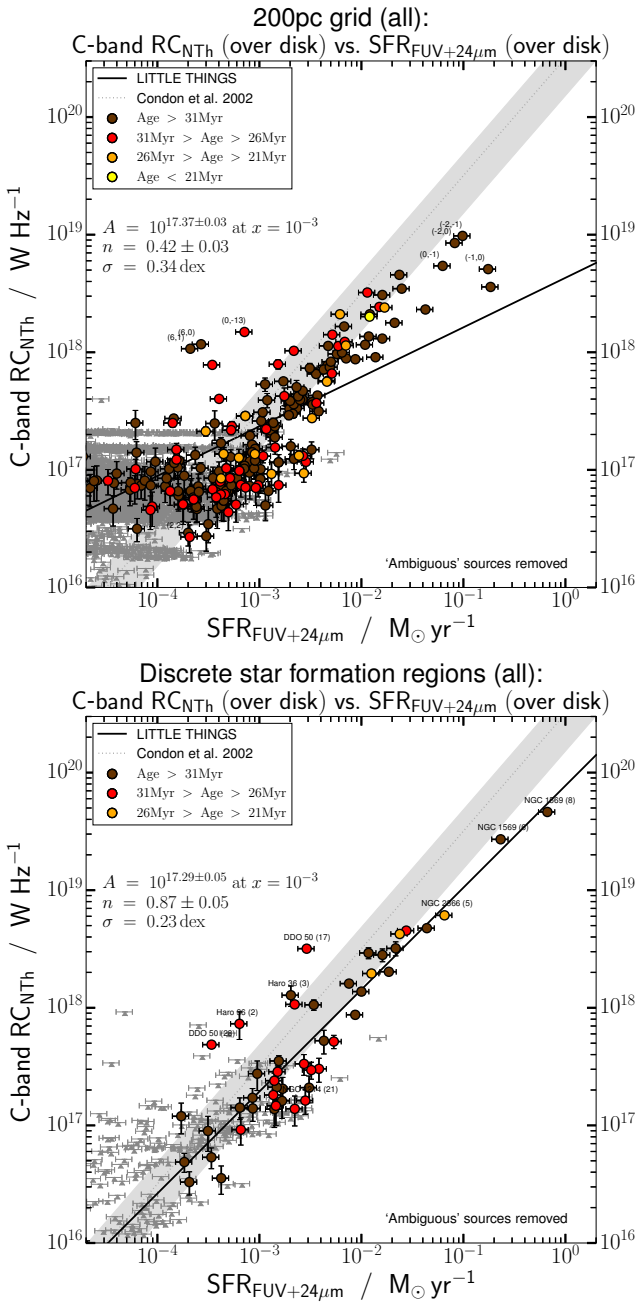

FIGURE 5.2: The resolved RC_{NTh}–SFR relation of all the galaxies using a grid of 200 pc square cells (top) and discrete SF complexes (bottom) coloured by the time elapsed since the onset of SF. Both definite background sources and 'ambiguous sources have been removed. The solid line is the best-fit power law to the data points. We show the RC_{NTh}–SFR relation derived in Equation 5.1. The errors introduced by our conversion are reflected by the grey shaded band. Regions that exhibited less than $3\,\sigma$ RC emission are represented by grey stars.

TABLE 5.2: **RESOLVED EMISSION FROM 200 PC SQUARE CELLS**

(1) Name of galaxy; (2 & 3) Size (major and minor axes) and position angle (P.A) of optical disk (Hunter & Elmegreen, 2006); (4 & 5) Equatorial coordinates (J2000) of bottom-left corner of square cell; (6) RC flux density; (7) Hα flux; (8) *GALEX* FUV flux density; (9) *Spitzer* 70μm FIR flux density; (10) *Spitzer* 24μm FIR flux density; (11) *C*-band ($\sim$ 6 GHz) radio continuum non-thermal (synchrotron) flux density. All $\mathrm{RC_{NTh}}$ emission is assumed to be synchrotron and is measured after subtracting an inferred $\mathrm{RC_{Th}}$ component from the total RC (Deeg et al., 1997); (12) Equipartition magnetic field strength in the plane of the sky (see Equation 3 of Beck & Krause, 2005).

Galaxy	Size	P.A.	R.A.	Dec.	*C*-band RC	Hα	FUV	24μm MIR	70μm FIR	*C*-band $\mathrm{RC_{NTh}}$	$B_{\rm eq}$
	($'$)	($^\circ$)	hh mm ss.s	dd mm ss.s	(mJy)	(10^{-13} ergs s^{-1} cm^{-2})	(mJy)	(10^{-2} Jy)	(10^{-2} Jy)	(mJy)	(μG)
(1)	(2)	(3)	(4)	(5)	(6)	(7)	(8)	(9)	(10)	(11)	(12)
NGC 1569	2.3 × 1.3	−59	4 30 45.4	64 51 8.00	2.62 ± 0.05	11.05 ± 0.17	3.01 ± 0.06	9.94 ± 0.65	63.07 ± 0.41	1.57 ± 0.06	17
NGC 1569	2.3 × 1.3	−59	4 30 44.6	64 51 0.22	0.26 ± 0.02	1.99 ± 0.07	0.36 ± 0.02	0.68 ± 0.24	14.79 ± 0.24	0.07 ± 0.02	13
NGC 1569	2.3 × 1.3	−59	4 30 49.1	64 51 15.06	2.74 ± 0.06	13.61 ± 0.17	1.86 ± 0.04	10.90 ± 0.69	186.10 ± 0.69	1.44 ± 0.06	16
NGC 1569	2.3 × 1.3	−59	4 30 48.3	64 51 7.28	43.83 ± 0.07	253.00 ± 3.37	112.30 ± 3.77	247.60 ± 0.89	679.10 ± 0.82	19.79 ± 0.33	28
NGC 1569	2.3 × 1.3	−59	4 30 47.6	64 50 59.50	37.12 ± 0.07	225.70 ± 3.37	99.11 ± 3.14	229.20 ± 0.89	659.80 ± 0.87	15.70 ± 0.33	27
NGC 1569	2.3 × 1.3	−59	4 30 46.9	64 50 51.72	2.44 ± 0.06	11.92 ± 0.15	2.82 ± 0.06	9.50 ± 0.69	164.20 ± 0.68	1.30 ± 0.06	16
NGC 1569	2.3 × 1.3	−59	4 30 51.3	64 51 6.56	2.78 ± 0.06	11.83 ± 0.15	2.71 ± 0.06	8.55 ± 0.69	140.20 ± 0.69	1.66 ± 0.06	17
NGC 1569	2.3 × 1.3	−59	4 30 50.5	64 50 58.78	32.82 ± 0.07	170.80 ± 1.98	40.10 ± 0.89	117.00 ± 0.89	549.90 ± 0.89	16.61 ± 0.20	27
NGC 1569	2.3 × 1.3	−59	4 30 49.8	64 50 51.00	14.87 ± 0.07	92.92 ± 0.97	31.47 ± 0.72	46.80 ± 0.89	350.20 ± 0.83	6.04 ± 0.12	21
NGC 1569	2.3 × 1.3	−59	4 30 49.1	64 50 43.22	2.79 ± 0.06	11.59 ± 0.14	1.89 ± 0.04	5.90 ± 0.69	110.30 ± 0.69	1.69 ± 0.06	17

To calibrate the $\mathrm{RC_{NTh}}$–SFR relation, it was assumed to take a power-law form

$$\frac{L_{\mathrm{NTh}}}{\mathrm{W\,Hz^{-1}}} = A\left(\frac{\mathrm{SFR}}{\mathrm{M_\odot\,yr^{-1}}}\right)^n \tag{5.3}$$

where A and n are free parameters obtained through a bivariate least-squares optimisation fit. Table 5.3 summarises the $\mathrm{RC_{NTh}}$–SFR fit parameters for each galaxy: the normalisation and gradient. The scatter is also included and the total number of data points that went towards the fitting procedure.

The galaxies were chosen based on the significant RC emission observed in Chapter 4, observed on scales ranging from 10s to 100s of pc (see RC–based masking technique in Section 4.3.3). Yet despite this, when examined on scales of 200 pc, the RC emission in many of the galaxies falls below the $3\,\sigma$ threshold within the 200 pc cells—Table 5.3 documents many galaxies that contain no 200 pc cells that yield a S/N of greater than 3 (column 5). This came down to the fact that these galaxies exhibited weak RC emission ($\sim$ 3–5σ) on small scales (10s of pc) which, when combined with the rest of the signal from the 200 pc cell, became diluted in the noise. With so few significant data points for most galaxies (see column 5), it was decided to study the sample as a whole rather than examine each galaxy individually.

When examining the sample as a whole, Figure 5.2 shows that, when observing the $\mathrm{RC_{NTh}}$–SFR relation on scales of X pc, a $\mathrm{RC_{NTh}}$ 'excess' is observed in regions of little SF activity (SFR $\lesssim 10^{-4}\,\mathrm{M_\odot\,yr^{-1}}$), where the excess ranges anywhere from a factor of 2 up to factors of 50 in the most extreme cases. This was a S/N ratio effect—these low SFR data points are close to the $3\,\sigma$ noise level and thus occupy an incomplete region of the $\mathrm{RC_{NTh}}$–SFR parameter space. The X pc cells containing a $\mathrm{RC_{NTh}}$ 'excess' may be the tips of the icebergs, i.e., there may be just as many regions deficient in RC but falling below the sensitivity limit.

Therefore, we have attempted to deal with this issue in the following way: an iterative approach was used to determine approximately above what minimum SFR activity the resolved $\mathrm{RC_{NTh}}$–SFR relation was valid. Firstly, the best-fit $\mathrm{RC_{NTh}}$–SFR relation parameters were determined for the whole data set. Then, the best-fit parameters were recalculated with the exclusion of data points closest to the noise level[4] (inclusion region is highlighted in light grey in Figure 5.3). New best-fit $\mathrm{RC_{NTh}}$–SFR parameters were calculated from the data points in this shaded region, and the

[4]This is done by drawing a perpendicular line to the best-fit $\mathrm{RC_{NTh}}$–SFR relation, and excluding those data points that fall below it (this parameter space below the perpendicular line is assumed to be the most incomplete).

TABLE 5.3: **THE BEST-FIT PARAMETERS FOR THE $\mathrm{RC_{NTh}}$–SFR RELATION FOR INDIVIDUAL GALAXIES USING 200 PC SQUARE CELLS**

(1) Name of galaxy; (2 & 3) Fit parameters for the $\mathrm{RC_{NTh}}$–SFR relation assuming the form $\log L_{6\mathrm{GHz}} = n \log(\mathrm{SFR}) + A$, where $L_{6\mathrm{GHz}}$ is the $\mathrm{RC_{NTh}}$ luminosity at 6 GHz in $\mathrm{W\,Hz^{-1}}$ and SFR is in units of $\mathrm{M_\odot\,yr^{-1}}$ (see Equation 5.3); (4) Scatter of the $\mathrm{RC_{NTh}}$–SFR relation; (5) Number of 200 pc cells that exhibited significant RC emission. The relation was not parameterised for those galaxies that exhibited too few significant data points.

Galaxy	$\mathrm{RC_{NTh}}$ Luminosity–SFR Relation			Number
	A	n	σ	N
(1)	(2)	(3)	(4)	(5)
DDO 43	...	...	...	0
DDO 46	...	...	...	0
DDO 47	...	...	...	0
DDO 50	18.4 ± 0.4	0.32 ± 0.10	0.28	28
DDO 53	...	...	...	3
DDO 63	16.5 ± 0.1	-0.06 ± 0.03	0.04	5
DDO 69	...	...	...	0
DDO 70	16.7 ± 0.4	0.05 ± 0.08	0.12	5
DDO 75	...	...	...	3
DDO 126	...	...	...	4
DDO 133	...	...	...	1
DDO 155	...	...	...	0
DDO 168	...	...	...	3
DDO 210	...	...	...	0
Haro 29	18.2 ± 0.8	0.17 ± 0.20	0.43	5
Haro 36	...	...	...	3
IC 1613	...	...	...	0
IC 10	...	...	...	0
Mrk 178	...	...	...	0
NGC 1569	19.7 ± 0.1	0.85 ± 0.04	0.15	66
NGC 2366	19.0 ± 0.3	0.63 ± 0.10	0.23	20
NGC 3738	18.4 ± 0.3	0.26 ± 0.11	0.16	9
NGC 4214	18.0 ± 0.2	0.23 ± 0.06	0.34	49
Sag DIG	...	...	...	0
UGC 8508	...	...	...	0
VIIZw 403	18.3 ± 0.6	0.41 ± 0.18	0.16	22
WLM	...	...	...	3

iterative process continued. When the best-fit parameters converged for consecutive iterations, the $\mathrm{RC_{NTh}}$–SFR relation was then assumed to be valid for that highlighted region. This iterative process is illustrated in Figure 5.3 and the results are summarised in Table 5.4.

When observing the $\mathrm{RC_{NTh}}$–SFR relation using discrete SF complexes, this $\mathrm{RC_{NTh}}$ 'excess' at low SFR is absent; this is because each discrete SF region a) is centred on a

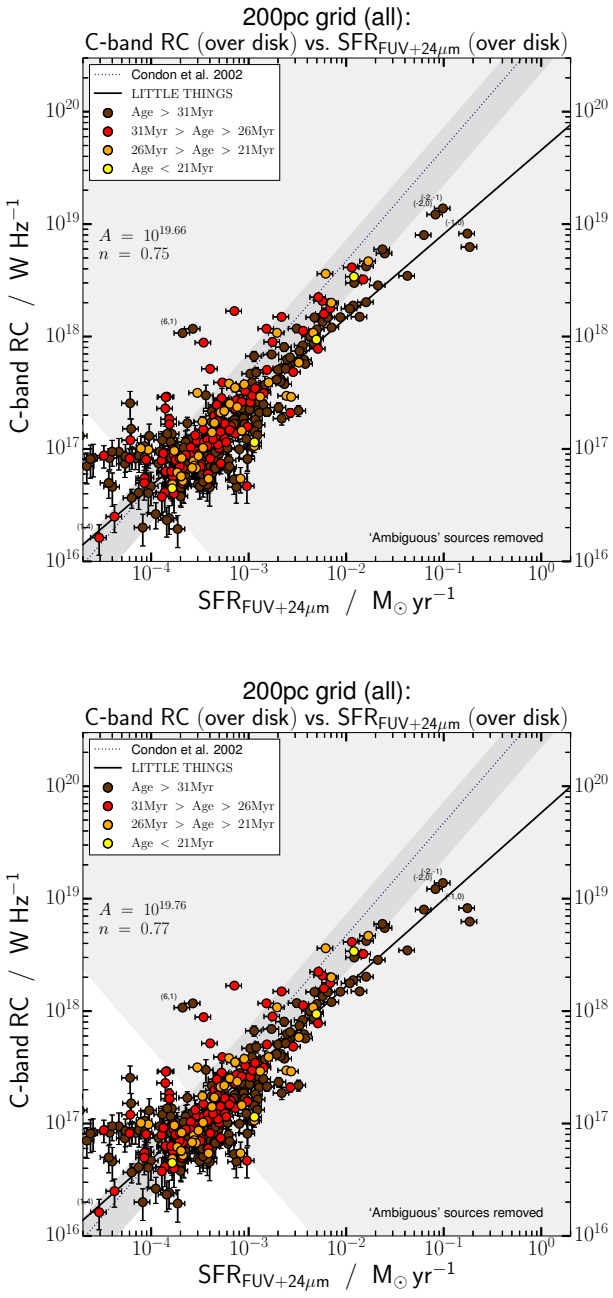

FIGURE 5.3: Iterative process to find where the best-fit parameters for the $\mathrm{RC_{NTh}}$–SFR converge. With each consecutive iteration (moving from top to bottom), the cells with the lowest SFR are removed from the fitting process (illustrated by the light grey shaded region). In each iteration, only data points within the light grey shaded region contribute to the fitting procedure. Eventually, the effects of the RC excess at low SFR is removed and the best-fit parameters (normalisation and gradient) converge to a stable value. As it is just the iterative process that is being highlighted, the numerous upper-limits have not been plotted for clarity.

region of significant Hα emission and so is biased to containing good RC signal, and b) covers a relatively large area making the S/N ratio low.

Table 5.4 summarises the $\mathrm{RC_{NTh}}$–SFR relation on scales of 200 pc, 300 pc, 500 pc,

and 700 pc; however, since these best-fit parameters were ascertained through the iterative process, they are only valid for regions with a SFR greater than $\mathrm{SFR}_{\mathrm{min}}$ (stated in column 6). There is some indication that the gradient becomes shallower as smaller scales are probed—this could be explained by CRe diffusion, which would be more apparent on smaller scales than on larger ones.

Table 5.4 also displays the $\mathrm{RC}_{\mathrm{NTh}}$–SFR relation for discrete SF complexes (which vary from sizes of a few 10s of pc up to 500 pc). Due to the superior S/N ratio yielded by this method, this relation is valid down to a SFR of $\sim 2 \times 10^{-4} \mathrm{M}_{\odot}\,\mathrm{yr}^{-1}$. Since the discrete SF regions probe active regions of SF, this is probably the most appropriate method with which to calibrate the $\mathrm{RC}_{\mathrm{NTh}}$–SFR relation. This relation can be inverted so that it may be used to infer the SFR from a $\mathrm{RC}_{\mathrm{NTh}}$ luminosity, and is

$$\frac{\mathrm{SFR}}{\mathrm{M}_{\odot}\,\mathrm{yr}^{-1}} = 1.36 \times 10^{-23} \left(\frac{L_{\mathrm{NTh}}}{\mathrm{W\,Hz}^{-1}} \right)^{1.15}. \tag{5.4}$$

To re-iterate, this $\mathrm{RC}_{\mathrm{NTh}}$ conversion factor is valid only for resolved regions forming stars at a rate of $\gtrsim 2 \times 10^{-4} \mathrm{M}_{\odot}\,\mathrm{yr}^{-1}$.

Intrinsic Scatter of $\mathrm{RC}_{\mathrm{NTh}}$-inferred SFR

The intrinsic scatter in SFR relations arises since the SF process itself is rapid, whereas the secondary effects (i.e., the observable emission) happen over a longer period and varies in intensity. When observing SF regions, SFR conversions become vulnerable to the time-varying intensity of emission, e.g., the behaviour of Hα and FUV emission following a burst of SF (see Figure 5.4). Despite the fact that emission at all times is caused by the same SF event, observers will view it at a random time t_{obs} and this random sampling of a time-varying signal gives an intrinsic uncertainty in SFR conversions. In the case of Hα (and thus $\mathrm{RC}_{\mathrm{Th}}$), Leroy et al. (2012) find the uncertainty to be 0.36 dex (once emission had fallen to 5% of the value at 1 Myr).

In a similar vein to Leroy et al. (2012), the intrinsic uncertainty in $\mathrm{RC}_{\mathrm{NTh}}$-inferred SFR was estimated by noting the observable $\mathrm{RC}_{\mathrm{NTh}}$ emission at random times between the SF event ($t = 0$) and a time t_{obs}. Leroy et al. (2012) used Starburst99 data, however there is no non–thermal information available from Starburst99, so we created a simple model using first principles—the aim is to model the $\mathrm{RC}_{\mathrm{NTh}}$ luminosity as a function of time.

We start with a Kroupa (2001) IMF, where the number of stars, N, within a stellar mass bin ranging from m to $m + \mathrm{d}m$ is described by $dN/dm \propto m^{-2.3}$ for stars with $M > 1 M_{\odot}$. A population of N stars is generated, while adhering to this stellar IMF

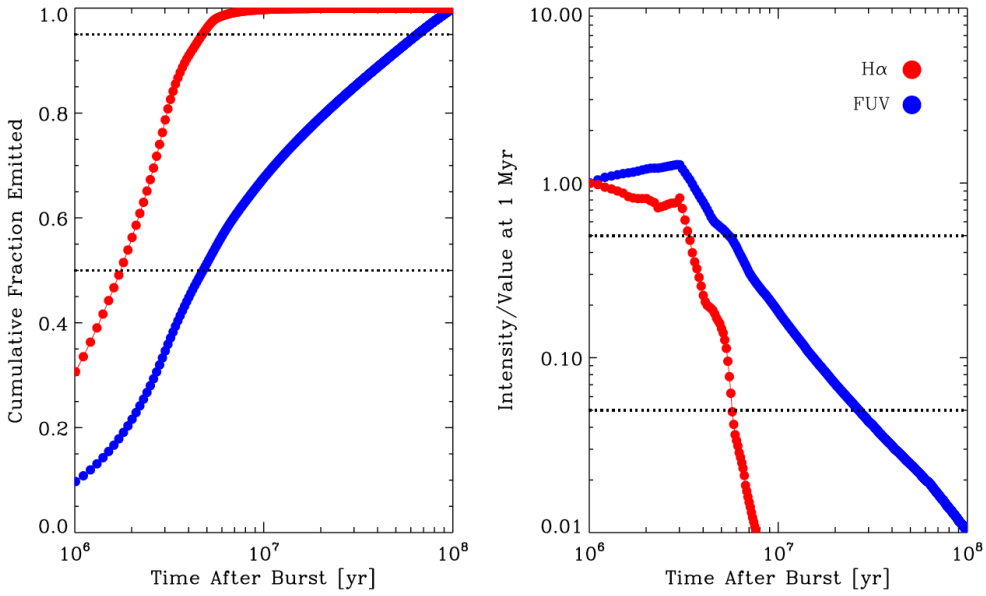

FIGURE 5.4: Behaviour of Hα (red) and FUV (blue) emission following a burst of SF (Leroy et al., 2012). The model was based on Starburst99 calculations assuming an instantaneous burst of star formation. As a function of time following the burst, the panels show cumulative emission (left) and intensity of emission compared to that at 1 Myr (right).

TABLE 5.4: **THE BEST-FIT PARAMETERS FOR THE $\mathrm{RC_{NTh}}$–SFR RELATION FOR THE SAMPLE AS A WHOLE AT VARIOUS SCALES**

(1) Scale of $\mathrm{RC_{NTh}}$–SFR relation; (2 & 3) Fit parameters for the $\mathrm{RC_{NTh}}$–SFR relation using N data points assuming the form $\log L_{6\mathrm{GHz}} = n \log(\mathrm{SFR}) + A$, where $L_{6\mathrm{GHz}}$ is the $\mathrm{RC_{NTh}}$ luminosity at 6 GHz in W Hz^{-1}, SFR is in units of $\mathrm{M_\odot\ yr^{-1}}$, and A is the normalisation with reference to a SFR of $1\ \mathrm{M_\odot\ yr^{-1}}$; (4) Scatter of the $\mathrm{RC_{NTh}}$–SFR relation; (5) Number of regions that exhibited significant RC emission. (6 & 7) The best fit parameters in columns 2 and 3 become invalid below a SFR of $\mathrm{SFR_{min}}$ ($\mathrm{M_\odot\ yr^{-1}}$) which is equivalent to a SFRD ($10^{-3}\mathrm{M_\odot\ yr^{-1}\ kpc^{-2}}$).

Scale	$\mathrm{RC_{NTh}}$ Luminosity–SFR Relation					
	n	A	σ	$N(>3\sigma)$	$\mathrm{SFR_{min}}$	$\Sigma_{\mathrm{SFR,min}}$
(1)	(2)	(3)	(4)	(5)	(6)	(7)
200 pc	0.65 ± 0.06	$2.19 \times 10^{19} \pm 39\%$	0.27	104	0.5×10^{-3}	0.013
300 pc	0.77 ± 0.05	$4.12 \times 10^{19} \pm 38\%$	0.26	100	0.3×10^{-3}	0.003
500 pc	0.85 ± 0.08	$6.46 \times 10^{19} \pm 56\%$	0.25	45	1.0×10^{-3}	0.004
700 pc	0.81 ± 0.08	$5.80 \times 10^{19} \pm 52\%$	0.24	41	1.0×10^{-3}	0.002
Discrete SF Regions	0.87 ± 0.05	$7.94 \times 10^{19} \pm 42\%$	0.23	48	0.2×10^{-3}	...

and entered into the simulation at random times between 0 and 10 Myr to approximate a burst of SF with an average SFR of $\sim 0.1\ \mathrm{M_\odot\ yr^{-1}}$. Since $\mathrm{RC_{NTh}}$ emission is only concerned with the high-mass tail of the IMF ($M > 8\,M_\odot$), only this section of the IMF is populated. The lifetime of a star with mass, M is:

$$\frac{t}{\mathrm{yr}} = t_\odot \left(\frac{M}{M_\odot}\right)^a, \tag{5.5}$$

and thus the stellar IMF can be converted into the rate of SNe production. It is the shocks from SNe that accelerate the CRe; alternatively, this can be interpreted as a

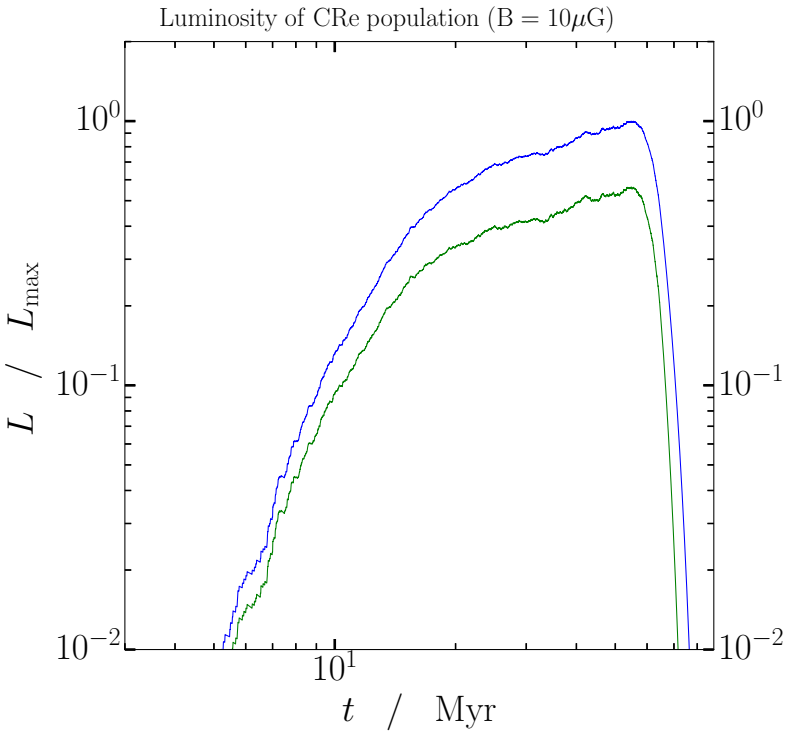

FIGURE 5.5: The intensity of $\mathrm{RC_{NTh}}$ emission relative to its maximum value which occurs at $\sim$ 55 Myr. This simulation was made to follow the evolution of $\mathrm{RC_{NTh}}$ emission, and was done through the following steps: 1) randomly populate Kroupa (2001) stellar IMF above $8\,M_\odot$ with 10000 stars; 2) calculate numbers of SNe expected in 10^4 yr time-bins after a burst of SF; 3) assume that the energy input per SN that goes into the population of CRe is independent of the mass of the supernova progenitor; 4) step through simulation in timesteps of 10^4 yr injecting new ensembles of CRe from new SNe, while ageing the whole population, until the emission becomes undetectable.

to further radiate some of their energy over the timestep of 10^4 yr. This process is repeated until the emission becomes undetectable.

The main caveat in this simulation is that the magnetic field strength is assumed to remain constant at $\sim 10\,\mu$G. In reality, the level of turbulence will decay with time leading to lower magnetic field strengths. Also, effectively, the simulation is carried out within a closed box, i.e, there is no CRe escape and the emission of all CRe is summed (i.e., it is an unresolved region, or a *calorimeter*). Over periods of 10s of Myr, CRe can diffuse out to ~ 1 kpc (see Section 1.3.3), and so this simulation is valid only for a region of ~ 1 kpc in size.

The result of this simulation is presented in Figure 5.5. The $\mathrm{RC_{NTh}}$ luminosity remains quite stable over the 60 Myr following the SF episode—only changing by a factor of ~ 2 between 15 and 55 Myr. The peak $\mathrm{RC_{NTh}}$ intensity occurs during the flurry of SN activity at around 55 Myr when the SNe rate is at its highest. After this, no new CRe are injected, and the population of CRe freely radiate, rapidly reducing

the emission.

To estimate the intrinsic uncertainty in $\mathrm{RC_{NTh}}$-inferred SFR, we attempt to make t_{obs} as similar as to what was done in Leroy et al. (2012) (the time at which emission had fallen to 5% of its value at $1\,\mathrm{Myr}$). Due to the nature of $\mathrm{RC_{NTh}}$ emission, there is no emission at $1\,\mathrm{Myr}$, so we use t_{obs} as the time taken for the $\mathrm{RC_{NTh}}$ luminosity to fall to 5% of L_{max} (corresponding to $t \sim 60\,\mathrm{Myr}$ in a magnetic field of $10\,\mu\mathrm{G}$). For comparison, Leroy et al. (2012) find t_{obs} to be $30\,\mathrm{Myr}$ for FUV and $6\,\mathrm{Myr}$ for Hα, which in itself highlights the promise of using $\mathrm{RC_{NTh}}$ as a SFR tracer as it lasts for such a long time.

By observing the $\mathrm{RC_{NTh}}$ emission at random times between $0\,\mathrm{Myr}$ and t_{obs}, we find that the intrinsic scatter is $0.16\,\mathrm{dex}$ (a factor of ~ 1.5). This means that, in addition to the uncertainties of the $\mathrm{RC_{NTh}}$–SFR conversion factors stated in Table 5.4, the intrinsic uncertainty also must be taken into account. It must be noted however that the intrinsic uncertainty of $0.16\,\mathrm{dex}$ is relevant to any *one* burst of SF—this uncertainty will decrease if multiple SF complexes are observed in the same region. As larger volumes of the galaxy are integrated, stochastic effects (e.g., the random initiation of a single SF event) become less important, leading to quantities tending towards the globally averaged value (e.g., see Equation 5.1 which states the galaxy-wide $\mathrm{RC_{NTh}}$–SFR relation inferred from Condon, 1992).

Observed Scatter of the Resolved $\mathrm{RC_{NTh}}$–SFR relation

The observed scatter of the resolved $\mathrm{RC_{NTh}}$–SFR relation can also be attributed to the mode of SF in the galaxy. To highlight this point, the $\mathrm{RC_{NTh}}$–SFR relation of DDO 50 and NGC 1569 are displayed in Figure 5.6 (see also tabulated parameters in Table 5.3).

The $\mathrm{RC_{NTh}}$–SFR relations of DDO 50 and NGC 1569 are quite distinct, especially when viewed in terms of the spread, having 0.28 and $0.15\,\mathrm{dex}$ scatter, respectively. This can be explained by their global behaviour, i.e., their mode of SF: NGC 1569 is going through a galaxy-wide star forming event, whereas DDO 50 has numerous star forming events that most probably started independently of one another and at different times. This is supported by the Hα morphologies of the two galaxies: NGC 1569 is dominated by pervasive emission on kpc scales while DDO 50 is limited to a small number of isolated pockets on scales of a few $100\,\mathrm{pc}$ (see Appendix C for resolved maps at multiple wavelengths).

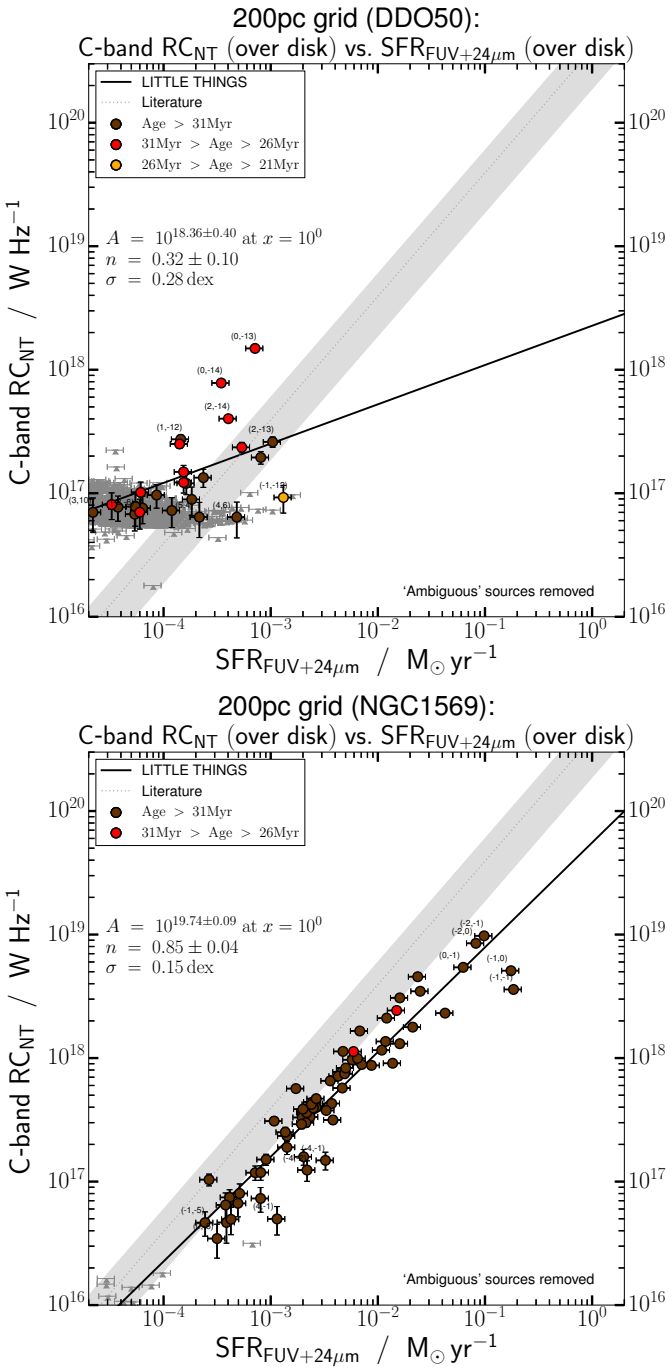

FIGURE 5.6: The resolved total RC_{NTh}–SFR relation of DDO 50 (top) and NGC 1569 (bottom) using a grid of 200 pc square cells. Both definite background sources and 'ambiguous sources have been removed. The solid line is the best-fit power law to the data points. We show the Condon (1992) RC_{NTh}–SFR relation from Equation 5.1. Regions that exhibited less than $3\,\sigma$ RC emission are represented by grey upper limits.

Regions Devoid of Current Star Formation Activity

In contrast to spiral galaxies where SF (and the associated RC) is present across the disk, SF in dwarf galaxies is more stochastic and so RC emission tends to appear

only where there happens to be a random instance of SF activity. The ISM by its very definition exhibits little SF and as such little RC, too, due to the lack of H II regions, relatively high escape fraction of CRe (e.g., Bell, 2003; Lacki et al., 2010) and weak magnetic field strengths across the disk (e.g., $2\,\mu$G according to Roychowdhury & Chengalur, 2012; $< 4.2\,\mu$G according to Chyży et al., 2011).

But one example of bright RC emission in the ISM is highlighted in Figure 5.7 (top). DDO 50 sports an extended structure of $\mathrm{RC_{NTh}}$ emission that is positioned between and to the west of two massive complexes of Hα separated by 500 pc. The ISM in this region may be being compressed (from the convergent pressure of the two SF regions) to the extent that magnetic fields become strong enough that CRe diffusing into it from the same SF regions emit significant $\mathrm{RC_{NTh}}$ emission. To investigate this, the distribution of gas (dominated by the atomic phase of hydrogen which can be traced through its 21 cm emission) is shown in Figure 5.7 (bottom). The extended $\mathrm{RC_{NTh}}$ emission marked in the bottom panel is coincident with high densities of hydrogen. Local compression of magnetic fields cannot be ruled out as a contributing factor to the $\mathrm{RC_{NTh}}$ emission; this phenomenon has been seen in M 51 where strong gas compression in the spiral shocks is put forward as the reason behind the step-up in RC intensity from the interarm regions to the arm regions (Fletcher et al., 2011).

In this respect, the RC on scales of a few 100 pc is not a perfect tracer of the location of SF, but rather hints that there are multiple sites of SF in the vicinity that are interacting. This breakdown in the spatial alignment of SF and RC could be confirmed by looking at the spectral index of the $\mathrm{RC_{NTh}}$—a steep value would indicate an aged CRe population hinting that they originated from a distant location.

Once kpc scales are investigated, this $\mathrm{RC_{NTh}}$ emission from the ISM becomes drowned out by the brighter emission from the SF regions themselves which, in the case of DDO 50, are located no further than about 500 pc away from the $\mathrm{RC_{NTh}}$ dominated ISM.

Properties of Magnetic Fields

To gain a first order handle of magnetic field strengths, equipartition of the magnetic field energy density and CRe on scales of ~ 200 pc was assumed (synthesised beam size of $\sim 12''$ at 3.5 Mpc). Resolved maps of $\mathrm{RC_{NTh}}$ surface brightness allowed the magnetic field to be estimated assuming a disk scale height of 400 pc (Banerjee et al., 2011). This provided resolved images of magnetic field strength (see DDO 50 and NGC 1569 for example in Figure 5.8).

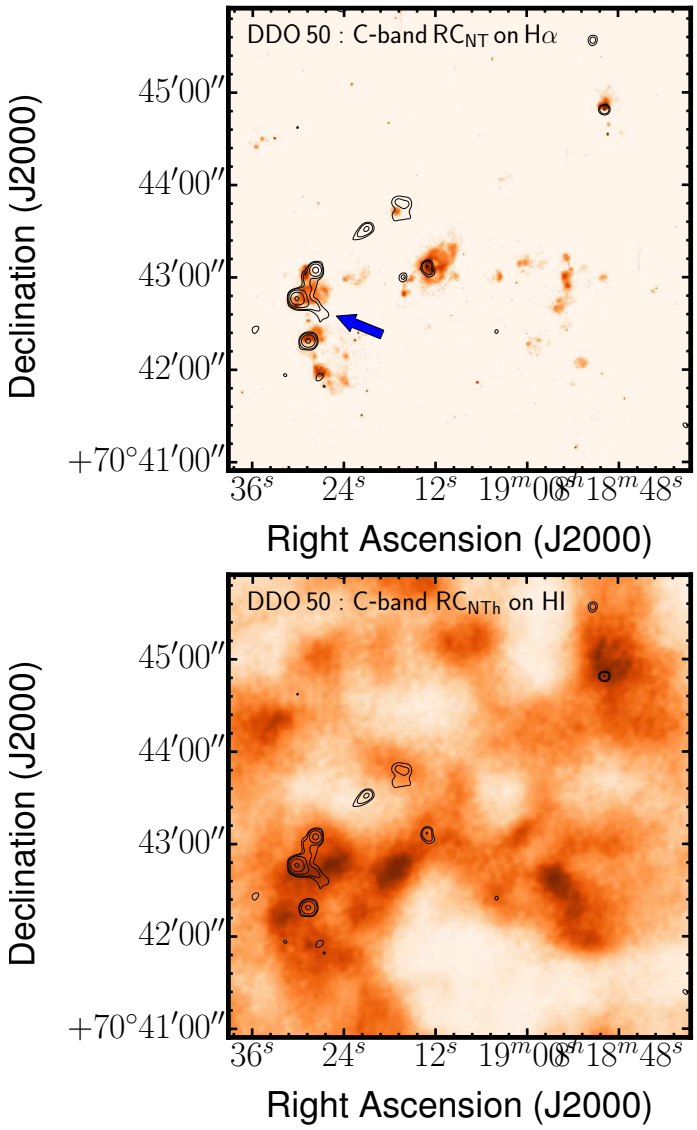

FIGURE 5.7: $\mathrm{RC_{NTh}}$ emission in the ISM of DDO 50. *Top:* Rare case of significant RC emission (marked by arrow) observed in the ISM. $\mathrm{RC_{NTh}}$ flux contours are shown overlaid on Hα emission. This case shows strong $\mathrm{RC_{NTh}}$ emission between, and to the west of, two large Hα complexes. *Bottom:* $\mathrm{RC_{NTh}}$ emission overlaid on H I. The extended $\mathrm{RC_{NTh}}$ emission in the ISM (marked in the top panel) is coincident with high densities of Hydrogen. In both images, RC contours are shown at 17, 28, 61, 160, and 457 μJy beam^{-1}.

In dwarf galaxies, Chyży et al. (2011) show that, for their 7 detections, the magnetic field strength is related to the SFRD through:

$$B \propto \Sigma_{\mathrm{SFR}}^{0.25\pm0.06}. \tag{5.7}$$

Whether this is a direct or indirect correlation is open to debate. Chyży et al. (2011) ascribe a direct relation between B and SFR: they attribute the "presence of weak magnetic fields to low star formation", ruling out the notion of an inverse correlation, i.e., that weak magnetic fields would arise due to high rates of SF since the fields and

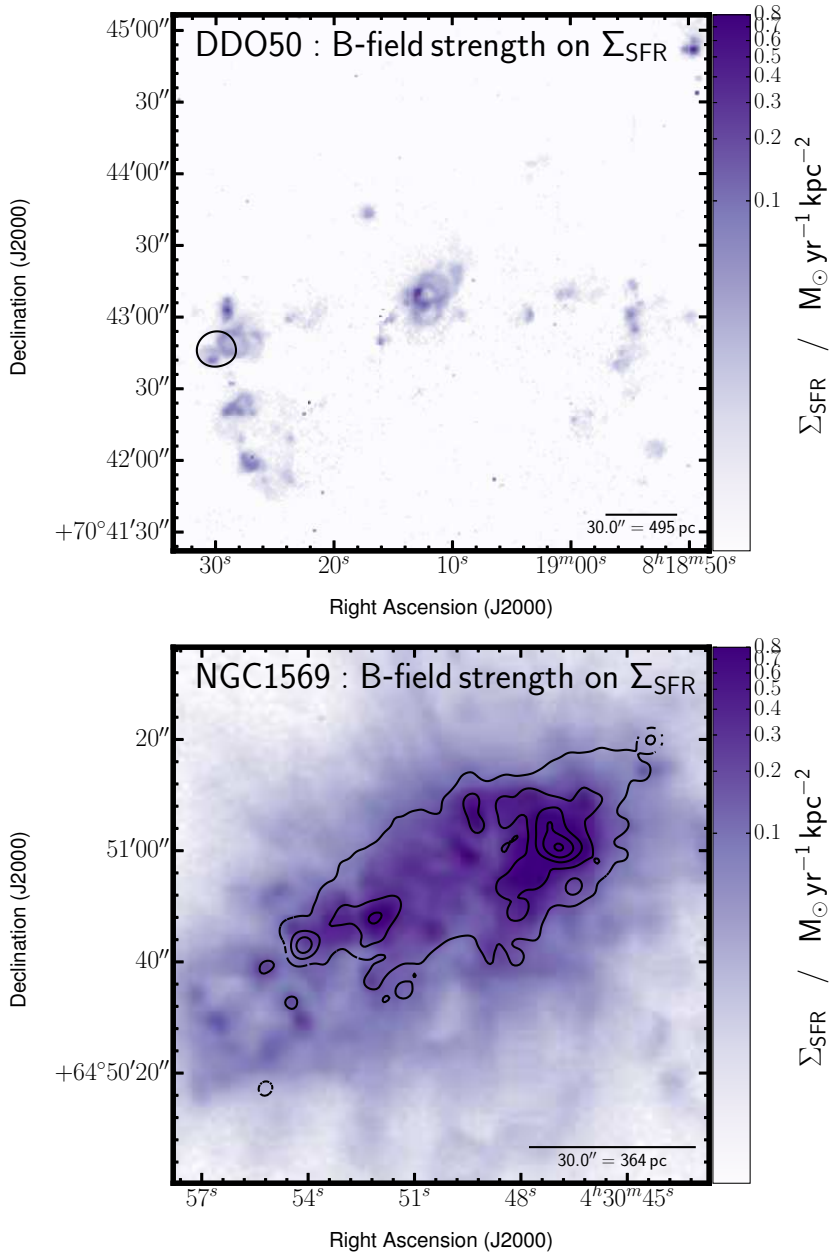

FIGURE 5.8: Contours of magnetic field strength in DDO 50 (top) and NGC 1569 (bottom) overlaid on SFRD. The magnetic field contours start at a level of 10 μG and increases in steps of 10 μG thereafter.

CRe may escape in galactic winds. Van Eck et al. (2015), however, adopt a different approach: they imply an indirect relation between B and SFR: they are both linked to the density of the gas. In the case of an ideal plasma, the magnetic field is frozen into the gas, and so higher gas densities lead to higher magnetic field strengths (see Equation 1 of Van Eck et al., 2015).

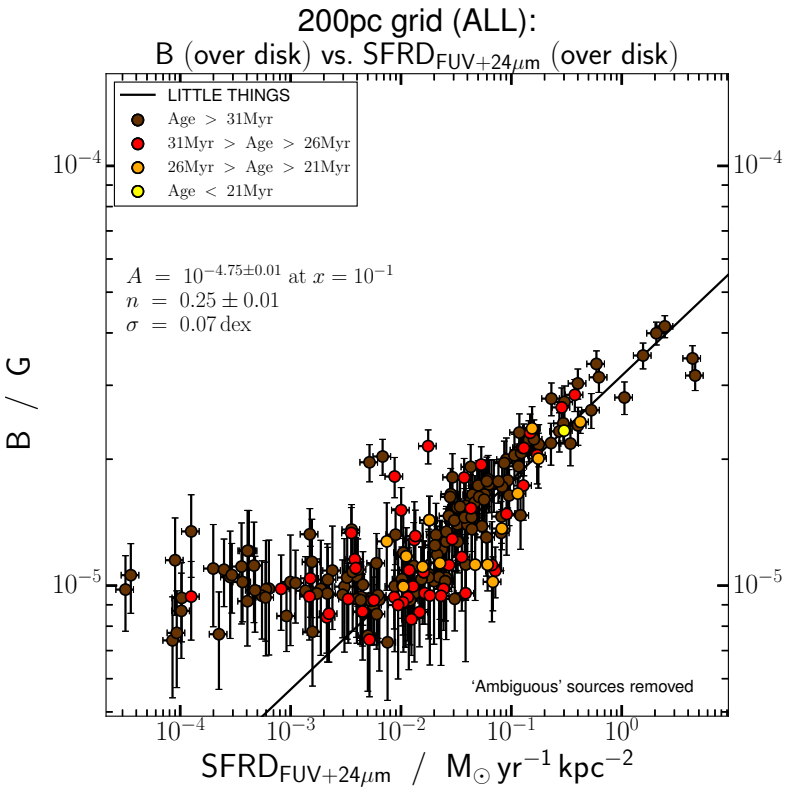

FIGURE 5.9: Magnetic field strength as a function of SFRD. All the galaxies are included, where each data point corresponds to a unique 200 pc square cell in the plane of the galaxy.

As previously discussed, the tendency to level-off at low SFRD observed in Figure 5.9 is most likely a S/N effect. Therefore, to err on the side of caution, if regions with SFRD $\lesssim 0.01\,\mathrm{M}_\odot\,\mathrm{yr}^{-1}\,\mathrm{kpc}^{-2}$ are excluded from the analysis, then the power law gradient of 0.25 ± 0.01 is consistent with that observed by Chyży et al. (2011).

Radial Profile of the Radio Continuum in Selected SF Complexes

Owing to the sporadic nature of SF in dwarf galaxies, the associated $\mathrm{RC_{NTh}}$ emission presents itself as isolated pockets of emission surrounded by an ISM void of emission. With this in mind, dwarf galaxies are ideal environments in which to study the behaviour of the CRe and associated $\mathrm{RC_{NTh}}$ emission belonging to an *individual* SF complex.

To investigate the behaviour of CRe and $\mathrm{RC_{NTh}}$ radial profiles of emission in individual, isolated SF complexes were made. There were a number of isolated SF regions that were sufficiently bright and resolved to allow a radial profile: DDO 50 (W), DDO 53 (N), NGC 1569 (main SF complex), NGC 2366 (main Hα complex), NGC 4214

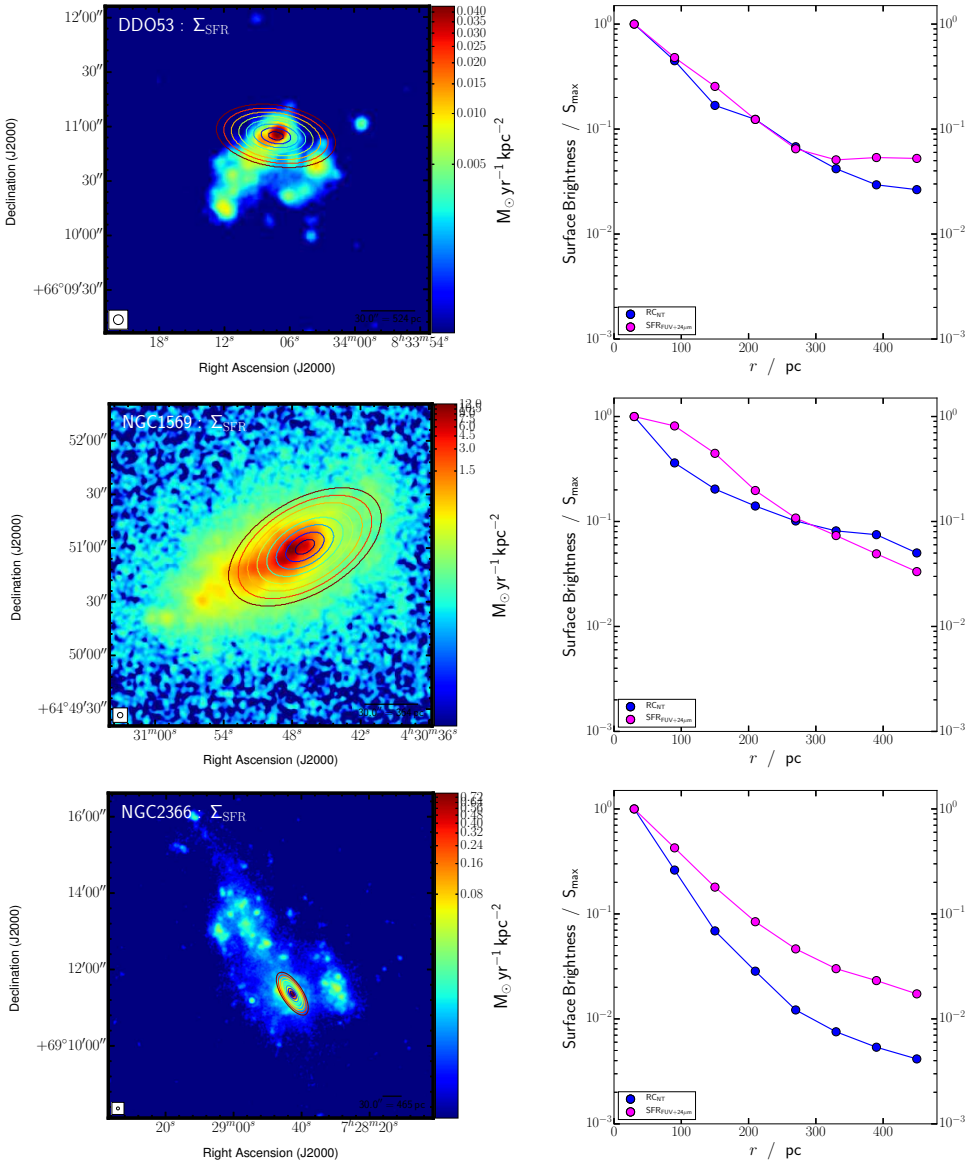

FIGURE 5.10: *Left:* Σ_{SFR} overlaid by 60 pc annuli centred on selected peaks of RC_{NTh} emission. *Right:* Radial profiles normalised to peak brightness were generated by integrating the SFRD and RC_{NTh} surface brightness in each annulus. To highlight the range of RC_{NTh} profiles observed, DDO 53, NGC 1569, and NGC 2366 are shown as examples.

(N and S). Figure 5.10 shows how the radial analysis was performed—concentric annuli were placed in the plane of the disk, in this case, around the peak of RC_{NTh} emission. Emission was then summed in each annulus and plotted. Annuli were aligned with the plane of the disk since no CRe halo is expected in dwarf galaxies, and with this little RC_{NTh} emission from 'above' or 'below' the disk; that is to say, we did not expect an isotropic distribution of RC_{NTh} emission around a SF region.

In the case of NGC 1569, the SFRD shows a declining profile while the RC_{NTh}

shows a flatter profile; the flatness may be caused by CRe diffusion. Contrast this with the case of NGC 2366's main SF complex, where the $\mathrm{RC_{NTh}}$ emission decreases at a faster rate than the SFRD, hinting at CRe escape. It is possible to discern the two CRe transport mechanisms: CRe escape would exhibit a relatively shallow $\mathrm{RC_{NTh}}$ spectral index (assuming that the escape time is shorter than the CRe lifetime) while the CRe diffusion would result in a steeper $\mathrm{RC_{NTh}}$ spectral index due to ageing of the CRe population. This distinction is important since the $\mathrm{RC_{NTh}}$ spectral index could then be used as a proxy for the age of a burst of SF (as will be seen in Section 6.3.2).

Importance of CRe lifetime in Calibrating the RC–SFR Relation

Longer CRe lifetime allows more time for individual CRe to escape the galaxy, which would then manifest itself as a reduction in the $\mathrm{RC_{NTh}}$ emitted. Therefore, it is important to know what fraction of the CRe are escaping to properly calibrate the $\mathrm{RC_{NTh}}$–SFR relation.

In a magnetic field of strength, B, a CRe will emit synchrotron emission at a frequency, ν if it has a Lorentz factor

$$\gamma = \left(\frac{2\pi m_e}{e}\right)^{1/2}\sqrt{\frac{\nu}{B}} \tag{5.8}$$

(Longair, 1981), where $(2\pi m_e/e)^{1/2} = 5.98\times10^{-6}\,\mathrm{kg^{1/2}\,C^{-1/2}}$. For example, a CR$e$ would require a Lorentz factor between 12000 and 17000 to emit at *C*-band in a magnetic field of 10 μG. The luminosity of a single CRe is heavily dependent on the CRe's Lorentz factor

$$L_{\mathrm{CRe}} = \frac{4}{3}\sigma_T c\frac{B^2}{2\mu_0}\gamma^2 \tag{5.9}$$

(Longair, 1981) and, when combined with Equation 5.8, means the Lorentz factor of a single CRe at $t = t_0$ evolves over a time interval, Δt, according to

$$\gamma(t_0+\Delta t) = \frac{1}{\frac{1}{\gamma(t_0)} + k_{\mathrm{CRe}}B^2\Delta t} \tag{5.10}$$

This step is shown in more detail in Section 6.3.2. After rearranging, this means that it takes a time

$$t = \frac{1}{k_{\mathrm{CRe}}B^2}\left(\frac{1}{\gamma(t_0)} - \frac{1}{\gamma(t)}\right) \tag{5.11}$$

for the CRe to reduce its Lorentz factor from $\gamma(t_0)$ to $\gamma(t)$, where $k_{\mathrm{CRe}} = 2\sigma_T/3m_e c\mu_0$ or $0.129\,\mathrm{s^3\,A^2\,kg^{-2}}$ (SI units). This is equivalent to the time taken for the CRe to go from emitting at a frequency ν_{high} to a frequency ν_{low}. Therefore, by merging equations 5.8 and 5.11, the CRe has an effective lifetime of:

$$t = \left(\frac{9m_e c^2\mu_0^2 e}{8\pi\sigma_T^2}\right)^{1/2} B^{-3/2}\times\left(\frac{1}{\sqrt{\nu_{\mathrm{high}}}} - \frac{1}{\sqrt{\nu_{\mathrm{low}}}}\right) \tag{5.12}$$

where $(9m_e c^2 \mu_0^2 e/8\pi\sigma_T^2)^{1/2} = 1.294 \times 10^6$ $\mathrm{kg^{3/2}\,C^{1/2}\,s^{-3}\,A^{-2}}$. For reference, the timescales yielded by Equation 6.8 are similar to those implied from Equation 2 of Heesen et al. (2009). At higher frequencies, the energy contained within CRe is radiated more quickly and so CRe have less time to diffuse or be advected into the extragalactic medium before they start emitting in a lower frequency band. For example, in a typical magnetic field strength of $10\,\mu$G, a CRe has a lifetime of 6 Myr at *C*-band (4–8 GHz), but 12 Myr at *L*-band (1–2 GHz).

With knowledge of the magnetic field strength, a resolved image can be made of the CRe lifetime (i.e., the timescale over which it can be observed in a given frequency band)—this is shown in Figure 5.11. If the local CRe lifetime (i.e., from Equation 6.8) is less than the local outflow timescale or diffusion timescale, then that CRe will emit all of its energy before it escapes—locally, this region would be a CRe *calorimeter*. This can be seen in Figure 5.11, where the CRe lifetime near sites of SF are shorter due to the higher levels of magnetic field turbulence, and thus these regions are locally more 'calorimetric' than the ISM.

In the case of NGC 1569, the CRe have a lifetime of under 1.6 Myr. For the gas to be ejected out of the plane of the galaxy (400 pc; Banerjee et al., 2011) before the CRe has time to emit all of its radiation at *C*-band, then the gas would need to be escaping the plane with a velocity of:

$$h_{\mathrm{scale}}/t_{\mathrm{CRe}} \sim 240\,\mathrm{km\,s^{-1}} \tag{5.13}$$

or greater where h_{scale} is the scale height of the galaxy (400 pc; Banerjee et al., 2011) and t_{CRe} is the CRe lifetime in a particular frequency band (Equation 6.8). A CRe bulk speed of $240\,\mathrm{km\,s^{-1}}$ is not unreasonable—for example, a disk wind speed of $300 \pm 30\mathrm{km\,s^{-1}}$ was measured in NGC 253 (Heesen et al., 2009). Emission line data would be needed to empirically ascertain the outflow speed, and if were found to exceed a speed of $240\,\mathrm{km\,s^{-1}}$, then the observed $\mathrm{RC_{NTh}}$ deficiency on a global scale could be attributed, at least in part, to the advection of gas.

The strong magnetic fields can act to confine the CRe long enough that they freely emit through all of *C*-band, whereas at *L*-band, it can be a different matter: CRe lifetimes are longer as the kinetic energy of CRe is lower and thus they emit radiation at a lower rate. This provides more time for galactic outflows to advect the CRe out before the CRe emitting in the 1–2 GHz band lose all their energy.

The deficiency of RC in the ISM of dwarf galaxies can be attributed to both weak magnetic fields and the low mass of the galaxy. The weaker magnetic fields do give CRe larger radii of gyration, but it is not this that leads to them escaping the galaxy: it is rather that the weaker magnetic fields give the CRe longer lifetimes, and thus

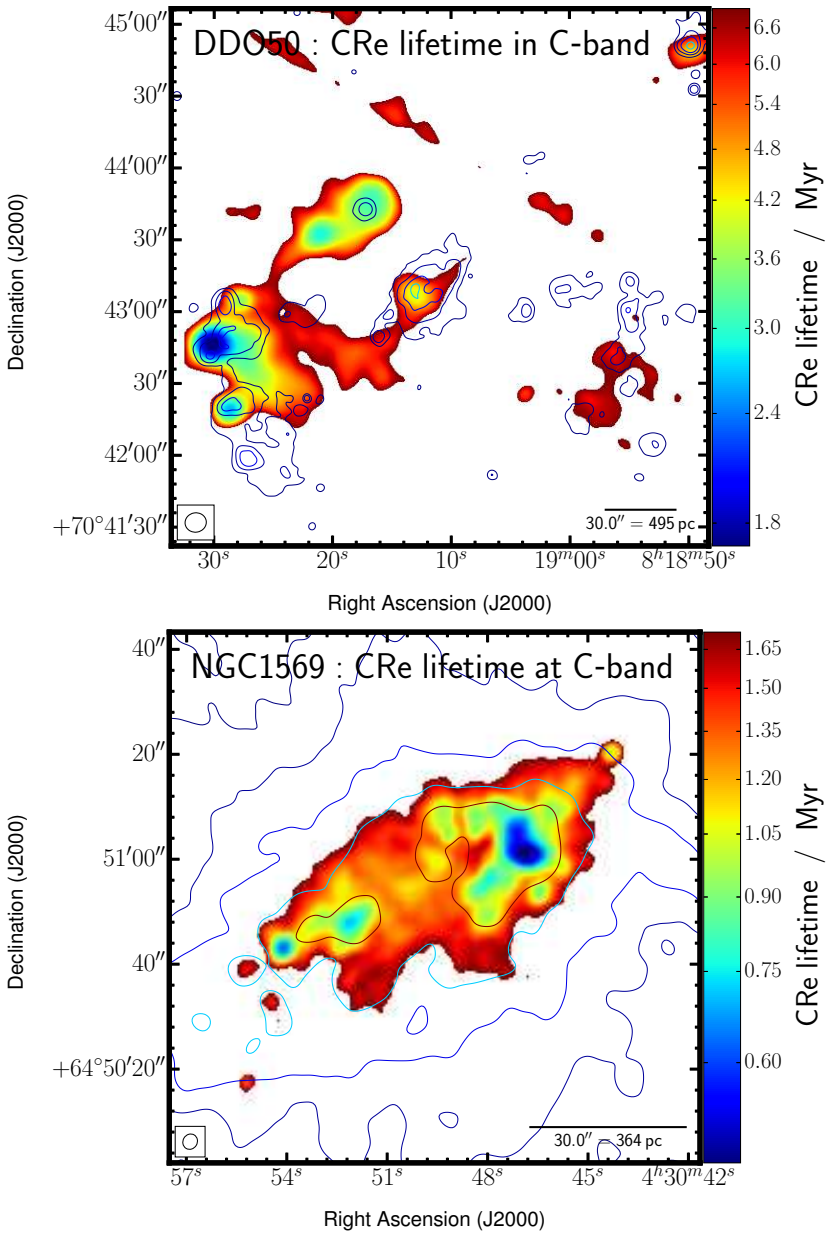

FIGURE 5.11: Given the local magnetic field strengths inferred from resolved maps of the RC_{NTh} surface brightness, an estimate of the CRe lifetime can be calculated. Examples are shown for DDO 50 (top) and NGC 1569 (bottom).

more time to be advected out of the galaxy with gas outflows, or diffuse. The low mass of dwarf galaxies make them more vulnerable to outflows.

5.5 Summary

On a resolved scale, dwarf galaxies show remarkable variation in their observed properties. Large-scale processes are thought to play a minimal role and so stochastic

effects dominate, and this introduces a large spread (due to random sampling of time domain) in characteristics. Nonetheless, using the $\mathrm{RC_{NTh}}$ to trace SF on a local scale has proven to be robust.

The results found in this chapter are summarised thus:

- Calibrating the resolved $\mathrm{RC_{NTh}}$–SFR relation was best done when using discrete SF regions. The calibration allows the SFR to be inferred from an observed $\mathrm{RC_{NTh}}$ luminosity, and takes the form:

$$\frac{\mathrm{SFR}}{\mathrm{M_\odot\,yr^{-1}}} = 1.36 \times 10^{-23} \left(\frac{L_{\mathrm{NTh}}}{\mathrm{W\,Hz^{-1}}} \right)^{1.15} \tag{5.14}$$

  with an uncertainty of $\pm 38\%$. This relation, however, was formulated based on *C*-band observations and is only valid for resolved regions forming stars at a rate $\gtrsim 2 \times 10^{-4} \mathrm{M_\odot\ yr^{-1}}$ (see Table 5.4). Despite the low flux densities of $\mathrm{RC_{NTh}}$ measurements, the $\mathrm{RC_{NTh}}$ still works well as a SFR tracer whereas Hα, which is largely dependent on stars with mass $\gtrsim 18\,\mathrm{M_\odot}$, and is thus dependent on the high mass tail of the stellar IMF, will suffer from stochasticity.

- The deficiency of RC in dwarf galaxies can be attributed to both weak magnetic fields and the low mass of the galaxy (see Section 5.4.1). Weaker magnetic fields give the CRe longer lifetimes, and thus more time to be advected out of the galaxy with the magnetic fields frozen into the gas in outflows, or diffuse.

6

Resolved Spectral Index in Dwarf Galaxies

6.1 Introduction

As mentioned in Chapter 5, the synchrotron component of the RC has the potential to serve as a SF tracer. The $\mathrm{RC_{NTh}}$ finds its origins in SNR whose progenitors are massive, short-lived stars. The supernova shock accelerates CRe to ultra–relativistic velocities, which then spiral around magnetic fields producing synchrotron radiation. CRe will typically last 10s of Myr after their initial acceleration, and an ensemble of CRe may diffuse or be advected out to around a kpc from the SF region of origin. Further details can be found in Section 1.3.3.

The spectral index of the $\mathrm{RC_{NTh}}$ emission, α_{NTh}, is defined through

$$\frac{L_1}{L_2} = \left(\frac{\nu_1}{\nu_2}\right)^{\alpha_{\mathrm{NTh}}} \tag{6.1}$$

where L_1 is the luminosity or flux observed at a frequency of ν_1, and L_2 is the luminosity or flux observed at a frequency of ν_2. It is an important property of the RC

since it defines the form of the RC spectrum, especially at low frequencies. The energy injection spectrum of CRe that are responsible for the $\mathrm{RC_{NTh}}$ emission follows a power law distribution. The $\mathrm{RC_{NTh}}$ spectral index steepens with time as the CRe population ages due to the energy-dependent luminosity of CRe; this is in stark contrast to the spectral index of the purely thermal, i.e., free-free emission, component, which is -0.1 and remains at this value throughout the lifetime of the H II region. The steepening of the $\mathrm{RC_{NTh}}$ spectral index has important consequences for inferring the time elapsed since the CRe were injected, i.e., steeper $\mathrm{RC_{NTh}}$ spectral indices are indicative of older populations of CRe, which must have come from SN events longer ago. The $\mathrm{RC_{NTh}}$ spectral index, α_{NTh}, can be grouped into three main categories: "young" ($\alpha_{\mathrm{NTh}} > -0.7$), "intermediate" ($-1.0 < \alpha_{\mathrm{NTh}} < -0.7$), and "old" ($\alpha_{\mathrm{NTh}} < -1.0$).

Inferring α_{NTh} from observations is hampered by the fact that the $\mathrm{RC_{NTh}}$ can be co-spatial with $\mathrm{RC_{Th}}$, which itself has a distinct spectral energy distribution and has an *a priori* unknown luminosity. There are indirect methods to ascertain the amount of $\mathrm{RC_{Th}}$ emission by scaling line emission (e.g., Hα or Pa-α), and then subtracting that from the total RC (e.g., Niklas & Beck, 1997; Murphy et al., 2011; Tabatabaei et al., 2013).

Studies of the spectral index on a resolved basis have been limited to bright, nearby dwarf galaxies, e.g., IC 10 (at *C*-band; Heesen et al., 2011, 2015), NGC 4214 (between *L*- and *X*-band; Kepley et al., 2011), and NGC 1569 (Lisenfeld et al., 2004; Kepley et al., 2010). Even then, with the exception of Heesen et al. (2015), it was the spectral index of *total* RC that was examined, which of course has contamination from the $\mathrm{RC_{Th}}$ component.

In this chapter, we expand on these case studies by examining the resolved spectral index in 4 dwarf galaxies: DDO 50, NGC 1569, NGC 2366, and NGC 4214, mainly focussing on the $\mathrm{RC_{NTh}}$. Our study uses more sensitive observations than previous studies, and extends from *L*-band (1–2 GHz; 30–15 cm) through to *Ku*-band (12–18 GHz; 2.5–1.7 cm). The aim is to calibrate the $\mathrm{RC_{NTh}}$ luminosity in conjunction with the $\mathrm{RC_{NTh}}$ spectral index to gauge information on the SF history over the previous 3–70 Myr.

6.2 Observations and Data Reduction

6.2.1 Sample

The LITTLE THINGS sample consists of 40 gas–rich dwarf galaxies all within 11 Mpc—further details of the sample can be found in Chapter 2. The brightest galaxies were observed to ensure that significant emission would be observed over the *whole* RC spectrum (1–18 GHz) on a *resolved* basis. The 4 dwarf galaxies chosen were: DDO 50, NGC 1569, NGC 2366, and NGC 4214. These galaxies all showed an integrated 6 GHz (5 cm) RC flux density between 8 and 150 mJy, and importantly, their emission was well resolved.

6.2.2 Observations

To sufficiently sample the RC spectrum, it was decided to acquire flux densities between *L*-band and *Ku*-band, yielding over ~ 1 dex coverage in frequency. Additionally, between *L*- and *Ku*-band, there is a good mix of $\mathrm{RC_{Th}}$ and $\mathrm{RC_{NTh}}$ making the spectral decomposition of the RC independent of optical data, such as Hα, possible.

Lower frequencies than *L*-band were avoided as, below this, the resolution of the VLA would become too low in comparison with the other bands. Higher frequencies than *Ku*-band were not attempted due to a combination of a significant decrease in receiver sensitivity and small primary beam.

The RC observations were taken with the NRAO VLA as part of project IDs 12A-234, 13B-041, and 14B-359 between March 2012 and March 2015. To sufficiently sample the RC spectrum, the galaxies were observed at *L*-, *S*-, *C*-, *X*-, and *Ku*-band—the instrumental setups are summarised in Table 6.1 and the bands that each galaxy was observed in are shown in Table 6.2.

All of the observations were taken using the 8-bit samplers. At *S*-, *C*-, *X*-, and *Ku*-band, this provided 2 GHz of bandwidth coverage. At these bands, the bandwidth was split into two IFs, each IF at full polarisation. Each IF held 8 spectral windows which, in turn, contained 64 channels of width 2 MHz. The centres of each IF were placed in such a way as to provide good in-band spectral coverage and to optimise coverage in the (*u*,*v*) plane. In the case of the *L*-band observations, the bandwidth was limited to 1 GHz; each IF held 8 spectral windows comprising 64 channels each, where each channel had instead a bandwidth of 1 MHz.

Archival Radio Continuum Observations

In order to supplement our own observations, some observations were taken from the VLA archive and processed. In particular:

- archival *Ku*-band observations of DDO 50 (project ID: 11B-032) were processed and then mosaicked with our own;
- to increase the spectral coverage of NGC 1569 as much as possible, an archived data set taken at *Ka*-band was processed to supplement our own observations (project ID: 11B-078);
- due to our lack of *L*-band data of NGC 4214, an archival data set was used (project ID: AK606), although the resolution and sensitivity was not optimal.

6.2.3 Calibration and Imaging

The data reduction and calibration of all bands was performed in much the same way as was done for the *C*-band observations (see Chapter 3 for details). In summary, the data were calibrated using CASA. The usual calibration steps were implemented by using one of four NRAO calibrators to calibrate the flux scale, and a nearby ($< 10°$) calibrator to correct the complex gain on timescales ranging from 5 minutes at *Ku*-band to 50 minutes at *L*-band. Both prior to and after calibration, visibilities were automatically flagged by `tflagdata(mode='tfcrop')` (Rau & Pramesh 2003) and `tflagdata(mode='rflag')` (based on AIPS; Greisen 2011) and then inspected by eye.

As a final step, flags were applied based on the rms of amplitudes in the cleanest spectral window—this proved very successful in removing low-level RFI in all spectral windows (see Section 3.5).

We generated images of our targets by means of CASA's `clean` algorithm, using the Multi–Scale, Multi–Frequency Synthesis (MS–MFS) algorithm as developed

TABLE 6.1: **INSTRUMENTAL SETUP OF THE VLA FOR PROJECTS RELATED THE RC SPECTRAL INDEX STUDY OF A SUB-SAMPLE OF THE LITTLE THINGS GALAXIES**

(1) Band; (2) VLA configuration; (3) Projects used to take observations; (4) Total bandwidth used within band (all 8-bit samplers); (5) The frequency at the centre of each of the two IFs; (6) The expected rms noise when natural weighting is used; (7) The largest angular scale to which the VLA is sensitive.

Band	Configuration	Project ID	Bandwidth (GHz)	IF Centres (GHz)	Sensitivity (μJy beam^{-1})	LAS ($'$)
(1)	(2)	(3)	(4)	(5)	(6)	(7)
L	B	13B-041; 14B-359	1.0	1.264 & 1.776	12.4	2.0
L	C	13B-041; 14B-359	1.0	1.264 & 1.776	15.2	16.2
S	B	14B-359	2.0	2.500 & 3.500	5.7	1.0
S	C	13B-041; 14B-359	2.0	2.500 & 3.500	5.8	8.2
C	C	12A-234	2.0	5.000 & 7.400	5.3	4.0
X	C	13B-041; 14B-359	2.0	8.500 & 9.500	4.5	2.4
Ku	D	13B-041	2.0	13.500 & 14.500	5.6	1.6

TABLE 6.2: **BANDS COVERED BY THE RC OBSERVATIONS FOR A SUB-SAMPLE OF THE LITTLE THINGS GALAXIES**

(1) Galaxy name; (2 & 3) B- and C-configuration observations at *L*-band; (4 & 5) B- and C-configuration observations at *S*-band; (6) C-configuration observation at *C*-band; (7) C-configuration observation at *X*-band; (8) D-configuration observation at *Ku*-band; (9) D-configuration observation at *Ka*-band.

Galaxy	*L*-band		*S*-band		*C*-band	*X*-band	*Ku*-band	*Ka*-band
	B	C	B	C	C	C	D	D
(1)	(2)	(3)	(4)	(5)	(6)	(7)	(8)	(9)
DDO 50	✔	✔	×	✔	✔	✔	✔	×
NGC 1569	✔	×	✔	×	✔	✔	×	✔
NGC 2366	✔	✔	×	✔	✔	✔	✔	×
NGC 4214	✔	✔	✔	✔	✔	✔	✔	×

by Rau & Cornwell (2011). To optimise the signal-to-noise ratio, a clean based on natural weighting of the visibilities was performed in all cases (which translates as `robust=+2.0` in CASA's `clean` algorithm).

In such faint, extended objects as dwarf galaxies, contamination from background sources is an important issue. Therefore, care was taken into removing obvious background sources (refer back to Section 4.3.2 for the methodology behind the exclusion of background sources).

6.2.4 Ancillary Data

This study pays special attention to the separation of the RC into its $\mathrm{RC_{Th}}$ and $\mathrm{RC_{NTh}}$ components through a spectral fit. In order to estimate the reliability of our $\mathrm{RC_{Th}}$ maps, we used ancillary Hα data which we then converted to an expected $\mathrm{RC_{Th}}$ map using the Hα–$\mathrm{RC_{Th}}$ conversion factor of Deeg et al. (1997):

$$\frac{\mathrm{RC_{Th}}}{\mathrm{W\,m^{-2}}} = 1.14 \times 10^{-25} \left(\frac{\nu}{\mathrm{GHz}}\right)^{-0.1} \times \left(\frac{T_e}{10^4\,\mathrm{K}}\right)^{0.34} \frac{\mathrm{F_{H\alpha}}}{\mathrm{ergs\,s^{-1}\,cm^{-2}}}. \quad (6.2)$$

The Hα line emission maps (see Hunter et al., 2012 for details) are continuum subtracted and the fluxes corrected for [NII] contribution. Hunter et al. (2012) used Burstein & Heiles (1982) values to correct the Hα flux for foreground reddening.

6.3 Results

6.3.1 Radio Continuum Images

The RC maps of the 4 dwarf galaxies are presented in Figures 6.1–6.4. For each galaxy, images taken between *L*- and *Ka*-band are shown at matched resolution and uniform scaling to ease comparison.

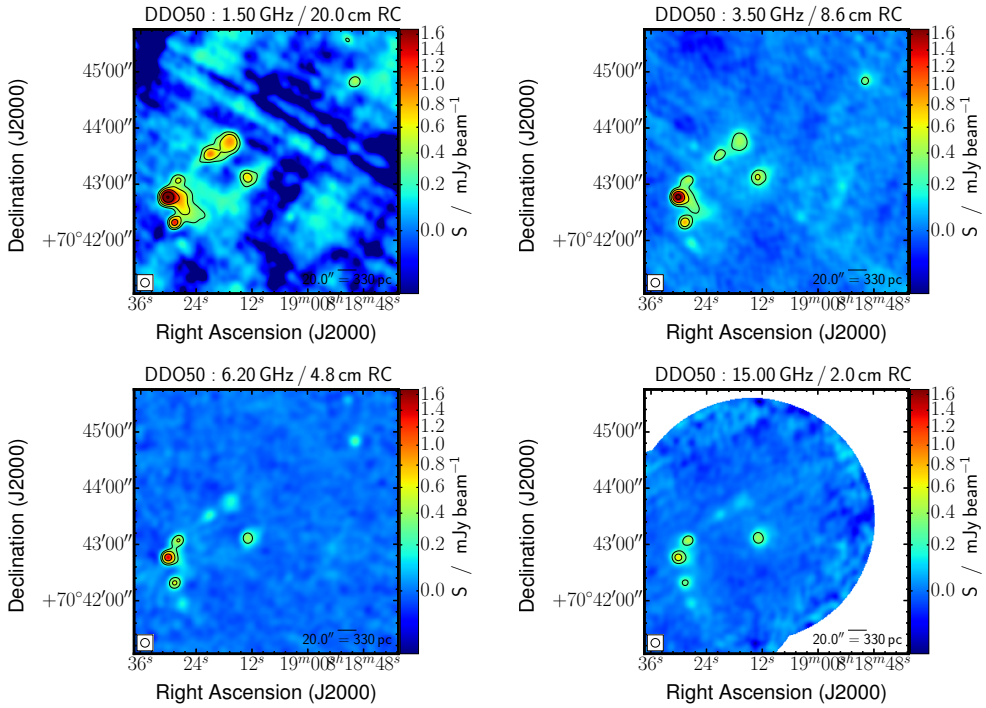

FIGURE 6.1: Radio continuum images of DDO 50 at *L*-, *S*-, *C*-, and *Ku*-band. In all images, the FWHM shown in the lower left is $\sim 10''$, the intensity has been scaled identically, and contours are shown at 0.25×2^n mJy beam^{-1} where $n \geq 0$. In the case of the *Ku*-band image, the blank areas represent regions of sky where the VLA sensitivity is below 50% of that in the centre of the field.

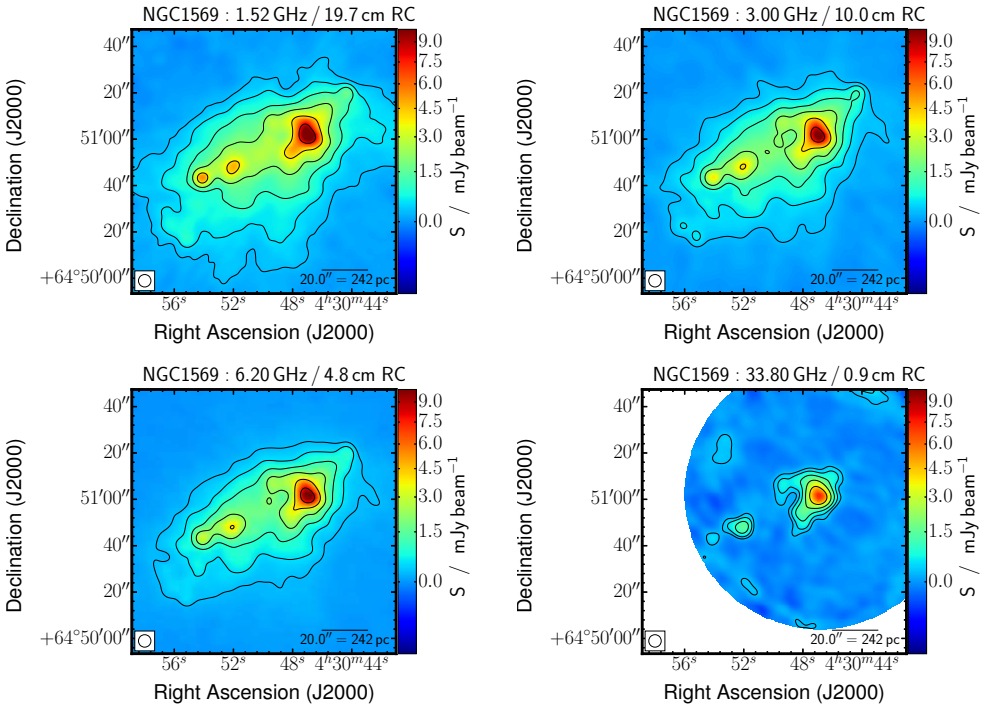

FIGURE 6.2: Radio continuum images of NGC 1569 at *L*-, *S*-, *C*-, and *Ka*-band. In all images, the FWHM shown in the lower left is $\sim 5''$, the intensity has been scaled identically, and contours are shown at 0.25×2^n mJy beam^{-1} where $n \geq 0$. In the case of the *Ka*-band image, the blank areas represent regions of sky where the VLA sensitivity is below 50% of that in the centre of the field.

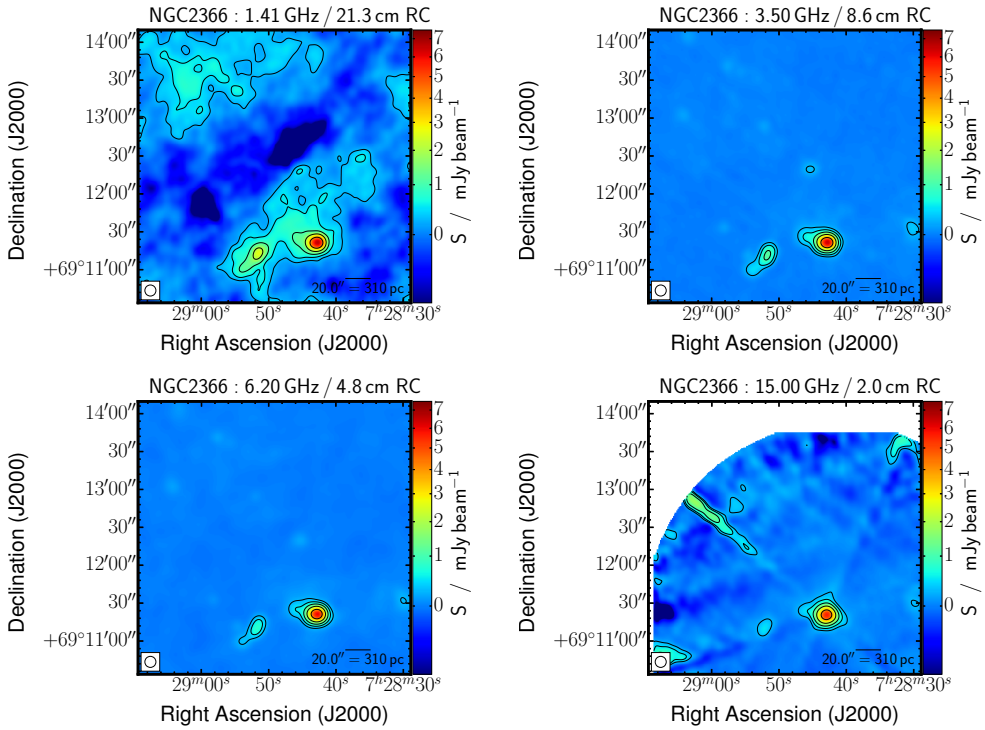

FIGURE 6.3: Radio continuum images of NGC 2366 at *L*-, *S*-, *C*-, and *Ku*-band. In all images, the FWHM shown in the lower left is $\sim 10''$, the intensity has been scaled identically, and contours are shown at 0.25×2^n mJy beam^{-1} where $n \geq 0$. In the case of the *Ku*-band image, the blank areas represent regions of sky where the VLA sensitivity is below 50% of that in the centre of the field.

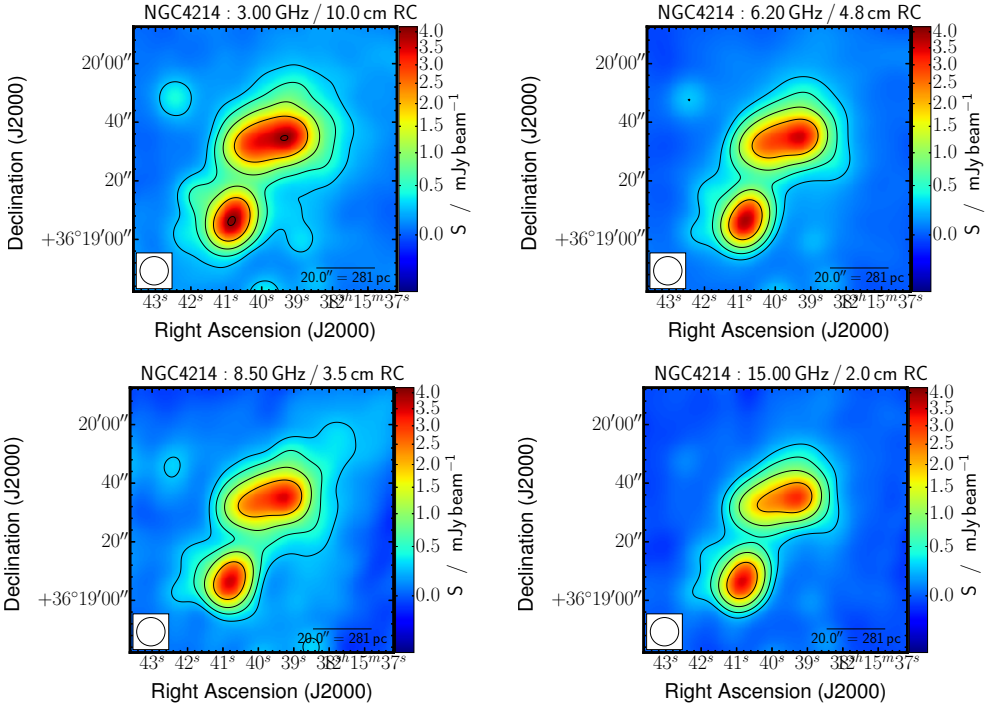

FIGURE 6.4: Radio continuum images of NGC 4214 at *S*-, *C*-, *X*-, and *Ku*-band. In all images, the FWHM shown in the lower left is $\sim 10''$, the intensity has been scaled identically, and contours are shown at 0.25×2^n mJy beam^{-1} where $n \geq 0$.

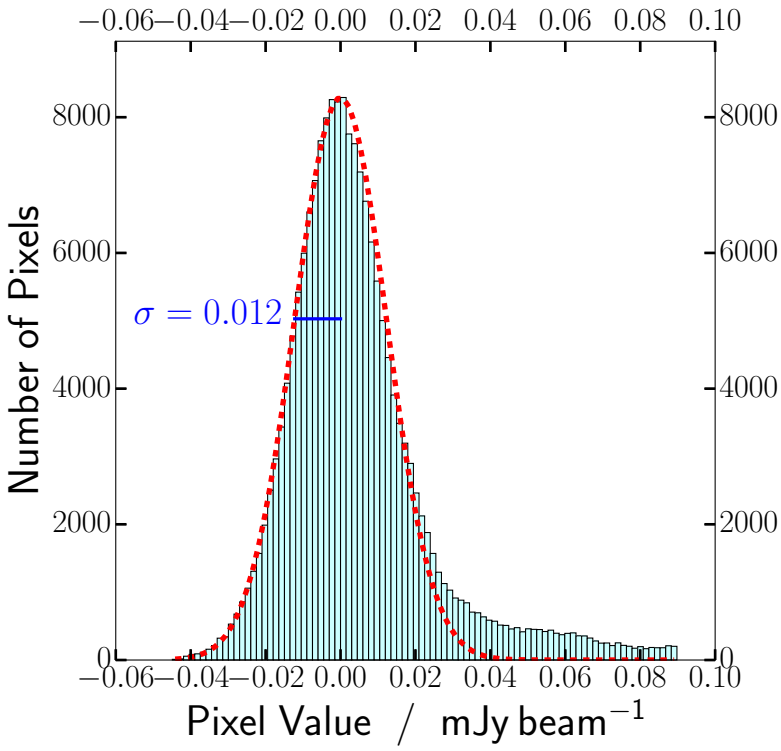

FIGURE 6.5: Histogram of pixel values from a RC image. A Gaussian was fitted to the histogram only for those pixels with a negative value (red thick-dashed line). From this Gaussian, the 1-σ noise level was determined which in this example was about 12μJy beam^{-1} (blue line). 'Genuine' emission presents itself as an excess above the red dashed line.

Due to using `robust=+2.0` (natural) weighting when generating the RC images, some low-level image artefacts show up in the general background that remained below the noise in the `robust=0.0` maps. Generally, to determine the background noise, a region devoid of emission is chosen while avoiding artefacts and the rms noise is inferred from that. But instead of this, a histogram of image pixels is plotted, and a Gaussian distribution fitted to the pixels of *negative* value. Figure 6.5 shows one such example—the noise presents itself as the Gaussian distribution centred around zero, and 'genuine' emission can be seen on the 'positive' side. This method allows the whole image to be used instead of a select region. In an image that consists of genuine emission and noise, negative values will only come from noise (assuming that all emission has been well modelled and there is no negative bowl resulting from extended emission which the interferometer was not able to register due to missing short spacings).

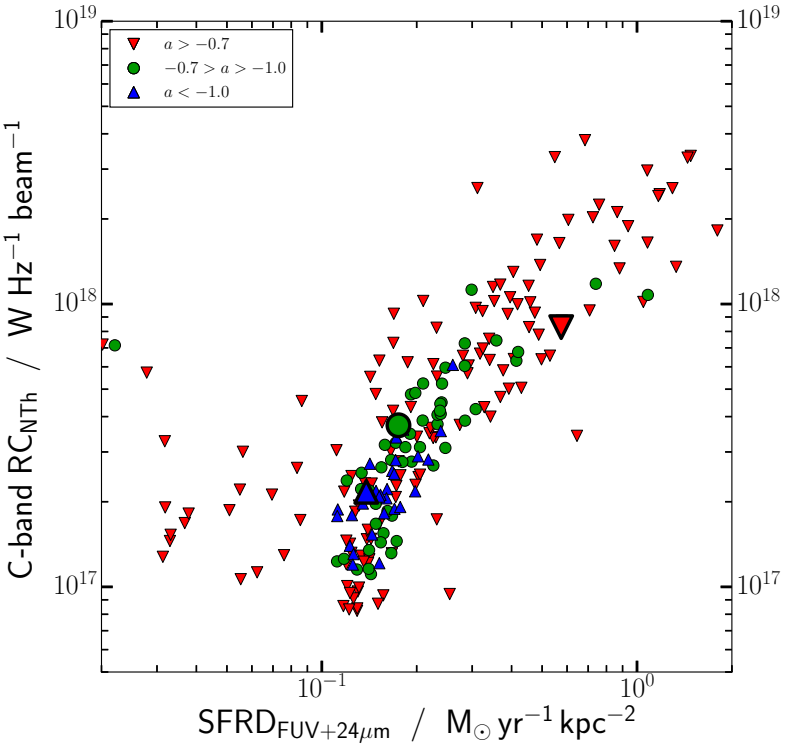

FIGURE 6.6: Total *C*-band $\mathrm{RC_{NTh}}$ as a function of the SFRD (Leroy et al., 2012). Points have been grouped into one of 3 spectral index bins—"young" ($\alpha_{\mathrm{NTh}} > -0.7$; red), "intermediate" ($-1.0 < \alpha_{\mathrm{NTh}} < -0.7$; green), and "old" ($\alpha_{\mathrm{NTh}} < -1.0$; blue)—calculated from within *C*-band (see Equation 1.14). Due to limitations of in-band sensitivity, this analysis has only been done on DDO 50, NGC 1569, NGC 2366, and NGC 4214. See Figures 3 and 6 from Heesen et al. (2014) for a similar analysis on scales of 700 and 1200 pc.

6.3.2 Radio Continuum Spectral Index

Regions of Relatively High SFR

Regions of high SFR activity ($\gtrsim 0.1\,\mathrm{M_\odot\,yr^{-1}\,kpc^{-2}}$) are radio dim with respect to the Condon et al. (2002) relation by a factor of 2 (refer back to Figure 5.2). Despite their dimness, these regions still harbour sufficient $\mathrm{RC_{NTh}}$ signal to allow the spectral index to be calculated. Since the spectral index holds information related to age, it has the potential to break the degeneracy between the $\mathrm{RC_{NTh}}$ luminosity at a time t following a SF event, and the intensity of said SF event.

Figure 6.6 shows a pixel-by-pixel plot of *C*-band $\mathrm{RC_{NTh}}$ surface brightness as a function of SFRD in the brightest galaxies (due to limitations of in-band sensitivity). Points have been grouped into one of 3 spectral index bins—"young" ($\alpha_{\mathrm{NTh}} > -0.7$; red), "intermediate" ($-1.0 < \alpha_{\mathrm{NTh}} < -0.7$; green), and "old" ($\alpha_{\mathrm{NTh}} < -1.0$; blue)—calculated from within *C*-band (see Equation 1.14).

Since the spectral index groups show considerable overlap, the average RC and

SFR has also been shown for each spectral index bin (larger symbols). These averages illustrate that shallow spectral indices ("young" CRe) are spatially coincident with those regions that are most actively forming stars. The steeper spectral indices ("old", or aged CRe) reside in regions with ~ 5 times lower $\mathrm{RC_{NTh}}$ luminosity and ~ 5 times lower SFR.

Timescale over which RC_{NTh} can be used as a Star Formation Rate Tracer

To examine the importance that time has on the $\mathrm{RC_{NTh}}$ and the spectral index, we implement a simple model to follow the evolution of CRe (and the associated $\mathrm{RC_{NTh}}$) as a function of time following a SF event (refer back to Section 5.4.1 and Figure 5.5). In brief, a population of stars was generated, adhering to the Kroupa (2001) stellar IMF. From this, a SN rate was calculated. The resulting SNRs were all assumed to last 10^4 yr, during which they transfer a proportion of their kinetic energy to CRe that follow a power law with a gradient of -2.7. The population of CRe are allowed to radiate some of their energy in a magnetic field of strength $10\,\mu$G, yielding the $\mathrm{RC_{NTh}}$ luminosity.

In this section, we will show that $\mathrm{RC_{NTh}}$ emission can be used as a SF tracer for approximately 5–70 Myr following a SF episode; in other words, observing $\mathrm{RC_{NTh}}$ emission implies that there has been SF in the last 5–70 Myr. This lower limit of 5 Myr for the time range stems from the fact that the SN rate takes a few Myr to reach appreciable levels following the burst of SF and so the associated $\mathrm{RC_{NTh}}$ emission also takes a similar time to become observable. The upper limit of 70 Myr was calculated by using the latest possible time for a SN progenitor to exist after a SF episode (~ 55 Myr for a star of mass $8\,\mathrm{M_\odot}$), and adding on to this the maximum possible time that CRe could exist following acceleration in a SNR. To calculate the maximum lifetime of a CRe, we started with the power radiated by an individual CRe, which can be expressed as:

$$\frac{d\gamma}{dt} = -k(B)\gamma^2. \tag{6.3}$$

(Longair, 1981), where γ is the Lorentz factor of the CRe, and t is the time available for radiating away the energy. Other variables have been grouped into the term $k(B) = 2\sigma_T B^2/(3m_e c\mu_0)$, where B is the magnetic field strength, σ_T the Thompson cross section, m_e the mass of an electron, c the speed of light, and μ_0 the permeability of free space. This implies that

$$\frac{d\gamma}{\gamma^2} = -k(B)\,dt \tag{6.4}$$

which when solved is

$$\frac{1}{\gamma} = k(B)t + C \tag{6.5}$$

where C is a constant of integration. When the CRe is injected at $t = t_0$, we designate its Lorentz factor as γ_0, which allows us to solve for C, giving

$$C = \frac{1}{\gamma_0} - k(B)t_0, \tag{6.6}$$

which can then be substituted back into Equation 6.5 yielding (rearranging)

$$\gamma = \frac{1}{\frac{1}{\gamma_0} + k(B)\Delta t}. \tag{6.7}$$

Here, $t - t_0$ has been replaced by Δt. Physically, this equation describes the final Lorentz factor, γ, of the CRe after a time interval, Δt, given that it started with an intial Lorentz factor, γ_0. The maximum time that it can take for a CRe to go from emitting at γ_0 to emitting at γ is as the initial Lorentz factor approaches infinity. With this, Δt can be approximated by

$$\Delta t = \frac{1}{k(B)\gamma_{\rm final}}. \tag{6.8}$$

For the CRe to end up emitting with a frequency of $4\,$GHz (the low end of *C*-band), this maximum lifetime is approximately $20\,$Myr in a magnetic field strength of 10μG. The CRe that last $20\,$Myr are the highest energy CRe of which there are few and so the associated $\mathrm{RC_{NTh}}$ emission is faint; therefore, even though $\mathrm{RC_{NTh}}$ emission is theoretically visible till about $20\,$Myr after the SN, sensitivity limitations reduce this observable window to about $15\,$Myr (as shown in Figure 5.5).

What this means for the $\mathrm{RC_{NTh}}$–SFR relation is that $\mathrm{RC_{NTh}}$ emission can be used as a SF tracer up to approximately $70\,$Myr following a SF episode; that is to say, detectable $\mathrm{RC_{NTh}}$ emission at *C*-band can not have originated from a SN that happened more than $15\,$Myr ago, and the progenitor of that SN can have a maximum age of $55\,$Myr.

Improving the Robustness of the RC_{NTh}–SFR Calibration

As with most SF tracers, there is a ubiquitous problem with the degeneracy between the strength of a SF episode, and the amount of resulting emission at a time following said SF episode. For instance, weak emission a long time after a strong SF episode may be justifiably interpreted as having come from a more recent, albeit weaker SF episode.

In the case of Leroy et al. (2012), they find that due to this degeneracy, estimates of the FUV-based SFR for *individual* SF regions have uncertainties of $0.44\,$dex, and from

the analysis in Chapter 5, estimates of $\mathrm{RC_{NTh}}$-based SFR for *individual* SF regions have uncertainties of 0.16 dex.

To improve the robustness of the $\mathrm{RC_{NTh}}$–SFR relation, implementing the $\mathrm{RC_{NTh}}$ spectral index as a second parameter is suggested to aid breaking this degeneracy. To do this, the same model outlined in Section 5.4.1 is used which follows how the $\mathrm{RC_{NTh}}$ luminosity evolves with time following a SF episode. This is illustrated in Figure 6.7, where points are coloured according to the $\mathrm{RC_{NTh}}$ spectral index between CRe emitting at 4 GHz and those emitting at 8 GHz.

Following the short burst of SF, the associated $\mathrm{RC_{NTh}}$ emission remains visible from about 5 Myr through to approximately 70 Myr. The peak $\mathrm{RC_{NTh}}$ intensity occurs during the flurry of SN activity at around 55 Myr when the SN rate is at its highest. The total $\mathrm{RC_{NTh}}$ luminosity remains quite constant over the 60 Myr following the SF episode, highlighting its potential to be used to infer the current SFR.

However, the model does not trace absolute luminosities, and so in its current form, it cannot be used to calibrate SFRs. The model can, however, view the evolution of the $\mathrm{RC_{NTh}}$ luminosity with respect to a *reference value*, which does allow it to follow the $\mathrm{RC_{NTh}}$ spectral index (in this case, the *C*-band spectral index). Between approximately 5 and 20 Myr, the $\mathrm{RC_{NTh}}$ spectral index steadily declines from approximately -0.4 to -0.7. This period allows the $\mathrm{RC_{NTh}}$ spectral index to be calibrated to infer the time elapsed, t, since a burst of SF, and is approximated by

$$\frac{t}{\mathrm{Myr}} = -25\alpha_{\mathrm{NTh}}. \tag{6.9}$$

From about 20–55 Myr, the $\mathrm{RC_{NTh}}$ spectral index then remains at a constant value of -0.8 until the last SN progenitors end their existence as SNe. During this period, the $\mathrm{RC_{NTh}}$ spectral index cannot be calibrated to infer the time elapsed since the burst of SF. From ~ 55 Myr onwards, no new CRe are injected and the spectral index steepens as the CRe age; the model implies that a $\mathrm{RC_{NTh}}$ spectral index steeper than -0.8 comes from CRe with an age greater than 55 Myr.

Figure 6.7 implies that less than a third of $\mathrm{RC_{NTh}}$-selected SF regions will exhibit a $\mathrm{RC_{NTh}}$ spectral index between -0.4 and -0.8, with the remaining regions showing a spectral index of -0.8. If a number of independent SF regions were to be taken together, then the emission-weighted spectral index would lie somewhere in between -0.7 and -0.8. This point may go some way to explaining why many galaxies, as a whole, exhibit a spectral index of about -0.7; that is to say, observing galaxies with a spectral index of approximately -0.7 may be the direct result of the steep spectral indices of -0.8 from older SF regions (20–55 Myr) dominating emission.

Note that the model, and Equation 6.9, are based on a constant magnetic field

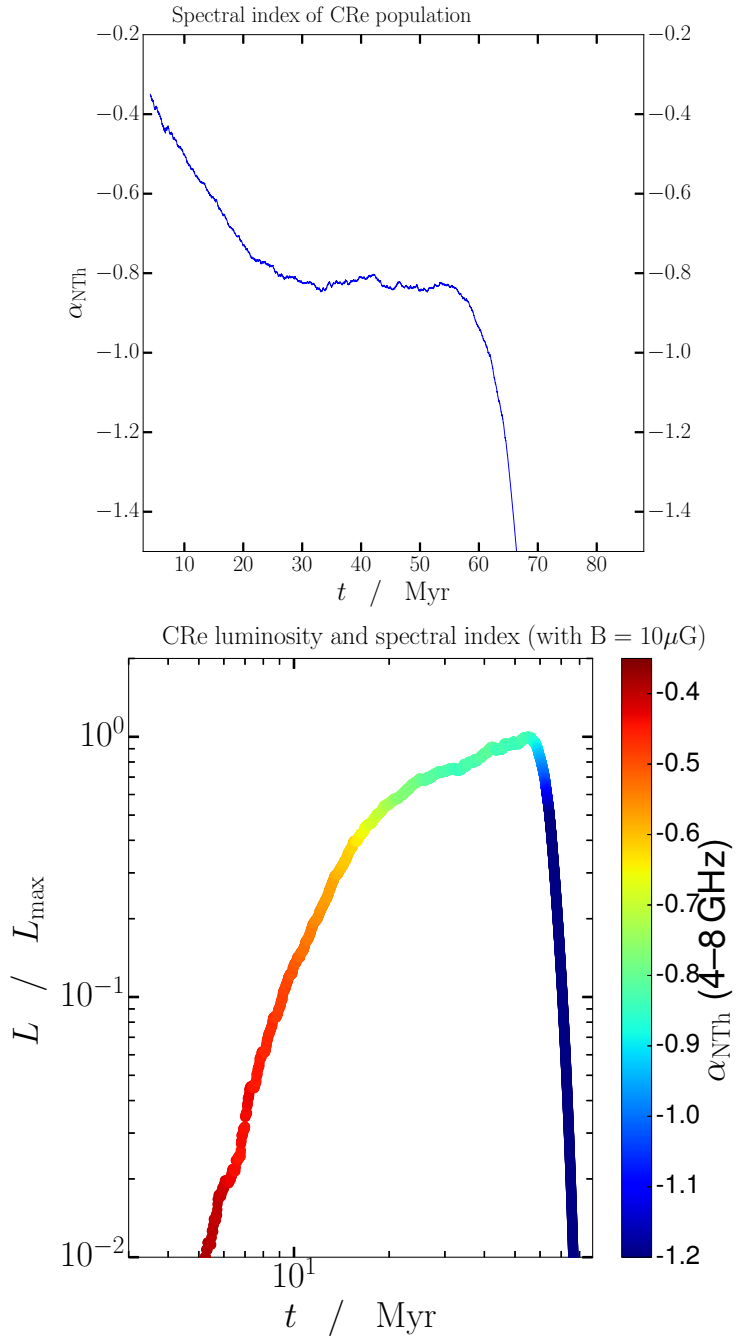

FIGURE 6.7: *Top:* Evolution of the $\mathrm{RC_{NTh}}$ spectral index: CRe injection initiates at $\sim$ 3.4 Myr, and then ceases at $\sim$ 55 Myr. This uses the same simulation as used in Figure 5.5, and the spectral index is calculated between 4 GHz and 8 GHz. *Bottom:* The luminosity of $\mathrm{RC_{NTh}}$ emission relative to a reference value (chosen as the maximum luminosity of CRe emitting at 4 GHz which occurs at $\sim$ 55 Myr). Points have been coloured according to the spectral index between CRe emitting at 4 GHz and those emitting at 8 GHz. This simulation was made using the same steps outlined in Figure 5.5.

strength of 10 μG for the first 20 Myr following the burst of SF.

Spectral Decomposition of the Radio Continuum

With multiple RC images observed at various frequencies and at matched resolution, the RC spectrum was sufficiently well sampled to allow a resolved decomposition into its $\mathrm{RC_{Th}}$ and $\mathrm{RC_{NTh}}$ components. The surface brightness of the galaxies was generally bright enough to allow the bands to be split into multiple sub-bands; this provided a greater number of spectral points, albeit with a slightly diminished S/N ratio. In general, 3 images were made in each band: one using the first IF, one using the second IF, and another using both IFs.

A pixel-by-pixel fit was made to the spectrum assuming that the surface brightness S at pixel (i,j) comprised a contribution from both a thermal and a non-thermal spectrum such that

$$\frac{S(i,j)}{\mathrm{Jy\,beam^{-1}}} = \frac{S_{\mathrm{Th}}(i,j)}{\mathrm{Jy\,beam^{-1}}}\left(\frac{\nu}{6\mathrm{GHz}}\right)^{-0.1} + \frac{S_{\mathrm{NTh}}(i,j)}{\mathrm{Jy\,beam^{-1}}}\left(\frac{\nu}{6\mathrm{GHz}}\right)^{\alpha_{\mathrm{NTh}}(i,j)}, \quad (6.10)$$

where the squares of the residuals were minimised to find which values of S_{Th}, S_{NTh}, and α_{NTh} best described the observed spectrum at each (i,j) pixel. In some cases, the noisy spectrum was best parameterised by a negative value of either $S_{\mathrm{Th}}(i,j)$ or $S_{\mathrm{NTh}}(i,j)$; but since this is not physical, the `lmfit` module as part of `python` was used due to its capability of allowing user-defined constraints—in this case, the fitted values of $S_{\mathrm{Th}}(i,j)$ or $S_{\mathrm{NTh}}(i,j)$ were not permitted to be less than 0. Only pixels where at least 4 spectral points had a S/N ratio greater than 5 were included in the resulting image; this was to ensure the resulting images were sufficiently reliable, whilst not limiting the fit to only small parts of the galaxy (i.e., the highest S/N regions). The spectral decomposition procedure allowed three images to be constructed:

- S_{Th}: a resolved picture of $\mathrm{RC_{Th}}$ emission (normalised at a reference frequency of 6 GHz);
- S_{NTh}: a resolved picture of $\mathrm{RC_{NTh}}$ emission (normalised at a reference frequency of 6 GHz);
- α_{NTh}: a resolved picture of the $\mathrm{RC_{NTh}}$ spectral index (which assumes a constant spectral index over the frequency range that the images cover).

along with the spectrum in any given pixel. These images and spectra are shown for each galaxy in Figures 6.8–6.11; they are completely independent of Hα scaling relations (e.g., the Hα-$\mathrm{RC_{Th}}$ scaling relation of Deeg et al., 1997).

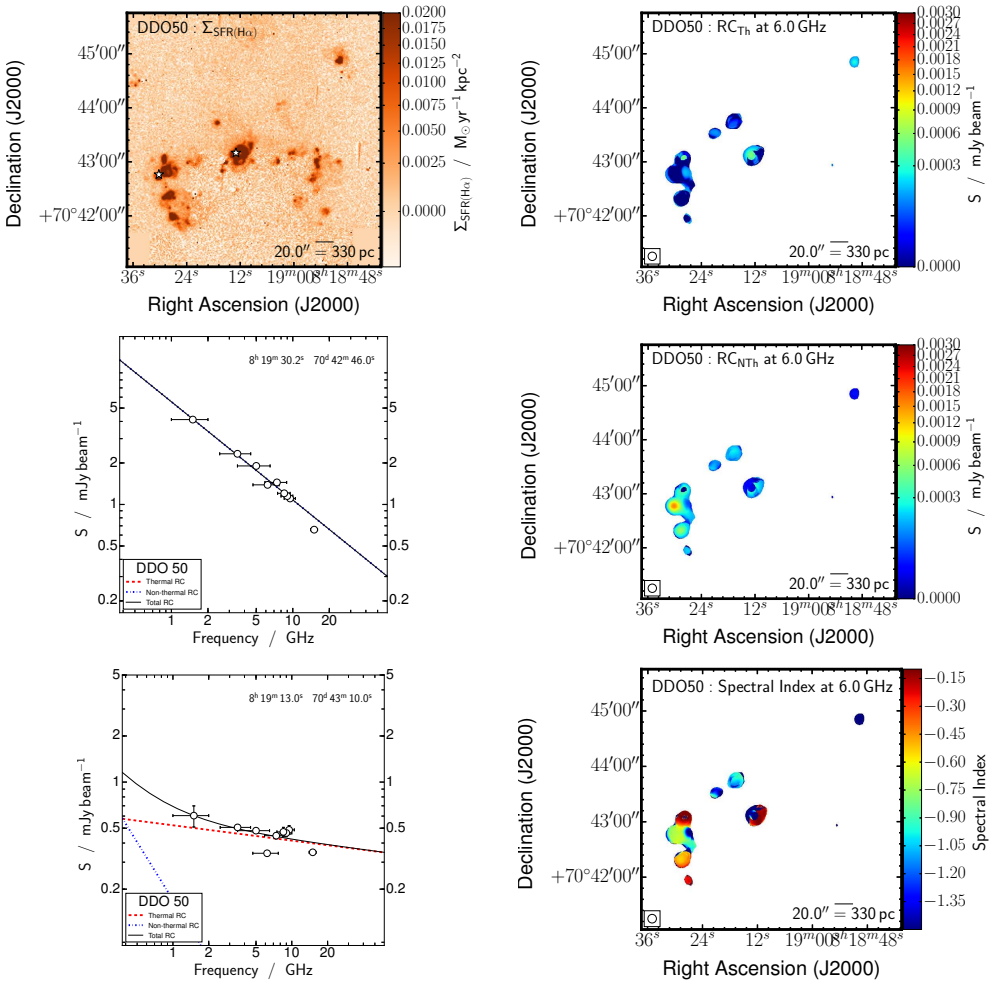

FIGURE 6.8: Hα image of DDO 50 (top-left) overlaid by star symbols marking two selected positions where the example spectra were taken (middle- and bottom-left). In fact, a single spectrum was made for every single (i, j) pixel—this allowed the construction of three images from the pixel-by-pixel fit to the spectral form described in Equation 6.10: $\mathrm{RC_{Th}}$(top-right), $\mathrm{RC_{NTh}}$ (middle-right), and spectral index of the $\mathrm{RC_{NTh}}$ (bottom-right). All of the data were used in the spectral decomposition.

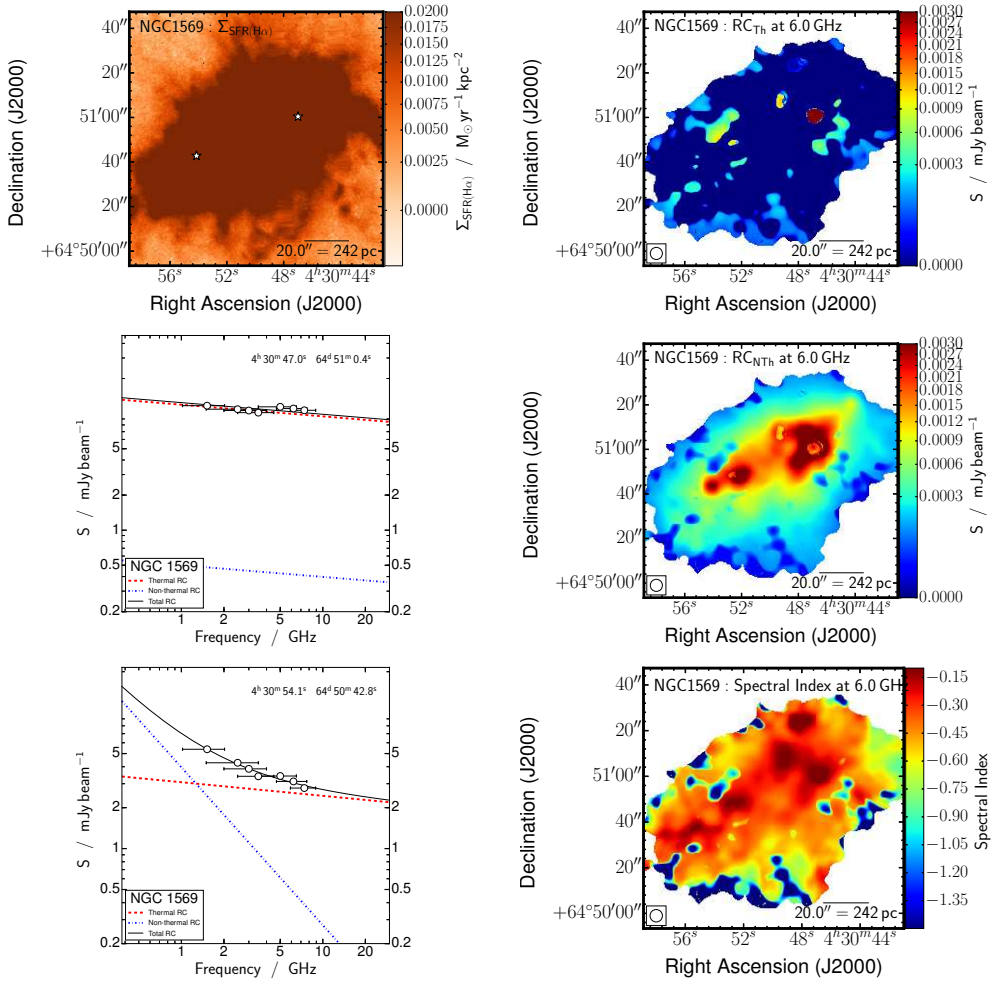

FIGURE 6.9: Hα image of NGC 1569 (top-left) overlaid by star symbols marking two selected positions where the example spectra were taken (middle- and bottom-left). In fact, a single spectrum was made for every single (i, j) pixel—this allowed the construction of three images from the pixel-by-pixel fit to the spectral form described in Equation 6.10: $\mathrm{RC_{Th}}$(top-right), $\mathrm{RC_{NTh}}$ (middle-right), and spectral index of the $\mathrm{RC_{NTh}}$ (bottom-right). Since *L*-band emission was observed on scales of 2′, it was decided to excise the *S*-band (B-configuration), *X*-band (C-configuration), and *Ku*-band (Dconfiguration) data from the spectral decomposition.

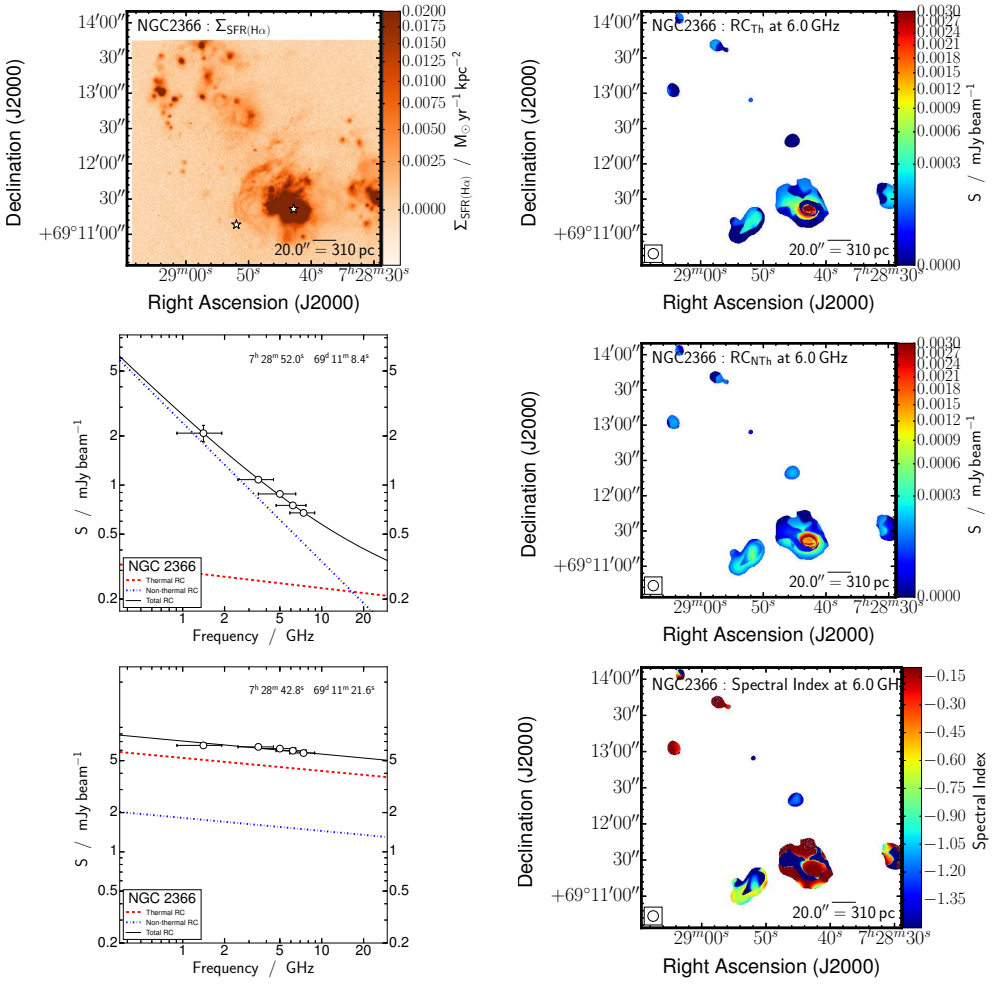

FIGURE 6.10: Hα image of NGC 2366 (top-left) overlaid by star symbols marking two selected positions where the example spectra were taken (middle- and bottom-left). In fact, a single spectrum was made for every single (i, j) pixel—this allowed the construction of three images from the pixel-by-pixel fit to the spectral form described in Equation 6.10: RC_{Th}(top-right), RC_{NTh} (middle-right), and spectral index of the RC_{NTh} (bottom-right). To avoid the possibility of missing large scale emission, the *X*-band (C-configuration) and *Ku*-band (D-configuration) data were excised from the spectral decomposition.

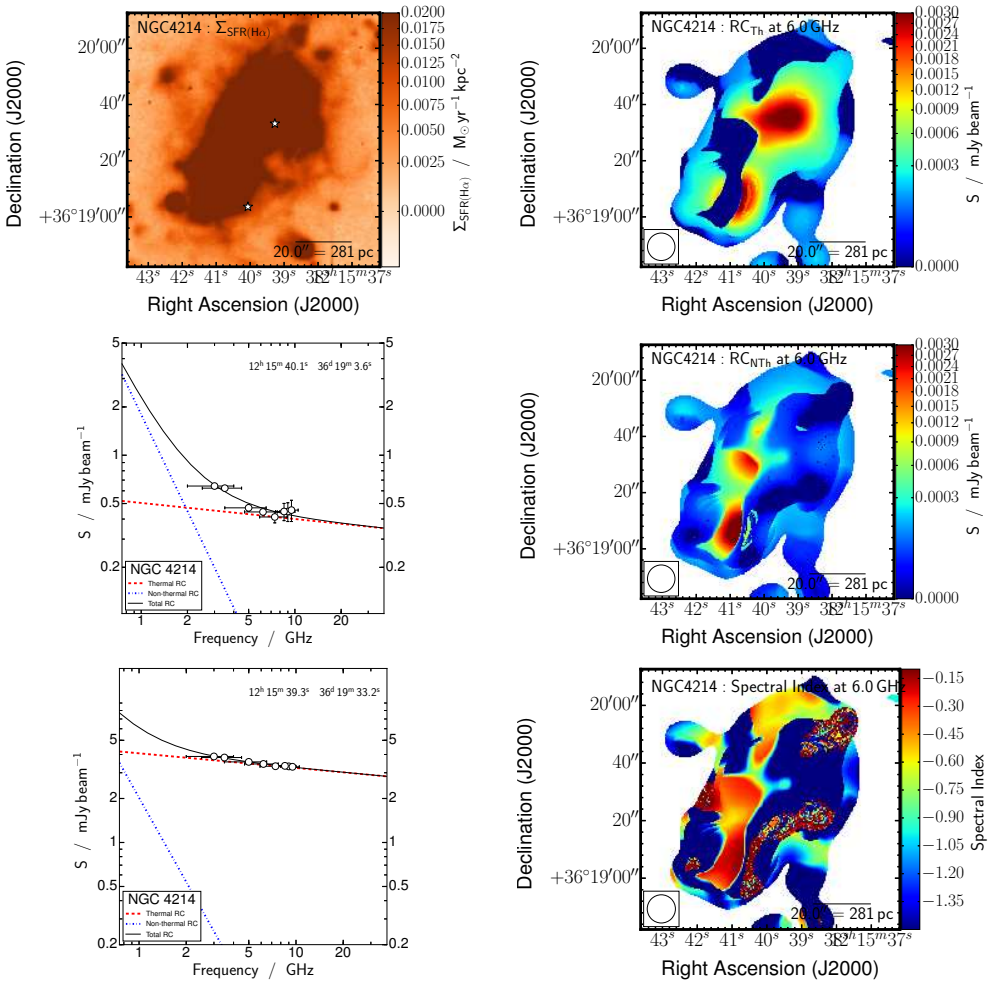

FIGURE 6.11: Hα image of NGC 4214 (top-left) overlaid by star symbols marking two selected positions where the example spectra were taken (middle- and bottom-left). In fact, a single spectrum was made for every single (i, j) pixel—this allowed the construction of three images from the pixel-by-pixel fit to the spectral form described in Equation 6.10: $\mathrm{RC_{Th}}$(top-right), $\mathrm{RC_{NTh}}$ (middle-right), and spectral index of the $\mathrm{RC_{NTh}}$ (bottom-right). Due to its poor resolution, the *L*-band data were excised from the spectral decomposition.

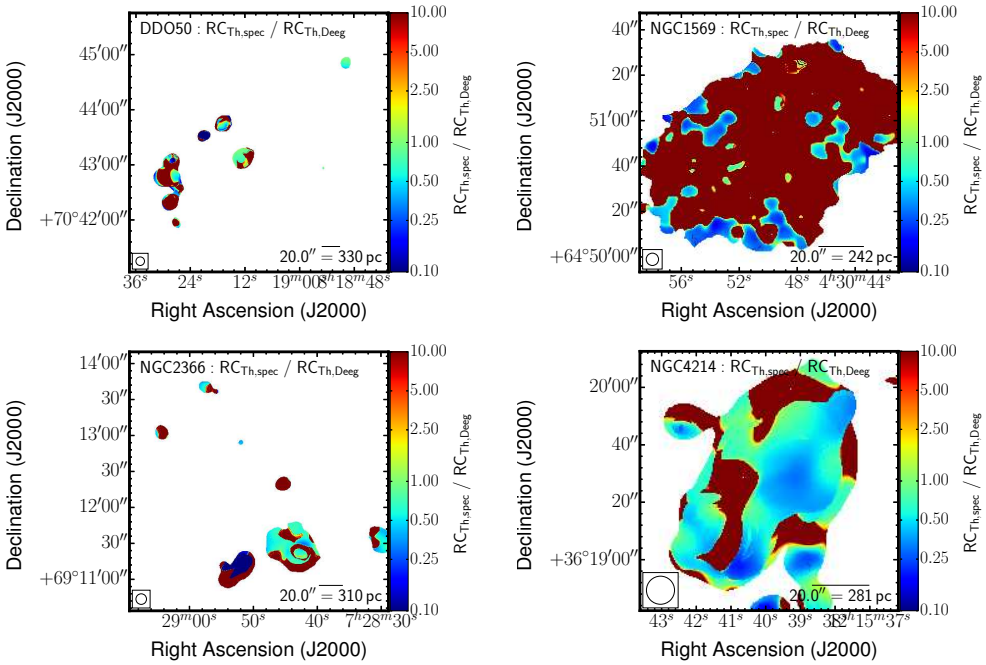

FIGURE 6.12: Ratio of the $\mathrm{RC_{Th}}$ inferred from the spectral decomposition ($\mathrm{RC_{Th,spec}}$) to that of the $\mathrm{RC_{Th}}$ made by scaling the Hα surface brightness ($\mathrm{RC_{Th,Deeg}}$). This is shown for DDO 50 (top-left), NGC 1569 (top-right), NGC 2366 (bottom-left), and NGC 4214 (bottom-right). Note: some regions show very high ratios. The S/N threshold in the spectral composition was set as $5\,\sigma_{\mathrm{rms}}$—where σ_{rms} is the rms background level—to ensure a reliable decomposition, while not limiting it to very small regions of the dwarf galaxy. Therefore, these high ratios are probably from 5–10 σ regions and thus have large associated uncertainties.

The $\mathrm{RC_{Th}}$ inferred from the spectral decomposition ($\mathrm{RC_{Th,spec}}$) was then compared with the $\mathrm{RC_{Th}}$ inferred from the Deeg et al. (1997) conversion factor ($\mathrm{RC_{Th,Deeg}}$) through their ratio,

$$R_{\mathrm{Th}} = \frac{\mathrm{RC_{Th,spec}}}{\mathrm{RC_{Th,Deeg}}}, \tag{6.11}$$

and is shown for the four galaxies in Figure 6.12. The value of R_{Th} typically lies between 0.25 and 1.00 meaning that the spectral decomposition generally inferred lower values of $\mathrm{RC_{Th}}$ emission than that predicted by theory (i.e., the Hα-$\mathrm{RC_{Th}}$ conversion factor of Deeg et al., 1997).

Regions that exhibit a ratio of greater than 1 can be explained by the presence of *in situ* dust—while the actual $\mathrm{RC_{Th}}$ present would be unaffected, the Hα emission would be absorbed leading to a lower inferred $\mathrm{RC_{Th}}$ intensity. However, the images do not show values of R_{Th} significantly greater than 1 showing that *in situ* dust does not have a significant effect, much as expected in the low metallicity and hence low dust environments.

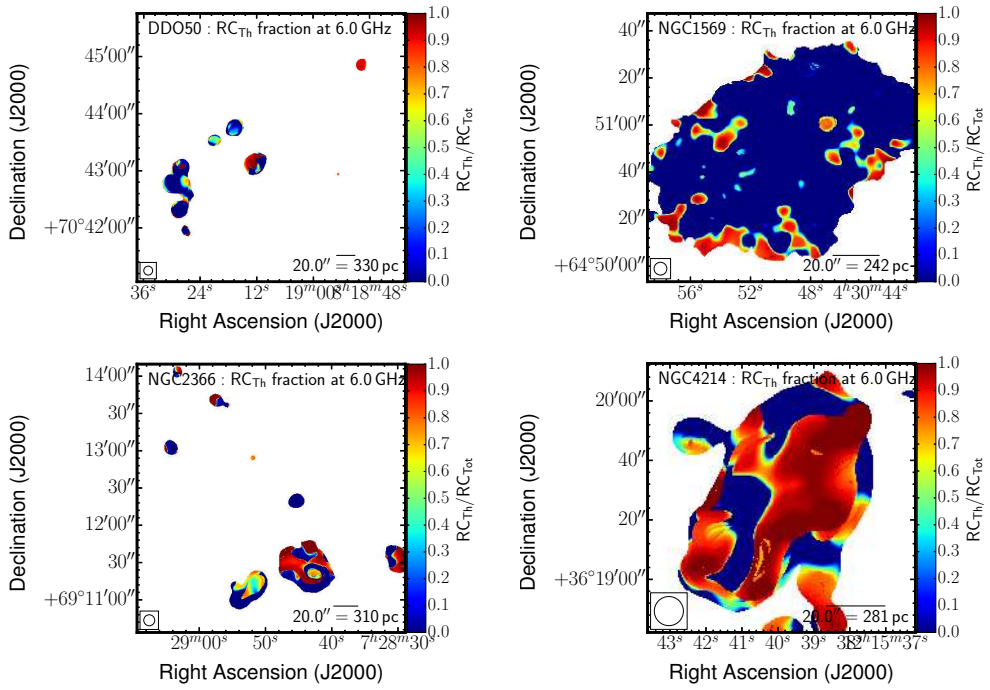

FIGURE 6.13: Thermal fraction inferred from the spectral decomposition, shown for DDO 50 (top-left), NGC 1569 (top-right), NGC 2366 (bottom-left), and NGC 4214 (bottom-right).

The spectral decomposition also allows the dominance of one emission mechanism over the other to be viewed through the thermal fraction, defined as

$$f_{\mathrm{Th}} = \frac{\mathrm{RC_{Th}}}{\mathrm{RC_{Th}} + \mathrm{RC_{NTh}}}. \tag{6.12}$$

and is shown for the four galaxies in Figure 6.13.

Implication of Spectral Decomposition

This section is devoted to interpreting the spectral decomposition of each galaxy, paying special attention to how our inferred images relate to the galaxy's morphology and known properties.

DDO 50: Over the whole galaxy, the spectral decomposition finds a relatively low thermal fraction of 23%. Most of the $\mathrm{RC_{Th}}$ emission comes from the central H II region, while the $\mathrm{RC_{NTh}}$ originates mainly from the SF complexes in the east.

On scales of 100s of pc, the SF complexes show $\mathrm{RC_{NTh}}$ spectral indices ranging from shallow values of -0.4 (CRe age of $\lesssim 10$ Myr according to Equation 6.9) to steep values of -1.0 (CRe age $\gtrsim 60$ Myr). The main SF complex in the east (marked by

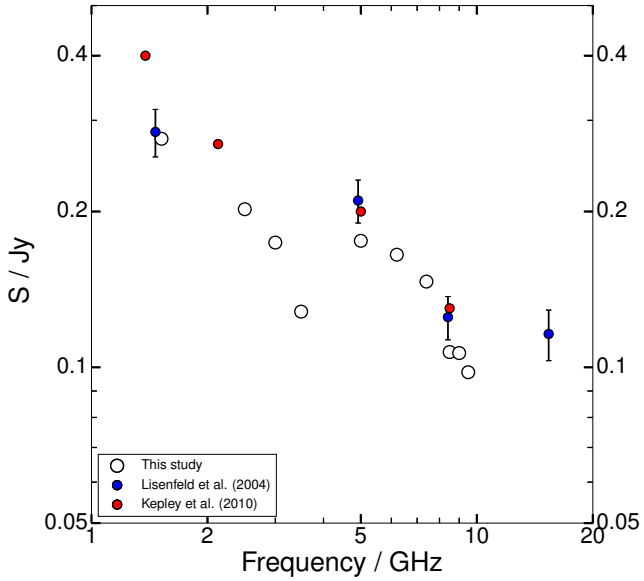

FIGURE 6.14: Integrated RC spectrum of NGC 1569 comparing flux densities from this study (white) to those of Lisenfeld et al., 2004 (blue) and Kepley et al., 2010 (red).

the star symbol in Figure 6.8) shows spatial variation in its $\mathrm{RC_{NTh}}$ spectral index—ranging from -0.6 in the SF region's centre to steeper than -1.20 towards its periphery some 200 pc away—this is likely the direct consequence of CRe ageing and illustrates that it is possible for CRe to diffuse 100s of pc without being lost to the IGM.

NGC 1569: Figure 6.14 shows that while our *L*- and *C*-band measurements agree well with Lisenfeld et al. (2004), the other bands appear deficient. It is known from the *L*-band image that RC emission in NGC 1569 reaches up to scales of $2'$. Therefore, to avoid including images which may not have been sensitive to large scale emission, we excised the *S*-band (B-configuration), *X*-band (C-configuration), and *Ka*-band (D-configuration) observations from our analysis. This left 4 spectral points across 0.7 dex in frequency with which to fit the 3-parameter spectrum. We note that in limiting the spectrum to between 1 and 8 GHz, the spectral decomposition had only the portion of the spectrum that is traditionally dominated by the $\mathrm{RC_{NTh}}$ component and so, not surprisingly, inferred a spectrum dominated by $\mathrm{RC_{NTh}}$ emission.

The galaxy as a whole is dominated by a pervasive $\mathrm{RC_{NTh}}$ component as seen in Figure 6.9 (middle-right) making a low thermal fraction of 10%. This can be explained by the elevated level of SF that the galaxy has experienced from about 100 Myr ago to around 4–10 Myr ago (Lisenfeld et al., 2004)—leaving enough time

for the $\mathrm{RC_{Th}}$ to fade and for the $\mathrm{RC_{NTh}}$ to ramp up. We note that Kepley et al. (2010) find a thermal fraction of 40–50% 'in the centre', although their method differs from ours in that they scaled Hα emission to infer $\mathrm{RC_{Th}}$[1].

The $\mathrm{RC_{NTh}}$ spectral index steepens with distance from the galaxy's centre, going from a value of approximately -0.3 to -0.6. This behaviour is consistent with the fact that SF occurs mainly in the centre, and that CRe would then diffuse, and age, with distance from the centre. These $\mathrm{RC_{NTh}}$ spectral indices are consistent with CRe ages $\lesssim 15$ Myr, although it is noted that the magnetic field strength used in the model was $10\,\mu$G which is lower than that observed in NGC 1569 (see Figure 5.8).

NGC 1569 has a relatively large angular size. Therefore, to ensure the best quality spectral decomposition, we would need reliable high-frequency flux densities corrected for missing large scale emission, something that we lacked this time around.

NGC 2366: The spectral decomposition shows the galaxy as a whole to have a relatively high thermal fraction of 48%. This is mainly down to the main H II complex which itself is dominated by the $\mathrm{RC_{Th}}$ component (see bottom-left panel of Figure 6.10) hinting that this is a young SF region that has not yet had the time to produce significant numbers of SNRs.

NGC 4214: This galaxy is dominated by two main SF complexes (marked by the star symbols in Figure 6.11). Both NGC 4214-I (northern complex) and NGC 4214-II (southern complex) are young stellar associations (3.0–3.5 and 1.0–2.0 Myr, respectively; MacKenty et al., 2000; Srivastava et al., 2014), explaining why, as a whole, the galaxy has a relatively high thermal fraction of 66%.

It is in the regions where the spectral decomposition inferred significant quantities of $\mathrm{RC_{NTh}}$ that the inferred $\mathrm{RC_{NTh}}$ spectral index is most accurate; these regions exhibit shallow indices of -0.3 to -0.6 which implies SF activity starting $\lesssim 15$ Myr according to the calibration in Equation 6.9.

6.4 Summary

In this chapter, a CRe model was used to follow the evolution of the $\mathrm{RC_{NTh}}$ component's properties. The simulation showed that:

- $\mathrm{RC_{NTh}}$ emission is visible from approximately 5 up to 70 Myr following a SF episode;

[1] Apart from this, NGC 1569 lies in a region of relatively high Galactic extinction, hampering accurate Hα measurements.

- $\mathrm{RC}_{\mathrm{NTh}}$ luminosity reaches its peak approximately 55 Myr after the SF episode (when CRe are resident in a magnetic field strength of $10\,\mu$G which is typical of the SF regions in LITTLE THINGS);
- $\mathrm{RC}_{\mathrm{NTh}}$ luminosity remains nearly constant over the 60 Myr following the SF episode, highlighting its potential to be used to infer SFR;
- The $\mathrm{RC}_{\mathrm{NTh}}$ spectral index evaluated around *C*-band (i.e., 4–8 GHz) can be calibrated to infer the time elapsed since a burst of SF by $t[\mathrm{Myr}] = -25\alpha_{\mathrm{NTh}}$, for values of α_{NTh} between -0.4 and -0.7;
- $\mathrm{RC}_{\mathrm{NTh}}$ spectral indices of -0.8 are consistent with ages between 20 and 55 Myr. After ~ 60 Myr, the $\mathrm{RC}_{\mathrm{NTh}}$ intensity quickly falls limiting the precision of spectral index calculations.

Multifrequency observations taken with the VLA (from *L*-band through to *Ka*-band; 1–33 GHz) were used at matched resolution (~ 5–$10''$; B-, C-, and D-configuration) to investigate the properties of $\mathrm{RC}_{\mathrm{NTh}}$ emission in 4 dwarf galaxies: DDO 50, NGC 1569, NGC 2366, and NGC 4214. Our findings are that:

- regions of relatively high SF are radio dim with respect to the Condon (1992) relation by a factor of 2 (see Section 6.3.2);
- spectral decomposition of the RC offers an Hα-independent way to infer the $\mathrm{RC}_{\mathrm{Th}}$, $\mathrm{RC}_{\mathrm{NTh}}$, and $\mathrm{RC}_{\mathrm{NTh}}$ spectral index (α_{NTh});
- the four galaxies displayed a mix in their RC makeup: DDO 50 and NGC 1569 were shown to have a low thermal fraction of 23% and 10%, respectively, at *C*-band, while NGC 2366 and NGC 4214 were shown to have higher thermal fractions of 48% and 66%, respectively;
- NGC 1569 exhibited steepening of the $\mathrm{RC}_{\mathrm{NTh}}$ spectral index further from the galaxy's centre, which is consistent with SF activity being located at the centre combined with CRe diffusion.

The spectral decomposition was based on a two component spectrum, which as a preliminary study, was suitable. However, more sensitive observations (corrected for short spacings) would allow a more robust fit to the model. In addition to this, the potential curvature of the $\mathrm{RC}_{\mathrm{NTh}}$ spectrum could be taken into account using, e.g., Broadband Radio Astronomy ToolS (BRATS; Harwood et al., 2013), as was done in the pilot study on the non-thermal superbubble in IC 10 by Heesen et al. (2015).

7

Conclusion

7.1 Background

This thesis focussed on examining *to what extent the RC could be used to probe SF in dwarf galaxies*. Star formation is an important, on-going process in the Universe, driving galaxy formation and evolution. Acquiring accurate measurements of SF thus becomes crucial in order to understand galaxies.

To eliminate uncertainties introduced by extinction by dust in the optical, the RC was suggested to be a useful SF probe mainly since it has a clear link to recent and on-going SF. Importantly, it is not absorbed by dust, and so it potentially offers an unhindered view into regions of SF. As radio technology improves further, RC surveys will probe the fainter, more quiescent regime of the radio sky. Having a robust manner by which to convert RC luminosities to SFR has the potential to provide millions of independent SFR measurements out to intermediate redshifts.

Therefore, in order to investigate the degree to which the RC can be used to infer SFR, the 40 dwarf galaxies that make up the LITTLE THINGS sample were chosen as the bedrock of the thesis due to the large range of galactic parameters that they

covered. Dwarf galaxies were chosen as the object of interest due to their simplicity and similarity to high redshift objects—they are physically small, have low mass, and have low quantities of dust (but with the caveat that gas fraction and SF in local dwarfs are quite unlike that in high-redshift galaxies, e.g., Oesch et al., 2016).

The RC data used to examine the dwarf galaxies was acquired with the VLA in bands ranging from *L*-band through to *Ku*-band (between 1 and 33 GHz), and using B-, C-, and D-configurations to achieve a high, matched resolution of the resulting images (between 3 and 10″).

7.2 The Radio Continuum in Dwarf Galaxies

7.2.1 Global RC

Two-thirds of the 40 LITTLE THINGS galaxies exhibit significant RC emission originating from the galaxy itself, 17 of which were new RC detections. The majority of galaxies displayed RC in isolated pockets coincident with SF regions; the ISM was observed to be largely void of $\mathrm{RC_{NTh}}$ emission. These general points agree with that expected given current models of dwarf galaxies: given their low mass, SF is episodic and sporadic (hence the isolated pockets of RC emission) because their large-scale processes play a limited role in initiating SF; their low mass also means that spiral arms are weaker and so with little differential rotation, magnetic fields are weaker in the ISM leading to a higher escape probability of CRe.

In a little more detail, the results from Chapter 4 are that:

- contamination from background sources was a prominent issue in earlier, low resolution studies. Earlier studies reporting linear relations (e.g, RC–SFR; the RC–FIR 'conspiracy') in dwarf galaxies could, in part, be attributed to contamination from background galaxies that themselves fall on such relations;

- our resolution allowed us to single out background sources. A total of 27 out of the 40 LITTLE THINGS galaxies exhibit significant RC emission originating from the galaxy itself; 17 are new RC detections. The flux densities of our brighter dwarfs agree with the literature;

- the average thermal fraction is $39 \pm 7\%$ at 6 GHz, whilst the non–thermal fraction is $61 \pm 7\%$. The $\mathrm{RC_{NTh}}$ fraction is lower than that found in larger spirals; this is despite the fact that the $\mathrm{RC_{Th}}$ emission may be reduced, in an absolute sense (Lee et al., 2009), in dwarf galaxies;

- the LITTLE THINGS galaxies diverge from the Condon et al. (2002) RC–SFR relation at a SFR of $0.1\mathrm{M}_{\odot}\,\mathrm{yr}^{-1}$. The sample has a power–law slope of $\sim 1.2 \pm 0.1$ with a scatter of $0.2\,\mathrm{dex}$. For SFRs of about $10^{-4}\mathrm{M}_{\odot}\,\mathrm{yr}^{-1}$, the observed RC is a factor of 10 deficient from that predicted from the Condon et al. (2002) relation. We interpret this as an underproduction of the $\mathrm{RC}_{\mathrm{NTh}}$ component due to CRe escape;
- the dwarf galaxies are consistent with the linear Yun et al. (2001) RC–FIR (flux density) trend (see Figure 4.12). The scatter of the relation increases significantly below $70\mu\mathrm{m}$ FIR $\sim 1\,\mathrm{Jy}$ ($6\,\mathrm{GHz}$ RC $\sim 2\,\mathrm{mJy}$);
- our data are consistent with the linear Yun et al. (2001) RC–FIR (luminosity) trend (see Figure 4.11) suggesting that the 'conspiracy' of the RC–FIR relation continues to hold even for dwarf galaxies;
- in a few dwarf galaxies, the equipartition magnetic field strength reaches as high as $30\,\mu\mathrm{G}$ in multiple $100\,\mathrm{pc}$ regions, and in one case, $70\,\mu\mathrm{G}$;
- most SF regions do not possess such strong magnetic field strengths. The average strength of the transverse magnetic field is $\sim 9.4\mu\mathrm{G}$ (from only the regions that exhibited significant RC emission). This value is consistent with that of larger galaxies (e.g., $9.7\mu\mathrm{G}$ in WSRT SINGS; Heesen et al., 2014). This suggests that it is the escape of CRe that is responsible for the deficient $\mathrm{RC}_{\mathrm{NTh}}$ emission (see Figure 4.8). Once in the ISM, the CRe may: 1) radiate at a slower rate than in SF regions, and move into the IGM before they have the time to radiate all their energy, or 2) continue to diffuse but, because they continue to radiate and lose energy, the frequency of synchrotron emission shifts gradually to lower frequencies to the extent that emission falls outside of *C*-band. As a result, interstellar regions can be largely void of $\mathrm{RC}_{\mathrm{NTh}}$ emission.

The most important result to come from Chapter 4 is the SFR calibration: the inversion of the RC–SFR relation described in Equation 4.9 allows the observed RC luminosity of a dwarf galaxy to be used to infer the SFR, and is given by

$$\frac{\mathrm{SFR}}{\mathrm{M}_{\odot}\,\mathrm{yr}^{-1}} = 5 \times 10^{-18} \left(\frac{\mathrm{RC}}{\mathrm{W\,Hz}^{-1}} \right)^{0.85} . \tag{7.1}$$

with a scatter of $0.2\,\mathrm{dex}$. The shallow gradient of the relation means that, for a SFR of about $10^{-4}\mathrm{M}_{\odot}\,\mathrm{yr}^{-1}$, the observed RC is a factor of 10 deficient from that predicted from the Condon et al. (2002) relation. This calibration of the *C*-band RC is appropriate for dwarf galaxies that have a global SFR of between approximately 1×10^{-3} and $0.1\mathrm{M}_{\odot}\,\mathrm{yr}^{-1}$.

7.2.2 Localised $\mathrm{RC_{NTh}}$

On a resolved scale, dwarf galaxies are varied in their observed properties. Large-scale processes were seen to play a minimal role allowing stochastic effects to dominate; this introduced a large spread in observed properties (due to random sampling of the time domain). Nonetheless, using the $\mathrm{RC_{NTh}}$ to trace SF on a local scale did prove to be robust.

In a little more detail, the deficiency of RC in dwarf galaxies can be attributed to both weak magnetic fields and the low mass of the galaxy (see Section 5.4.1). Weaker magnetic fields give the CRe longer lifetimes, and thus more time to be advected out of the galaxy with the magnetic fields frozen into the gas in outflows, or diffuse.

The key finding in Chapter 5 was that using the $\mathrm{RC_{NTh}}$–SFR relation calibrated using discrete SF complexes (as opposed to, e.g., 200 pc square cells) gave the most useable SFR calibrator. Inverting the $\mathrm{RC_{NTh}}$–SFR relation defined in Table 5.4 allows the observed $\mathrm{RC_{NTh}}$ luminosity associated with SF complexes to be used to infer resolved SFRs, and is given by

$$\frac{\mathrm{SFR}}{\mathrm{M_\odot\,yr^{-1}}} = 1.36 \times 10^{-23} \left(\frac{L_{\mathrm{NTh}}}{\mathrm{W\,Hz^{-1}}} \right)^{1.15} \tag{7.2}$$

with an uncertainty of $\pm 38\%$.

The steepness of the relation is thought to have arisen due to the effects of CRe transport. This is supported by the observation that regions of relatively high SF were radio dim with respect to the Condon et al. (2002) relation by a factor of 2, while bright $\mathrm{RC_{NTh}}$ emission was observed in a region totally void of on-going SF. But diffusion was not the only cause of the $\mathrm{RC_{NTh}}$ deficiency (i.e., the steep relation): escape of CRe from the galaxy also played a part. Weaker magnetic fields in the ISM[1] give the CRe longer lifetimes, and thus more time to be advected out of the galaxy with the magnetic fields frozen into the gas in outflows, or diffuse.

The calibration, however, was formulated based on *C*-band observations and is only valid for resolved regions forming stars at a rate $\gtrsim 2 \times 10^{-4}\,\mathrm{M_\odot\,yr^{-1}}$ (see Table 5.4). Despite the low flux densities of $\mathrm{RC_{NTh}}$ measurements, the $\mathrm{RC_{NTh}}$ still works well as a SFR tracer whereas Hα, which is largely dependent on stars with mass $\gtrsim 18\,\mathrm{M_\odot}$, and is thus dependent on the high mass tail of the stellar IMF, will suffer from stochasticity.

[1] In a few dwarfs, the magnetic field strength reaches as high as 30 μG in multiple 100 pc regions, and in one case, 70 μG

7.2.3 $\mathrm{RC_{NTh}}$ Spectral Index

Through implementing a simple CRe model (outlined in Section 5.4.1), the evolution of the associated $\mathrm{RC_{NTh}}$ emission was tracked immediately following a burst of SF. In particular, the simulation implied that:

- $\mathrm{RC_{NTh}}$ emission is visible from approximately 5 up to 70 Myr following a SF episode;
- $\mathrm{RC_{NTh}}$ luminosity reaches its peak approximately 55 Myr after the SF episode;
- $\mathrm{RC_{NTh}}$ luminosity remains nearly constant over the 60 Myr following the SF episode, highlighting its potential to be used to infer SFR;
- $\mathrm{RC_{NTh}}$ spectral indices of -0.8 are consistent with ages between 20 and 55 Myr. After ~ 60 Myr, the $\mathrm{RC_{NTh}}$ intensity quickly falls limiting the precision of spectral index calculations.

The simulation also implied that the $\mathrm{RC_{NTh}}$ spectral index evaluated around *C*-band (i.e., 4–8 GHz) can be calibrated to infer the time elapsed since a burst of SF by

$$\frac{t}{\mathrm{Myr}} = -25\alpha_{\mathrm{NTh}}. \tag{7.3}$$

for values of α_{NTh} between -0.4 and -0.7.

For the galaxies that displayed $\mathrm{RC_{NTh}}$ emission that was bright enough and sufficiently well resolved, a spectral decomposition of the RC spectrum was performed to infer Hα-independent $\mathrm{RC_{Th}}$, $\mathrm{RC_{NTh}}$, and $\mathrm{RC_{NTh}}$ spectral index maps. Multi-frequency observations taken with the VLA (from *L*-band through to *Ka*-band; 1–33 GHz) were used at matched resolution ($\sim$ 5–10″; B-, C-, and D-configuration) to investigate the properties of $\mathrm{RC_{NTh}}$ emission in 4 dwarf galaxies: DDO 50, NGC 1569, NGC 2366, and NGC 4214. The spectral decompositions showed that:

- the four galaxies displayed a mix in their RC makeup: DDO 50 and NGC 1569 were shown to have a low thermal fraction of 23% and 10%, respectively, at *C*-band, while NGC 2366 and NGC 4214 were shown to have higher thermal fractions of 48% and 66%, respectively;
- NGC 1569 exhibited steepening of the $\mathrm{RC_{NTh}}$ spectral index further from the galaxy's centre, which is consistent with SF activity being at the centre combined with CRe diffusion.

It was also found that regions of relatively high SF are radio dim with respect to the Condon (1992) relation by a factor of 2 (see Section 6.3.2).

The spectral decomposition was based on a two component spectrum, which as a preliminary study, was suitable. However, more sensitive observations (corrected for short spacings) would allow a more robust fit to the model. In addition to this, the potential curvature of the $\mathrm{RC_{NTh}}$ spectrum could be taken into account using, e.g., Broadband Radio Astronomy ToolS (Harwood et al., 2013), as was done in the pilot study on the non-thermal superbubble in IC 10 by Heesen et al. (2015).

7.2.4 Overview

Dwarf galaxies are not only faint in the RC due to their lower SF activity, but they are also *fainter than expected* due to a deficiency of $\mathrm{RC_{NTh}}$ attributed to CRe escape. Nonetheless, the total RC *can* be used to probe SF in dwarf galaxies not only on a global scale, but also within discrete SF complexes 10s to 100s of pc in size. Theoretically, the total RC can be used right from the onset of a burst of SF (where $\mathrm{RC_{Th}}$ will dominate) up to $\sim 70\,\mathrm{Myr}$, at which point $\mathrm{RC_{NTh}}$ will dominate. Calibrated by the RC obervations in this thesis, both resolved and global SFRs of gas rich, low mass galaxies can be inferred with an uncertainty of $\pm 0.2\,\mathrm{dex}$; the relations allow SFRs of between approximately 2×10^{-4} and $0.1\mathrm{M}_\odot\,\mathrm{yr}^{-1}$ to be inferred.

7.3 Future Work

7.3.1 Obvious Avenues

On the observational side, any continued study into the RC in these galaxies would, of course, benefit greatly from an increased signal-to-noise ratio. Whether this much needed increased S/N would come from proposing for more time on the VLA, or by employing the superior qualities of the SKA in a few years time is a matter for debate, but it is clear that, despite the VLA's unsurpassed sensitivity (as of 2015), it is perhaps *still* not quite sensitive enough to properly observe a large sample of these low-surface brightness galaxies. With this in mind, the inclusion of single-dish data or, at the very least D-configuration data (especially for *L*-, *S*-, and *C*-band), is strongly recommended, ensuring that no flux would be missing from the (u, v) data. With improved accuracy, more detailed spectral analysis could be performed using either the simplistic 3-parameter model outlined in Section 6.3.2, or more advanced algorithms such as, e.g., BRATS (Harwood et al., 2013).

On the theoretical side, one avenue to go down would be to build upon the preliminary work based on the simple CRe model implemented in Chapters 5 and 6.

A suitable code has already been earmarked to examine the propagation of CRe in dwarf galaxies: DRAGON[2], the creator of which, Daniele Gaggero, has expressed interest in tailoring the model in the remit of dwarf galaxies. The background of this would-be study is discussed in more detail in Section 7.3.2.

With these observational and theoretical aspects addressed, the next obvious leap would be to apply the knowledge to larger systems such as spiral galaxies, much like Heesen et al. (2014). Despite spiral galaxies being more 'messy' than dwarf galaxies, they are essentially a collection of dwarf-like SF complexes, under the influence of global mechanisms (spiral density waves, and a pervasive magnetic field). By calibrating the RC as a SFR indicator in spiral galaxies, the possible avenues expand to the realm of cosmology.

7.3.2 Cosmic Ray electron propagation in Dwarf Galaxies

One of the simplest and earliest models invoked to explain $\mathrm{RC_{NTh}}$ was the calorimetric model of Völk (1989). This was later superseded by more realistic models such as that of Lisenfeld et al. (1996) and Lacki et al. (2010), inspiring the notion of CRe escape (e.g., Heesen et al., 2014). However, one thing all models have in common is that the CRe flux achieves a steady state as a function of scale height. In dwarf galaxies, star formation (and thus the generation of new populations of CRe) has a more stochastic/sporadic nature than in spiral galaxies. A steady state of CRe flux cannot be attained, especially locally on scales of a few $100\,\mathrm{pc}$. Therefore, a time-dependent model must be made.

Physically, it is well understood how $\mathrm{RC_{Th}}$ emission is generated and the variables are well known. However, without *a priori* knowledge of the magnetic field strength and orientation in dwarf galaxies, it is difficult to explain $\mathrm{RC_{NTh}}$ emission on large scales, let alone as a function of time.

Explaining $\mathrm{RC_{NTh}}$ emission on large scales has the potential to tie together the observational aspects of Chapters 4, 5, and 6. A simple model of Cosmic Ray electrons in dwarf galaxies is proposed (see Figure 7.1). The model's structure is justified by measurements taken of the dwarf galaxies observed in this study: the dwarf galaxy itself assumes cylindrical symmetry, and a single star formation region is placed on the midplane. In the star formation region, the turbulent magnetic field peaks at $30\,\mu\mathrm{G}$ and then radially declines to the ambient level of $2\,\mu\mathrm{G}$ in the interstellar regions. Outside the confines of the dwarf galaxy, the magnetic field strength is zero allowing the free escape of CRe into the intragalactic medium (no synchrotron

[2] www.dragonproject.org/Home.html

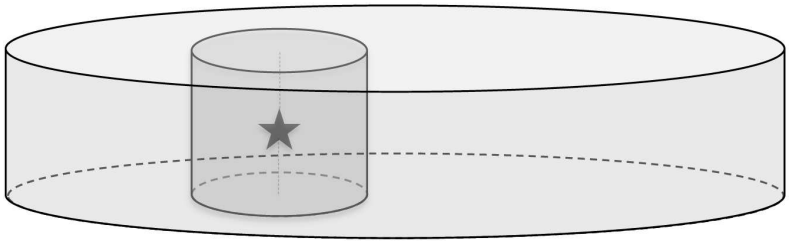

FIGURE 7.1: The toy model structure of the dwarf galaxy used in DRAGON. The dwarf galaxy itself assumes cylindrical symmetry, and a single star formation region ($\star$-symbol) is placed on the midplane. At $\star$, the turbulent magnetic field peaks at $30\,\mu$G and then radially declines to the ambient level of $2\,\mu$G in the interstellar regions. Outside the confine of the dwarf galaxy, the magnetic field strength is zero allowing the free escape of CRe into the intragalactic medium (no synchrotron emission expected).

emission expected).

A suitable code has already been chosen to examine the propagation of CRe in dwarf galaxies: DRAGON. This package assumes a cylindrical model making it ideal for studies of CRe dynamics in dwarf galaxies. The inputs required are the gas distribution, the CRe source distribution, and the CRe diffusion coefficients.

The main point of interest is: *why is there a lack of synchrotron emission in dwarf galaxies, and especially so in the interstellar medium?* This lack of synchrotron emission can be ascribed to either:

- energy loss of CRe: by the time the CRe enter the interstellar medium, they have lost sufficient energy that they simply emit outside the observation band, or

- CRe loss from galaxy: the magnetic field strength in the interstellar medium is weak enough that, once the CRe enter the interstellar medium, they rapidly traverse the scaleheight of the galaxy and escape before losing significant amounts of their energy.

The purpose of this future work would be to ascribe our observations to one of these hypotheses.

In addition to this, the resolved model of CRe propagation would also have a number of other applications, adding significantly to the analysis investigating:

- the radial profiles of $\mathrm{RC}_{\mathrm{NTh}}$ emission around SF complexes (see Section 5.4.1). Higher resolution observations of these regions would allow a detailed look at CRe diffusion in and around regions that have recently formed stars;

- inferring the time elapsed since the onset of a SF event (see model from Section 5.4.1). We used a constant magnetic field of $\sim 10\,\mu$G whereas the model

would use a more realistic picture of magnetic field strength decreasing further from the SF region's centre.

A

An accelerated, point charge

The *electromagnetic force* is one of the four forces of nature and makes a fundamental link between charges and the origins of photons. Changes of a charged particle's state are conveyed by emission of a photon. This can be a change in energy level, or physical motion (i.e., acceleration).

In the case of the radio continuum, it is primarily, the acceleration of free electrons that leads to the emission of photons. The acceleration originates from one of two mechanisms: an interaction with a) another charged particle (electrostatics), or b) a magnetic field (eletrodynamics).

The remainder of this Appendix details the physical process behind the emission of the RC at wavelengths relevant to this study, borrowing heavily from Chapters 7 and 8 of Longair (1981).

A.1 Mechanism

To understand why an acceleration of an electron would result in the emission of a photon, Purcell (1963)[1] invokes a simplified situation where a charged particle

[1] See also physics.weber.edu/schroeder/mrr/MRRtalk.html

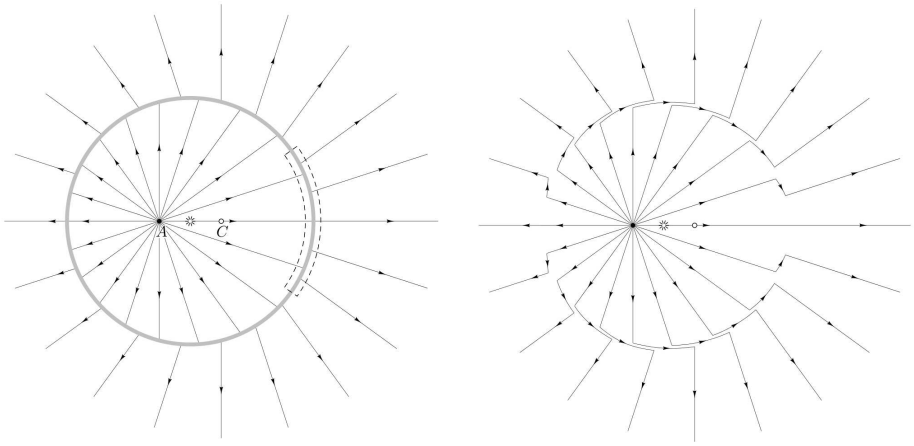

FIGURE A.1: *Left:* A charged particle moves from C to A in a time interval, T. The electric field line pattern propagates away from the charged particle at c (denoted by arrows). *Right:* The result of the change in position is a rapid change of electric field orientation (within the shaded shell).

moves from C to A in a time interval, T (see Figure A.1). After remaining at A for a time $T_{\rm sit}$, the presence of the charged particle will be felt only within its lightcone, i.e., the electric field lines will fill a volume of radius $cT_{\rm sit}$ centred on A (direction of electric field propagation is denoted by the arrows). Beyond this radius, the electric field lines have not yet had sufficient time to propagate. Instead, the electric field line pattern beyond this is dictated by where the charged particle was prior to being at A (i.e., when it was at C). Therefore, beyond $cT_{\rm sit}$, the electric field lines appear to be propagating away from the charged particle's prior position at C. The result is that a discontinuity in the electric field line pattern appears (see left panel of Figure A.1).

In reality, the discontinuity is a rapid change in electric field orientation (as it took a time T to move from C to A). The volume of space occupied by this rapidly changing electric field is void of any charge, and since "electric flux through any closed surface is proportional to the enclosed electric charge" (Gauss' Law), the electric field lines entering the shell (from when the particle was at A) must match up with the electric field lines leaving the region (from when the particle was at C). The result is that the electric field orientation 'jumps', being strongest in the direction perpendicular to the acceleration (see right panel of Figure A.1). The 'jump' has its field orientation perpendicular to the radial field emanating from A or C—this transverse component is referred to as the *radiation field*.

Figure A.2 (left) now shows the electric field seen at two times: at t_0 (black dot) and after a time T (white dot). When examining this transverse component in a little more detail (see Figure A.2), it becomes apparent that the transverse change in

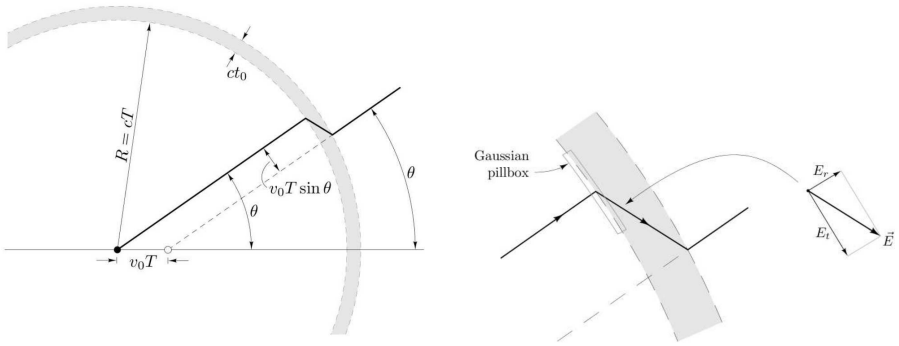

FIGURE A.2: *Left:* A charged particle moves from the black dot to the white dot with a velocity v_0 over a time, T. The width of the shaded shell corresponds to the interval of time over which the particle has changed direction. *Right:* This change in direction results in a perpendicular and parallel component with respect to the original electric field.

electric field is $v_0T\sin(\theta)$, while the radial change is ct_0:

$$\frac{E_\perp}{E_{||}} = \frac{v_0T\sin(\theta)}{ct_0}, \tag{A.1}$$

$$E_\perp = \frac{aT\sin(\theta)}{c}\cdot E_{||}. \tag{A.2}$$

Figure A.2 (right) shows an infinitesimally small volume, where the electric field that enters is given by

$$E_{||} = \frac{1}{4\pi\epsilon_0}\frac{q}{R^2}. \tag{A.3}$$

The short edges of the volume are sufficiently small that flux entering or leaving is negligible, implying that the remaining edge (outside curve of volume) must have the same radial component as the inner edge. By combining this result with Equation A.2, the magnitude of the transverse electric field is

$$E_\perp = \frac{1}{4\pi\epsilon_0}\cdot\frac{qa\sin(\theta)}{c^2R}. \tag{A.4}$$

The transverse component of the electric field is proportional to $1/R$ while the radial component is proportional to $1/R^2$. Consequently, for large values of R, the transverse component dominates the radial component. The propagated energy held in the electric and magnetic fields have an energy density

$$\begin{aligned} U_{E+B} &= \frac{1}{2}\left(\epsilon_0E^2 + \frac{B^2}{\mu_0}\right) \\ &= h\nu \end{aligned}$$

where h is Plank's constant and ν is the frequency of oscillation of the electric field. It is this energy that is propagated away from the accelerated charge. On a microscopic level, the energy of electrons is in kinetic form (e.g., thermal motion in H II regions,

or ultra-relativistic motion responsible for synchrotron emission)—the propagating electric field draws on the electron's reservoir of kinetic energy leading to slower speeds of individual electrons; macroscopically speaking, the population of electrons cools.

In summary, if a detector is placed near a motionless charged particle, it will detect no transverse electric field. Once the electron starts to move, a transverse electric field is generated and this propagates towards the detector eventually allowing the measurement of a non-zero transverse field. Once the electron returns to rest, the transverse electric field will once more be read as zero.

This allows a powerful way of interpreting light. It is no longer a photon, but rather a pulse of electric field. Conversely, to make a photon, one needs only superpose a number of electric field pulses of varying durations and amplitudes. This forms the basis of the spectral analysis of light making use of Fourier analysis.

A.2 Power

As the shell (pulse of transverse electric field) propagates and expands, the transverse component dominates the radial component, meaning that the total electric field can be adequately described by only the transverse component, which we use to find the energy density

$$\begin{aligned}\frac{\mathrm{d}E}{\mathrm{d}V} &= \frac{1}{2}\epsilon_0|\vec{E}|^2 \\ &= \frac{1}{2}\epsilon_0\left(\frac{1}{4\pi\epsilon_0}\,\frac{qa\sin(\theta)}{c^2R}\right)^2 \\ &= \frac{1}{32\pi^2\epsilon_0}\,\frac{q^2a^2}{c^4R^2}\sin^2(\theta). \end{aligned} \tag{A.5}$$

which is direction-dependent. As previously mentioned, the energy density is greatest in the direction perpendicular to the acceleration, but there are directions where the energy density is zero. Consequently, when integrated over all angles, the energy density is expected to be lower than that in the perpendicular direction. Integrating over all directions yields

$$\begin{aligned}\frac{\mathrm{d}E}{\mathrm{d}V} &= \frac{1}{32\pi^2\epsilon_0}\,\frac{q^2a^2}{c^4R^2}\int_0^{2\pi}\sin^2(\theta)\,\mathrm{d}\theta \\ &= \frac{1}{48\pi^2\epsilon_0}\,\frac{q^2a^2}{c^4R^2}. \end{aligned} \tag{A.6}$$

which is the energy density in the propagating shell. Equation A.6 can now be integrated over the volume of the shell to find the total radiated energy,

$$\begin{aligned} E &= \frac{1}{48\pi^2\epsilon_0}\frac{q^2a^2}{c^4}\int\frac{1}{R^2}\,\mathrm{d}V \\ &= \frac{1}{48\pi^2\epsilon_0}\frac{q^2a^2}{c^4}\,4\pi\int_{cT}^{cT+ct_0}\mathrm{d}R \\ &= \frac{1}{12\pi\epsilon_0}\frac{q^2a^2}{c^4}\,ct_0 \\ &= \frac{1}{12\pi\epsilon_0}\frac{q^2a^2t_0}{c^3}. \end{aligned} \tag{A.7}$$

The total radiated energy in the propagating shell of electric field is now described by Equation A.7. There is also a propagating magnetic field which contains an equal amount of energy. The schematic originally invoked was that a charged particle changed its direction in a timescale t_0. Therefore, the power radiated due to the acceleration over a time, t_0 is expressed by

$$\begin{aligned} P &= \frac{E}{t_0} \\ &= \frac{1}{12\pi\epsilon_0}\frac{q^2a^2t_0}{c^3t_0} \\ &= \frac{q^2}{6\pi\epsilon_0c^3}\,a^2 \end{aligned} \tag{A.8}$$

and is known as the *Larmor formula*.

The *Larmor formula* only holds true in frames of reference where $\frac{v}{c}\sim 0$. In the case of synchrotron emission, the emitting electrons are adhering to the *Larmor formula* in their frame of reference. However, to us, the observer, relativity must be taken into account—to do this, the electron's properties (described by its 4-vector) must have a *Lorentz transformation* applied to them.

In general, a Lorentz transformation is given by

$$X' = L\,X \tag{A.9}$$

where L is the *Lorentz matrix*, X represents the 4-vector properties in the electron's frame of reference, and X' are the 4-vector properties in the observer's (our) frame of reference. The 4-vector can describe a number of properties including: position, velocity, acceleration, momentum, force, energy, power etc. In all cases, the '4D-magnitude' of X' and X must be equal[2], such that

$$[X_1']^2 - [X_2']^2 - [X_3']^2 - [X_4']^2 = [X_1]^2 - [X_2]^2 - [X_3]^2 - [X_4]^2 \tag{A.10}$$

[2]If they were not equal, then this would break laws of conservation: the total integrated power in different inertial frames would be different. Disagreements of total integrated power between different frames of reference may imply that certain frames of reference could obtain energy for free, just by switching to a different frame with respect to a power source

where each subscript refers to each of the 4-vector components. The resulting magnitude is non-Euclidean. Even though individual components may change (e.g. position component; $X'_n \neq X_n$), the magnitude of the 4-vector in *Minkowsky space* is always *Lorentz invariant*.

In the case of the *Larmor formula*, it is the acceleration that is of interest. To look at the acceleration relativistically, we perform the *Lorentz transformation* on the acceleration 4-vector, such that

$$\begin{pmatrix} \gamma & -\gamma\frac{v}{c} & 0 & 0 \\ -\gamma\frac{v}{c} & \gamma & 0 & 0 \\ 0 & 0 & 1 & 0 \\ 0 & 0 & 0 & 1 \end{pmatrix} \gamma \begin{pmatrix} \frac{\partial \gamma c}{\partial t} \\ \frac{\partial \gamma v_x}{\partial t} \\ \frac{\partial \gamma v_y}{\partial t} \\ \frac{\partial \gamma v_z}{\partial t} \end{pmatrix} = \begin{pmatrix} \gamma^4 c\frac{\vec{v}\,\vec{a}}{c^2} \\ \gamma^2 a_x + \gamma^4 v_x \frac{\vec{v_x}\,\vec{a}}{c^2} \\ \gamma^2 a_y + \gamma^4 v_y \frac{\vec{v_y}\,\vec{a}}{c^2} \\ \gamma^2 a_z + \gamma^4 v_z \frac{\vec{v_z}\,\vec{a}}{c^2} \end{pmatrix}$$

where

$$\gamma\frac{\partial(\gamma c)}{\partial t} \equiv \gamma^4 c\frac{\vec{v}\,\vec{a}}{c^2} \tag{A.11}$$

and

$$\gamma\frac{\partial(\gamma\vec{v})}{\partial t} \equiv \gamma^2\vec{a} + \gamma^4\vec{v}\frac{\vec{v_x}\,\vec{a}}{c^2}. \tag{A.12}$$

The acceleration 4-vector in the electron's frame and in the observer's frame can now be equated, given that their '4D-magnitudes' in *Minkowsky space* should be equal:

$$\begin{pmatrix} 0 \\ \vec{a} \end{pmatrix} = \begin{pmatrix} \gamma^4 c\frac{\vec{v}\,\vec{a}}{c^2} \\ \gamma^2\vec{a} + \gamma^4\vec{v}\frac{\vec{v_x}\,\vec{a}}{c^2} \end{pmatrix}$$

where the left hand side is the acceleration vector in the electron's frame of reference, and the right hand side is the observed acceleration. After rearranging, the square of the electron's acceleration is

$$\begin{aligned} \Rightarrow 0^2 - \vec{a}^2 &= \left(\gamma^4 c\frac{\vec{v}\,\vec{a}}{c^2}\right)^2 - \left(\gamma^2\vec{a} + \gamma^4\vec{v}\frac{\vec{v_x}\,\vec{a}}{c^2}\right)^2 \\ -\vec{a}^2 &= -\gamma^4\left(\vec{a}^2 + \frac{\gamma^2}{c^2}\left(\vec{v}\,\vec{a}\right)^2\right). \end{aligned} \tag{A.13}$$

The observed acceleration, $\vec{a}$, in Equation A.13 can be decomposed into parallel ($a_{||}$) and perpendicular ($a_\perp$) components with respect to the electron's motion by

$\vec{a} = a_{||} + a_{\perp}$. Thus, the square of the electron's acceleration can be expressed as

$$\begin{aligned} a^2 &= \gamma^4\Big(\vec{a}^2 + \frac{\gamma^2}{c^2}\big(\vec{v}\,\vec{a}\big)^2\Big) \\ &= \gamma^4\Big(a_{||}^2 + a_{\perp}^2 + \frac{\gamma^2}{c^2}\big(\vec{v}\,\vec{a_{||}} + \vec{v}\,\vec{a_{\perp}}\big)^2\Big) \\ &= \gamma^4\Big(a_{||}^2 + a_{\perp}^2 + \frac{\gamma^2}{c^2}\big(\vec{v}\,\vec{a_{||}}\big)^2\Big) \\ &= \gamma^4\Big(a_{||}^2 + a_{\perp}^2 + \frac{\gamma^2}{c^2}v^2 a_{||}^2\Big) \\ &= \gamma^4\Big(a_{\perp}^2 + a_{||}^2\big(1 + \gamma^2\frac{v^2}{c^2}\big)\Big) \end{aligned} \tag{A.14}$$

where $||$ and $\perp$ refer to the acceleration's orientation with respect to the direction of velocity. The initially non-relativistic motion in the electron's frame can now be expressed in any frame by substituting Equation A.14 into Equation A.15. This yields the *relativistic Larmor formula*:

$$P = \frac{q^2}{6\pi\epsilon_0 c^3}\,\gamma^4\Big(a_{\perp}^2 + a_{||}^2\big(1 + \gamma^2\frac{v^2}{c^2}\big)\Big) \tag{A.15}$$

A.3 Synchrotron Emission

A.3.1 Mechanism

Synchrotron emission is the relativistic extreme of cyclotron emission, which itself results from the deflection (acceleration) of charged particles due to a magnetic field. When Equation A.14 is defined not in terms of a, but force per unit mass, F/m, then it changes to

$$a = \frac{F}{m} = \gamma^4\Big(\frac{F_{\perp}^2}{m^2} + \frac{F_{||}^2}{m^2}\big(1 + \gamma^2\frac{v^2}{c^2}\big)\Big) \tag{A.16}$$

where, due to the $1/m^2$ term, electrons emit 4×10^6 times more than a proton in the same magnetic field. The electron has mass, m_e, charge, e, and it's velocity-vector, $\vec{v}$, is constantly altered by the perpendicular force, $\vec{F}$, acted upon it due to a magnetic field, $\vec{B}$. If the velocity vector is perpendicular to the magnetic field line, then the electron will follow a circular path, where the centripetal force comes entirely from the Lorentz force. From this, the radius of the circle, otherwise known as the radius of gyration can be found, which is

$$r_g = \frac{\gamma m_e c}{eB} \tag{A.17}$$

where, since the electron is ultra-relativistic, the velocity of the electron has been approximated by the speed of light and the rest-frame momentum has been scaled up by the Lorentz factor, γ. Invariably though, the electron will have some component

of its velocity parallel to the magnetic field lines. In this case, it will follow a helical motion.

When taking a typical magnetic field strength of $5 \times 10^{-11}\,\mathrm{T}$ and a γ-value of 100 (i.e. $v \sim c$), the electron's radius of gyration is approximately $9 \times 10^{6}\,\mathrm{km}$, which would take approximately $190\,\mathrm{s}$ to complete one orbit (going at a speed, c). This implies a gyration frequency of $\sim 0.005\,\mathrm{Hz}$, a world away from the GHz-values of the radio regime. But as explained in Section 1.3.3, the observed emission is dominated by the short pulse of light emitted when the electron travels towards the observer; the short pulse can be constructed by multiple photons mainly in the GHz regime. The beaming means that most of the radiation is received when the CRe is moving between two points separated by $\theta = \frac{2}{\gamma}\mathrm{radians}$[3].

A.3.2 Power

Since the electrons are relativistic, we must turn to Equation A.15 to gain insight into the power from synchrotron emission. Note that when the acceleration (force) on the electron lies perpendicular to the velocity (centripetal motion), then we are describing the synchrotron regime. Terms disappear due to the fact that $a_{||} = 0$ and $\vec{v} \cdot \vec{a_{\perp}} = 0$. Hence, Equation A.15 may be reduced to

$$\begin{aligned} P &= \frac{q^2}{6\pi\epsilon_0 c^3} \cdot \gamma^4 \left(a_{||}^2 + a_{\perp}^2 + \frac{\gamma^2}{c^2} \left(\vec{v} \cdot \vec{a_{||}} + \vec{v} \cdot \vec{a_{\perp}} \right)^2 \right) \\ &= \frac{\gamma^4 q^2}{6\pi\epsilon_0 c^3} a_{\perp}^2, \end{aligned} \tag{A.18}$$

i.e., that $a_{||} = 0$ and $\vec{v} \cdot \vec{a_{\perp}} = 0$), which is identical to Equation A.15 multiplied by a factor of γ^4, and reduces to the non-relativistic form when $v/c \sim 0$. The leading term has a value of $5.68 \times 10^{-54}\,\mathrm{kg\,m\,s^{-1}}$ for an electron.

But what is this acceleration, $a_{\perp}$? By equating the centripetal force to the Lorentz force, the centripetal acceleration can be expressed as

$$a_{\perp} = \frac{F}{m_e} = \frac{ecB}{\gamma m} \tag{A.19}$$

where since the electron is relativistic, v has been replaced by the speed of light and the rest-frame momentum has been scaled up by γ. This can be substituted into Equation A.18 such that

$$\begin{aligned} P &= \frac{\gamma^4 q^2}{6\pi\epsilon_0 c^3} \cdot a_{\perp}^2 \\ &= \frac{\gamma^4 e^2}{6\pi\epsilon_0 c^3} \cdot \frac{e^2 c^2 B^2 \sin^2(\alpha)}{\gamma^2 m_e^2} \qquad \text{(A.20)} \\ &= \frac{\gamma^2 e^4 B^2 \sin^2(\alpha)}{6\pi\epsilon_0 m_e^2 c} \qquad \text{(A.21)} \end{aligned}$$

[3] If $180 - \theta = 90 - \frac{1}{\gamma} + 90 - \frac{1}{\gamma}$, then this implies that $\theta = 2\frac{1}{\gamma}$

where α has been introduced as the *pitch angle*. By pitch angle, we refer to the angle that the electron's velocity makes with respect to the magnetic field line. By definition, $\alpha = 90$ degrees would imply circular motion (i.e. no 'forward' motion), and $\alpha = 0$ would describe electron motion parallel to field lines (i.e. no centripetal acceleration due to magnetic fields). Longair (1981) proceeds to manipulate Equation A.21 a little using the electromagnetic foundations of light ($c^2 = \frac{1}{\sqrt{\epsilon_0 \mu_0}}$) and the energy density of a magnetic field ($U_{mag} = \frac{1}{2}\frac{B^2}{\mu_0}$) to yield

$$P = 2\gamma^2 \Big(\frac{e^4}{6\pi\epsilon_0^2 c^4 m_e^2} \Big) c U_{mag} \sin^2(\alpha). \tag{A.22}$$

In the rest frame of the electron, the radiation emitted due to the acceleration is isotropic. However, since we observe the electron as relativistic, we do not observe isotropic emission—it is instead concentrated in the direction of electron travel in a process called *beaming*. Note that over any given solid angle, the power P' will not necessarily be equal to P, but the total power over $4\pi r^2$ is the same since the power 4-vector is a *Lorentz invariant*.

B

VLA Processes

B.1 CASA's `clean` Function Parameters

With the CASA measurement set fully calibrated and clean (i.e., flagged), an interactive session of CASA's `clean` function can be used to generate an image. Typically, the following parameters were defined, where `spw`, `threshold`, `multiscale`, `imsize`, `cell`, and `field` were defined on an observation-specific basis.

```
clean(
     vis            = [Measurement Set],
     imagename      = [Image Name],
     spw            = '0~15',           # Use all 16 spectral windows if possible
     mode           = 'mfs',            # Multi-frequency Synthesis (Rau 2011)
     gain           = 0.1,
     threshold      = '0.02mJy',        # About 3-4 times the rms
     psfmode        = 'clarkstokes',    #
     scaletype      = 'SAULT',          #
     multiscale     = [0,s1,s2,...],    # s=5*3^n where n>0 (Rau 2011)
     smallscalebias = 0.2,              #
     imsize         = [1024],           # Depends on location of bright sources
     cell           = ['0.7arcsec'],
     stokes         = 'I',
     weighting      = 'natural',
     nterms         = 2,                # Generate spectral index map
     field          = [ID of target],
     interactive    = True
)
```

B.2 Creating a VLA Scheduling Block

An `.xml` file can be used to generate scheduling blocks in the NRAO's Observation Preparation Tool via `File -> Import XML`. This method of scheduling block generation is much quicker than using the slow GUI, and encourages consistency between scheduling blocks. The following is a general template:

```
# Scans for SB ID [number - doesn't matter]

# Output created on [Ddd Mmm DD HH:MM:SS UTC YYYY - doesn't matter]

#               PI - 5638
#          Project - 13B-041
#    Program Block - C
# Scheduling Block - DDO155 (S) Rise
#           Status - Not Submitted
#    Approx Length - [HH.HH - doesn't matter] hours
# LST Start Ranges - 09:00:00-11:45:00,
#          API Max - 60.0d
#         Wind Max - 100.0m/s

VERSION; 3;

 SRC-CAT; 13B-041,VLA,;
HDWR-CAT; 13B-041,NRAO Defaults,;

SCHED-BLOCK; DDO155 (S) Rise; Dynamic; 1; 2014-11-19; 09:00:00-11:45:00, ; 0.0; C; 225.0; \
  35.0; N; N; w=100.0,p=60.0; \
  Do not execute if Scheduling Block ID [enter ID] has been/will be observed.;

  STD; Dummy S; 1331+305=3C286; S16f5DC; DUR; 0h 1m 0s; CCW; N; N; N; N; SetAtnGain,; ;
  LOOP-START; Flux S; 10; N; ;
    STD; ; 1331+305=3C286; S16f5DC; DUR; 0h 1m 0s; ; N; N; N; N; CalBP,CalFlux,CalPolAng,CalPolLeak,; ;
  LOOP-END;
  LOOP-START; Target-Gain Loop; 3; N; ;
    LOOP-START; Target S; 12; N; ;
      STD; ; DDO155; S16f5DC; DUR; 0h 1m 0s; ; N; N; N; N; ObsTgt,; ;
    LOOP-END;
    LOOP-START; Gain S; 6; N; ;
      STD; ; J1254+1141; S16f5DC; DUR; 0h 1m 0s; ; N; N; N; N; CalGain,; ;
    LOOP-END;
  LOOP-END;
  LOOP-START; Flux S; 10; N; ;
    STD; ; 1331+305=3C286; S16f5DC; DUR; 0h 1m 0s; ; N; N; N; N; CalBP,CalFlux,CalPolAng,CalPolLeak,; ;
  LOOP-END;
```

C

4–8 GHz Radio Continuum Images of the LITTLE THINGS sample

In this section, we provide images of LITTLE THINGS. We show RC flux density contours superposed on ancillary LITTLE THINGS images (Hunter et al., 2012). As the dwarf galaxies are faint, extended RC emission does not show well when plotting contours at the native resolution. Therefore, for the lowest surface brightness contour, we smooth the RC image with a Gaussian kernel up to 2.5 times the native resolution, and use a contour level of $2.5\,\sigma_{\rm smooth}$ where $\sigma_{\rm smooth}$ is the rms noise in the smoothed map. The remaining contours are drawn at $(2+2^n)\sigma_{\rm native}$, where $\sigma_{\rm native}$ is the rms noise in the original maps (i.e., before smoothing) and $n \geq 0$. Where the ancillary data were available, we also show the following images: Hα; *GALEX* FUV; *Spitzer* 24 and 70μm images; FUV-inferred $\Sigma_{\rm SFR}$ from Leroy et al. (2012).

We provide images of the following dwarf galaxies: CVn I DwA (Figure C.1), DDO 43 (Figure C.2), DDO 46 (Figure C.3), DDO 47 (Figure C.4), DDO 50 (Figure C.5), DDO 52 (Figure C.6), DDO 53 (Figure C.7), DDO 63 (Figure C.8), DDO 69 (Figure C.9), DDO 70 (Figure C.10), DDO 75 (Figure C.11), DDO 87 (Figure C.12), DDO 101 (Figure C.13), DDO 126 (Figure C.14), DDO 133 (Figure C.15), DDO 154 (Figure C.16),

DDO 155 (Figure C.17), DDO 165 (Figure C.18), DDO 167 (Figure C.19), DDO 168 (Figure C.20), DDO 187 (Figure C.21), DDO 210 (Figure C.22), DDO 216 (Figure C.23), F564 V3 (Figure C.24), Haro 29 (Figure C.25), Haro 36 (Figure C.26), IC 10 (Figure C.27), IC 1613 (Figure C.28), LGS 3 (Figure C.29), M81 DwA (Figure C.30), Mrk 178 (Figure C.31), NGC 1569 (Figure C.32), NGC 2366 (Figure C.33), NGC 3738 (Figure C.34), NGC 4163 (Figure C.35), NGC 4214 (Figure C.36), Sag DIG (Figure C.37), UGC 8508 (Figure C.38), VII Zw 403 (Figure C.39), and WLM (Figure C.40).

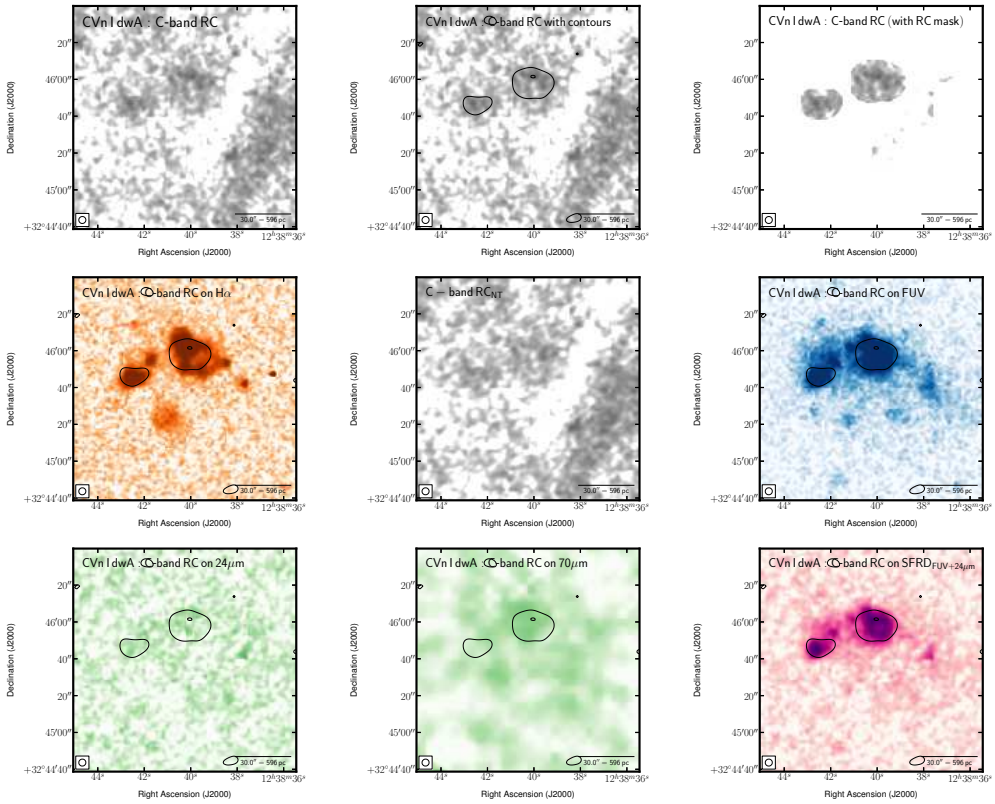

FIGURE C.1: Multi-wavelength coverage of CVn I dwA displaying a $2.0' \times 2.0'$ area. We show total RC flux density at the native resolution (top left) and again with contours (top centre). The lowest contour highlights low–surface brightness emission at a level of $28.5\,\mu\mathrm{Jy\,beam^{-1}}$—this is 2.5 times the rms after smoothing the native image by a factor of 2.5. The other contours are placed following $(2 + 2^n)\sigma_{\mathrm{native}}$, where $n \geq 0$ and both the rms ($\sigma_{\mathrm{native}} = 4.56\,\mu\mathrm{Jy\,beam^{-1}}$) and the resolution ($\mathrm{FWHM_{native}} = 3.8 \times 3.8$ arcsec) are taken from the native resolution image. These same contours are also superposed on ancillary LITTLE THINGS images where possible: Hα (middle left); $\mathrm{RC_{NTh}}$ obtained by subtracting the expected $\mathrm{RC_{Th}}$ based on the Hα-$\mathrm{RC_{Th}}$ scaling factor of Deeg et al. (1997) from the total RC; *GALEX* FUV (middle right); *Spitzer* $24\,\mu\mathrm{m}$ (bottom left); *Spitzer* $70\,\mu\mathrm{m}$ (bottom centre); FUV+24μm–inferred SFRD from Leroy et al., 2012 (bottom right). We also show the RC that was isolated by the RC–based masking technique (top right). The greyscale intensity scales used are arbitrary to best highlight structure.

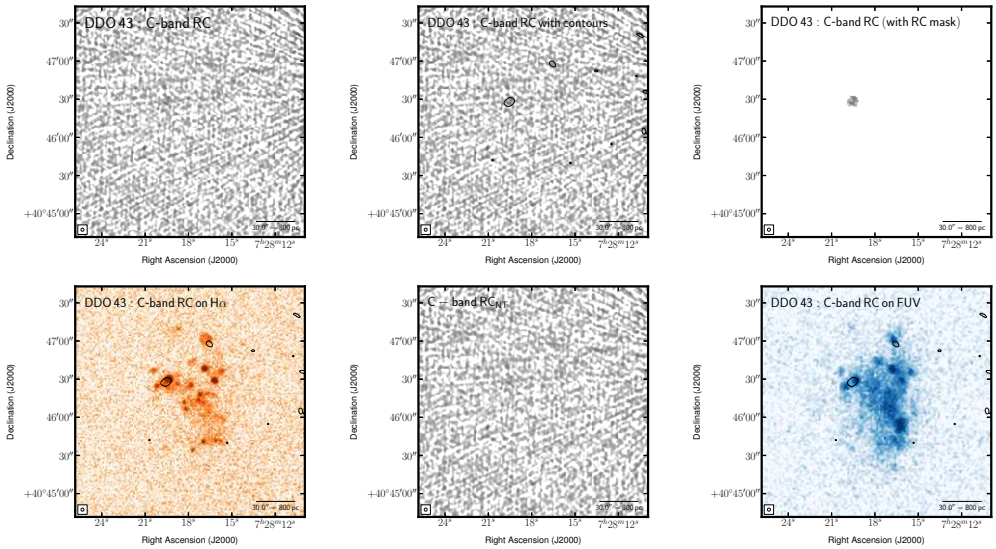

FIGURE C.2: Multi-wavelength coverage of DDO 43 displaying a $3.0' \times 3.0'$ area. We show total RC flux density at the native resolution (top left) and again with contours (top centre). The lowest contour highlights low–surface brightness emission at a level of $43.1\,\mu\mathrm{Jy\,beam^{-1}}$—this is 2.5 times the rms after smoothing the native image by a factor of 2.5. The other contours are placed following $(2 + 2^n)\sigma_{\mathrm{native}}$, where $n \geq 0$ and both the rms ($\sigma_{\mathrm{native}} = 6.89\,\mu\mathrm{Jy\,beam^{-1}}$) and the resolution ($\mathrm{FWHM_{native}} = 2.5 \times 2.3$ arcsec) are taken from the native resolution image. These same contours are also superposed on ancillary LITTLE THINGS images where possible: Hα (middle left); $\mathrm{RC_{NTh}}$ obtained by subtracting the expected $\mathrm{RC_{Th}}$ based on the Hα-$\mathrm{RC_{Th}}$ scaling factor of Deeg et al. (1997) from the total RC; *GALEX* FUV (middle right). We also show the RC that was isolated by the RC–based masking technique (top right). The greyscale intensity scales used are arbitrary to best highlight structure.

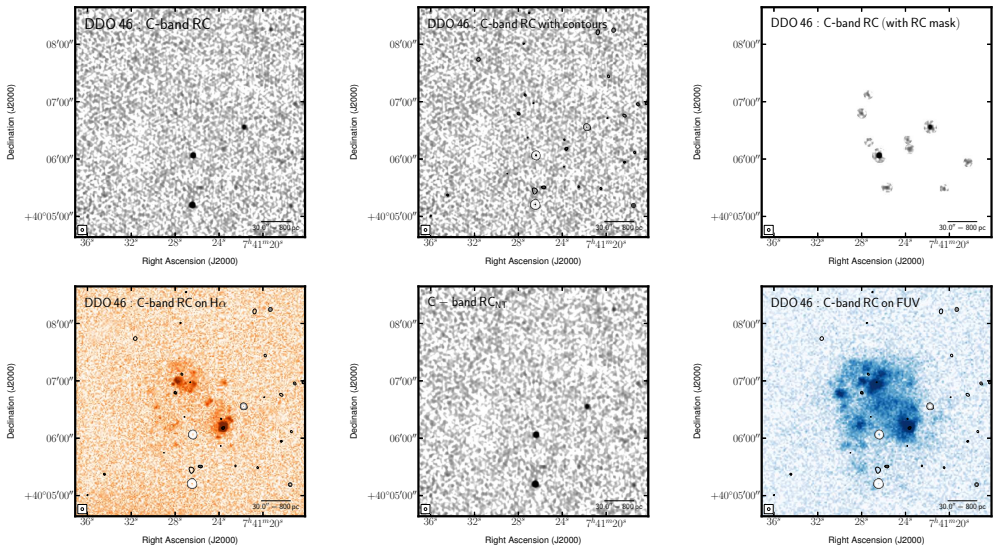

FIGURE C.3: Multi-wavelength coverage of DDO 46 displaying a $4.0' \times 4.0'$ area. We show total RC flux density at the native resolution (top left) and again with contours (top centre). The lowest contour highlights low–surface brightness emission at a level of $31.7\,\mu\mathrm{Jy\,beam^{-1}}$—this is 2.5 times the rms after smoothing the native image by a factor of 2.5. The other contours are placed following $(2 + 2^n)\sigma_{\mathrm{native}}$, where $n \geq 0$ and both the rms ($\sigma_{\mathrm{native}} = 5.06\,\mu\mathrm{Jy\,beam^{-1}}$) and the resolution ($\mathrm{FWHM_{native}} = 3.0 \times 2.8$ arcsec) are taken from the native resolution image. These same contours are also superposed on ancillary LITTLE THINGS images where possible: Hα (middle left); $\mathrm{RC_{NTh}}$ obtained by subtracting the expected $\mathrm{RC_{Th}}$ based on the Hα-$\mathrm{RC_{Th}}$ scaling factor of Deeg et al. (1997) from the total RC; *GALEX* FUV (middle right). We also show the RC that was isolated by the RC–based masking technique (top right). The greyscale intensity scales used are arbitrary to best highlight structure.

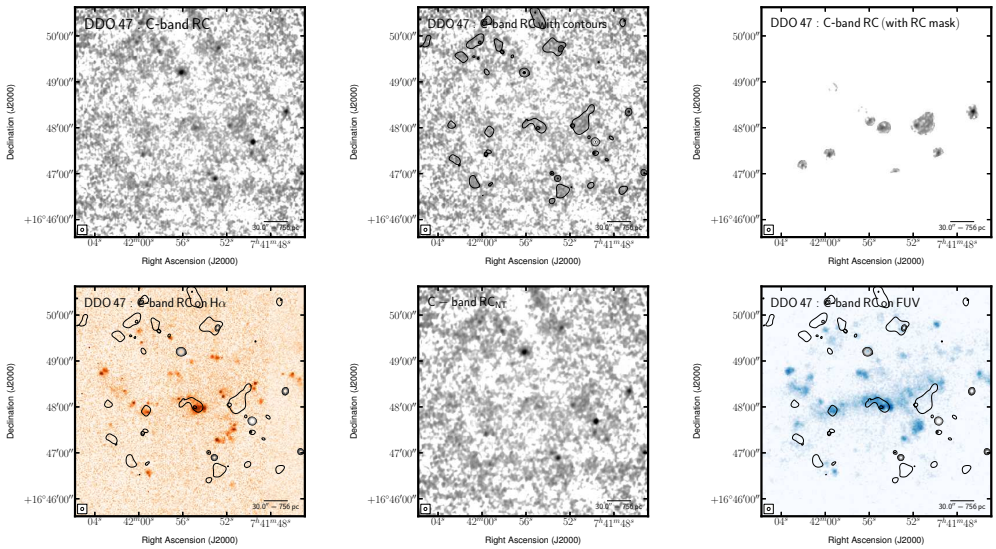

FIGURE C.4: Multi-wavelength coverage of DDO 47 displaying a $5.0' \times 5.0'$ area. We show total RC flux density at the native resolution (top left) and again with contours (top centre). The lowest contour highlights low–surface brightness emission at a level of $26.8\,\mu\mathrm{Jy\,beam^{-1}}$—this is 2.5 times the rms after smoothing the native image by a factor of 2.5. The other contours are placed following $(2 + 2^n)\sigma_{\mathrm{native}}$, where $n \geq 0$ and both the rms ($\sigma_{\mathrm{native}} = 4.29\,\mu\mathrm{Jy\,beam^{-1}}$) and the resolution ($\mathrm{FWHM_{native}} = 4.1 \times 3.8$ arcsec) are taken from the native resolution image. These same contours are also superposed on ancillary LITTLE THINGS images where possible: Hα (middle left); $\mathrm{RC_{NTh}}$ obtained by subtracting the expected $\mathrm{RC_{Th}}$ based on the Hα-$\mathrm{RC_{Th}}$ scaling factor of Deeg et al. (1997) from the total RC; *GALEX* FUV (middle right). We also show the RC that was isolated by the RC–based masking technique (top right). The greyscale intensity scales used are arbitrary to best highlight structure.

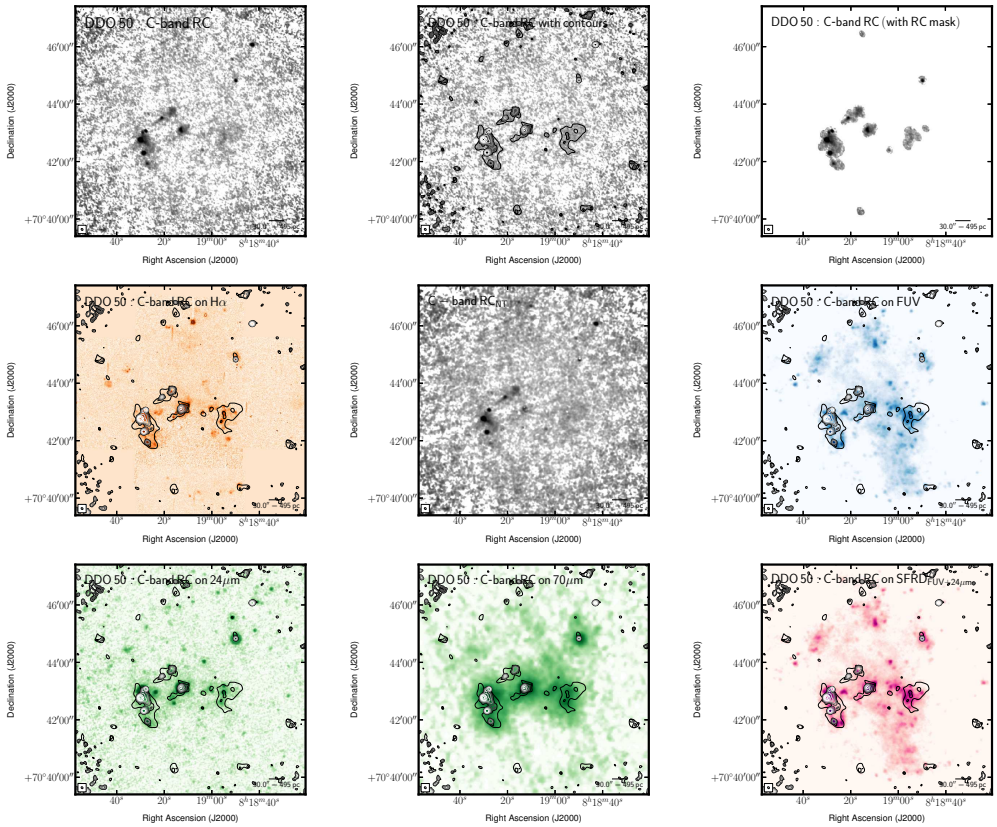

FIGURE C.5: Multi-wavelength coverage of DDO 50 displaying a $8.0' \times 8.0'$ area. We show total RC flux density at the native resolution (top left) and again with contours (top centre). The lowest contour highlights low–surface brightness emission at a level of $34.4\,\mu\mathrm{Jy\,beam^{-1}}$—this is 2.5 times the rms after smoothing the native image by a factor of 2.5. The other contours are placed following $(2 + 2^n)\sigma_{\mathrm{native}}$, where $n \geq 0$ and both the rms ($\sigma_{\mathrm{native}} = 5.50\,\mu\mathrm{Jy\,beam^{-1}}$) and the resolution ($\mathrm{FWHM_{native}} = 4.4 \times 3.5$ arcsec) are taken from the native resolution image. These same contours are also superposed on ancillary LITTLE THINGS images where possible: Hα (middle left); $\mathrm{RC_{NTh}}$ obtained by subtracting the expected $\mathrm{RC_{Th}}$ based on the Hα-$\mathrm{RC_{Th}}$ scaling factor of Deeg et al. (1997) from the total RC; *GALEX* FUV (middle right); *Spitzer* 24 μm (bottom left); *Spitzer* 70 μm (bottom centre); FUV+24μm–inferred SFRD from Leroy et al., 2012 (bottom right). We also show the RC that was isolated by the RC–based masking technique (top right). The greyscale intensity scales used are arbitrary to best highlight structure.

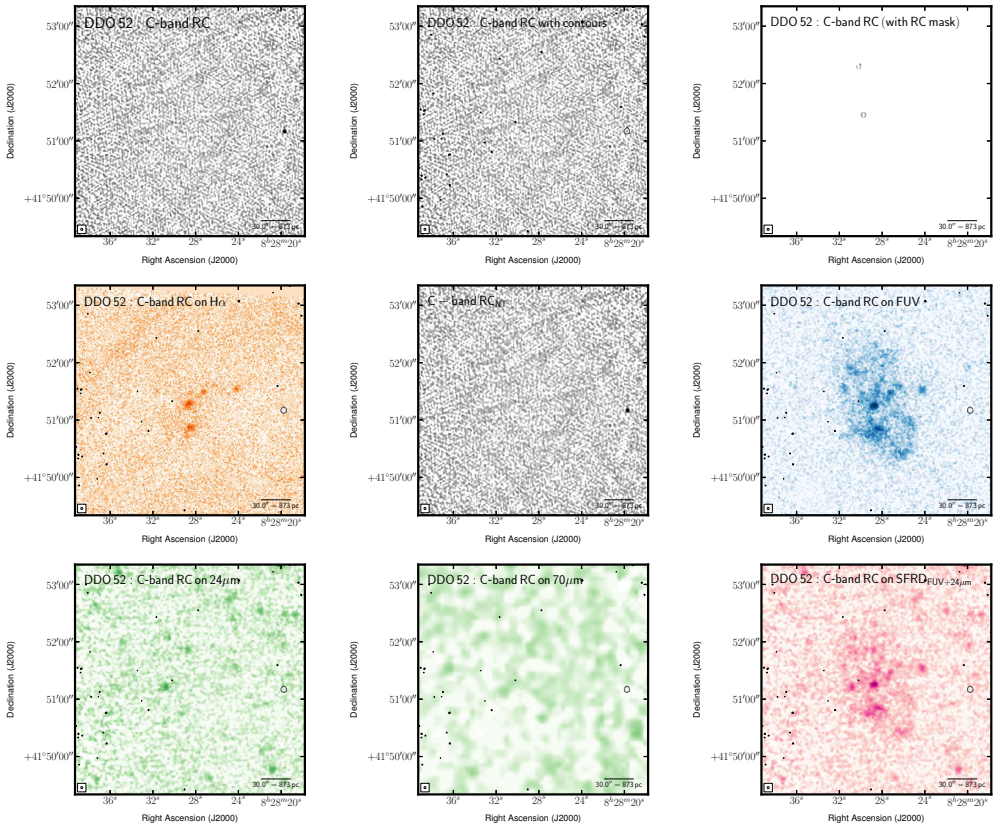

FIGURE C.6: Multi-wavelength coverage of DDO 52 displaying a $4.0' \times 4.0'$ area. We show total RC flux density at the native resolution (top left) and again with contours (top centre). The lowest contour highlights low–surface brightness emission at a level of $51.8\,\mu\mathrm{Jy\,beam^{-1}}$—this is 2.5 times the rms after smoothing the native image by a factor of 2.5. The other contours are placed following $(2 + 2^n)\sigma_{\mathrm{native}}$, where $n \geq 0$ and both the rms ($\sigma_{\mathrm{native}} = 8.29\,\mu\mathrm{Jy\,beam^{-1}}$) and the resolution ($\mathrm{FWHM_{native}} = 2.2 \times 2.0$ arcsec) are taken from the native resolution image. These same contours are also superposed on ancillary LITTLE THINGS images where possible: Hα (middle left); $\mathrm{RC_{NTh}}$ obtained by subtracting the expected $\mathrm{RC_{Th}}$ based on the Hα-$\mathrm{RC_{Th}}$ scaling factor of Deeg et al. (1997) from the total RC; *GALEX* FUV (middle right); *Spitzer* 24 μm (bottom left); *Spitzer* 70 μm (bottom centre); FUV+24μm–inferred SFRD from Leroy et al., 2012 (bottom right). We also show the RC that was isolated by the RC–based masking technique (top right). The greyscale intensity scales used are arbitrary to best highlight structure.

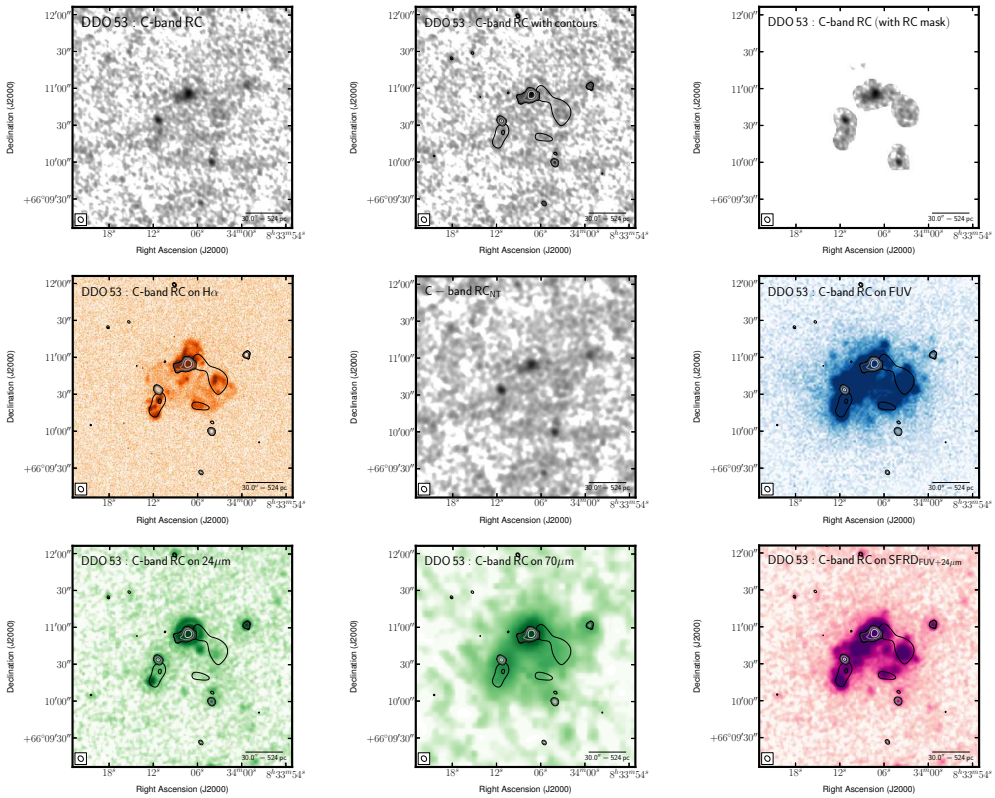

FIGURE C.7: Multi-wavelength coverage of DDO 53 displaying a $3.6' \times 3.6'$ area. We show total RC flux density at the native resolution (top left) and again with contours (top centre). The lowest contour highlights low–surface brightness emission at a level of $34.0\,\mu\mathrm{Jy\,beam^{-1}}$—this is 2.5 times the rms after smoothing the native image by a factor of 2.5. The other contours are placed following $(2 + 2^n)\sigma_{\mathrm{native}}$, where $n \geq 0$ and both the rms ($\sigma_{\mathrm{native}} = 5.44\,\mu\mathrm{Jy\,beam^{-1}}$) and the resolution ($\mathrm{FWHM_{native}} = 4.9 \times 4.0$ arcsec) are taken from the native resolution image. These same contours are also superposed on ancillary LITTLE THINGS images where possible: Hα (middle left); $\mathrm{RC_{NTh}}$ obtained by subtracting the expected $\mathrm{RC_{Th}}$ based on the Hα-$\mathrm{RC_{Th}}$ scaling factor of Deeg et al. (1997) from the total RC; *GALEX* FUV (middle right); *Spitzer* 24 μm (bottom left); *Spitzer* 70 μm (bottom centre); FUV+24μm–inferred SFRD from Leroy et al., 2012 (bottom right). We also show the RC that was isolated by the RC–based masking technique (top right). The greyscale intensity scales used are arbitrary to best highlight structure.

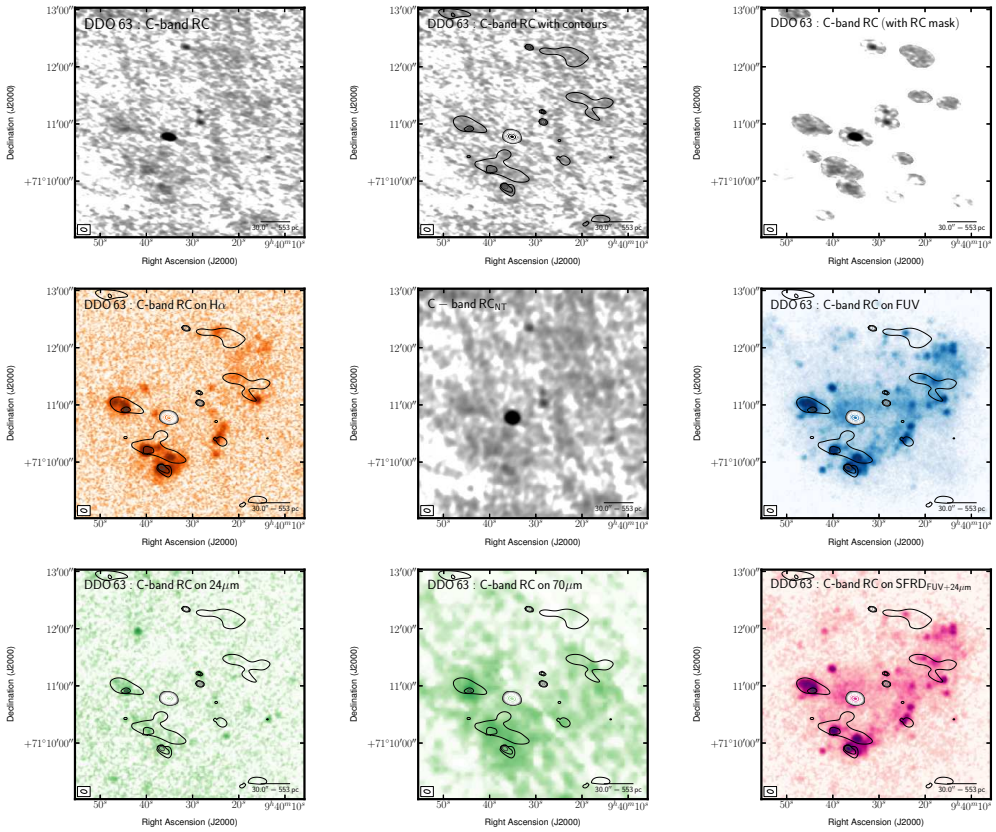

FIGURE C.8: Multi-wavelength coverage of DDO 63 displaying a $4.0' \times 4.0'$ area. We show total RC flux density at the native resolution (top left) and again with contours (top centre). The lowest contour highlights low–surface brightness emission at a level of $26.7\,\mu\mathrm{Jy\,beam^{-1}}$—this is 2.5 times the rms after smoothing the native image by a factor of 2.5. The other contours are placed following $(2 + 2^n)\sigma_{\mathrm{native}}$, where $n \geq 0$ and both the rms ($\sigma_{\mathrm{native}} = 4.28\,\mu\mathrm{Jy\,beam^{-1}}$) and the resolution ($\mathrm{FWHM_{native}} = 6.7 \times 3.7$ arcsec) are taken from the native resolution image. These same contours are also superposed on ancillary LITTLE THINGS images where possible: Hα (middle left); $\mathrm{RC_{NTh}}$ obtained by subtracting the expected $\mathrm{RC_{Th}}$ based on the Hα-$\mathrm{RC_{Th}}$ scaling factor of Deeg et al. (1997) from the total RC; *GALEX* FUV (middle right); *Spitzer* 24 μm (bottom left); *Spitzer* 70 μm (bottom centre); FUV+24μm–inferred SFRD from Leroy et al., 2012 (bottom right). We also show the RC that was isolated by the RC–based masking technique (top right). The greyscale intensity scales used are arbitrary to best highlight structure.

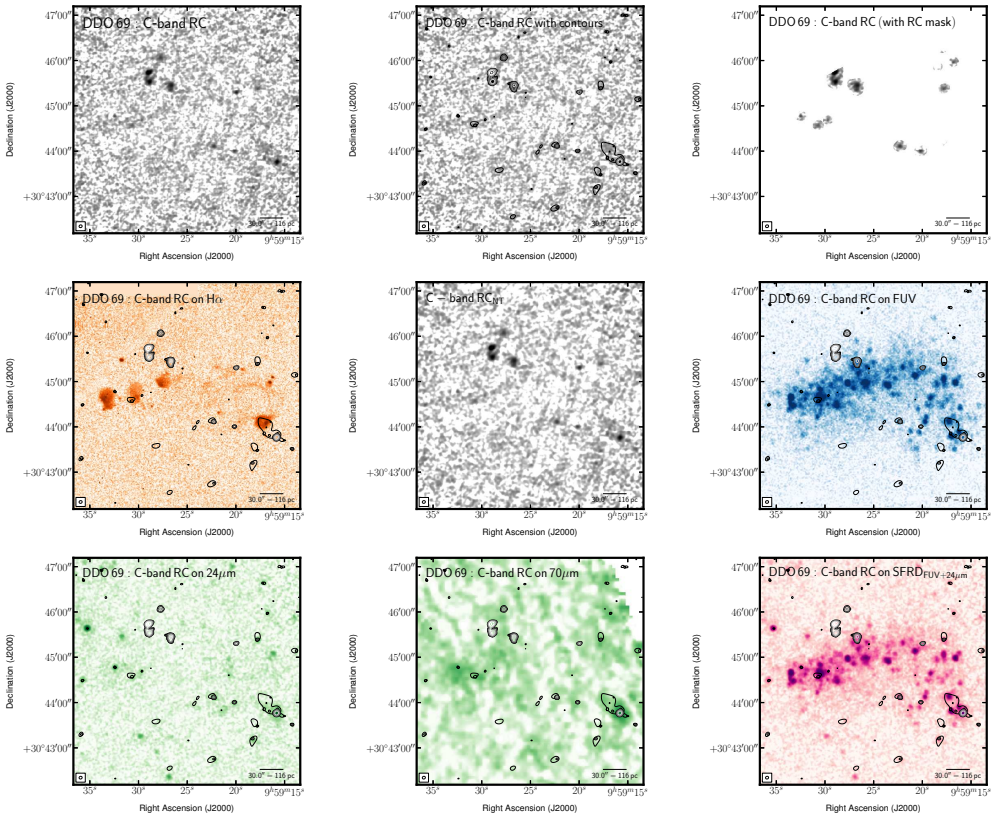

FIGURE C.9: Multi-wavelength coverage of DDO 69 displaying a $5.0' \times 5.0'$ area. We show total RC flux density at the native resolution (top left) and again with contours (top centre). The lowest contour highlights low–surface brightness emission at a level of $24.8\,\mu\mathrm{Jy\,beam^{-1}}$—this is 2.5 times the rms after smoothing the native image by a factor of 2.5. The other contours are placed following $(2 + 2^n)\sigma_{\mathrm{native}}$, where $n \geq 0$ and both the rms ($\sigma_{\mathrm{native}} = 3.97\,\mu\mathrm{Jy\,beam^{-1}}$) and the resolution ($\mathrm{FWHM_{native}} = 4.1 \times 3.6$ arcsec) are taken from the native resolution image. These same contours are also superposed on ancillary LITTLE THINGS images where possible: Hα (middle left); $\mathrm{RC_{NTh}}$ obtained by subtracting the expected $\mathrm{RC_{Th}}$ based on the Hα-$\mathrm{RC_{Th}}$ scaling factor of Deeg et al. (1997) from the total RC; *GALEX* FUV (middle right); *Spitzer* $24\,\mu\mathrm{m}$ (bottom left); *Spitzer* $70\,\mu\mathrm{m}$ (bottom centre); FUV+24μm–inferred SFRD from Leroy et al., 2012 (bottom right). We also show the RC that was isolated by the RC–based masking technique (top right). The greyscale intensity scales used are arbitrary to best highlight structure.

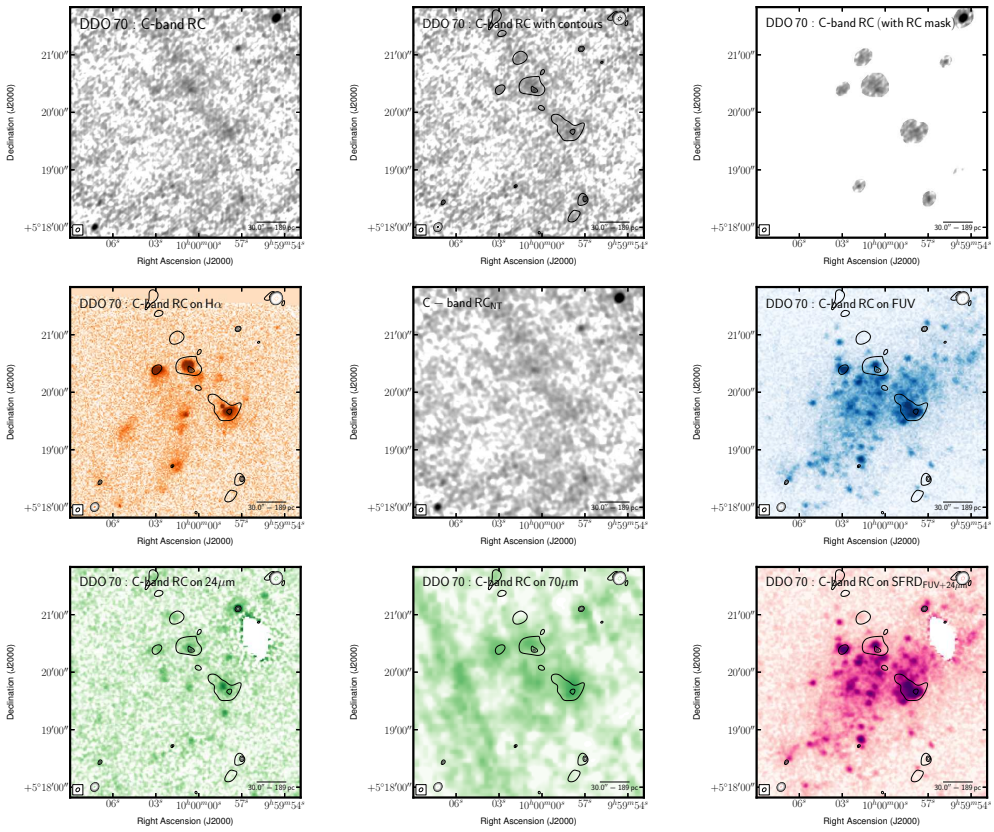

FIGURE C.10: Multi-wavelength coverage of DDO 70 displaying a $4.0' \times 4.0'$ area. We show total RC flux density at the native resolution (top left) and again with contours (top centre). The lowest contour highlights low–surface brightness emission at a level of $36.2\,\mu\mathrm{Jy\,beam^{-1}}$—this is 2.5 times the rms after smoothing the native image by a factor of 2.5. The other contours are placed following $(2 + 2^n)\sigma_{\mathrm{native}}$, where $n \geq 0$ and both the rms ($\sigma_{\mathrm{native}} = 5.80\,\mu\mathrm{Jy\,beam^{-1}}$) and the resolution ($\mathrm{FWHM_{native}} = 4.5 \times 3.4$ arcsec) are taken from the native resolution image. These same contours are also superposed on ancillary LITTLE THINGS images where possible: Hα (middle left); $\mathrm{RC_{NTh}}$ obtained by subtracting the expected $\mathrm{RC_{Th}}$ based on the Hα-$\mathrm{RC_{Th}}$ scaling factor of Deeg et al. (1997) from the total RC; *GALEX* FUV (middle right); *Spitzer* 24 μm (bottom left); *Spitzer* 70 μm (bottom centre); FUV+24μm–inferred SFRD from Leroy et al., 2012 (bottom right). We also show the RC that was isolated by the RC–based masking technique (top right). The greyscale intensity scales used are arbitrary to best highlight structure.

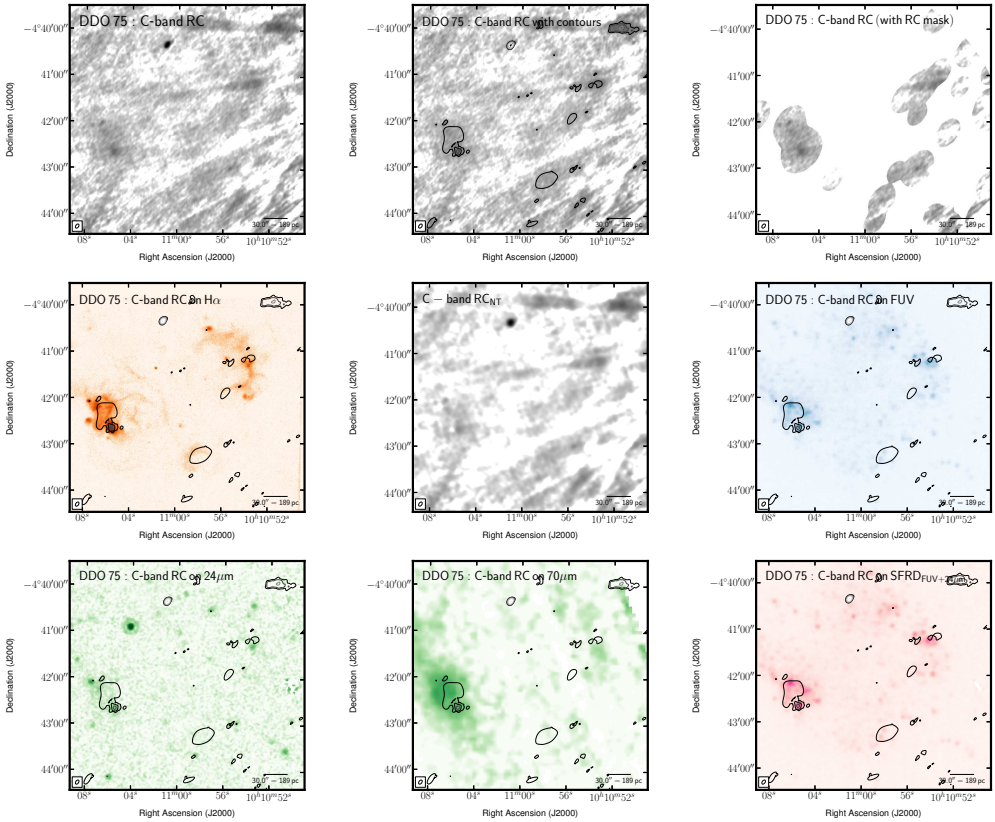

FIGURE C.11: Multi-wavelength coverage of DDO 75 displaying a $6.3' \times 6.3'$ area. We show total RC flux density at the native resolution (top left) and again with contours (top centre). The lowest contour highlights low–surface brightness emission at a level of $82.6\,\mu\mathrm{Jy\,beam^{-1}}$—this is 2.5 times the rms after smoothing the native image by a factor of 2.5. The other contours are placed following $(2 + 2^n)\sigma_{\mathrm{native}}$, where $n \geq 0$ and both the rms ($\sigma_{\mathrm{native}} = 13.22\,\mu\mathrm{Jy\,beam^{-1}}$) and the resolution ($\mathrm{FWHM_{native}} = 6.0 \times 3.8$ arcsec) are taken from the native resolution image. These same contours are also superposed on ancillary LITTLE THINGS images where possible: Hα (middle left); $\mathrm{RC_{NTh}}$ obtained by subtracting the expected $\mathrm{RC_{Th}}$ based on the Hα-$\mathrm{RC_{Th}}$ scaling factor of Deeg et al. (1997) from the total RC; *GALEX* FUV (middle right); *Spitzer* $24\,\mu\mathrm{m}$ (bottom left); *Spitzer* $70\,\mu\mathrm{m}$ (bottom centre); FUV+24μm–inferred SFRD from Leroy et al., 2012 (bottom right). We also show the RC that was isolated by the RC–based masking technique (top right). The greyscale intensity scales used are arbitrary to best highlight structure.

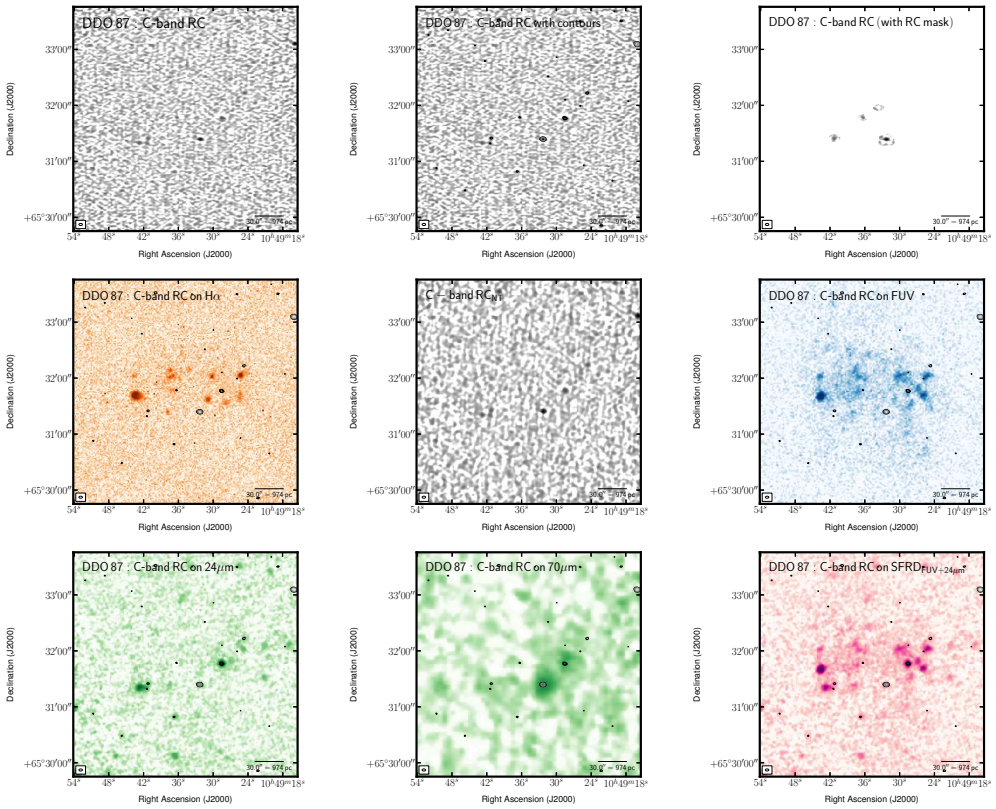

FIGURE C.12: Multi-wavelength coverage of DDO 87 displaying a $4.0' \times 4.0'$ area. We show total RC flux density at the native resolution (top left) and again with contours (top centre). The lowest contour highlights low–surface brightness emission at a level of $38.8\,\mu\mathrm{Jy\,beam^{-1}}$—this is 2.5 times the rms after smoothing the native image by a factor of 2.5. The other contours are placed following $(2 + 2^n)\sigma_{\mathrm{native}}$, where $n \geq 0$ and both the rms ($\sigma_{\mathrm{native}} = 6.21\,\mu\mathrm{Jy\,beam^{-1}}$) and the resolution ($\mathrm{FWHM_{native}} = 3.8 \times 2.2$ arcsec) are taken from the native resolution image. These same contours are also superposed on ancillary LITTLE THINGS images where possible: Hα (middle left); $\mathrm{RC_{NTh}}$ obtained by subtracting the expected $\mathrm{RC_{Th}}$ based on the Hα-$\mathrm{RC_{Th}}$ scaling factor of Deeg et al. (1997) from the total RC; *GALEX* FUV (middle right); *Spitzer* 24 μm (bottom left); *Spitzer* 70 μm (bottom centre); FUV+24μm–inferred SFRD from Leroy et al., 2012 (bottom right). We also show the RC that was isolated by the RC–based masking technique (top right). The greyscale intensity scales used are arbitrary to best highlight structure.

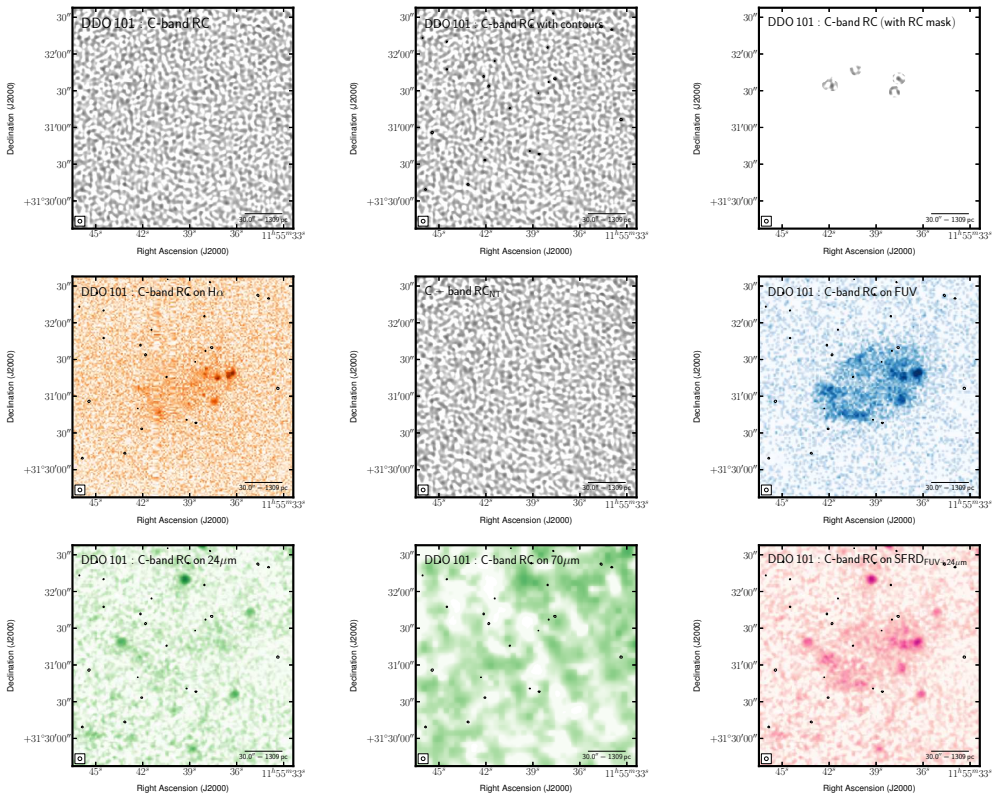

FIGURE C.13: Multi-wavelength coverage of DDO 101 displaying a $3.0' \times 3.0'$ area. We show total RC flux density at the native resolution (top left) and again with contours (top centre). The lowest contour highlights low–surface brightness emission at a level of $94.3\,\mu\mathrm{Jy\,beam^{-1}}$—this is 2.5 times the rms after smoothing the native image by a factor of 2.5. The other contours are placed following $(2 + 2^n)\sigma_{\mathrm{native}}$, where $n \geq 0$ and both the rms ($\sigma_{\mathrm{native}} = 15.09\,\mu\mathrm{Jy\,beam^{-1}}$) and the resolution ($\mathrm{FWHM_{native}} = 3.1 \times 3.0$ arcsec) are taken from the native resolution image. These same contours are also superposed on ancillary LITTLE THINGS images where possible: Hα (middle left); $\mathrm{RC_{NTh}}$ obtained by subtracting the expected $\mathrm{RC_{Th}}$ based on the Hα-$\mathrm{RC_{Th}}$ scaling factor of Deeg et al. (1997) from the total RC; *GALEX* FUV (middle right); *Spitzer* 24 μm (bottom left); *Spitzer* 70 μm (bottom centre); FUV+24μm–inferred SFRD from Leroy et al., 2012 (bottom right). We also show the RC that was isolated by the RC–based masking technique (top right). The greyscale intensity scales used are arbitrary to best highlight structure.

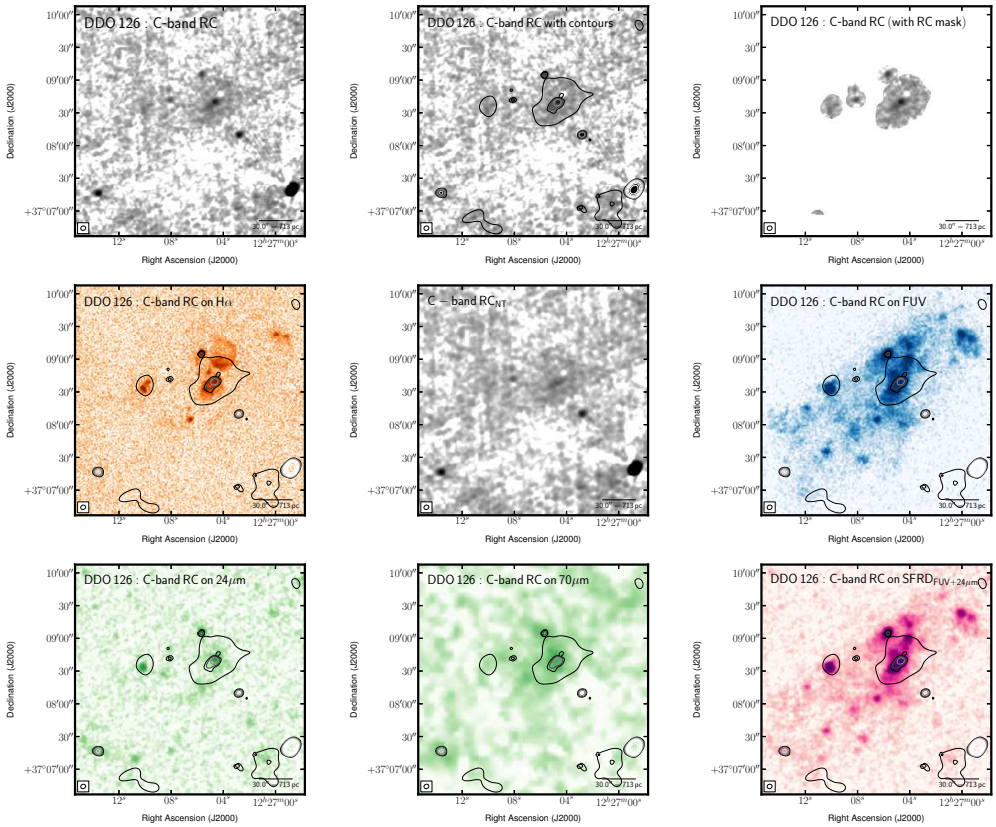

FIGURE C.14: Multi-wavelength coverage of DDO 126 displaying a $3.5' \times 3.5'$ area. We show total RC flux density at the native resolution (top left) and again with contours (top centre). The lowest contour highlights low–surface brightness emission at a level of $33.5\,\mu\mathrm{Jy\,beam^{-1}}$—this is 2.5 times the rms after smoothing the native image by a factor of 2.5. The other contours are placed following $(2 + 2^n)\sigma_{\mathrm{native}}$, where $n \geq 0$ and both the rms ($\sigma_{\mathrm{native}} = 5.36\,\mu\mathrm{Jy\,beam^{-1}}$) and the resolution ($\mathrm{FWHM_{native}} = 4.6 \times 4.0$ arcsec) are taken from the native resolution image. These same contours are also superposed on ancillary LITTLE THINGS images where possible: Hα (middle left); $\mathrm{RC_{NTh}}$ obtained by subtracting the expected $\mathrm{RC_{Th}}$ based on the Hα-$\mathrm{RC_{Th}}$ scaling factor of Deeg et al. (1997) from the total RC; *GALEX* FUV (middle right); *Spitzer* 24 μm (bottom left); *Spitzer* 70 μm (bottom centre); FUV+24μm–inferred SFRD from Leroy et al., 2012 (bottom right). We also show the RC that was isolated by the RC–based masking technique (top right). The greyscale intensity scales used are arbitrary to best highlight structure.

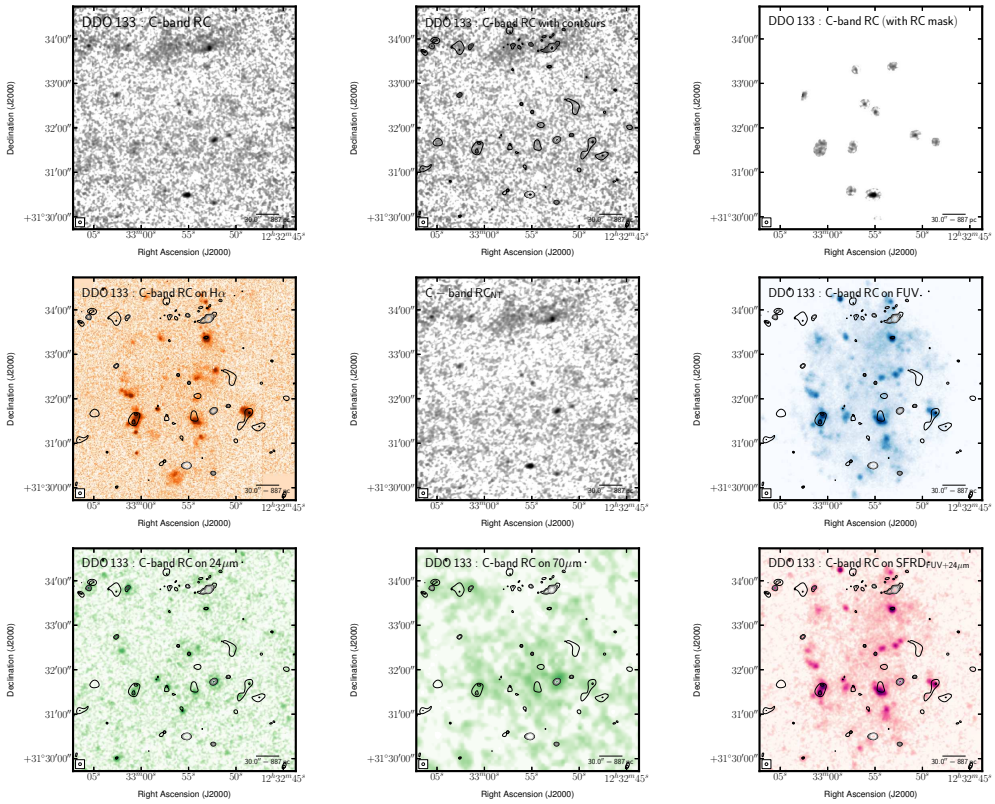

FIGURE C.15: Multi-wavelength coverage of DDO 133 displaying a $5.0' \times 5.0'$ area. We show total RC flux density at the native resolution (top left) and again with contours (top centre). The lowest contour highlights low–surface brightness emission at a level of $27.2\,\mu\mathrm{Jy\,beam^{-1}}$—this is 2.5 times the rms after smoothing the native image by a factor of 2.5. The other contours are placed following $(2 + 2^n)\sigma_{\mathrm{native}}$, where $n \geq 0$ and both the rms ($\sigma_{\mathrm{native}} = 4.36\,\mu\mathrm{Jy\,beam^{-1}}$) and the resolution ($\mathrm{FWHM_{native}} = 3.8 \times 3.7$ arcsec) are taken from the native resolution image. These same contours are also superposed on ancillary LITTLE THINGS images where possible: Hα (middle left); $\mathrm{RC_{NTh}}$ obtained by subtracting the expected $\mathrm{RC_{Th}}$ based on the Hα-$\mathrm{RC_{Th}}$ scaling factor of Deeg et al. (1997) from the total RC; *GALEX* FUV (middle right); *Spitzer* 24 μm (bottom left); *Spitzer* 70 μm (bottom centre); FUV+24μm–inferred SFRD from Leroy et al., 2012 (bottom right). We also show the RC that was isolated by the RC–based masking technique (top right). The greyscale intensity scales used are arbitrary to best highlight structure.

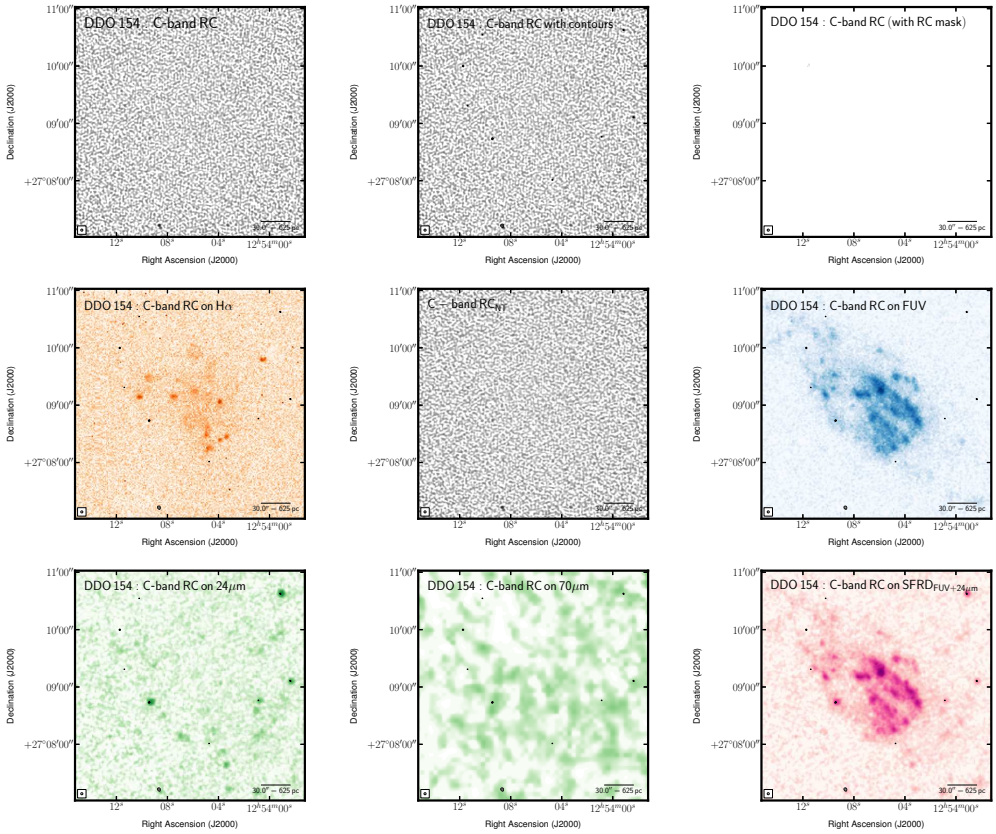

FIGURE C.16: Multi-wavelength coverage of DDO 154 displaying a $4.0' \times 4.0'$ area. We show total RC flux density at the native resolution (top left) and again with contours (top centre). The lowest contour highlights low–surface brightness emission at a level of $45.6\,\mu\mathrm{Jy\,beam^{-1}}$—this is 2.5 times the rms after smoothing the native image by a factor of 2.5. The other contours are placed following $(2 + 2^n)\sigma_{\mathrm{native}}$, where $n \geq 0$ and both the rms ($\sigma_{\mathrm{native}} = 7.29\,\mu\mathrm{Jy\,beam^{-1}}$) and the resolution ($\mathrm{FWHM_{native}} = 2.2 \times 2.2$ arcsec) are taken from the native resolution image. These same contours are also superposed on ancillary LITTLE THINGS images where possible: Hα (middle left); $\mathrm{RC_{NTh}}$ obtained by subtracting the expected $\mathrm{RC_{Th}}$ based on the Hα-$\mathrm{RC_{Th}}$ scaling factor of Deeg et al. (1997) from the total RC; *GALEX* FUV (middle right); *Spitzer* 24 μm (bottom left); *Spitzer* 70 μm (bottom centre); FUV+24μm–inferred SFRD from Leroy et al., 2012 (bottom right). We also show the RC that was isolated by the RC–based masking technique (top right). The greyscale intensity scales used are arbitrary to best highlight structure.

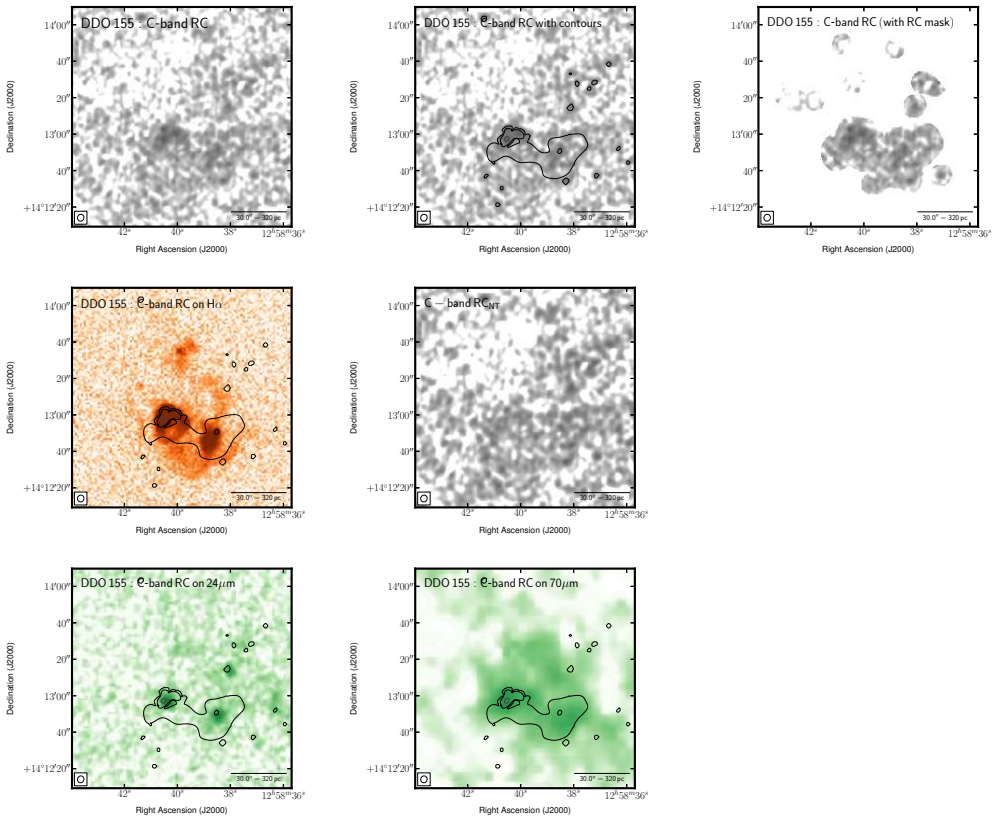

FIGURE C.17: Multi-wavelength coverage of DDO 155 displaying a $2.0' \times 2.0'$ area. We show total RC flux density at the native resolution (top left) and again with contours (top centre). The lowest contour highlights low–surface brightness emission at a level of $23.1\,\mu\mathrm{Jy\,beam^{-1}}$—this is 2.5 times the rms after smoothing the native image by a factor of 2.5. The other contours are placed following $(2 + 2^n)\sigma_{\mathrm{native}}$, where $n \geq 0$ and both the rms ($\sigma_{\mathrm{native}} = 3.70\,\mu\mathrm{Jy\,beam^{-1}}$) and the resolution ($\mathrm{FWHM_{native}} = 3.8 \times 3.5$ arcsec) are taken from the native resolution image. These same contours are also superposed on ancillary LITTLE THINGS images where possible: Hα (middle left); $\mathrm{RC_{NTh}}$ obtained by subtracting the expected $\mathrm{RC_{Th}}$ based on the Hα-$\mathrm{RC_{Th}}$ scaling factor of Deeg et al. (1997) from the total RC; *Spitzer* 24 μm (bottom left); *Spitzer* 70 μm (bottom centre). We also show the RC that was isolated by the RC–based masking technique (top right). The greyscale intensity scales used are arbitrary to best highlight structure.

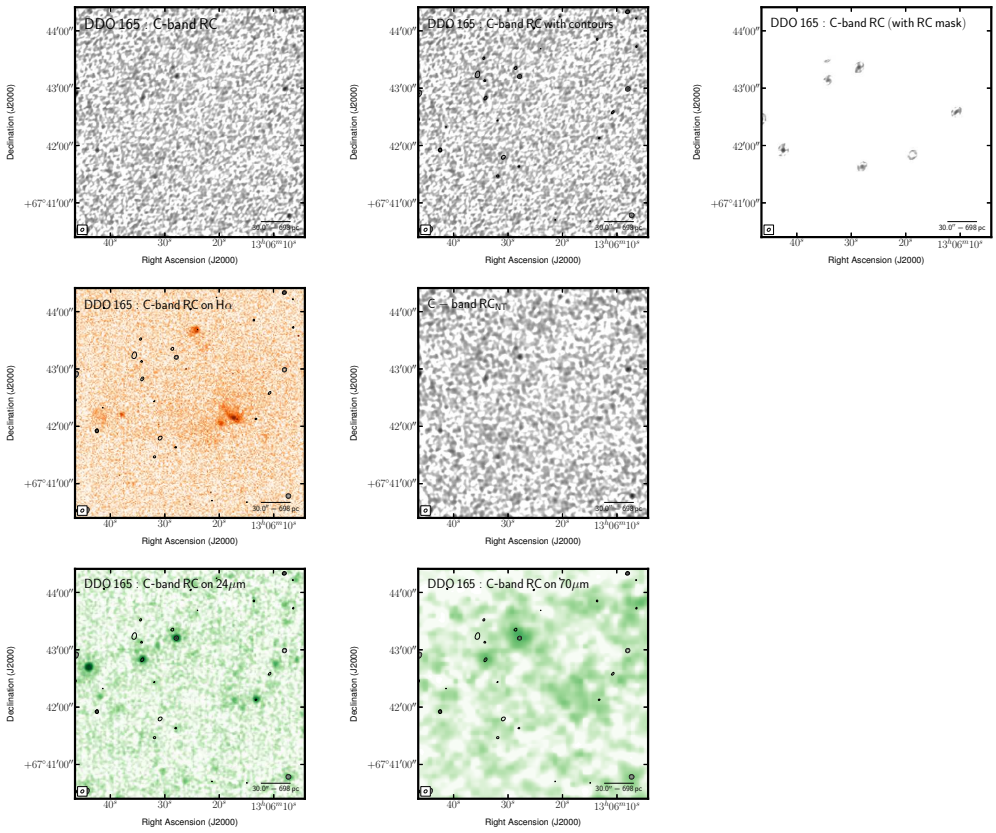

FIGURE C.18: Multi-wavelength coverage of DDO 165 displaying a $4.0' \times 4.0'$ area. We show total RC flux density at the native resolution (top left) and again with contours (top centre). The lowest contour highlights low–surface brightness emission at a level of $28.4\,\mu\mathrm{Jy\,beam^{-1}}$—this is 2.5 times the rms after smoothing the native image by a factor of 2.5. The other contours are placed following $(2 + 2^n)\sigma_{\mathrm{native}}$, where $n \geq 0$ and both the rms ($\sigma_{\mathrm{native}} = 4.54\,\mu\mathrm{Jy\,beam^{-1}}$) and the resolution ($\mathrm{FWHM_{native}} = 3.7 \times 2.8$ arcsec) are taken from the native resolution image. These same contours are also superposed on ancillary LITTLE THINGS images where possible: Hα (middle left); $\mathrm{RC_{NTh}}$ obtained by subtracting the expected $\mathrm{RC_{Th}}$ based on the Hα-$\mathrm{RC_{Th}}$ scaling factor of Deeg et al. (1997) from the total RC; *Spitzer* 24 μm (bottom left); *Spitzer* 70 μm (bottom centre). We also show the RC that was isolated by the RC–based masking technique (top right). The greyscale intensity scales used are arbitrary to best highlight structure.

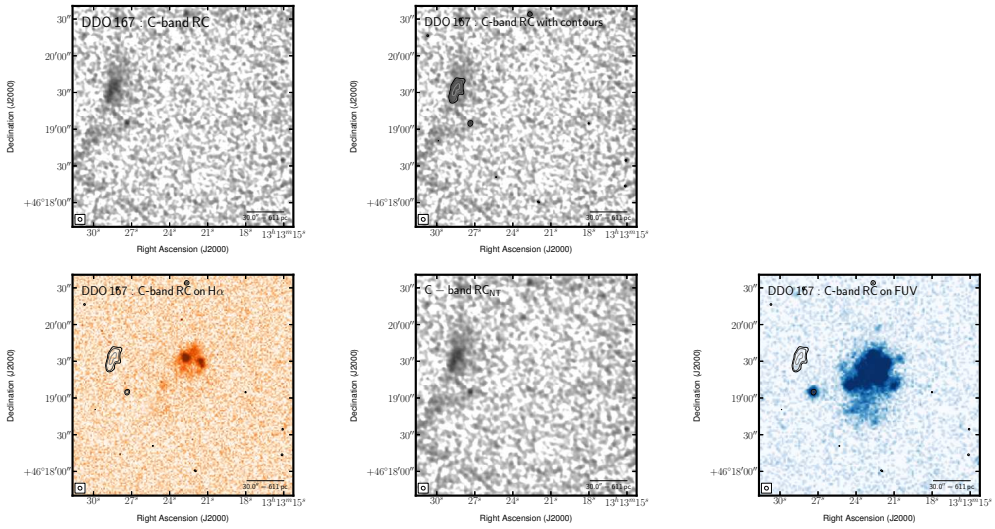

FIGURE C.19: Multi-wavelength coverage of DDO 167 displaying a $3.0' \times 3.0'$ area. We show total RC flux density at the native resolution (top left) and again with contours (top centre). The lowest contour highlights low–surface brightness emission at a level of $32.0\,\mu\mathrm{Jy\,beam^{-1}}$—this is 2.5 times the rms after smoothing the native image by a factor of 2.5. The other contours are placed following $(2 + 2^n)\sigma_{\mathrm{native}}$, where $n \geq 0$ and both the rms ($\sigma_{\mathrm{native}} = 5.11\,\mu\mathrm{Jy\,beam^{-1}}$) and the resolution ($\mathrm{FWHM_{native}} = 3.3 \times 3.0$ arcsec) are taken from the native resolution image. These same contours are also superposed on ancillary LITTLE THINGS images where possible: Hα (middle left); $\mathrm{RC_{NTh}}$ obtained by subtracting the expected $\mathrm{RC_{Th}}$ based on the Hα-$\mathrm{RC_{Th}}$ scaling factor of Deeg et al. (1997) from the total RC; *GALEX* FUV (middle right). No significant RC was observed. The greyscale intensity scales used are arbitrary to best highlight structure.

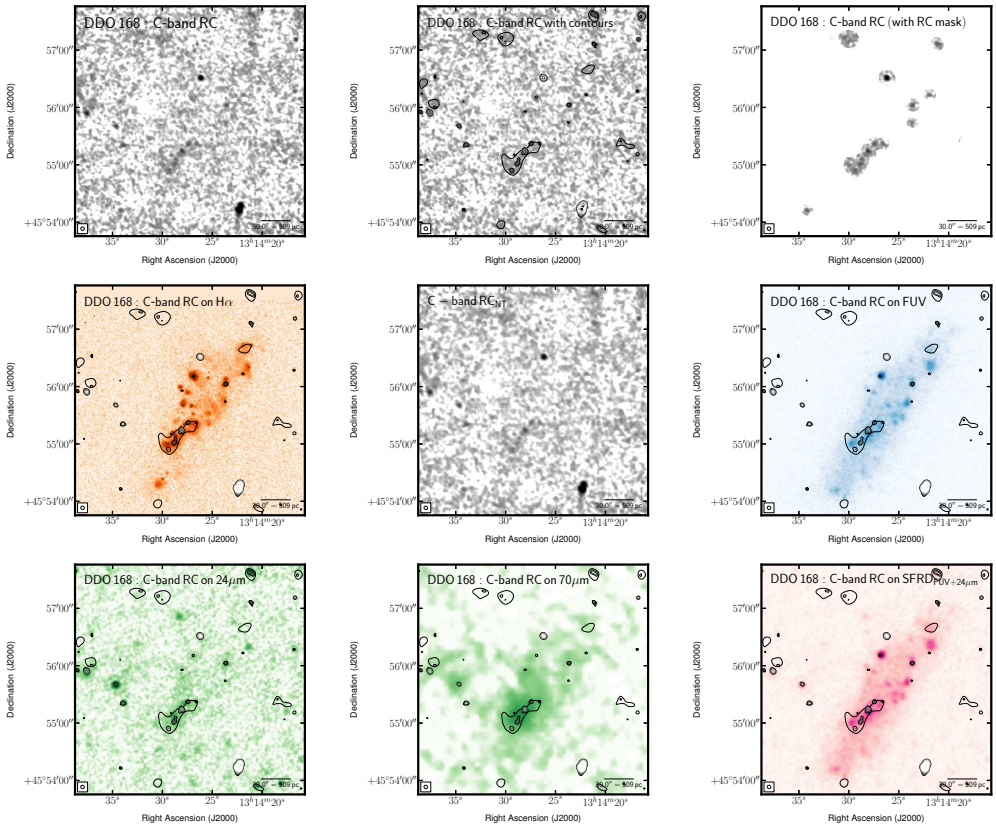

FIGURE C.20: Multi-wavelength coverage of DDO 168 displaying a $4.0' \times 4.0'$ area. We show total RC flux density at the native resolution (top left) and again with contours (top centre). The lowest contour highlights low–surface brightness emission at a level of $27.8\,\mu\mathrm{Jy\,beam^{-1}}$—this is 2.5 times the rms after smoothing the native image by a factor of 2.5. The other contours are placed following $(2 + 2^n)\sigma_{\mathrm{native}}$, where $n \geq 0$ and both the rms ($\sigma_{\mathrm{native}} = 4.44\,\mu\mathrm{Jy\,beam^{-1}}$) and the resolution ($\mathrm{FWHM_{native}} = 3.9 \times 3.5$ arcsec) are taken from the native resolution image. These same contours are also superposed on ancillary LITTLE THINGS images where possible: Hα (middle left); $\mathrm{RC_{NTh}}$ obtained by subtracting the expected $\mathrm{RC_{Th}}$ based on the Hα-$\mathrm{RC_{Th}}$ scaling factor of Deeg et al. (1997) from the total RC; *GALEX* FUV (middle right); *Spitzer* 24 μm (bottom left); *Spitzer* 70 μm (bottom centre); FUV+24μm–inferred SFRD from Leroy et al., 2012 (bottom right). We also show the RC that was isolated by the RC–based masking technique (top right). The greyscale intensity scales used are arbitrary to best highlight structure.

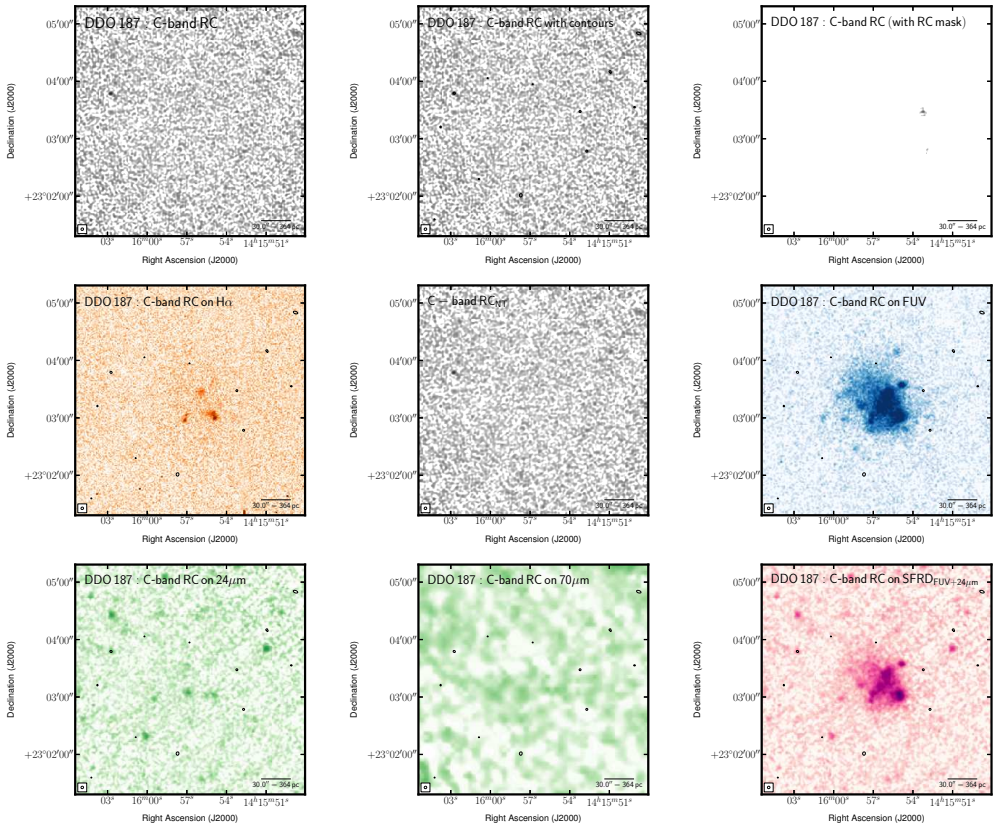

FIGURE C.21: Multi-wavelength coverage of DDO 187 displaying a $4.0' \times 4.0'$ area. We show total RC flux density at the native resolution (top left) and again with contours (top centre). The lowest contour highlights low–surface brightness emission at a level of $43.1\,\mu\mathrm{Jy\,beam^{-1}}$—this is 2.5 times the rms after smoothing the native image by a factor of 2.5. The other contours are placed following $(2 + 2^n)\sigma_{\mathrm{native}}$, where $n \geq 0$ and both the rms ($\sigma_{\mathrm{native}} = 6.90\,\mu\mathrm{Jy\,beam^{-1}}$) and the resolution ($\mathrm{FWHM_{native}} = 2.7 \times 2.5$ arcsec) are taken from the native resolution image. These same contours are also superposed on ancillary LITTLE THINGS images where possible: Hα (middle left); $\mathrm{RC_{NTh}}$ obtained by subtracting the expected $\mathrm{RC_{Th}}$ based on the Hα-$\mathrm{RC_{Th}}$ scaling factor of Deeg et al. (1997) from the total RC; *GALEX* FUV (middle right); *Spitzer* $24\,\mu\mathrm{m}$ (bottom left); *Spitzer* $70\,\mu\mathrm{m}$ (bottom centre); FUV+24μm–inferred SFRD from Leroy et al., 2012 (bottom right). We also show the RC that was isolated by the RC–based masking technique (top right). The greyscale intensity scales used are arbitrary to best highlight structure.

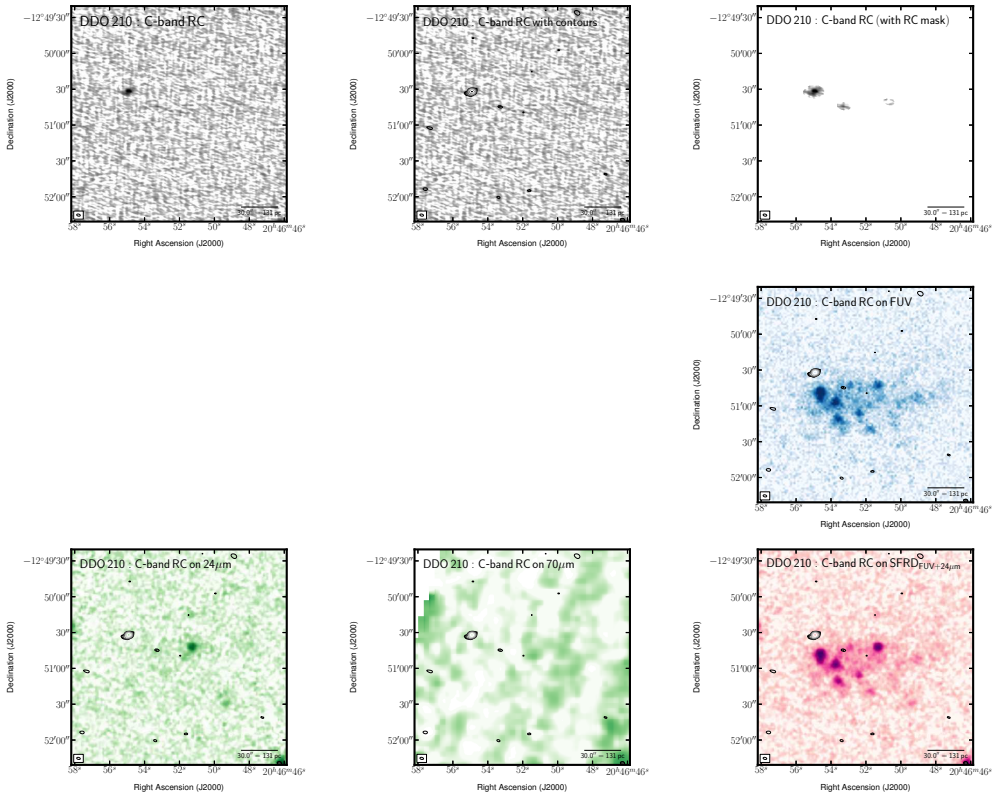

FIGURE C.22: Multi-wavelength coverage of DDO 210 displaying a $3.0' \times 3.0'$ area. We show total RC flux density at the native resolution (top left) and again with contours (top centre). The lowest contour highlights low–surface brightness emission at a level of $29.0\,\mu\mathrm{Jy\,beam^{-1}}$—this is 2.5 times the rms after smoothing the native image by a factor of 2.5. The other contours are placed following $(2 + 2^n)\sigma_{\rm native}$, where $n \geq 0$ and both the rms ($\sigma_{\rm native} = 4.65\,\mu\mathrm{Jy\,beam^{-1}}$) and the resolution ($\mathrm{FWHM_{native}} = 3.1 \times 1.7$ arcsec) are taken from the native resolution image. These same contours are also superposed on ancillary LITTLE THINGS images where possible: *GALEX* FUV (middle right); *Spitzer* 24 μm (bottom left); *Spitzer* 70 μm (bottom centre); FUV+24μm–inferred SFRD from Leroy et al., 2012 (bottom right). We also show the RC that was isolated by the RC–based masking technique (top right). The greyscale intensity scales used are arbitrary to best highlight structure.

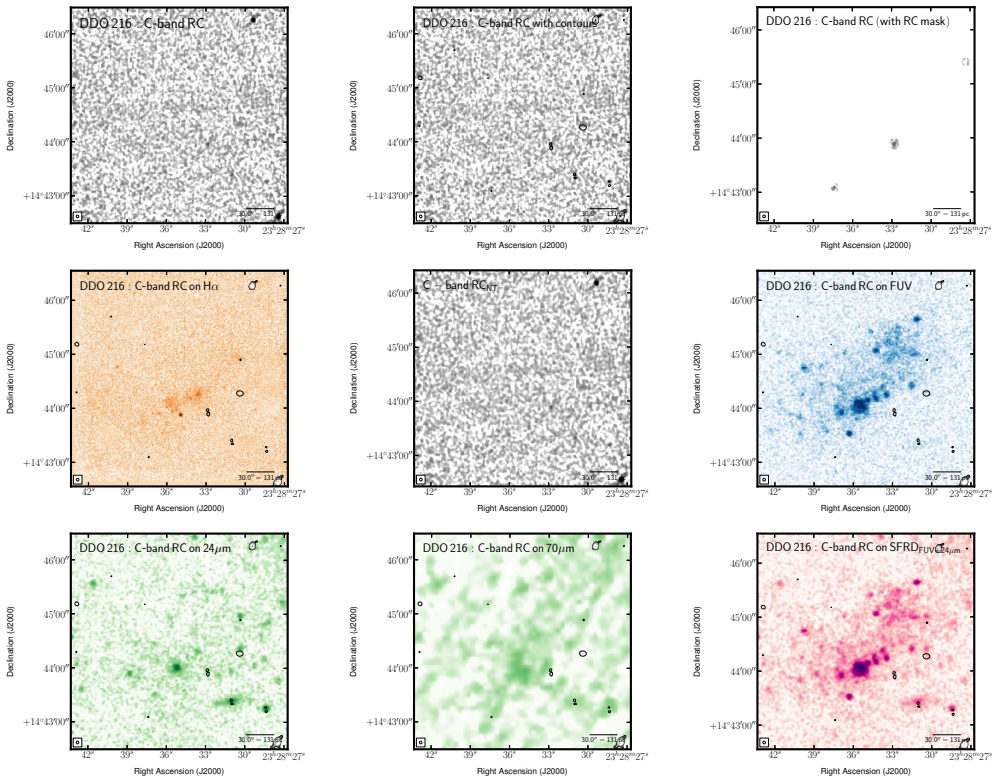

FIGURE C.23: Multi-wavelength coverage of DDO 216 displaying a $-3.7' \times -3.7'$ area. We show total RC flux density at the native resolution (top left) and again with contours (top centre). The lowest contour highlights low–surface brightness emission at a level of $31.9\,\mu\mathrm{Jy\,beam^{-1}}$—this is 2.5 times the rms after smoothing the native image by a factor of 2.5. The other contours are placed following $(2 + 2^n)\sigma_{\mathrm{native}}$, where $n \geq 0$ and both the rms ($\sigma_{\mathrm{native}} = 5.10\,\mu\mathrm{Jy\,beam^{-1}}$) and the resolution ($\mathrm{FWHM_{native}} = 3.1 \times 2.9$ arcsec) are taken from the native resolution image. These same contours are also superposed on ancillary LITTLE THINGS images where possible: Hα (middle left); $\mathrm{RC_{NTh}}$ obtained by subtracting the expected $\mathrm{RC_{Th}}$ based on the Hα-$\mathrm{RC_{Th}}$ scaling factor of Deeg et al. (1997) from the total RC; *GALEX* FUV (middle right); *Spitzer* $24\,\mu\mathrm{m}$ (bottom left); *Spitzer* $70\,\mu\mathrm{m}$ (bottom centre); FUV+24μm–inferred SFRD from Leroy et al., 2012 (bottom right). We also show the RC that was isolated by the RC–based masking technique (top right). The greyscale intensity scales used are arbitrary to best highlight structure.

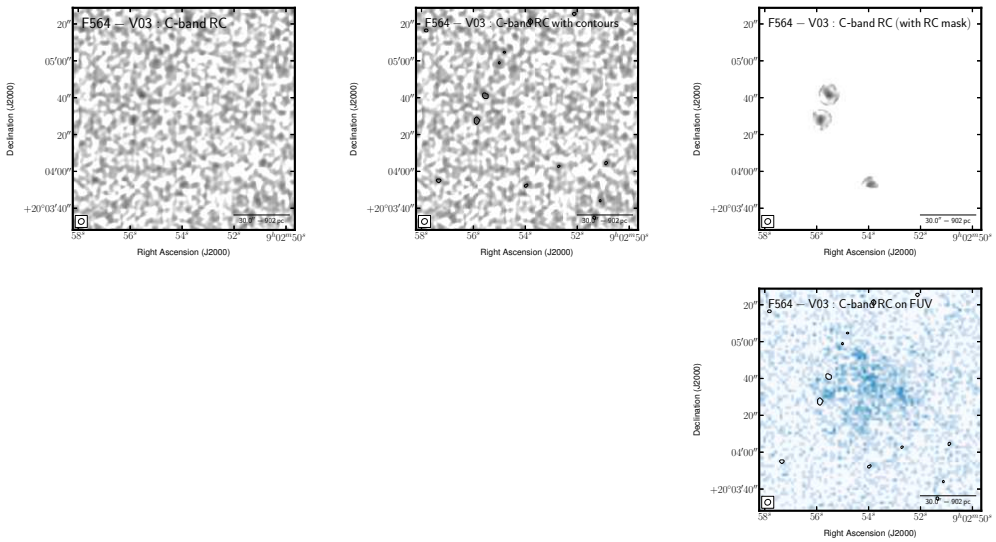

FIGURE C.24: Multi-wavelength coverage of F564-V03 displaying a $2.0' \times 2.0'$ area. We show total RC flux density at the native resolution (top left) and again with contours (top centre). The lowest contour highlights low–surface brightness emission at a level of $34.0\,\mu\mathrm{Jy\,beam^{-1}}$—this is 2.5 times the rms after smoothing the native image by a factor of 2.5. The other contours are placed following $(2 + 2^n)\sigma_{\mathrm{native}}$, where $n \geq 0$ and both the rms ($\sigma_{\mathrm{native}} = 5.44\,\mu\mathrm{Jy\,beam^{-1}}$) and the resolution ($\mathrm{FWHM_{native}} = 3.3 \times 3.0$ arcsec) are taken from the native resolution image. These same contours are also superposed on ancillary LITTLE THINGS images where possible: *GALEX* FUV (middle right). We also show the RC that was isolated by the RC–based masking technique (top right). The greyscale intensity scales used are arbitrary to best highlight structure.

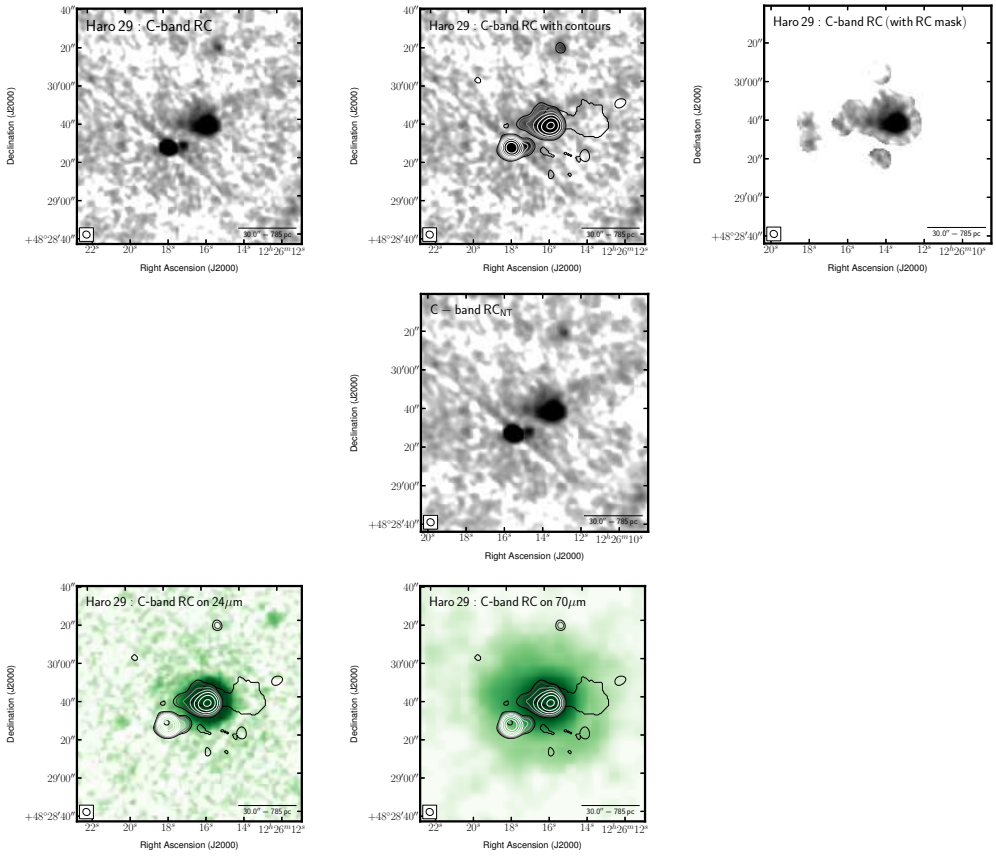

FIGURE C.25: Multi-wavelength coverage of Haro 29 displaying a $2.0' \times 2.0'$ area. We show total RC flux density at the native resolution (top left) and again with contours (top centre). The lowest contour highlights low–surface brightness emission at a level of $31.8\,\mu\mathrm{Jy\,beam^{-1}}$—this is 2.5 times the rms after smoothing the native image by a factor of 2.5. The other contours are placed following $(2 + 2^n)\sigma_{\mathrm{native}}$, where $n \geq 0$ and both the rms ($\sigma_{\mathrm{native}} = 5.09\,\mu\mathrm{Jy\,beam^{-1}}$) and the resolution ($\mathrm{FWHM_{native}} = 3.9 \times 3.6$ arcsec) are taken from the native resolution image. These same contours are also superposed on ancillary LITTLE THINGS images where possible: Hα (middle left); $\mathrm{RC_{NTh}}$ obtained by subtracting the expected $\mathrm{RC_{Th}}$ based on the Hα-$\mathrm{RC_{Th}}$ scaling factor of Deeg et al. (1997) from the total RC; *GALEX* FUV (middle right); *Spitzer* $24\,\mu\mathrm{m}$ (bottom left); *Spitzer* $70\,\mu\mathrm{m}$ (bottom centre); FUV+24μm–inferred SFRD from Leroy et al., 2012 (bottom right). We also show the RC that was isolated by the RC–based masking technique (top right). The greyscale intensity scales used are arbitrary to best highlight structure.

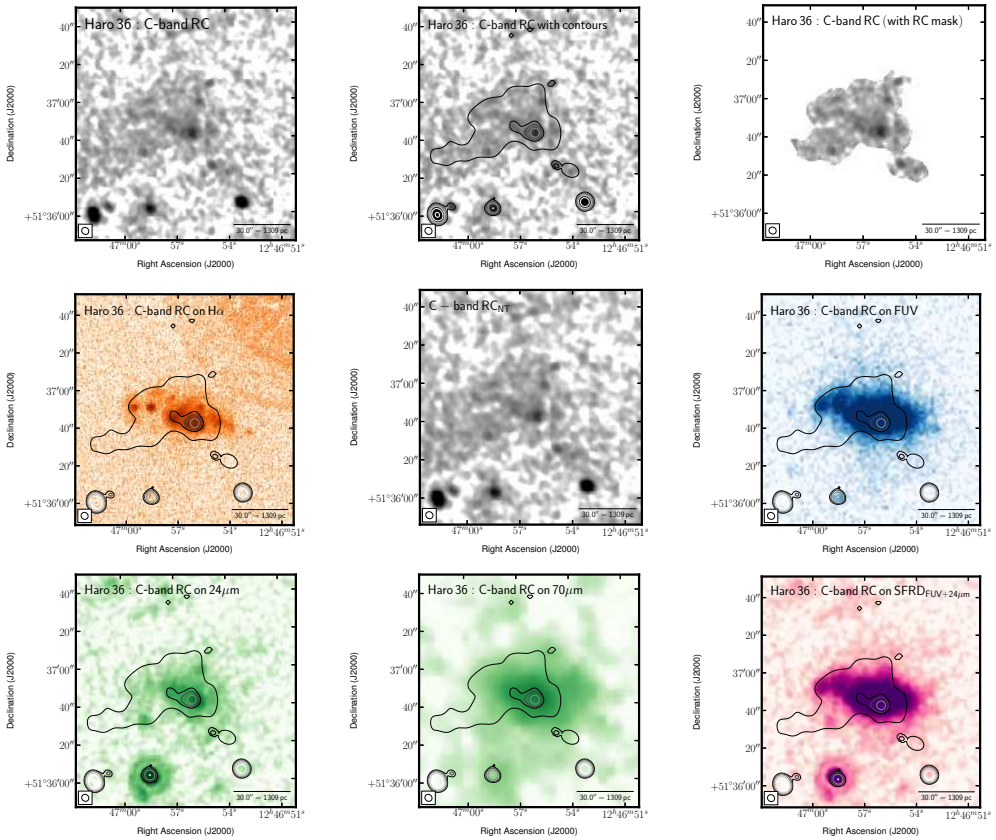

FIGURE C.26: Multi-wavelength coverage of Haro 36 displaying a $2.0' \times 2.0'$ area. We show total RC flux density at the native resolution (top left) and again with contours (top centre). The lowest contour highlights low–surface brightness emission at a level of $32.3\,\mu\mathrm{Jy\,beam^{-1}}$—this is 2.5 times the rms after smoothing the native image by a factor of 2.5. The other contours are placed following $(2 + 2^n)\sigma_{\mathrm{native}}$, where $n \geq 0$ and both the rms ($\sigma_{\mathrm{native}} = 5.17\,\mu\mathrm{Jy\,beam^{-1}}$) and the resolution ($\mathrm{FWHM_{native}} = 3.9 \times 3.6$ arcsec) are taken from the native resolution image. These same contours are also superposed on ancillary LITTLE THINGS images where possible: Hα (middle left); $\mathrm{RC_{NTh}}$ obtained by subtracting the expected $\mathrm{RC_{Th}}$ based on the Hα-$\mathrm{RC_{Th}}$ scaling factor of Deeg et al. (1997) from the total RC; *GALEX* FUV (middle right); *Spitzer* 24 μm (bottom left); *Spitzer* 70 μm (bottom centre); FUV+24μm–inferred SFRD from Leroy et al., 2012 (bottom right). We also show the RC that was isolated by the RC–based masking technique (top right). The greyscale intensity scales used are arbitrary to best highlight structure.

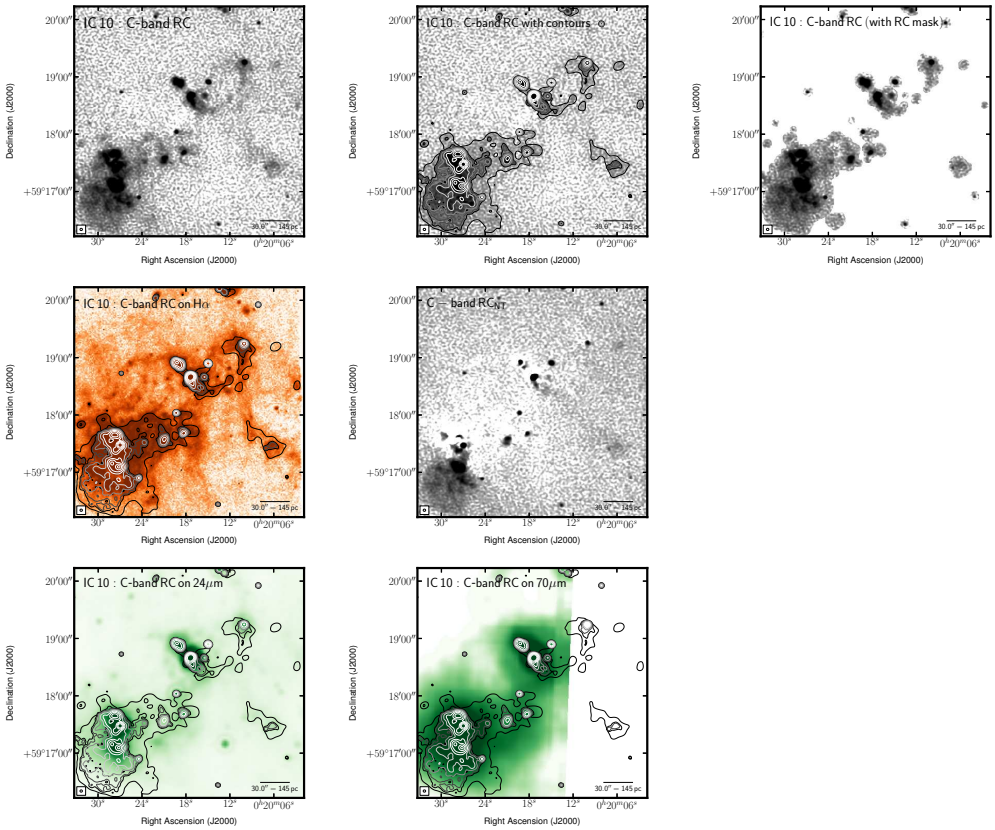

FIGURE C.27: Multi-wavelength coverage of IC 10 displaying a $4.0' \times 4.0'$ area. We show total RC flux density at the native resolution (top left) and again with contours (top centre). The lowest contour highlights low–surface brightness emission at a level of $49.0\,\mu\mathrm{Jy\,beam^{-1}}$—this is 2.5 times the rms after smoothing the native image by a factor of 2.5. The other contours are placed following $(2 + 2^n)\sigma_{\mathrm{native}}$, where $n \geq 0$ and both the rms ($\sigma_{\mathrm{native}} = 7.84\,\mu\mathrm{Jy\,beam^{-1}}$) and the resolution ($\mathrm{FWHM_{native}} = 2.6 \times 2.3$ arcsec) are taken from the native resolution image. These same contours are also superposed on ancillary LITTLE THINGS images where possible: Hα (middle left); $\mathrm{RC_{NTh}}$ obtained by subtracting the expected $\mathrm{RC_{Th}}$ based on the Hα-$\mathrm{RC_{Th}}$ scaling factor of Deeg et al. (1997) from the total RC; *Spitzer* 24 μm (bottom left); *Spitzer* 70 μm (bottom centre). We also show the RC that was isolated by the RC–based masking technique (top right). The greyscale intensity scales used are arbitrary to best highlight structure.

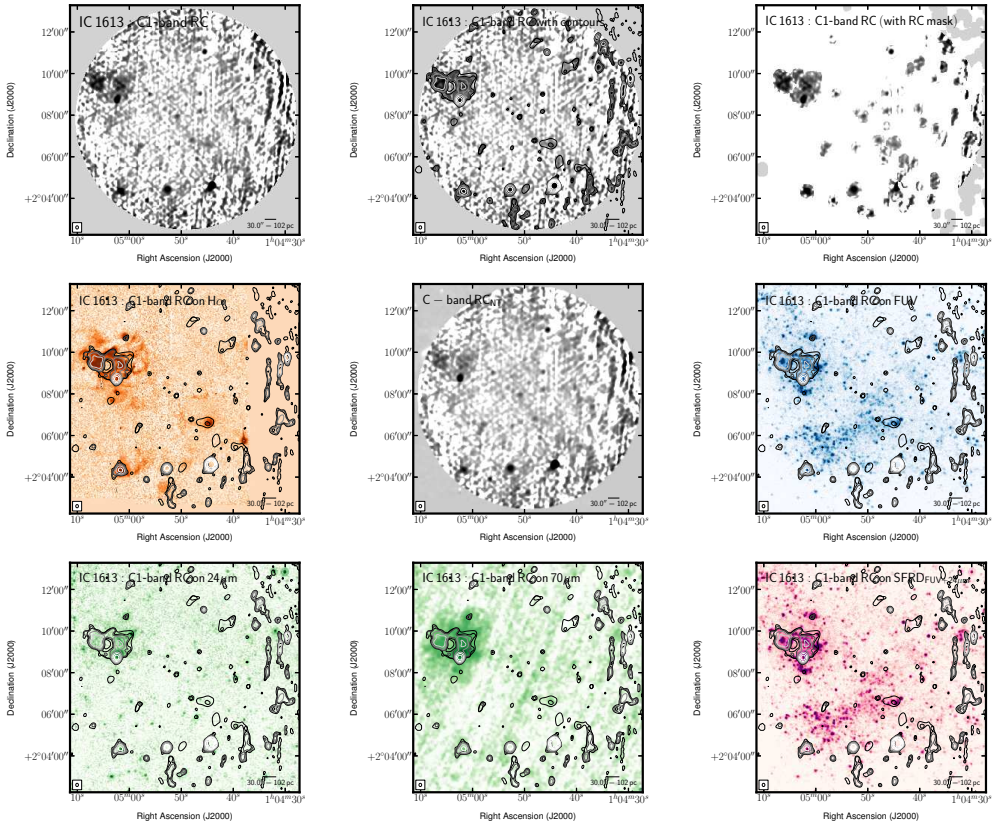

FIGURE C.28: Multi-wavelength coverage of IC 1613 displaying a $11.1' \times 11.1'$ area. We show total RC flux density at the native resolution (top left) and again with contours (top centre). The lowest contour highlights low–surface brightness emission at a level of $31.8\,\mu\mathrm{Jy\,beam^{-1}}$—this is 2.5 times the rms after smoothing the native image by a factor of 2.5. The other contours are placed following $(2 + 2^n)\sigma_{\mathrm{native}}$, where $n \geq 0$ and both the rms ($\sigma_{\mathrm{native}} = 5.08\,\mu\mathrm{Jy\,beam^{-1}}$) and the resolution ($\mathrm{FWHM_{native}} = 9.3 \times 7.8$ arcsec) are taken from the native resolution image. These same contours are also superposed on ancillary LITTLE THINGS images where possible: Hα (middle left); $\mathrm{RC_{NTh}}$ obtained by subtracting the expected $\mathrm{RC_{Th}}$ based on the Hα-$\mathrm{RC_{Th}}$ scaling factor of Deeg et al. (1997) from the total RC; *GALEX* FUV (middle right); *Spitzer* 24 μm (bottom left); *Spitzer* 70 μm (bottom centre); FUV+24μm–inferred SFRD from Leroy et al., 2012 (bottom right). We also show the RC that was isolated by the RC–based masking technique (top right). The greyscale intensity scales used are arbitrary to best highlight structure. In the case of the RC images, only regions of sky where the VLA sensitivity was above 50% of that in the centre of the field are shown.

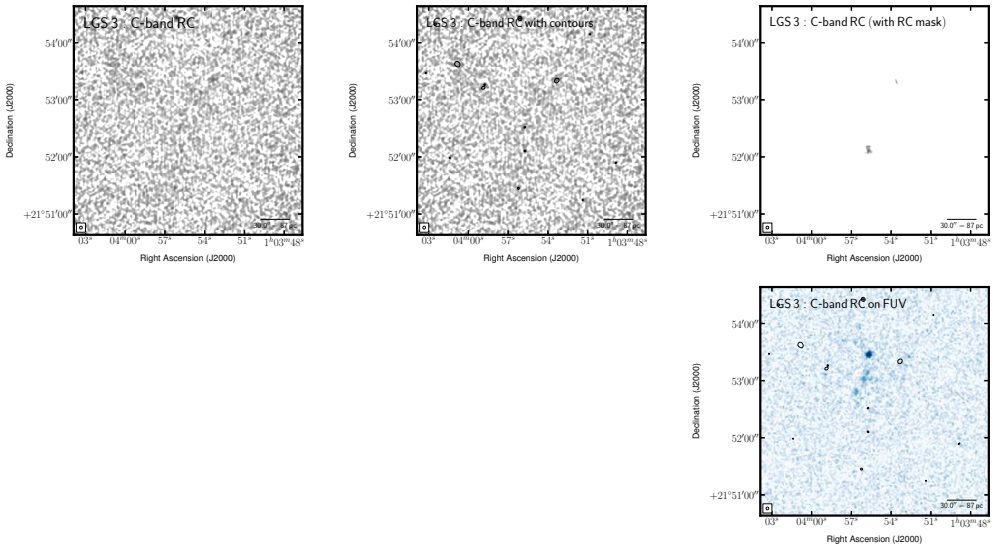

FIGURE C.29: Multi-wavelength coverage of LGS 3 displaying a $4.0' \times 4.0'$ area. We show total RC flux density at the native resolution (top left) and again with contours (top centre). The lowest contour highlights low–surface brightness emission at a level of $34.7\,\mu\mathrm{Jy\,beam^{-1}}$—this is 2.5 times the rms after smoothing the native image by a factor of 2.5. The other contours are placed following $(2 + 2^n)\sigma_{\mathrm{native}}$, where $n \geq 0$ and both the rms ($\sigma_{\mathrm{native}} = 5.54\,\mu\mathrm{Jy\,beam^{-1}}$) and the resolution ($\mathrm{FWHM_{native}} = 3.0 \times 2.8$ arcsec) are taken from the native resolution image. These same contours are also superposed on ancillary LITTLE THINGS images where possible: *GALEX* FUV (middle right). We also show the RC that was isolated by the RC–based masking technique (top right). The greyscale intensity scales used are arbitrary to best highlight structure.

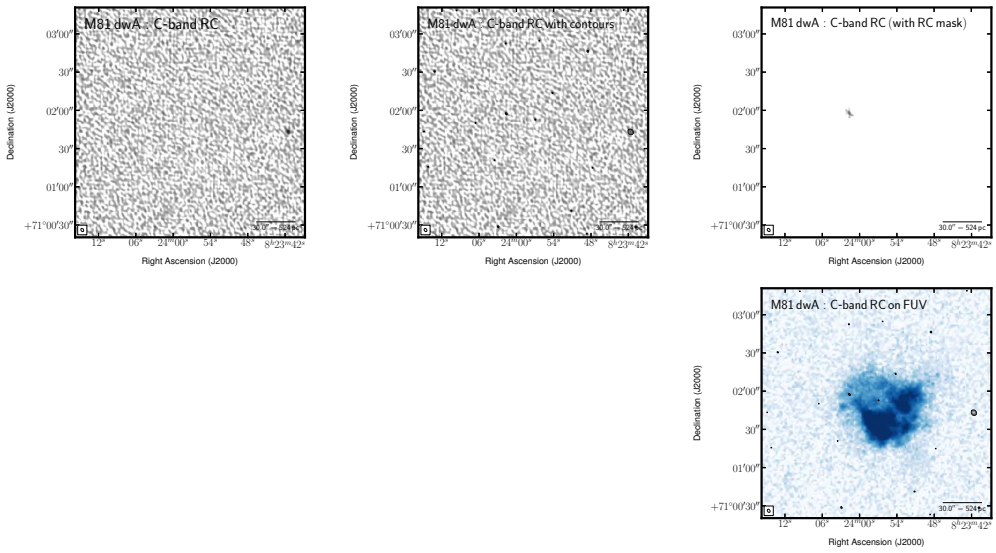

FIGURE C.30: Multi-wavelength coverage of M81 dwA displaying a $3.0' \times 3.0'$ area. We show total RC flux density at the native resolution (top left) and again with contours (top centre). The lowest contour highlights low–surface brightness emission at a level of $67.3\,\mu\mathrm{Jy\,beam^{-1}}$—this is 2.5 times the rms after smoothing the native image by a factor of 2.5. The other contours are placed following $(2 + 2^n)\sigma_{\mathrm{native}}$, where $n \geq 0$ and both the rms ($\sigma_{\mathrm{native}} = 10.77\,\mu\mathrm{Jy\,beam^{-1}}$) and the resolution ($\mathrm{FWHM_{native}} = 2.7 \times 1.9$ arcsec) are taken from the native resolution image. These same contours are also superposed on ancillary LITTLE THINGS images where possible: *GALEX* FUV (middle right). We also show the RC that was isolated by the RC–based masking technique (top right). The greyscale intensity scales used are arbitrary to best highlight structure.

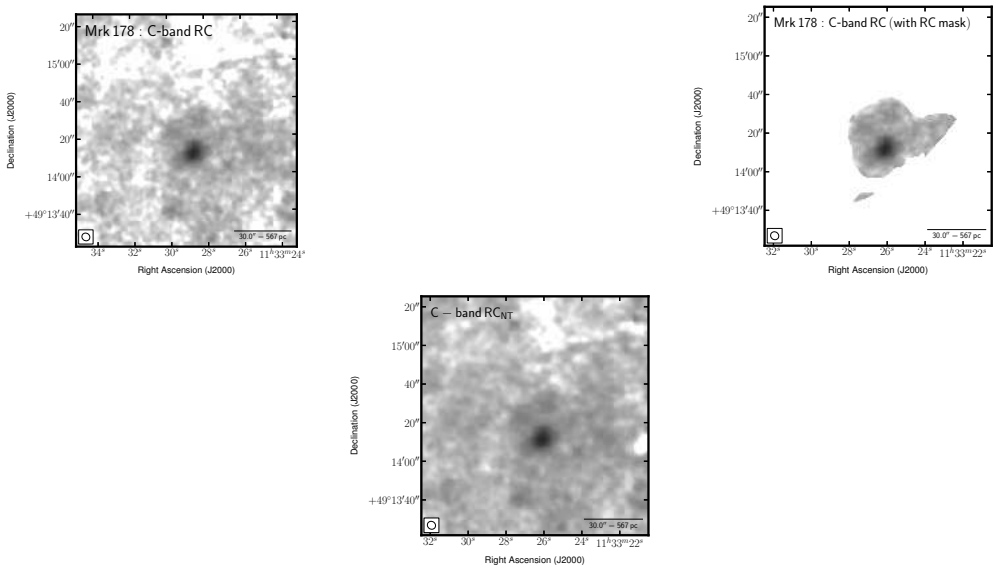

FIGURE C.31: Multi-wavelength coverage of Mrk 178 displaying a $2.0' \times 2.0'$ area. We show total RC flux density at the native resolution (top left) and again with contours (top centre). The lowest contour highlights low–surface brightness emission at a level of $58.7\,\mu\mathrm{Jy\,beam^{-1}}$—this is 2.5 times the rms after smoothing the native image by a factor of 2.5. The other contours are placed following $(2 + 2^n)\sigma_{\mathrm{native}}$, where $n \geq 0$ and both the rms ($\sigma_{\mathrm{native}} = 9.39\,\mu\mathrm{Jy\,beam^{-1}}$) and the resolution ($\mathrm{FWHM_{native}} = 4.4 \times 4.0$ arcsec) are taken from the native resolution image. These same contours are also superposed on ancillary LITTLE THINGS images where possible: Hα (middle left); $\mathrm{RC_{NTh}}$ obtained by subtracting the expected $\mathrm{RC_{Th}}$ based on the Hα-$\mathrm{RC_{Th}}$ scaling factor of Deeg et al. (1997) from the total RC; *Spitzer* 24 μm (bottom left); *Spitzer* 70 μm (bottom centre). We also show the RC that was isolated by the RC–based masking technique (top right). The greyscale intensity scales used are arbitrary to best highlight structure.

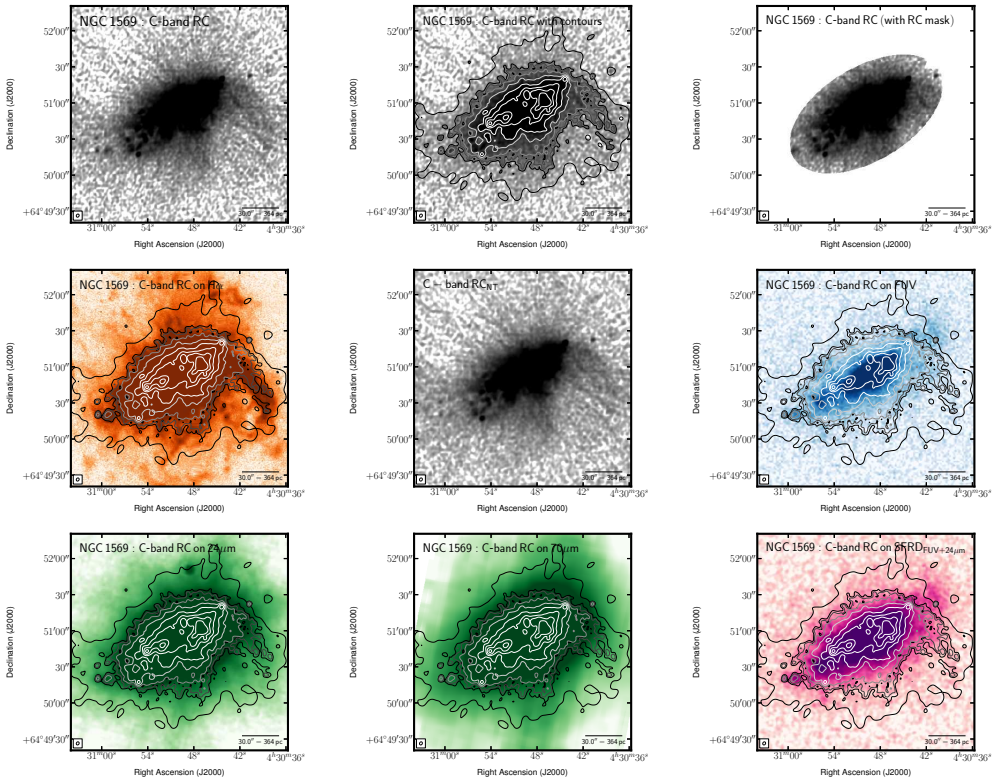

FIGURE C.32: Multi-wavelength coverage of NGC 1569 displaying a $3.0' \times 3.0'$ area. We show total RC flux density at the native resolution (top left) and again with contours (top centre). The lowest contour highlights low–surface brightness emission at a level of $43.6\,\mu\mathrm{Jy\,beam^{-1}}$—this is 2.5 times the rms after smoothing the native image by a factor of 2.5. The other contours are placed following $(2 + 2^n)\sigma_{\mathrm{native}}$, where $n \geq 0$ and both the rms ($\sigma_{\mathrm{native}} = 6.98\,\mu\mathrm{Jy\,beam^{-1}}$) and the resolution ($\mathrm{FWHM_{native}} = 2.7 \times 2.3$ arcsec) are taken from the native resolution image. These same contours are also superposed on ancillary LITTLE THINGS images where possible: Hα (middle left); $\mathrm{RC_{NTh}}$ obtained by subtracting the expected $\mathrm{RC_{Th}}$ based on the Hα-$\mathrm{RC_{Th}}$ scaling factor of Deeg et al. (1997) from the total RC; *GALEX* FUV (middle right); *Spitzer* 24 μm (bottom left); *Spitzer* 70 μm (bottom centre); FUV+24μm–inferred SFRD from Leroy et al., 2012 (bottom right). We also show the RC that was isolated by the RC–based masking technique (top right). The greyscale intensity scales used are arbitrary to best highlight structure.

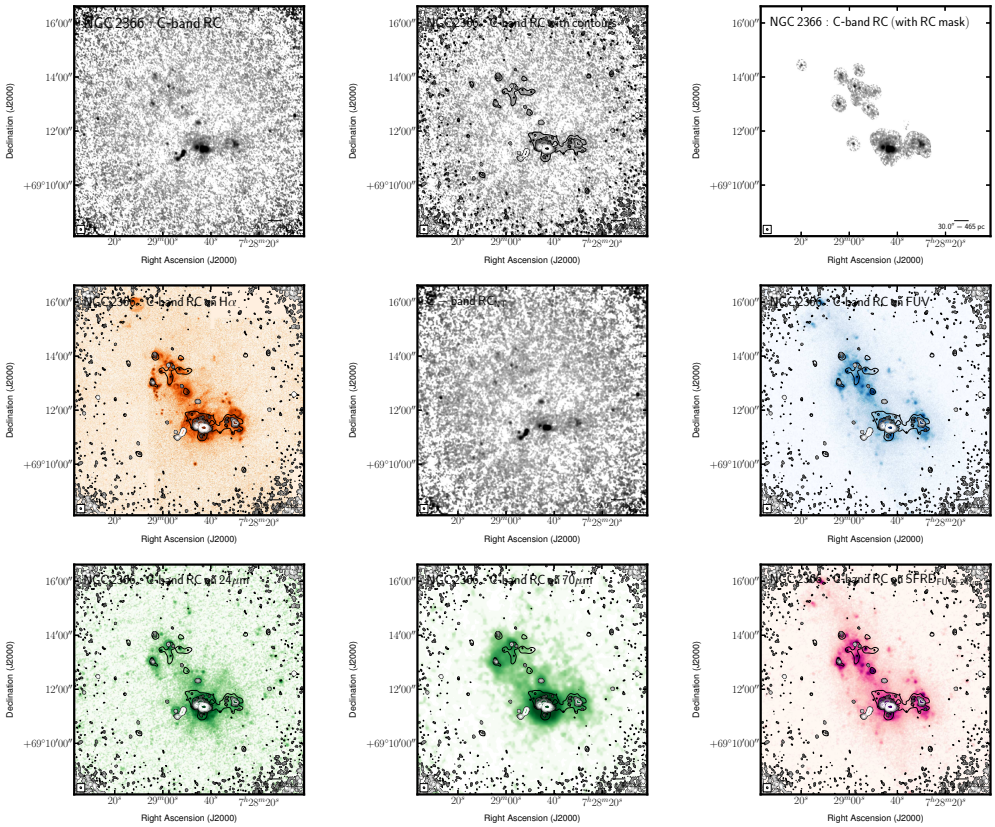

FIGURE C.33: Multi-wavelength coverage of NGC 2366 displaying a $8.5' \times 8.5'$ area. We show total RC flux density at the native resolution (top left) and again with contours (top centre). The lowest contour highlights low–surface brightness emission at a level of $31.8\,\mu\mathrm{Jy\,beam^{-1}}$—this is 2.5 times the rms after smoothing the native image by a factor of 2.5. The other contours are placed following $(2 + 2^n)\sigma_{\mathrm{native}}$, where $n \geq 0$ and both the rms ($\sigma_{\mathrm{native}} = 5.09\,\mu\mathrm{Jy\,beam^{-1}}$) and the resolution ($\mathrm{FWHM_{native}} = 4.2 \times 3.4$ arcsec) are taken from the native resolution image. These same contours are also superposed on ancillary LITTLE THINGS images where possible: Hα (middle left); $\mathrm{RC_{NTh}}$ obtained by subtracting the expected $\mathrm{RC_{Th}}$ based on the Hα-$\mathrm{RC_{Th}}$ scaling factor of Deeg et al. (1997) from the total RC; *GALEX* FUV (middle right); *Spitzer* $24\,\mu\mathrm{m}$ (bottom left); *Spitzer* $70\,\mu\mathrm{m}$ (bottom centre); FUV+24μm–inferred SFRD from Leroy et al., 2012 (bottom right). We also show the RC that was isolated by the RC–based masking technique (top right). The greyscale intensity scales used are arbitrary to best highlight structure.

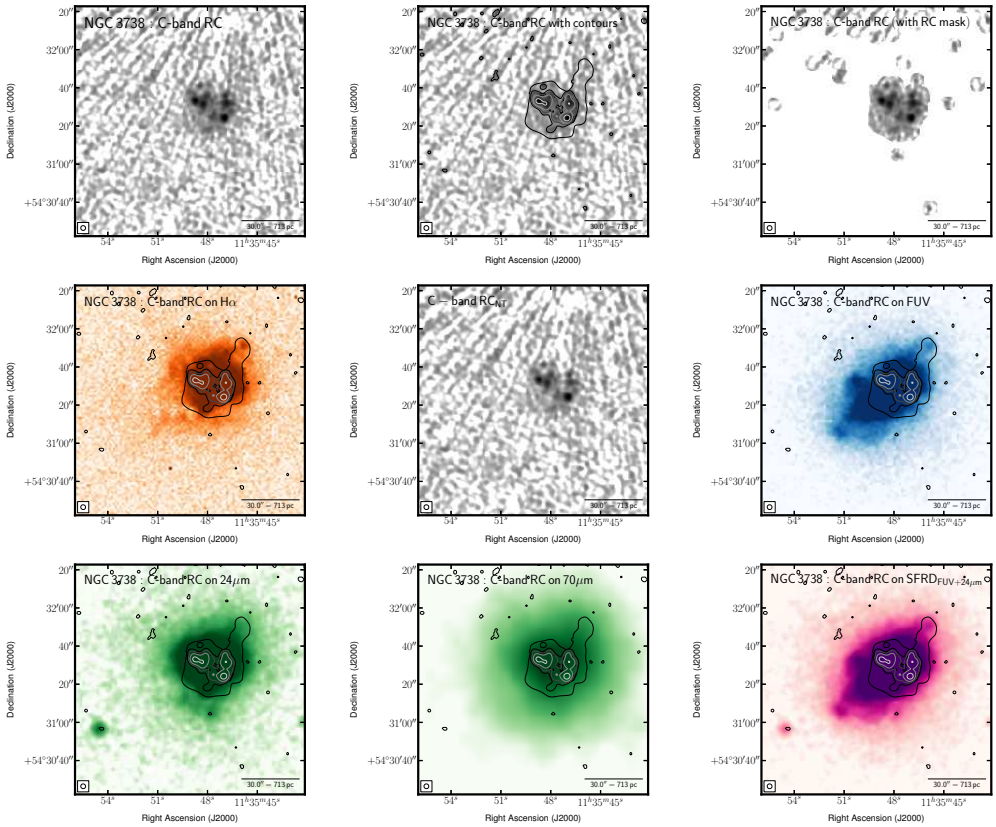

FIGURE C.34: Multi-wavelength coverage of NGC 3738 displaying a $2.0' \times 2.0'$ area. We show total RC flux density at the native resolution (top left) and again with contours (top centre). The lowest contour highlights low–surface brightness emission at a level of $47.5\,\mu\mathrm{Jy\,beam^{-1}}$—this is 2.5 times the rms after smoothing the native image by a factor of 2.5. The other contours are placed following $(2 + 2^n)\sigma_{\mathrm{native}}$, where $n \geq 0$ and both the rms ($\sigma_{\mathrm{native}} = 7.60\,\mu\mathrm{Jy\,beam^{-1}}$) and the resolution ($\mathrm{FWHM_{native}} = 2.5 \times 2.5$ arcsec) are taken from the native resolution image. These same contours are also superposed on ancillary LITTLE THINGS images where possible: Hα (middle left); $\mathrm{RC_{NTh}}$ obtained by subtracting the expected $\mathrm{RC_{Th}}$ based on the Hα-$\mathrm{RC_{Th}}$ scaling factor of Deeg et al. (1997) from the total RC; *GALEX* FUV (middle right); *Spitzer* 24 μm (bottom left); *Spitzer* 70 μm (bottom centre); FUV+24μm–inferred SFRD from Leroy et al., 2012 (bottom right). We also show the RC that was isolated by the RC–based masking technique (top right). The greyscale intensity scales used are arbitrary to best highlight structure.

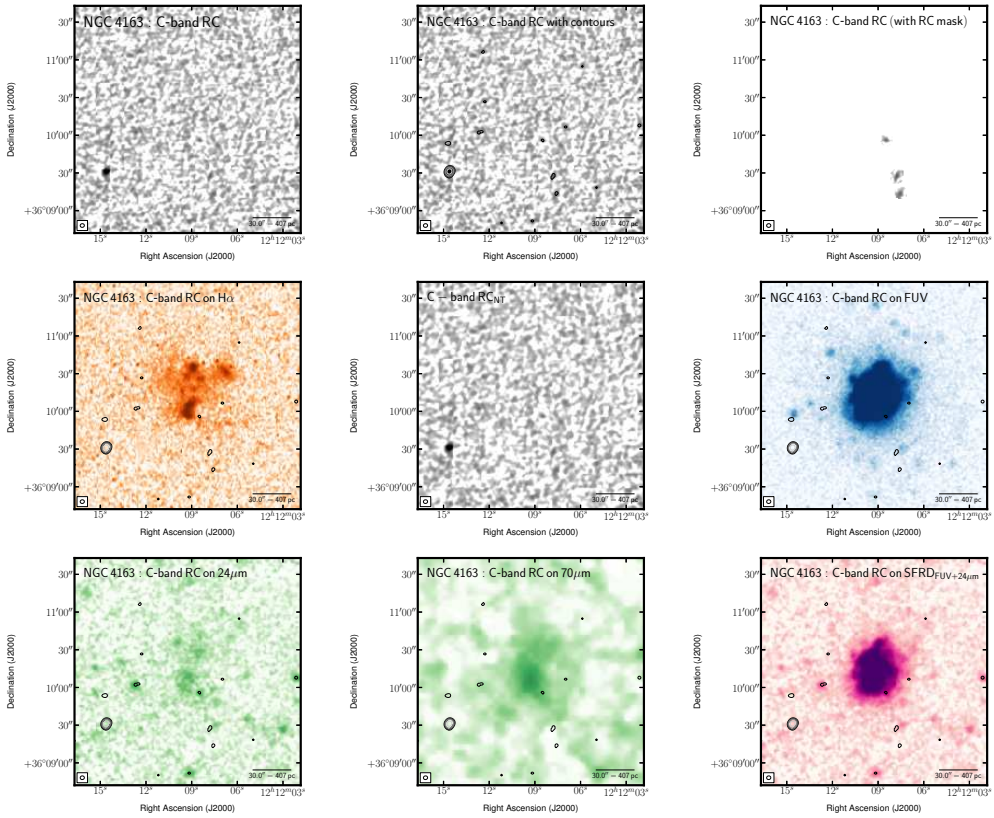

FIGURE C.35: Multi-wavelength coverage of NGC 4163 displaying a $3.0' \times 3.0'$ area. We show total RC flux density at the native resolution (top left) and again with contours (top centre). The lowest contour highlights low–surface brightness emission at a level of $28.3\,\mu\mathrm{Jy\,beam^{-1}}$—this is 2.5 times the rms after smoothing the native image by a factor of 2.5. The other contours are placed following $(2 + 2^n)\sigma_{\mathrm{native}}$, where $n \geq 0$ and both the rms ($\sigma_{\mathrm{native}} = 4.53\,\mu\mathrm{Jy\,beam^{-1}}$) and the resolution ($\mathrm{FWHM_{native}} = 3.3 \times 2.9$ arcsec) are taken from the native resolution image. These same contours are also superposed on ancillary LITTLE THINGS images where possible: Hα (middle left); $\mathrm{RC_{NTh}}$ obtained by subtracting the expected $\mathrm{RC_{Th}}$ based on the Hα-$\mathrm{RC_{Th}}$ scaling factor of Deeg et al. (1997) from the total RC; *GALEX* FUV (middle right); *Spitzer* $24\,\mu$m (bottom left); *Spitzer* $70\,\mu$m (bottom centre); FUV+24μm–inferred SFRD from Leroy et al., 2012 (bottom right). We also show the RC that was isolated by the RC–based masking technique (top right). The greyscale intensity scales used are arbitrary to best highlight structure.

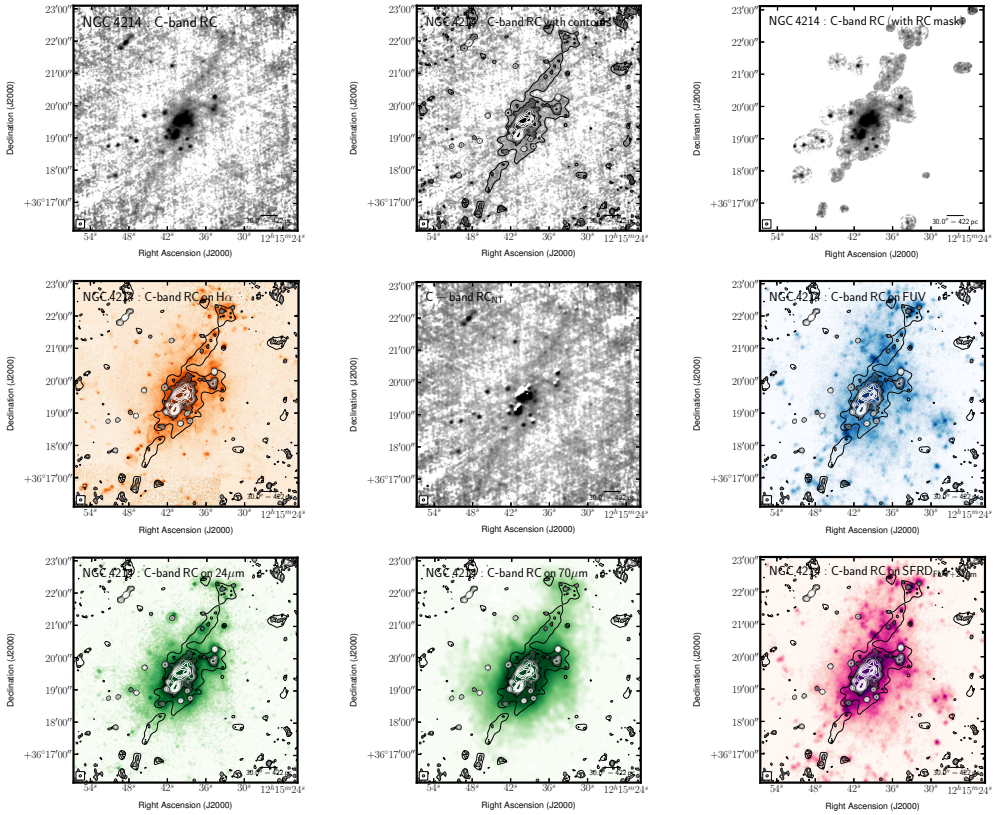

FIGURE C.36: Multi-wavelength coverage of NGC 4214 displaying a $7.0' \times 7.0'$ area. We show total RC flux density at the native resolution (top left) and again with contours (top centre). The lowest contour highlights low–surface brightness emission at a level of $39.0\,\mu\mathrm{Jy\,beam^{-1}}$—this is 2.5 times the rms after smoothing the native image by a factor of 2.5. The other contours are placed following $(2 + 2^n)\sigma_{\mathrm{native}}$, where $n \geq 0$ and both the rms ($\sigma_{\mathrm{native}} = 6.24\,\mu\mathrm{Jy\,beam^{-1}}$) and the resolution ($\mathrm{FWHM_{native}} = 4.5 \times 4.0$ arcsec) are taken from the native resolution image. These same contours are also superposed on ancillary LITTLE THINGS images where possible: Hα (middle left); $\mathrm{RC_{NTh}}$ obtained by subtracting the expected $\mathrm{RC_{Th}}$ based on the Hα-$\mathrm{RC_{Th}}$ scaling factor of Deeg et al. (1997) from the total RC; *GALEX* FUV (middle right); *Spitzer* 24 μm (bottom left); *Spitzer* 70 μm (bottom centre); FUV+24μm–inferred SFRD from Leroy et al., 2012 (bottom right). We also show the RC that was isolated by the RC–based masking technique (top right). The greyscale intensity scales used are arbitrary to best highlight structure.

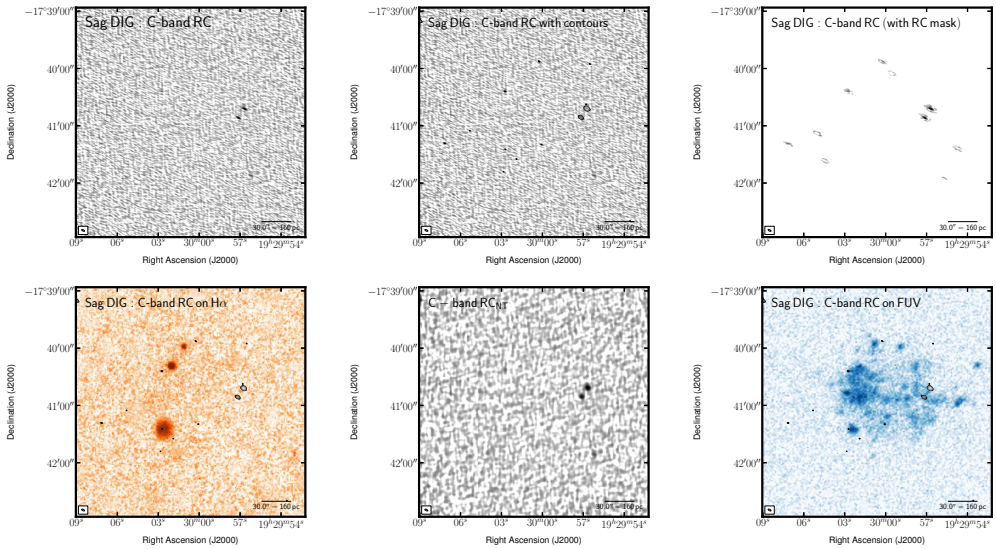

FIGURE C.37: Multi-wavelength coverage of Sag DIG displaying a $4.0' \times 4.0'$ area. We show total RC flux density at the native resolution (top left) and again with contours (top centre). The lowest contour highlights low–surface brightness emission at a level of $51.4\,\mu\mathrm{Jy\,beam^{-1}}$—this is 2.5 times the rms after smoothing the native image by a factor of 2.5. The other contours are placed following $(2 + 2^n)\sigma_{\mathrm{native}}$, where $n \geq 0$ and both the rms ($\sigma_{\mathrm{native}} = 8.23\,\mu\mathrm{Jy\,beam^{-1}}$) and the resolution ($\mathrm{FWHM_{native}} = 3.5 \times 1.4$ arcsec) are taken from the native resolution image. These same contours are also superposed on ancillary LITTLE THINGS images where possible: Hα (middle left); $\mathrm{RC_{NTh}}$ obtained by subtracting the expected $\mathrm{RC_{Th}}$ based on the Hα-$\mathrm{RC_{Th}}$ scaling factor of Deeg et al. (1997) from the total RC; *GALEX* FUV (middle right). We also show the RC that was isolated by the RC–based masking technique (top right). The greyscale intensity scales used are arbitrary to best highlight structure.

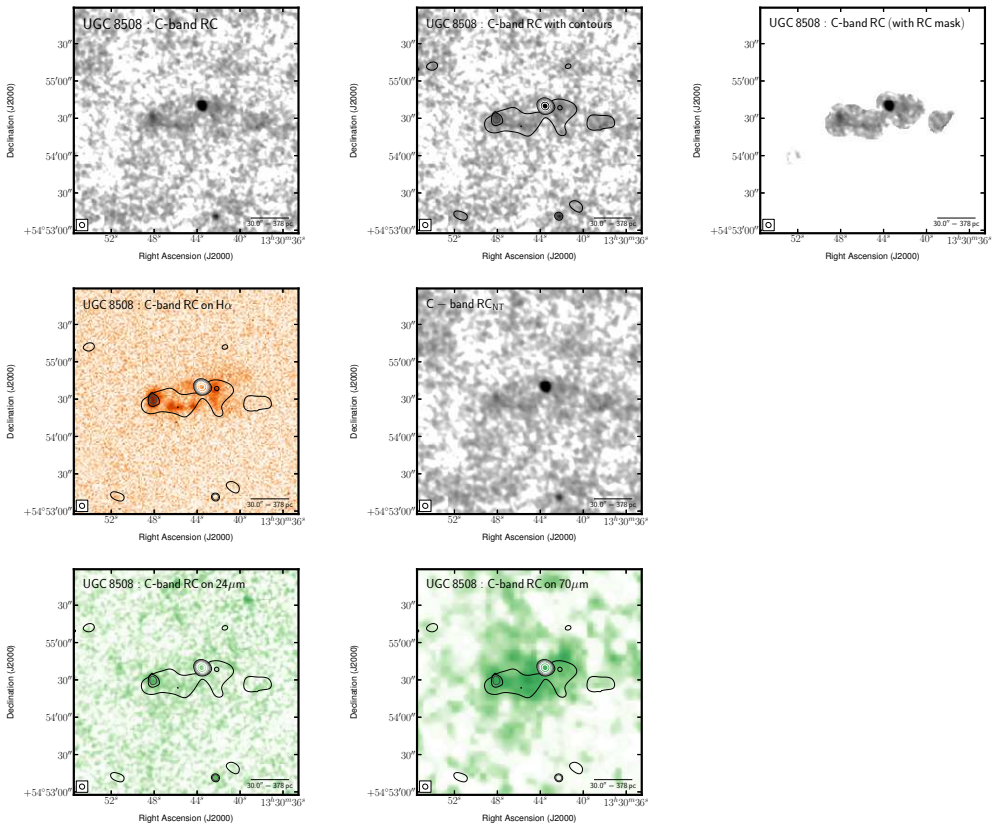

FIGURE C.38: Multi-wavelength coverage of UGC 8508 displaying a $3.0' \times 3.0'$ area. We show total RC flux density at the native resolution (top left) and again with contours (top centre). The lowest contour highlights low–surface brightness emission at a level of $29.6\,\mu\mathrm{Jy\,beam^{-1}}$—this is 2.5 times the rms after smoothing the native image by a factor of 2.5. The other contours are placed following $(2 + 2^n)\sigma_{\mathrm{native}}$, where $n \geq 0$ and both the rms ($\sigma_{\mathrm{native}} = 4.74\,\mu\mathrm{Jy\,beam^{-1}}$) and the resolution ($\mathrm{FWHM_{native}} = 4.3 \times 4.0$ arcsec) are taken from the native resolution image. These same contours are also superposed on ancillary LITTLE THINGS images where possible: Hα (middle left); $\mathrm{RC_{NTh}}$ obtained by subtracting the expected $\mathrm{RC_{Th}}$ based on the Hα-$\mathrm{RC_{Th}}$ scaling factor of Deeg et al. (1997) from the total RC; *Spitzer* 24 μm (bottom left); *Spitzer* 70 μm (bottom centre). We also show the RC that was isolated by the RC–based masking technique (top right). The greyscale intensity scales used are arbitrary to best highlight structure.

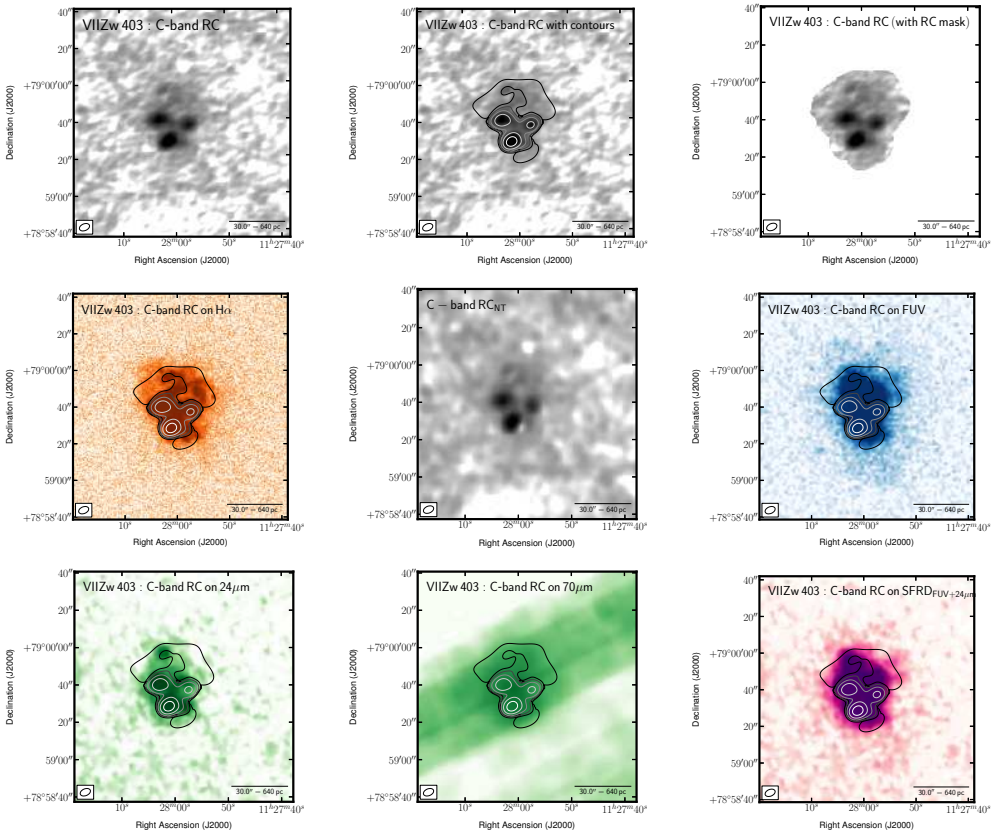

FIGURE C.39: Multi-wavelength coverage of VIIZw 403 displaying a $2.6' \times 2.6'$ area. We show total RC flux density at the native resolution (top left) and again with contours (top centre). The lowest contour highlights low–surface brightness emission at a level of $36.7\,\mu\mathrm{Jy\,beam^{-1}}$—this is 2.5 times the rms after smoothing the native image by a factor of 2.5. The other contours are placed following $(2 + 2^n)\sigma_{\mathrm{native}}$, where $n \geq 0$ and both the rms ($\sigma_{\mathrm{native}} = 5.88\,\mu\mathrm{Jy\,beam^{-1}}$) and the resolution ($\mathrm{FWHM_{native}} = 5.8 \times 3.7$ arcsec) are taken from the native resolution image. These same contours are also superposed on ancillary LITTLE THINGS images where possible: Hα (middle left); $\mathrm{RC_{NTh}}$ obtained by subtracting the expected $\mathrm{RC_{Th}}$ based on the Hα-$\mathrm{RC_{Th}}$ scaling factor of Deeg et al. (1997) from the total RC; *GALEX* FUV (middle right); *Spitzer* 24 μm (bottom left); *Spitzer* 70 μm (bottom centre); FUV+24μm–inferred SFRD from Leroy et al., 2012 (bottom right). We also show the RC that was isolated by the RC–based masking technique (top right). The greyscale intensity scales used are arbitrary to best highlight structure.

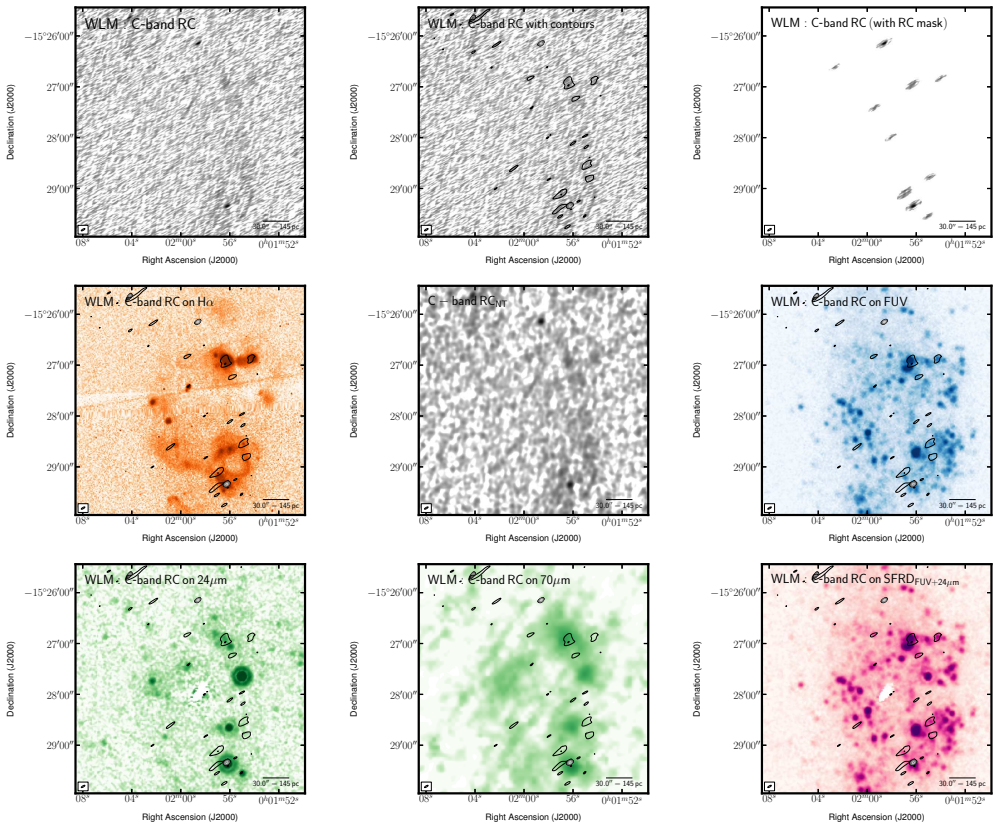

FIGURE C.40: Multi-wavelength coverage of WLM displaying a $4.5' \times 4.5'$ area. We show total RC flux density at the native resolution (top left) and again with contours (top centre). The lowest contour highlights low–surface brightness emission at a level of $33.3\,\mu\mathrm{Jy\,beam^{-1}}$—this is 2.5 times the rms after smoothing the native image by a factor of 2.5. The other contours are placed following $(2 + 2^n)\sigma_{\mathrm{native}}$, where $n \geq 0$ and both the rms ($\sigma_{\mathrm{native}} = 5.33\,\mu\mathrm{Jy\,beam^{-1}}$) and the resolution ($\mathrm{FWHM_{native}} = 5.0 \times 1.5$ arcsec) are taken from the native resolution image. These same contours are also superposed on ancillary LITTLE THINGS images where possible: Hα (middle left); $\mathrm{RC_{NTh}}$ obtained by subtracting the expected $\mathrm{RC_{Th}}$ based on the Hα-$\mathrm{RC_{Th}}$ scaling factor of Deeg et al. (1997) from the total RC; *GALEX* FUV (middle right); *Spitzer* 24 μm (bottom left); *Spitzer* 70 μm (bottom centre); FUV+24μm–inferred SFRD from Leroy et al., 2012 (bottom right). We also show the RC that was isolated by the RC–based masking technique (top right). The greyscale intensity scales used are arbitrary to best highlight structure.

D

Glossary

D.1 Relevant Physical Units

Throughout the thesis, SI units have been used; in addition to these, a few other units of measurement have been employed:

Å: Angstrom—1×10^{-10} m.

$M_\odot$: Solar mass—The baryonic mass tied up in the Sun taken to be $\sim \mathbf{2} \times \mathbf{10^{30}}$ kg.

pc: Parsec—The distance required for a foreground object to have a parallax of $\mathbf{1''}$ due to the Earth's orbit around the Sun with respect to objects at infinity; approximately equal to $\mathbf{3.26}$ ly.

D.2 Relevant Terms and Acronyms

The thesis contains lots of astronomy- and radio-specific jargon. This small section has been included as a reference guide:

Band: Arbitrary division of the radio spectrum—the VLA uses *L*-band for frequencies from **1–2** GHz, *S*-band for **2–4** GHz, *C*-band for **4–8** GHz, *X*-band for **8–12** GHz, and *Ku*-band for **12–18** GHz.

Beam: Synthesised beam—The point spread function of the interferometer as a whole usually expressed in FWHM (the full width of the near gaussian beam at half height).

CASA: Common Astronomy Software Applications—Python parser package geared towards the handling of interferometric data, especially from the VLA and ALMA.

CR*e*: Cosmic ray electron—ultra-relativistic (Lorentz factor greater than $\sim \mathbf{1000}$) electron accelerated in the shock fronts of SNe.

Equipartition: In the context of this thesis, this refers specifically to the equipartition (equal distribution) of energy density tied up in CR*e*, and in magnetic fields.

Flux density: Electromagnetic flux over a bandwidth of **1** Hz—in this respect, the term density refers to frequency space, not a volumetric density.

FIR: Far infrared—the region of the electromagnetic spectrum between wavelengths of approximately **50** and $\mathbf{1000}\mu\mathbf{m}$.

FUV: Far ultraviolet—the region of the electromagnetic spectrum between wavelengths of **1344** and **1786** Å sampled by the *GALEX* satellite.

Hα: the Balmer line emission resulting from the electronic transition characterised by the principle quantum number, n, changing from **3** down to **2** in Hydrogen.

H I: Atomic Hydrogen—Hydrogen in its ground state.

H II: Singularly Ionised Hydrogen—refers to Hydrogen while in its fully ionised state.

IF: Intermediate frequency—term given to the two sub-bands (A/C and B/D) used by the VLA obtained by either up- or down-converting the incoming radio frequency signal.

Interferometer: A device that correlates signal from two receivers.

MIR: Mid infrared—the region of the electromagnetic spectrum between wavelengths of approximately **5** and $\mathbf{50}\mu\mathbf{m}$.

MS: Measurement Set—The collection of data files containing (u, v) data and other observation specific information. Used with CASA.

RC: Radio continuum—the continuous spectrum of electromagnetic radiation found between the approximate wavelengths of **0.001** to **10** m.

RFI: Radio Frequency Interference—Unwanted emission of local origin at RC wavelengths (e.g., the Sun, mobile phones, satellite-based transmitters, microwave

ovens, etc.) The interference can be either wideband or narrowband, and can be either persistent or intermittent in time.

$\mathbf{RC_{NTh}}$: Non-thermal radio continuum—the contribution to the radio continuum spectrum that originates from non-thermal processes (e.g., through magnetic fields). Otherwise known as synchrotron radiation.

$\mathbf{RC_{Th}}$: Thermal radio continuum—the contribution to the radio continuum spectrum that originates from thermal processes (e.g., internal energy of a gas). Otherwise known as Brehmsstrahlung, or free-free radiation.

Scheduling Block: A piece of code that details a VLA observation including durations, celestial coordinates, and instrumental setups.

SF: Star formation—the process of converting gas into stellar mass.

SFR: Star formation rate—the rate at which stars are formed, usually in units of solar masses per year.

SN(e): Supernova(e)—the stellar explosion(s) resulting in a neutron star or black hole.

Spectral Window: A sub-band within a VLA IF; usually $\mathbf{8}$ spectral windows make up an IF.

VLA: NRAO Karl G. Jansky Very Large Array—an reconfigurable Y-shaped array of $\mathbf{27}$ interconnected radio telescopes, i.e., an interferometer. Each of the radio telescopes has an identical dish $\mathbf{25}$ m in size designed to observe electromagnetic radiation between wavelengths of $\mathbf{0.7}$ mm and $\mathbf{4}$ m.

References

Altschuler, D. R., Giovanardi, C., Giovanelli, R. & Haynes, M. P. 1984, AJ, 89, 224 23, 89

Appleton, P. N., Fadda, D. T., Marleau, F. R. et al. 2004, ApJS, 154, 147 26, 67

Asplund, M., Grevesse, N., Sauval, A. J., & Scott, P. 2009, ARA&A, 47, 481 8

Banerjee, A., Jog, C. J., Brinks, E. & Bagetakos, I. 2011, MNRAS, 415, 687 27, 107, 129, 135

Beck, R., & Krause, M. 2005, Astronomische Nachrichten, 326, 414 9, 83, 107, 120

Beck, R. 2009, Astrophysics and Space Sciences Transactions, 5, 43 28, 69

Bell, E. F. 2003, ApJ, 586, 794 28, 68, 108, 129

Bigiel, F., Leroy, A., Walter, F. et al. 2008, AJ, 136, 2846 3, 5, 68, 69, 92

Brown, R. H., & Hazard, C. 1951, MNRAS, 111, 357 21

Brown, R. H., & Hazard, C. 1961, MNRAS, 123, 279 22, 28

Burstein, D. & Heiles, C. 1982, AJ, 87, 1165 36, 144

Burstein, D., & Heiles, C. 1984, ApJS, 54, 33 33

Calzetti, D., Kennicutt, R. C., Engelbracht, C. W. et al. 2007, ApJ, 666, 870 6, 92

Calzetti, D., Wu, S.-Y., Hong, S. et al. 2010, ApJ, 714, 1256 9

Chomiuk, L. & Wilcots, E. M. 2009, AJ, 137, 3869 77, 80, 91, 96

Chyży, K. T., Wezgowiec, M., Beck, R. & Bomans, D. J. 2011, A&A, 529, A94 24, 69, 88, 116, 129, 130, 132

Condon, J. J. 1992, ARA&A, 30, 575 2, 9, 16, 20, 67, 118, 127, 128, 164, 169

Condon, J. J., Cotton, W. D., Greisen, E. W. et al. 1998, AJ, 115, 1693 23, 90

Condon, J. J., Cotton, W. D. & Broderick, J. J. 2002, AJ, 124, 675 7, 90, 93, 94, 95, 96, 97, 98, 99, 104, 105, 109, 150, 167, 168

Condon, J. J., & Ransom, S. M. 2010, Essential Radio Astronomy course, NRAO, www.cv.nrao.edu/course/astr534/ERA.shtml 10, 11, 12, 15, 47, 48

Cowie, L. L., Songaila, A., Hu, E. M., & Cohen, J. G. 1996, AJ, 112, 839 3, 8

da Cunha, E., Charlot, S., & Elbaz, D. 2008, MNRAS, 388, 1595 6

Dale, D. A., Cohen, S. A., Johnson, L. C. et al. 2009, ApJ, 703, 517 28, 36, 68, 108

Dickinson, C. 2013, Advances in Astronomy, 2013, 162478 7

Edge, D. O., Shakeshaft, J. R., McAdam, W. B., Baldwin, J. E., & Archer, S. 1959, MmRAS, 68, 37 21

de Jong, T., Klein, U., Wielebinski, R. & Wunderlich, E. 1985, A&A, 147, L6 26, 27, 67, 95, 97

Deeg, H.-J., Duric, N. & Brinks, E. 1997, A&A, 323, 323 xix, 2, 13, 77, 83, 90, 120, 144, 155, 160, 191, 192, 193, 194, 195, 196, 197, 198, 199, 200, 201, 202, 203, 204, 205, 206, 207, 208, 209, 210, 211, 213, 215, 216, 217, 218, 221, 222, 223, 224, 225, 226, 227, 228, 229, 230

Dubois, Y. & Teyssier, R. 2010, A&A, 523, A72 29, 69

Engelbracht, C. W., Blaylock, M., Su, K. Y. L. et al. 2007, PASP, 119, 994 37

Ferguson, A. M. N., Wyse, R. F. G., Gallagher, J. S., III, & Hunter, D. A. 1996, AJ, 111, 2265 4

Filipovic, M. D., Haynes, R. F., White, G. L., Jones, P. A., Klein, U. & Wielebinski, R. 1995, A&AS, 111, 311 24, 69

Filipovic, M. D., Haynes, R. F., White, G. L. & Jones, P. A. 1998, A&AS, 130, 421 24, 69

Fletcher, A., Beck, R., Shukurov, A., Berkhuijsen, E. M., & Horellou, C. 2011, MNRAS, 412, 2396 129

Galametz, M., Kennicutt, R. C., Calzetti, D., et al. 2013, MNRAS, 431, 1956 6

Gallagher, III, J. S. & Hunter, D. A. 1984, ARA&A, 22, 37 28, 69

Gil de Paz, A., Boissier, S., Madore, B. F. et al. 2007, ApJS, 173, 185 36

Harwood, J. J., Hardcastle, M. J., Croston, J. H., & Goodger, J. L. 2013, MNRAS, 435, 3353 164, 170

Häußler, B., Bamford, S. P., Vika, M., et al. 2013, MNRAS, 430, 330 8

Heesen, V., Beck, R., Krause, M. & Dettmar, R.-J. 2009, A&A, 494, 563 28, 29, 68, 69, 135

Heesen, V., Rau, U., Rupen, M. P., Brinks, E. & Hunter, D. A. 2011, ApJ, 739, L23 24, 25, 26, 29, 52, 69, 91, 140

Heesen, V., Brinks, E., Leroy, A. K. et al. 2014, AJ, 147, 103 xviii, 7, 14, 16, 25, 89, 93, 107, 109, 112, 150, 167, 171

Heesen, V., Brinks, E., Krause, M. G. H., et al. 2015, MNRAS, 447, L1 140, 164, 170

Helmboldt, J. F., Walterbos, R. A. M., Bothun, G. D., & O'Neil, K. 2005, ApJ, 630, 824 4

Helmboldt, J. F. 2005, Ph.D. Thesis (New Mexico State University, New Mexico, USA) 4

Helou, G., Soifer, B. T. & Rowan-Robinson, M. 1985, ApJ, 298, L7 26, 67

Hoeppe, G., Brinks, E., Klein, U. et al. 1994, AJ, 108, 446 23, 89

Hunter, D. A., & Gallagher, J. S., III 1992, ApJ, 391, L9 4

Hunter, D. A. & Elmegreen, B. G. 2004, AJ, 128, 2170 4, 10, 31, 33, 36, 78

Hunter, D. A. & Elmegreen, B. G. 2006, ApJS, 162, 49 31, 33, 82, 83, 116, 120

Hunter, D. A., Elmegreen, B. G., & Ludka, B. C. 2010, AJ, 139, 447 33

Hunter, D. A., Ficut-Vicas, D., Ashley, T. et al. 2012, AJ, 144, 134 31, 36, 70, 76, 78, 92, 108, 144, 189

Huynh, M. T., Hopkins, A. M., Lenc, E., et al. 2012, MNRAS, 426, 2342 81, 82

Illingworth, G. D., Magee, D., Oesch, P. A., et al. 2013, ApJS, 209, 6 8

Indebetouw, R., Matsuura, M., Dwek, E., et al. 2014, ApJ, 782, LL2 6

Irwin, J. A., Brar, R. S., Saikia, D. J. & Henriksen, R. N. 2013, MNRAS, 433, 2958 6, 9, 26, 104

Jansky, K. G. 1933, Nature, 132, 66 20

Kennicutt, R. C., Jr., & Kent, S. M. 1983, AJ, 88, 1094 4

Kennicutt, R. C., Jr. 1998, ApJ, 498, 541 4, 32

Kennicutt, R. C., Jr., Armus, L., Bendo, G., et al. 2003, PASP, 115, 928 6

Kennicutt, R. C., Jr., Lee, J. C., Funes, S. J., José G., Sakai, S., & Akiyama, S. 2008, ApJS, 178, 247 4

Kennicutt, R. C., & Evans, N. J. 2012, ARA&A, 50, 531 4

Kepley, A. A. and Mühle, S. and Everett, J. and Zweibel, E. G. and Wilcots, E. M. and Klein, U., 2010, ApJ, 712, 536 24, 25, 69, 140, 162, 163

Kepley, A. A., Zweibel, E. G., Wilcots, E. M., Johnson, K. E. & Robishaw, T. 2011, ApJ, 736, 139 24, 25, 69, 89, 118, 140

Klein, U., Weiland, H. & Brinks, E. 1991, A&A, 246, 323 28, 68

Klein, U., Giovanardi, C., Altschuler, D. R. & Wunderlich, E. 1992, A&A, 255, 49 23, 89

Klein, U. 1986, A&A, 168, 65 23, 89, 90

Koda, J., Yagi, M., Boissier, S. et al. 2012, ApJ, 749, 20 29, 68, 96

Kroupa, P. 2001, MNRAS, 322, 231 16, 17, 118, 124, 126, 151

Kunth, D., Östlin, G. 2000, A&A Rev., 10, 1 8

van der Kruit, P. C., & Allen, R. J. 1976, ARA&A, 14, 417 23

Lacki, B. C., Thompson, T. A. & Quataert, E. 2010, ApJ, 717, 1 2, 28, 68, 108, 129, 171

Lee, J. C., Gil de Paz, A., Tremonti, C., et al. 2007, Bulletin of the American Astronomical Society, 39, 895 5

Lee, J. C., Gil de Paz, A., Tremonti, C. et al. 2009, ApJ, 706, 599 5, 29, 68, 69, 92, 96, 105, 109, 166

Leitherer, C., Schaerer, D., Goldader, J. D., et al. 1999, ApJS, 123, 3 118

Leroy, A. K., Walter, F., Brinks, E., et al. 2008, AJ, 136, 2782 3

Leroy, A. K., Bigiel, F., de Blok, W. J. G. et al. 2012, AJ, 144, 3 3, 4, 6, 9, 77, 92, 94, 95, 98, 99, 112, 118, 124, 125, 127, 150, 152, 189, 191, 195, 196, 197, 198, 199, 200, 201, 202, 203, 204, 205, 206, 210, 211, 212, 213, 215, 216, 218, 222, 223, 224, 225, 226, 229, 230

Leverenz, H., & Filipović, M. D. 2013, Ap&SS, 343, 301 24, 69

Li, Y., Calzetti, D., Kennicutt, R. C. et al. 2010, ApJ, 725, 677 26, 68

Lintott, C. J., Schawinski, K., Slosar, A., et al. 2008, MNRAS, 389, 1179 8

Lisenfeld, U., Voelk, H. J., & Xu, C. 1996, A&A, 306, 677 171

Lisenfeld, U. & Ferrara, A. 1998, ApJ, 496, 145 5, 68, 69

Lisenfeld, U., Wilding, T. W. & Pooley, G. G. and 2004, MNRAS, 349, 1335 24, 25, 26, 69, 89, 91, 118, 140, 162

Longair, M. S. 1981, High Energy Astrophysics, Cambridge University Press 10, 106, 134, 151, 175, 183

MacKenty, J. W., Maíz-Apellániz, J., Pickens, C. E., Norman, C. A., & Walborn, N. R. 2000, AJ, 120, 3007 163

Maeder, A. & Meynet, G. 1989, A&A, 210, 155 13

Martin, N. F., Ibata, R. A., Chapman, S. C., Irwin, M. & Lewis, G. F. 2007, MNRAS, 380, 281 79

Mateo, M. L. 1998, ARA&A, 36, 435 79

Mathewson, D. S., Healey, J. R., & Rome, J. M. 1962, Australian Journal of Physics, 15, 369 21

Mathewson, D. S., & Healey, J. R. 1964, The Galaxy and the Magellanic Clouds, 20, 245 22

Mathewson, D. S., & Healey, J. R. 1964, The Galaxy and the Magellanic Clouds, 20, 245 22

McMullin, J. P., Waters, B., Schiebel, D., Young, W., & Golap, K. 2007, Astronomical Data Analysis Software and Systems XVI, 376, 127 52

Murphy, E. J. 2009, ApJ, 706, 482 2

Murphy, E. J., Condon, J. J., Schinnerer, E. et al. 2011, ApJ, 737, 67 2, 13, 18, 90, 140

Murphy, E. J., Bremseth, J., Mason, B. S., et al. 2012, ApJ, 761, 97 7, 118

Niklas, S., Klein, U. & Wielebinski, R. 1997, A&A, 322, 19 91

Niklas, S., & Beck, R. 1997, A&A, 320, 54 17, 140

Oesch, P. A., Brammer, G., van Dokkum, P. G., et al. 2016, ApJ, 819, 129 7, 166

Oey, M. S., Meurer, G. R., Yelda, S., et al. 2007, ApJ, 661, 801 4

Padovani, P. 2011, MNRAS, 411, 1547 2, 78

Parker, E. N. 1966, ApJ, 145, 811 21, 29

Papadopoulos, P. P. 2010, ApJ, 720, 226 68

Ploeckinger, S., Recchi, S., Hensler, G., & Kroupa, P. 2015, MNRAS, 447, 2512 29, 68, 69

Pooley, G. G. 1969, MNRAS, 144, 101 21, 22

Price, R. & Duric, N. 1992, ApJ, 401, 81 23, 27, 68, 97

Purcell, E. M. 1963, Berkeley Physics Course, New York: McGraw-Hill, 1963, edited by Purcell, Edward M., 175

Rau, U. & Cornwell, T. J. 2011, A&A, 532, A71 63, 71, 143

Reber, G. 1944, ApJ, 100, 279 21

Reynolds, S. P. 2008, ARA&A, 46, 89 13, 125

Roychowdhury, S. & Chengalur, J. N. 2012, MNRAS, 423, L127 23, 28, 69, 91, 107, 129

Schlafly, E. F., & Finkbeiner, D. P. 2011, ApJ, 737, 103 18

Schlegel, D. J., Finkbeiner, D. P. & Davis, M. 1998, ApJ, 500, 525 18

Skillman, E. D., Kennicutt, R. C., & Hodge, P. W. 1989, ApJ, 347, 875 32

Skrutskie, M. F., Cutri, R. M., Stiening, R., et al. 2006, AJ, 131, 1163 6

Srivastava, S., Kantharia, N. G., Basu, A., Srivastava, D. C., & Ananthakrishnan, S. 2014, MNRAS, 443, 860 163

Strong, A. W., Moskalenko, I. V., & Ptuskin, V. S. 2007, Annual Review of Nuclear and Particle Science, 57, 285 13

Stil, J. M. & Israel, F. P. 2002, A&A, 389, 29 75, 90

Stinson, G. S., Dalcanton, J. J., Quinn, T., Kaufmann, T. & Wadsley, J. 2007, ApJ, 667, 170 29, 69, 86, 115

Tabatabaei, F. S., Berkhuijsen, E. M., Frick, P., Beck, R., & Schinnerer, E. 2013, A&A, 557, AA129 18, 19, 140

Tabatabaei, F. S., Schinnerer, E., Murphy, E. J., et al. 2013, A&A, 552, AA19 19, 107, 108

Taylor, G. B., Carilli, C. L., & Perley, R. A. 1999, Astronomical Society of the Pacific Conference Series, 180, Synthesis Imaging in Radio Astronomy II 47

Tongue, T. D., & Westpfahl, D. J. 1995, AJ, 109, 2462 90

Toomre, A. 1964, ApJ, 139, 1217 3

Tully, R. B., & Fisher, J. R. 1977, A&A, 54, 661 32

Valiante, R., Schneider, R., Bianchi, S., & Andersen, A. C. 2009, MNRAS, 397, 1661 6

Van Eck, C. L., Brown, J. C., Shukurov, A., & Fletcher, A. 2015, ApJ, 799, 35 131

Völk, H. J. 1989, A&A, 218, 67 26, 68, 171

Walter, F., Brinks, E., de Blok, W. J. G., et al. 2008, AJ, 136, 2563 3

Weidner, C. & Kroupa, P. 2005, ApJ, 625, 754 5, 69

White, R. L., Becker, R. H., Helfand, D. J. & Gregg, M. D. 1997, ApJ, 475, 479 23

Wilson, T. L., Rohlfs, K., Hüttemeister, S. 2009, Tools of Radio Astronomy, by Thomas L. Wilson; Kristen Rohlfs and Susanne Hüttemeister. ISBN 978-3-540-85121-9. Published by Springer-Verlag, Berlin, Germany 10, 51, 55

Wright, E. L. 2006, PASP, 118, 1711 7

Wyder, T. K., Martin, D. C., Schiminovich, D. et al. 2007, ApJS, 173, 293 5, 29, 68

Wynn-Williams, C. G. & Becklin, E. E. 1986, ApJ, 308, 620 89

Xu, C. 1990, ApJ, 365, L47 68

Yan, L., Donoso, E., Tsai, C.-W., et al. 2013, AJ, 145, 55 2

Yun, M. S., Reddy, N. A. & Condon, J. J. 2001, ApJ, 554, 803 xviii, 6, 26, 28, 67, 68, 97, 98, 99, 100, 101, 102, 103, 104, 109, 167

Zhang, H.-X., Hunter, D. A., Elmegreen, B. G., Gao, Y. & Schruba, A. 2012, AJ, 143, 47 36, 76

Zhukovska, S., & Henning, T. 2013, A&A, 555, AA99 6